

**PREDICTING GRANULAR GROWTH PROCESSES:
MODEL DEVELOPMENT, IMPLEMENTATION AND
ASSESSMENT FOR INDUSTRIAL APPLICATIONS**

by

ASHUTOSH TAMRAKAR

A dissertation submitted to the

School of Graduate Studies

Rutgers, The State University of New Jersey

in partial fulfillment of the requirements

for the degree of

Doctor of Philosophy

Graduate Program in Chemical & Biochemical Engineering

Written under the direction of

Rohit Ramachandran

and approved by

New Brunswick, New Jersey

May, 2019

© 2019

Ashutosh Tamrakar

ALL RIGHTS RESERVED

ABSTRACT OF THE DISSERTATION

Predicting Granular Growth Processes: Model Development, Implementation and Assessment for Industrial Applications

by Ashutosh Tamrakar

Dissertation Director: Rohit Ramachandran

Growth of granular particles - whether desired or undesired - are quite common in various industrial operations from agro-chemical manufacturing to pharmaceutical product development to food and fine/specialty chemicals production. As such, their related problems and methods to predict their behavior have been widely discussed in various engineering fields. This work provides an in-depth description of the development, implementation and assessment of various predictive tools and techniques of granular growth processes including use of dimensionless groups, advanced computational models as well as multi-scale frameworks to improve the performance of these models. This study presents a comprehensive look at the current state-of-the-art computational techniques used in granular and multi-phase flows and presents a practical framework for incorporating design-based principles and developing predictive model-based analysis to understand granular processes through case studies. In the following thesis, three case studies involving manufacturing issues encountered in common unit operations are highlighted: (i) generation of undesired agglomeration during agitated filter-drying, (ii) formation of high/ low viscous regions during high-shear wet granulation with wet and dry binder addition, and (iii) prediction of granule size during top-spray fluidized

bed wet granulation. The frameworks presented in this study demonstrate a pragmatic process model development methodology by efficiently coupling multi-scale/multi-phase simulations and numerical techniques which can be used for effective process design, development and scale-up purposes.

Acknowledgements

My PhD career has really been a life-altering journey for me and I have many people whom I need to thank for their continued support and guidance through these years.

I would first like to thank my dissertation advisor, Dr. Rohit Ramachandran, for his counsel, support, and (foremost) patience while dealing with me. The opportunity to work on various industrial projects wouldn't have been possible without his encouragement. I would also like to thank my committee members for their thoughtful feedback through out the dissertation process: Dr. Marianthi Ierapetritou, Dr. Benjamin Glasser, Dr. Nina Shapley and Dr. Patrick M. Piccione (Syngenta).

Co-authors contributing to the publications featured in this dissertation include Dr. Patrick M. Piccione (Syngenta), Dr. Alfeno Gunadi (Syngenta), Dr. Alex Zheng (Syngenta), Dr. Dana Barrasso (PSE), Dr. Rohit Ramachandran (Rutgers), Dheeraj R. Devarampally (Rutgers), Sheng-Wen Chen (Rutgers), Subhodh Karkala (Rutgers) and Daniel Schankel (Rutgers).

I would like to thank the Process Studies Group (Technology and Engineering) at the Jealott's Hill International Centre, Syngenta Ltd. (Berkshire, UK) who contributed to discussions on this work including Martin Rudolph, Andrew Quarmby, Bevis Privett, Elin Rundquist, Michael Tebboth, Christophe Grosjean, Anita Rea, and Federica Cattani. In addition, I would also like to thank the team at the Drug Product Science and Technology, Bristol-Myers Squibb, New Brunswick, NJ, USA for providing information and technical discussions from their work: Preetanshu Pandey, Ajit Narang, Christopher Lewins, Steve Pafiakis, Brian Zacour, Dilbir S. Bindra, Jade Trinh, David Buckley, Shruti Gour, Shasad Sharif, Howard Stamato, Li Tao, Junshu Zhao, Jinjiang Li and Munir Hussain.

The following group members and colleagues at Rutgers have influenced this work:

Dr. Maitraye Sen, Dr. Anwesha Chaudhury, Dr. Ravendra Singh, Dr. Sarang Oka, Dr. Anik Chaturbedi, Shashank Venkat Muddu, Chandra Kanth Bandi, Nirupaplava Metta, Yuktेशwar Baranwal, Chaitanya Sampat, Indu Muthancheri and Franklin Bettencourt. In addition, I would also like to thank the brilliant undergraduates at Rutgers for their support with my work: Jinal Darji, Melissa Piccirillo, Michael Lemenze, Tripti Agrawal and Ryan Belfer.

This work was financially supported by Process Studies Group at Syngenta Ltd. (Berkshire, UK) and the National Science Foundation CAREER program through grant no. 1350152. I would also like to thank the Small Molecules Pharmaceutical Sciences Group at Genentech Inc. (South San Francisco, CA) and the Process Analytical Technology (US-PAT) Group at GlaxoSmithKline (Upper Merion, PA) for providing me with internship opportunities to financially support myself during my PhD career. In addition to their financial support, both Genentech and GlaxoSmithKline have given me countless opportunities to develop my skills and apply the theoretical concepts in industrial projects for which I am truly grateful.

Lastly, I would like to thank my family and friends, who were always around to encourage me. And to my lovely wife, Veronica Tamrakar, who inspires me everyday.

Dedication

This thesis is dedicated to my late parents,
Nhuchhe Ram Tamrakar and Sharada Tamrakar,
who cherished education above all.

Table of Contents

Abstract	ii
Acknowledgements	iv
Dedication	vi
List of Tables	xiii
List of Figures	xv
1. Introduction	1
1.1. Granular processes and the need for model development	1
1.2. Granular Process Modeling	2
1.2.1. Different Modeling Techniques	5
1.2.1.1. Granule Growth Regime Map	5
1.2.1.2. Population Balance Modeling (PBM)	7
1.2.1.3. Discrete Element Modeling (DEM)	10
1.2.1.4. Computational Fluid Dynamics (CFD)	13
1.2.1.5. Coupled PBM-DEM modeling	14
1.2.1.6. Coupled CFD-DEM modeling	15
1.2.2. Objectives of this work	16
I Specific Aim I: Development, Implementation and Assessment of using Dimensionless Groups to Predict Granule Growth Behavior	18
1.3. Overview	19
1.4. Publications	20

2. Using dimensionless groups to predict undesired granule growth behavior during agitated filter drying	21
2.1. Background	21
2.1.1. Isolation and drying of particulate products	21
2.1.2. Agitated filter drying	22
2.1.3. Particle Agglomeration Issues	25
2.1.4. Objectives	28
2.2. Development and Implementation of Granule Growth Regime Map for Agitated Drying	29
2.2.1. Granule Growth Regime Map	29
2.2.2. Granule Characterization Experiments	30
2.2.3. Granule Growth Regime Map Analysis	30
2.3. Parametric Study to Assess the Granule Growth Regime Map Predictions	36
2.3.1. Parametric Study: Bench-scale Agitated Drying Experiments . .	36
2.3.2. Parametric Study Analysis	40
2.3.2.1. Influence of residual liquid amount (liquid to solid ratio)	40
2.3.2.2. Influence of agitation	44
2.3.2.3. Influence of solvent choice	48
2.4. Conclusions	52
 II Specific Aim II: Development, Implementation and Assessment of using Mechanistic Studies to Understand Underlying Mechanisms of Granular Growth Processes	54
2.5. Overview	55
2.6. Publications	56
 3. Investigating particle-level dynamics in a lab-scale agitated filter dryer (AFD) using Discrete Element Method (DEM)	57
3.1. Background	58

3.1.1.	Agitated filter drying	58
3.1.2.	Modeling of agitated drying	60
3.1.3.	Objectives	64
3.2.	Model Development	65
3.2.1.	Contact force calculations	67
3.2.2.	Cohesion force calculation	68
3.2.3.	Heat Conduction calculation	72
3.2.4.	Particle Motion and Temperature analysis	73
3.2.5.	In-silico scale-up design	74
3.2.6.	Normalized parameter approach	78
3.3.	Effect of Material Parameters on the particle-scale dynamics	80
3.3.1.	Primary particle shape	80
3.3.2.	Primary particle size	81
3.3.3.	Effect of moisture content	82
3.3.4.	Effect of wash liquid type	83
3.4.	Effect of Operating Parameters on the particle-scale dynamics	84
3.4.1.	Effect of agitator design	84
3.4.2.	Effect of impeller movement	85
3.4.3.	Effect of agitation rate	86
3.4.4.	Effect of fill level	87
3.5.	Effect of Scale-up using different scaling constants on particle-scale dynamics	89

4.	Using DEM to quantitatively compare the effect of wet and dry binder addition in high-shear wet granulation processes	93
4.1.	Background	94
4.1.1.	Wet granulation process	94
4.1.2.	Modes of binder addition	95
4.1.3.	Objectives	96

4.2. Mathematical Model Development	98
4.2.1. DEM Configuration	98
4.2.1.1. DEM system design	100
4.2.1.2. Particle types and interaction	101
4.2.2. Contact force calculations	104
4.2.3. Cohesion force calculations	106
4.2.4. Body force calculations	109
4.2.5. Particle motion and position analysis	112
4.2.6. DEM model limitations	113
4.3. Experimental data	113
4.4. Comparative analysis between wet binder addition and dry binder addition	115
4.4.1. Differences between distribution of surface liquid viscosities . . .	120
4.4.2. Differences between the magnitude of liquid bridge forces . . .	124
4.4.3. Differences between distribution of average particle velocity . . .	125
4.4.4. Differences between particle collision frequencies and size of ag-	
glomerates	129
4.5. Conclusion	132

III Specific Aim III: Development, Implementation and Assessment of using Multi-scale Hybrid Models to Relate Particle-level Mechanisms to Bulk Behavior. 134

4.6. Overview	135
4.7. Publications	137

5. Multi-scale framework development of a fluidized bed wet granulation process 138

5.1. Background	139
5.1.1. Fluidized bed granulation	139
5.1.2. Fluidized bed granulation models	139

5.1.3. Objectives	143
5.2. Hybrid model development	144
5.2.1. Particle-scale: CFD-DEM simulations	145
5.2.2. Meso-scale: Two compartment PBM	148
5.2.3. Coupling of CFD-DEM outputs into PBM	152
5.3. Model Results and Discussion	157
5.3.1. Effect of liquid addition and air flow on particle diameter	157
5.3.2. Effect of liquid addition and air flow on average liquid content .	158
5.3.3. Effect of liquid addition and air flow on particle size distribution	159
5.4. Conclusion	160

6. Implementation and validation of a 3D CFD-DEM-PBM coupled top-spray fluidized bed wet granulation model	162
6.1. Objectives	163
6.2. CFD-DEM-PBM Model Development	163
6.2.1. System configuration	165
6.2.2. System scaling	168
6.2.3. CFD-DEM model equations	172
6.2.4. PBM model equations	175
6.3. CFD-DEM-PBM simulation design:	181
6.3.1. CFD-DEM simulations	181
6.3.2. PBM calculations	184
6.4. Validation experimentation	188
6.4.1. Experimental method	188
6.4.2. Response variables	189
6.5. Results and discussion	191
6.5.1. Impact on particle flow and circulation dynamics	191
6.5.2. Impact on particle collision dynamics	196
6.5.3. Impact on particle wetting and drying dynamics	199

6.5.4. Comparison with experimental data	204
6.6. Conclusions	209
 IV Conclusion	 212
 V Acknowledgment of Previous Publications	 216
 Bibliography	 218

List of Tables

2.1. Thermophysical properties of the pure solvents used in parametric study	37
2.2. Design space used in the parametric study of agitated drying	39
3.1. Design and operation variables in base case DEM simulation	65
3.2. Mathematical expressions for particle force calculation in DEM Particles model*	69
3.3. Parameters used in scaled AFD simulations	77
4.1. Operation variables changes before and after scale-down.	102
4.2. Input variables for the DEM simulation.	103
4.3. Customized combinations of interactions between different particle types in DEM	104
5.1. Physical properties of particles and equipment used in DEM-CFD simu- lation	149
6.1. Overview of CFD-DEM simulation configuration	167
6.2. Particle and fluid properties used for the scaled system in the CFD-DEM simulations	171
6.3. Design space for the CFD-DEM simulations	182
6.4. PBM granule size grid configuration	185
6.5. Process parameters and initial conditions used in PBM calculations . . .	186
6.6. Design of experiments for the fluidized bed granulation experiments . .	189
6.7. Geometric mean diameter and standard deviation of unmilled samples collected during granulation	190
6.8. Error in prediction of granule geometric mean diameter	208
6.9. Summary of impact of operating air flow rate on FBG operation	210
6.10. Summary of impact of operating air temperature on FBG operation . .	211

6.11. Summary of impact of operating binder spray rate on FBG operation . 211

List of Figures

1.1. Multiscale map of modeling granular processes.	3
1.2. Granule growth regime map developed by Iveson and Litster.	6
1.3. Discrete element method algorithm: Inputs, calculations and outputs . .	13
1.4. PBM-DEM coupled framework: Multi-scale model development through use of DEM feeding particle-level information to PBM which in turn provides the macroscopic data back to DEM.	15
1.5. Two-way DEM-CFD coupled framework: Information about particle mo- mentum, mass and energy is transferred between the two particle-level modeling techniques	16
2.1. Schematic of different operating stages of agitated filter drying process.	24
2.2. Experimental setup for granule yield strength test measurement.	31
2.3. Characterization of pseudo-granules developed for regime map analysis.	32
2.4. Prediction of granule growth mechanism using regime map analysis for different APAP-solvent systems.	34
2.5. Schematic of the bench-scale agitated drying apparatus.	38
2.6. Mean particle diameter, D_{50} , dynamic agglomeration profile of APAP- Methanol samples over time. Solvent type and agitation (50 rpm) held constant while varying L/S ratio.	41
2.7. EYECON images of the particulate sample over time with different L/S ratio of APAP with Methanol. Solvent type and agitation (50 rpm) held constant.	42
2.8. Dynamic profiles of APAP-Methanol samples over time with varying L/S ratio.	43

2.9. Aspect ratio of APAP-Methanol samples over time with varying L/S ratio. Bar plots represent aspect ratio values and overhead line plots outline the relative standard deviation of aspect ratio.	44
2.10. Comparison of A. Median particle diameter, D_{50} and B. Particle bed temperature profiles of APAP-Methanol samples over time with and without agitation.	45
2.11. EYECON images of the APAP-Methanol samples over time with different L/S ratio and without agitation.	46
2.12. Mean particle diameter, D_{50} , profile of APAP-solvent samples over time with and without agitation. L/S ratio and impeller speed are held constant at 15% and 50 RPM respectively.	47
2.13. A. Mean particle diameter, D_{50} B. Moisture content and C. Aspect ratio (with RSD) of agglomerate samples over time with different residual solvents. Runs were performed at 15% initial L/S ratio and with agitation (50rpm). Note for C. Bar plots represent aspect ratio values and overhead line plots outline the relative standard deviation of aspect ratio.	48
2.14. EYECON images of samples over time with different residual solvents. Runs performed at 15% L/S ratio and with agitation (50rpm)	49
2.15. Effect of APAP concentration on A. Solvent boiling point (C) from McLoughlin et al. (2003) B. Solvent kinematic viscosity (cSt) calculated from data presented in Ålander and Å. C. Rasmuson (2005), Rajagopal and Renold (2015) and Shaikh et al. (2011)	50
2.16. Mean particle diameter, D_{50} , dynamic agglomeration profile of APAP-Ethanol samples over time. Solvent type and agitation (50 rpm) held constant while varying L/S ratio.	51
3.1. Multitude of interacting parameters that influence agglomeration/attrition in agitated filter dryers	61

3.2.	Discrete Element Method (DEM) algorithm implemented in this study. In order to simulate the wet granular flow and heat transfer mechanics in the agitated drying system, a virtual liquid bridge model and a heat con- duction contact models were integrated into the DEM algorithm (added steps highlighted)	66
3.3.	Geometry of the 2L lab-scale agitated filter dryer. A. Experimental Agitated filter dryer setup (ProCept, Belgium) B. CAD drawing used in the DEM simulation of 2L lab-scale agitated filter dryer.	67
3.4.	Illustration of the internal particle flow and temperature distribution. Figures not to scale Top Flow colored based on particle velocities: lower velocity (in green), higher velocity (in red). Bottom Flow colored based on particle temperatures: Low temp (in blue then green), high temp (in red)	75
3.5.	DEM data sampling schematic. A. DEM data obtained from 2 levels of the particle bed. B. Data extracted from one quarter of the vessel . . .	76
3.6.	Different scales of filter dryer investigated in the DEM simulations (Top). The corresponding impeller rotation values and tip speed used according to different scaling indices (Bottom)	77
3.7.	Schematic for the normalization procedure used for comparing key particle- scale variables using a scaling index. An example of particle velocity information obtained from simulating the different scales of filter dryer using constant Reynolds number criteria is presented.	79
3.8.	Various shapes of granules formed during the bench-scale study of the AFD	80
3.9.	A. Different types of particle shapes simulated in DEM. The aspect ratio of particles and the principal diameter are provided. B. Effect of the particle shape on the average particle velocities and compression forces	81

3.10. A. Two different particle size distributions with average diameter of 5.4 mm and 2.7 mm were investigated in DEM. The effect of these particle size distribution on B. Average particle velocities, C. Average compression forces and D. Torque experienced by the impeller are provided. . .	82
3.11. Effect of moisture content of the powder bed (0, 5 and 15 %wt./wt. liquid) on the average particle velocities within the filter dryer. Six independent DEM simulations were performed at 3 different liquid content levels and 2 different fill levels (low fill: 65 vol% loading and high fill: 95 vol% loading). The average particle velocities were extracted at 3 layers within the filter dryer (as shown on the legend)	83
3.12. Effect of solvent properties – specific heat capacity and boiling point – on the maximum particle temperature observed in the filter cake. Two levels of solvent volume are investigated (at 5 and 15 %wt./wt. liquid) using values of pure Methanol and pure Ethanol solvents.	84
3.13. A. Three different impeller designed were simulated in DEM with a constant rotation rate of 50 RPM. The effect of impeller design on B. Average particle velocity magnitude, C. Average axial particle velocities.	85
3.14. A. The rotational directions of the impeller as it is lowered into the cake (in 2s time interval) B. Schematic of the impeller as it plies through the powder bed. The effect of CW and ACW rotation of the impeller as it is lowered on C. average particle velocities D. average compressive forces and E. bed voidage	86
3.15. A. The rotational directions of the impeller as it is removed from the cake. B. Schematic of the impeller as it plies through the powder bed. The effect of CW and ACW rotation of the impeller as it is removed on C. average particle velocities D. average compressive forces and E. bed voidage	87
3.16. Effect of impeller speed on the average particle velocities. Three impeller rotation rates at 10 RPM, 30 RPM and 60 RPM were investigated in DEM.	88

3.17. Two different particle fill levels at 65 <i>vol%</i> and 95 <i>vol%</i> were investigated in DEM. The effect of powder loading on A. Average particle velocities, B. Average compression forces are provided.	88
3.18. Effect of scale-up on the internal particle flow dynamics: X-, Z- and Angular velocity	89
3.19. Effect of scale-up on the collision and shear dynamics: relative collision velocity, no. of collisions and impeller torque	90
3.20. Effect of scale-up on the forces and energies dynamics: compressive forces, avg. kinetic energy and particle temperature	91
3.21. Scaling map for normalized granular flow parameters based on different scaling indices	92
4.1. Discrete Element Method (DEM) algorithm used in the study. The implementation of liquid addition, binder dissolution and liquid bridge forces unique to this work are highlighted.	99
4.2. DEM geometry of the 1-liter high shear granulator.	102
4.3. A flow sheet of how dissolution of the binder impacts the granulation. .	111
4.4. Effect of binder concentration on the viscosity, surface tension and contact angle of the solution. Data based on properties of hydroxypropyl cellulose binder obtained from literature Ashland (2012); Chang and Gray (1978); Mezdour et al. (2007); Pelofsky (1966).	112
4.5. Comparative differences between WBA and DBA system seen through experiment and numerical model developed by Chaturbedi et al. (2017). (Re-printed with permission of the author)	114
4.6. DEM snapshot of simulations with Wet Binder Addition (WBA) and Dry Binder Addition (DBA) systems colored by the viscosity value of the fluid in the particles. Note: the un-wetted particles are a fixed color of grey, the binder particles are fixed color of red, the free liquid droplets are a fixed color of green and only wetted granule particles vary in shades of blue.	116

4.7. The liquid content and binder dissolution curves in the Dry Binder Addition (DBA) system.	119
4.8. The liquid balance in WBA and DBA systems.	120
4.9. Distribution of granules with high ($\mu > 0.02Pa.s$) and low ($\mu \leq 0.02Pa.s$) viscosity of external liquid.	120
4.10. Average viscosity of high/low viscosity particles in the two systems. . .	121
4.11. Average viscosity of liquid in granules over the granulator height. The viscosity distribution profile at different time points (5s, 10s, 20s, 30s and 40s) are plotted in the same graph. The height of the vessel as well as height till the tip of the impeller are annotated.	122
4.12. Average viscosity of liquid in granules at different distance from the center of the granulator. The viscosity distribution profile at 5s, 10s, 20s, 30s and 40s time points are plotted in the same graph. The span of the impeller, the radius of the vessel as well as the position of the liquid spray nozzle area annotated.	123
4.13. Distribution of binder particle and liquid droplets seen from a top view of the granulator for a DBA system over time.	123
4.14. Capillary number (Ca) of the two systems over time.	125
4.15. Average magnitude of the liquid bridge force holding granules together in the two systems over time.	126
4.16. Average velocity of granules in the two system. Granules with high viscosity surface liquid and low viscosity surface liquid are differentiated.	126
4.17. Velocity profile of granules in Wet Binder Addition system showing dead zones with lowest particle velocities. Note: Snapshots are taken from the bottom of the granulator.	128
4.18. Sectional view of the granulator for both systems at $t = 40s$. Particles are colored based on individual particle velocities.	129
4.19. Collision frequency profiles of the two systems over time. Collision frequency of high/low viscosity granules in both systems are separated. . .	130

4.20. Average number of liquid bridges in place for a single granule over time.	131
5.1. Schematic of PBM-DEM-CFD multi-scale approach.	145
5.2. Schematic showing the equipment setup in the DEM-CFD model	146
5.3. Particle size distribution used in DEM-CFD simulations	148
5.4. Schematic diagram of the two compartments in fluidized bed granulation.	150
5.5. Determination of height of dry compartment using position of free liquid droplets from DEM-CFD simulation.	152
5.6. Fraction of total powder particles in spray/wet zone over time.	154
5.7. Size-dependent transfer rate of particles between the two compartments.	155
5.8. Collision frequency plot for 8m/s air flow rate (left column) and 10m/s (right column). Spray or wet compartments are illustrated in top row and the dry compartment are shown in the bottom row.	156
5.9. Median particle diameters (d_{50}) for different process parameters over time. Air flow rates are separated through columns and liquid addition rate are divided into different rows.	157
5.10. Average liquid content in each compartment for different process param- eters over time. Air flow rates are separated through columns and liquid addition rate are divided into different rows.	159
5.11. Final particle size distribution for different process parameters. Air flow rates are separated through columns and liquid addition rate are divided into different rows.	160
6.1. Schematic of the PBM-CFD-DEM multi-scale hybrid framework. Data transfer between Computational Fluid Dynamics (CFD) and Discrete El- ement Method (DEM) are coupled using a two-way approach while data from CFD-DEM are transferred one-way to a 2-compartmental Popula- tion Balance Model (PBM).	164

6.2. Geometry of the simulated fluidized bed granulator. The position of the virtual spray zone as well as the demarcation of the two PBM compartments are differentiated. For the CFD-DEM simulations, only the shaded portion of the schematic were rendered as the domain region.	166
6.3. Pressure drop across the fluidized bed for different inlet air flow rates. The theoretical ΔP expected for the system is shown in black dashed line. Inset view: Comparison of time-averaged pressure drop across all simulated conditions.	183
6.4. Snapshots of the CFD-DEM simulation captured every 1s for Sim# 3 showing bubbling fluidization. The snapshots are sliced along the X-Z plane and colored according to instantaneous particle velocities.	183
6.5. PBM update schematic. The mechanistic parameters in PBM were updated every 100g of binder added to match with the experimental methodology.	187
6.6. Mechanistic data used in the PBM rate kernels. Results from the CFD-DEM simulations performed with 80, 110 and 130 m^3/h flow rates were interpolated.	187
6.7. Instantaneous air flow velocities (Top) and solids volume fractions (Bottom) at different air flow rates (Q_g) at $T_g = 303$ K. (A) $Q_g = 80 m^3/h$, $t = 10$ s, (B) $Q_g = 110 m^3/h$, $t = 10$ s, and (C) $Q_g = 130 m^3/h$, $t = 10$ s, (D) $Q_g = 80 m^3/h$, $t = 10$ s, (E) $Q_g = 110 m^3/h$, $t = 10$ s, and (F) $Q_g = 130 m^3/h$, $t = 10$ s. The dashed lines represent demarcation of the Top and Bottom compartments.	192
6.8. Instantaneous particle velocities and positions at different air flow rates (Q_g) at $t = 10$ s and $T_g = 303$ K. (A) $Q_g = 80 m^3/h$, (B) $Q_g = 110 m^3/h$ and (C) $Q_g = 130 m^3/h$	192
6.9. Time-averaged particle velocities (v_p) at different inlet air flow rates (Q_g) and at different inlet air temperatures (T_g)	193
6.10. Time-averaged division of total particle number over top and bottom compartments at different initial conditions.	194

6.11. Time-averaged particle transfer ratio from one compartment to the other at different air flow rates and inlet air temperatures.	196
6.12. Comparison of particle collision frequencies (collisions per particle per particle sec) in Top and Bottom compartments over time at different inlet air flow rate (Q_g) conditions. $T_g = 303\text{K}$. The time-averaged mean values are plotted as dotted red lines.	197
6.13. Comparison of time-averaged particle collision frequencies ($C_{P,1}$) over bottom and top compartments at different inlet conditions.	198
6.14. Comparison of time-averaged particle collision energies (E_c) over bottom and top compartments at different inlet conditions.	199
6.15. Instantaneous particle residence time (RT_p) inside the spray zone at dif- ferent air flow rates (Q_g) at $T_g = 303\text{ K}$. (A) $Q_g = 80\text{ m}^3/\text{h}$, $t = 2\text{ s}$, (B) $Q_g = 110\text{ m}^3/\text{h}$, $t = 2\text{ s}$, and (C) $Q_g = 130\text{ m}^3/\text{h}$, $t = 2\text{ s}$, (D) Q_g $= 80\text{ m}^3/\text{h}$, $t = 10\text{ s}$, (E) $Q_g = 110\text{ m}^3/\text{h}$, $t = 10\text{ s}$, and (F) $Q_g = 130$ m^3/h , $t = 10\text{ s}$	200
6.16. Progression of particle residence time distribution inside the spray zone over time. $Q_g = 110\text{ m}^3/\text{h}$, $T_g = 303\text{ K}$	201
6.17. Particle residence time distributions inside the spray zone at different inlet air flow rates for the Top and Bottom compartments. The mean residence time is annotated.	202
6.19. 'Average rate of change in particle temperatures, \Re_{T_p} '	202
6.18. Instantaneous particle temperatures at different inlet air temperatures (T_g). (A) $Q_g = 80\text{ m}^3/\text{h}$, $T_g = 303\text{ K}$, $t = 2\text{ s}$, (B) $Q_g = 80\text{ m}^3/\text{h}$, T_g $= 323\text{ K}$, $t = 2\text{ s}$, (C) $Q_g = 80\text{ m}^3/\text{h}$, $T_g = 303\text{ K}$, $t = 10\text{ s}$, and (D) $Q_g = 80\text{ m}^3/\text{h}$, $T_g = 323\text{ K}$, $t = 10\text{ s}$	203
6.20. Average air temperatures within the fluidized bed at $T_g = 303\text{ K}$. (A) $Q_g = 80\text{ m}^3/\text{h}$, $t = 2\text{ s}$, (B) $Q_g = 110\text{ m}^3/\text{h}$, $t = 2\text{ s}$, (C) $Q_g = 130$ m^3/h , $t = 2\text{ s}$, (D) $Q_g = 80\text{ m}^3/\text{h}$, $t = 10\text{ s}$ (E) $Q_g = 110\text{ m}^3/\text{h}$, $t = 10$ s and (F) $Q_g = 130\text{ m}^3/\text{h}$, $t = 10\text{ s}$	205

6.21. Validation of CFD-DEM-PBM framework through comparison with experimental data for Batch #5, #6 and #9: Geometric mean diameter versus time.	206
6.22. Geometric mean diameter versus time for Batch #5, #6 and #9. . . .	208

Chapter 1

Introduction

1.1 Granular processes and the need for model development

Granular or particulate processes are widely used in the pharmaceutical/fine chemical industries for handling granular materials which consist of solid particulates in contact and the surrounding voids. Manufacturing unit operations such as powder blending, mixing, drying, granulation, compression, etc. have to deal with bulk flow/growth behavior of granular materials which are inherently discontinuous and heterogeneous. These macroscopic performances of the granular material are determined not only by how the discrete grains are arranged in space, but also by what kind of micro-mechanical interactions are operating between them.

Granular processes are thus governed by a number of underlying mechanisms which dictate the quality and rate of the process. Due to such complexity, there has been no fundamental model that can be applied to better design and operate granular processes for different types of equipment or at scale-up. The particle wetting rates during granulation, for instance, is highly dependent on the particle flow pattern which in turn is affected by the material properties of solids and liquids in the vessel as well as the operating conditions. The flow behavior of the powder within the granulator also depends on the geometry of the vessel itself. Several attempts are being made to understand the granular flow behavior but many aspects of the dynamics (including a more detailed study of the influence of vessel geometry, particulate flow properties, collision behavior etc.) using sophisticated predictive tools and techniques are yet to be developed.

The need to develop mechanistic understanding of granular processes also stems from the necessity to make the existing manufacturing processes cost effective and run faster - especially in the ever-increasing R&D cost landscape. According to Gernaey

et al. (2012), there are two ways to maximize the profits -particularly in pharmaceutical industry- (1) Rapid process development to prolong the patent life of a product and/or (2) Optimizing the production processes which would then allow companies to compete with generic drug manufacturers after the patent expiration. Use of efficient process modeling can help achieve both goals. The use of process modeling becomes especially relevant here since empirical studies of granular processes, which depends on several parameters, would require a large set of experiments which are impractical to perform (in terms of both cost and time).

1.2 Granular Process Modeling

Figure 1.1 illustrates the variety of different techniques used for modeling granular systems and highlights the general purposes of modeling at each level of these scales. As the techniques go from process-level scale, where bulk unit operations are investigated, to the molecular-level, where groups of molecules are simulated for understanding the surface chemistry, micro-kinetics, etc., both the characteristic length-scale of the particulates being simulated and the characteristic time-scale of the phenomena being captured decrease drastically. At the same time, the computational load for calculating associated mechanisms are increasing exponentially. This is simply due the increasing complexity of models as simulations transition from process-level to particle-level, which means the time-step of modeling techniques are getting significantly smaller.

For manufacturing industries, generally the application of modeling focuses on simulation on the process level to develop flow-sheets or control systems for the entire production line. A step below, at the macro-level modeling, the primary goal is often to build simulations that can characterize a single unit operation by analyzing all the significant phenomena occurring within that particular unit. While examining the underlying mechanisms in the process, the empirical relationships sometimes may not be able to account for the complex phenomena occurring and thus, will require more detailed investigation down to micro-/particle- level scale. At particle-level simulations, first principle-based science is applied to define the interactions of particles which lead to the bulk behavior. If the system is more intricate, molecular-level of modeling to

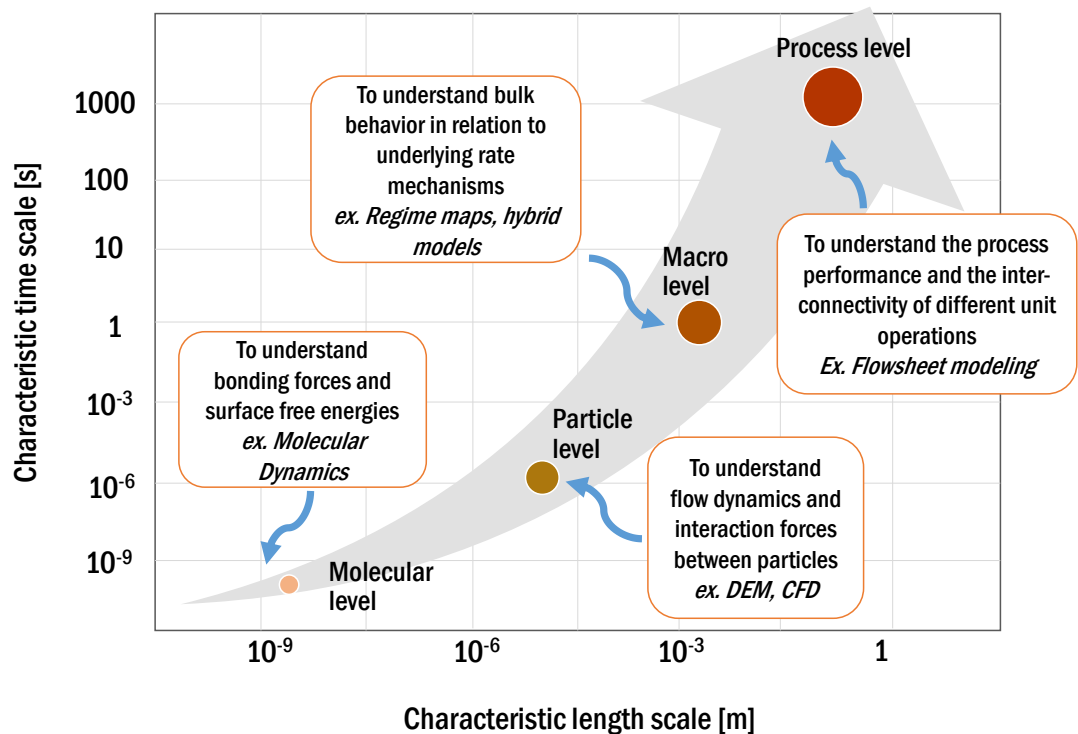


Figure 1.1: Multiscale map of modeling granular processes.

obtain detail information regarding molecular and/or surface energy dynamics may also be required.

The other caveat while carry out particulate modeling is to develop methods to connect the different scales of modeling. Especially when particle-level data needs to be interpreted at observable data scale which are collected during experimentation, a bridge between different modeling scales becomes vital. At the process or macro-level model development, for example, there are always empirical parameters which cannot be directly measured or reliably estimated from fitting experiment data. Such parameters can however be extracted from the smaller length-scale simulations to establish relationship with the empirical parameters in macro-level models. Vice versa, the high-fidelity data extracted from particle- or molecular-level simulations are difficult to validate experimentally and do not correlate directly with critical product outputs measured in lab. Interpretation of these data with a macro-level model, can establish relationship between detailed micro interactions and bulk behavior.

While different modeling methodologies are extensively reported in the chemical

engineering literature, only few studies exist which attempt to account for the multi-scale nature of a granular process explicitly. Population balance models (PBMs), for instance, have been used extensively in order to model granulation process. PBMs are used to calculate the rate processes (e.g., aggregation, consolidation and breakage) during granulation; however, traditionally these stochastic methods model processes without particle transport, implying that the system is perfectly mixed. For different granulation behaviors observed in different granulation systems such as high-shear equipment and fluidized beds, etc. where all powder particles are not wetted to the same degree, the assumption of uniformity breaks down. In such circumstances, compartmental PBMs have been proposed to account for the heterogeneous nature of liquid addition and powder mixing. The mechanistic information, used in calculation of aggregation and breakage kernels (i.e., effect of particle properties, spatial effect, collision frequency, particle velocity etc.) in individual compartments cannot be determined from a PBM alone. A one way coupled framework consisting of PBM and discrete element method (DEM) hybrid model has been reported Sen et al. (2012, 2014) in case of continuous mixing, in which the PBM consists of spatial discretization only (since there is no size change taking place during mixing). The DEM simulations were used to extract granulation kinetics and thereafter these results are used in PBM to simulate granule properties in high shear granulation Freireich et al. (2009, 2011); Gantt and Gatzke (2005). In other studies, computational fluid dynamics (CFD) models were coupled with population balance models to simulate particle size distribution in fluid bed granulation Rajniak et al. (2009, 2006). A CFD-PBM framework has been already implemented in order to model size change taking place in a particle-fluid system Drumm et al. (2009); Yan et al. (2011) and a PBM derived from kinetic theory of granular flow (KTGF) has been developed for fluidized melt granulation Tan et al. (2004). Hydrodynamic modeling of wet granulation process in an FBG using CFD principles has been reported by Rajniak et al. (2009).

The development and solution of a multi-scale model for any process is complex due to the different length and time scales involved. Moreover, various model forms

and scales must be efficiently integrated to relate formulation/material properties, processing conditions (CPPs) and equipment geometry at the micro/meso scale to the macro/application (CQAs) scale to extract maximum benefit and applicability of the model.

1.2.1 Different Modeling Techniques

The common techniques and approaches to modeling granulation processes are described below:

1.2.1.1 Granule Growth Regime Map

A popular exploratory method to predict granule growth mechanisms is to utilize the regime map developed by Iveson et al. (2001); Iveson and Litser (1998). The regime map, shown in Figure 1.2, attempts to forecast the granule growth processes based on the amount of granule deformation during agitation and the liquid saturation of the granules - quantified by dimensionless groups: Maximum Pore Saturation and Stokes deformation number. The granule growth regime map concepts have been used extensively in pharmaceutical industry for predicting the agglomeration phenomena during high shear mixing (Rough et al. (2005)) and wet granulation operations (Bouwman et al. (2005, 2006); Walker et al. (2007); Tu et al. (2009); Kayrak-Talay et al. (2013); Cavinato et al. (2010b)).

Using the dimensionless Maximum Pore Saturation and Stokes deformation number, the regime map distinguishes operating regions where different type of granule growth behavior is likely to occur. If non-existent to very little amount of liquid is present in the particle bed, granules either remain as free flowing powder or form weak nuclei due to van der Waals interaction which do not grow further. If very low level of liquid is available in the powder bed, nucleation-only behavior is predicted where granule growth relies solely on powder particles lumping together at wet spots to form weak nuclei. At a little higher liquid content and low deformation number, induction type behavior is anticipated where granules formed are so strong that they do not deform sufficiently to coalesce, and growth occurs by layering of the fines instead. Mechanistically, the

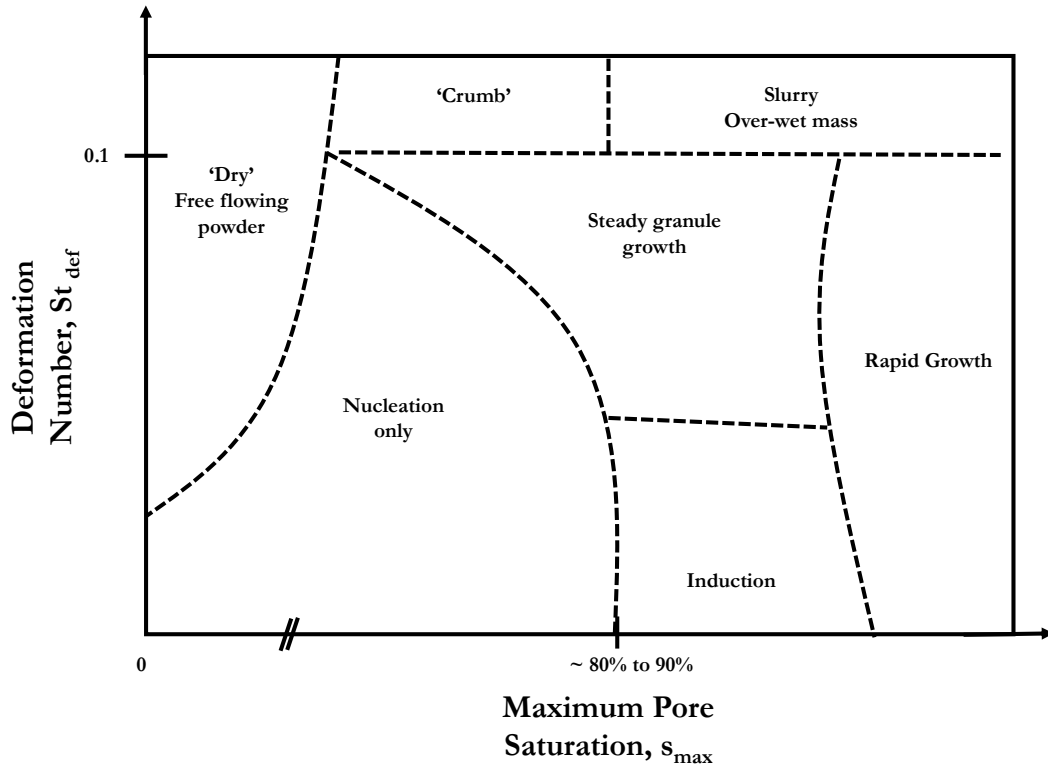


Figure 1.2: Granule growth regime map developed by Iveson and Litster.

granulation is delayed (induction) since the yield strength of the granules dominates the relative particle velocity and there is slow distribution of binder. This behavior is characterized by a sudden growth in granule size once its critical porosity has been achieved. At this stage the granule consolidation eventually squeezes liquid binder to the surface and rapid coalescence of the granules follows. The sudden growth in granule size makes the process difficult to control and to predict its end point. In another case, when the granules are more deformable (high St_{def}), they grow linearly with time - i.e. steady growth regime. These granules upon collision deform creating large surface area which promotes agglomeration. The more deformable the granules, the weaker they become and finally end up in the crumb region where granules break upon impact with impeller or wall. On the other extreme, however, if too much liquid is present in the

particle bed (pore saturation over 100%), the granules are formed within a short time from the start of process (rapid growth). The size of these granules gradually keeps increasing and eventually reaches a stable size. If the granules are highly deformable then the bed becomes over-wetted ending in slurry.

The granule growth regime map is, thus, helpful for understanding agglomeration during agitated drying particularly in terms of determining the type of granulation mechanisms at work and identifying process condition at which excessive agglomeration is taking place. By measuring the physical properties of the AI granules, the possible operating conditions where the large granules are forming can be quantified.

1.2.1.2 Population Balance Modeling (PBM)

Population balance models are the numerical methods to solve a class of differential equations that track the change in the distribution of particle properties over time. PBM equations generally divide particles or granules into discrete groups or bins based on their size and other properties such as porosity or liquid content etc. The algorithm then tracks the number of particles in each bin as different rate processes such as aggregation and breakage of particles alter the distribution. PBMs have been extensively applied to simulate many particulate systems. The general 1-D population balance equation is given by (Barrasso and Ramachandran (2015)).:

$$\frac{dF(x)}{dt} + \frac{\partial}{\partial x} \left[F(x) \frac{dx}{dt} \right] = R_{formation}(x) - R_{depletion}(x) \quad (1.1)$$

Where x represents the particle property (typically size), F is the number (or number density if normalized) of particles with that property. $R_{formation}$ and $R_{depletion}$ are terms relate to the rate of change in the number of that properties due to mechanisms such as aggregation, breakage, liquid addition and consolidation in process. We will get into these mechanisms later.

Traditionally one-dimensional (1-D) PBMs, which only consider a single particle property (generally solid content of granules) are used to study the wet granulation processes (Hounslow (1998)). The 1-D PBMs thus assume that other conditions/properties

are uniform in the system which isn't true in real case. As a result, multi-dimensional PBMs are generally proposed to account for the heterogeneities in the system (Poon et al. (2008)). Similar to 1-D PBMs, a 3-D PBMs can be expressed as follow:

$$\frac{dF(s, l, g)}{dt} + \frac{\partial}{\partial s} \left[F(x) \frac{dx}{dt} \right] = R_{formation}(x) - R_{depletion}(x) \quad (1.2)$$

Where s , l and g are the solid, liquid gas volumes of the particles respectively. The terms $R_{formation}$ and $R_{depletion}$ represent the rate of change in the number of particles in the bin due to formation or depletion. The 3-D PBMs can generally model complicated granule growth processes but are computationally intensive and require extensive empirical correlations and tuned parameters. In fact, to describe the rate of formation or depletion of particles, researchers often propose different empirical equations to characterize the various sub-mechanisms that are likely to be occurring. Take granulation in a high shear mixer for example, $R_{formation} + R_{depletion}$ is generally transformed into $R_{nuc} + R_{agg} + R_{break}$ three terms which represent nucleation, aggregation and breakage sub-mechanisms that directly influence the formation and depletion of particles. Overview descriptions of some general sub-mechanisms are provided below:

- **Aggregation:** mechanism refers to two or more particles sticking together to form a larger granule. This mechanism thus captures the granule size enlargement process. The net rate of change in the number of particles of individual bin groups can then be calculated as a combination of (i) the formation of the larger particle, and (ii) the depletion of the smaller particles involved in the aggregation. Typically, the rate at which the formation and depletion occurs is estimated by an empirical relationship via a rate kernel expression built into the aggregation mechanism. The purpose of these rate kernels generally is to estimate the likelihood of successful agglomeration between the two particles involved. To describe this aggregation rate kernel, various types of empirical kernels have been developed in literature; however, the process properties incorporated by these kernels make them limited to specific systems (Cameron et al. (2005)).

- **Breakage** mechanism in granular processing refers to the shattering or breaking of granules into smaller particulate pieces due to collisions with other particles or geometries in the system. The mathematical form to represent this mechanism is very similar to the aggregation process where the net change in the number of particles is represented through formation of smaller daughter particles and the loss of the larger granule involved in the breakage process. In addition, like the aggregation mechanism, different types of rate kernels have been developed to relate process parameters to the rate of breakage occurring with a granular process. For instance, Ramachandran et al. (2009) has proposed a mechanistic method to compute the breakage rate by estimating the external and internal stresses experienced by particles. The information and quality of the PBM model to represent the breakage process thus depends heavily on the rate kernels used.
- **Liquid addition** mechanism represents the introduction of liquid to the particles in the system. Generally, liquid or granulating fluid is added – typically sprayed or pumped through a nozzle– to a particle bed to initiate granule growth. A general assumption for liquid addition mechanism involves assuming that if the spray rate of the liquid is held constant, a uniform amount of liquid is received by each particle dependent on just their particle size. In order to incorporate the spatial heterogeneity of liquid received by particles in different areas of the granulator, advanced PBM models now are designed with multiple compartments to represent the various regional differences.
- **Consolidation** mechanism refers to the compaction process that occurs during granulation process where the liquid/air volumes present within the pores of the granules are squeezed out due to the forces experienced by these deformable granules. The consolidation of particles results in changes to both the porosity values and the liquid content properties of the granules. The work of Verkoeyen et al. (2002) is generally used to relate the rate of consolidation to material porosity and impeller speed in a high shear granulator.

In addition to the types of mechanisms involved in granulation, special care must

also be taken in addressing the type of numerical techniques used to solve the set of equations in the PBM model. There are several advanced techniques available to solve PBM model. A general method involves direct discretization approach to obtain the estimation of particle distribution. In addition, Monte Carlo methods are normally used in multi-component or poly-disperse population balance equations.

1.2.1.3 Discrete Element Modeling (DEM)

Proposed first by Cundall and Strack (1979), DEM is a method to simulate flow of bulk solids by solving the Newton's equation of motion for each and every individual particles within the solid phase. Thus, DEM methodology to represent granular process provides a more fundamental approach to study the granular behavior compared to the PBM approach.

In the DEM algorithm, the motion of each particle within the domain boundaries is calculated based on the total forces experienced by the particle - which is a sum of contact forces (between particles or with the vessel), cohesion forces (by virtue of liquid content or surface energies) and body forces (gravitations). Thus, to employ DEM simulations to represent a granular process, the first step involves developing the geometry of the system and incorporating the material properties of the vessel and particles that will affect the interaction of these elements. Once the geometry is created, DEM will simulate the movement of particle (generally represented by a sphere) using the type contact model defined by the user.

Normally, two types of contact model are available in DEM platforms: the soft sphere model or the hard sphere model (Mikami et al. (1998)). The hard particle approach assumes that the particles collide with each other instantaneously. On the other hand, the soft particle approach considers collisions as a continuous process that occurs over a period of time. In this approach, the interactive forces are treated as continuous functions of the distance between particles (Lian et al. (1998)). Normally for application in powder manufacturing operations, soft particle approach is generally more applicable to simulate the granulator behavior. Even within soft particle approach, a

number of different contact models are available for DEM users. Literature on comparisons between different contact models can be found in the review paper by Zhu et al. (2007). A popular contact model applied in DEM is a linear spring and dashpot model based on the work of Hertz-Mindlin. The mathematical form of this Hertz-Mindlin model is provided below which calculates the normal forces (F_n) and tangential forces (F_t) experienced by a particle (Tsuji et al. (1993)):

$$F_n = kx_n - \eta \frac{dx_n}{dt} \quad (1.3)$$

$$F_t = \begin{cases} kx_t - \eta \frac{dx_t}{dt} & \text{if } |F_t| \leq \mu |F_n| \\ \mu |F_n| \frac{x_t}{|x_t|} & \text{if } |F_t| > \mu |F_n| \end{cases} \quad (1.4)$$

$$\eta = -2lne / \sqrt{\pi^2 + (lne)^2} \quad (1.5)$$

where η is the damping coefficient, e the restitution, μ the friction coefficient. X_n the normal displacement, X_t the tangential displacement and k is the spring coefficient.

In the DEM algorithm, during every time step, the contact models are initiated every time the system detects a collision or contact based on the velocity and position of the particles in the last time step. If there is a collision between particle-particle or particle-geometry, the contact model is used to calculate the contact force between particles and geometry. The particle-particle collision is detected when there is a large enough overlap between particles. That is, the distance between the centers of the particles is smaller than the sum of their radii. For collision between the particle and the geometry the case will be the distance between center of the particle and contact point is smaller than the radius of the particle. A tiny overlapped is considered as deformation of the material.

Beside the contact forces, DEM methodology also considers other body forces such as gravity or cohesive forces such as electrostatic, liquid bridge forces to compute the total force applied on the individual particle. In DEM, mathematically:

$$\vec{F}_T = \vec{F}_C^N + \vec{F}_C^T + \vec{F}_B \quad (1.6)$$

Where, \vec{F}_T is the total force on the particle; \vec{F}_C^N and \vec{F}_C^T is the contact force in normal and tangential direction. And \vec{F}_B is the body force which is gravity in our system. Total force is then used to calculate the acceleration of the particle by Newton's 2nd law and compute the new velocity and position profile.

After setting up the contact model, the next step will be feeding the input variables. Typically, contact parameters and material properties are required to be set up before simulation starts. Contact parameters refer to the variables used to calculate the contact force between objects (particles or geometry). For example, coefficient of friction defines the friction force between surfaces; coefficient of restitution is used to derive the velocity of the rebound from the collision velocity. Material properties are used to determine the deformation of the objects such as Young's modules, providing the information of stiffness; Poisson's ratio defines the strain behavior of the material. These parameters can be determined by several material characterization methods (Bharadwaj et al. (2010); Ketterhagen et al. (2010)).

Another key parameter while developing DEM simulations is the time step or Rayleigh time step to be used during simulations. The DEM time step is generally estimated as a function of the time period of a shear wave passing through a solid particle. It can be computed by:

$$T_R = \pi R \left(\frac{\rho}{G} \right)^{\frac{1}{2}} / (0.1631\nu + 0.8766) \quad (1.7)$$

Where R is the radius of particle, ρ is the density of the particle, G is the shear module and ν is the Poisson's ratio (DEMSolutions (2014)). Typically, an appropriate setting of DEM time step can range from $0.2T_R$ to $0.4T_R$.

Several commercial and open-source software for DEM methodologies are available in the market including EDEM (DEM Solutions), STAR-CCM+ (CD-adapco), Rocky (ESSS), LIGGGHTS, Blaze-DEM etc.

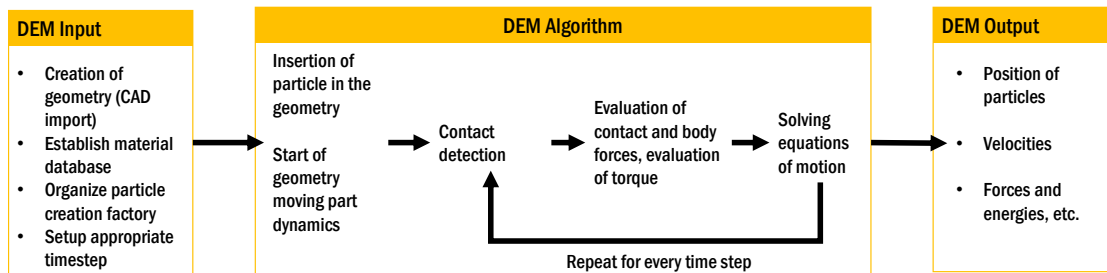


Figure 1.3: Discrete element method algorithm: Inputs, calculations and outputs

1.2.1.4 Computational Fluid Dynamics (CFD)

Computational Fluid Dynamics (CFD) has been widely used in chemical industry to model internal and external fluid flows. In general, CFD simulations have been used to optimize processes, reduce the energy costs and create new designs without wasting resources by performing experiments. In pharmaceutical industry, these simulations are used to model fluid flow in several manufacturing processes such as pneumatic mixing, separation, and fluidized bed operations (Ierapetritou and Ramachandran (2016)). CFD algorithms calculate the fluid flow field by solving the volume averaged Navier – Stokes, energy and species conservation equations over the discretized region.

The use of CFD provides a distinct advantage of providing in-depth information regarding the flow field within the domain of interest. This is done by discretizing the entire region into cells; volume averaged conservation equations of mass, momentum, species and energy are then solved over this region. Due to the large number of discretized cells in a given region, CFD simulations are often computationally very expensive. The accuracy of the solution generally increases with increase in number of cells in the region but using a smaller grid size for discretization results in longer computational time. Most commercial CFD software such as StarCCM+, ANSYS Fluent and other open source software provide parallel computing options to speed up the computational processes. Another important note regarding use of CFDs to model granular process involves the approach used to introduce the solid granular phase within the continuous fluid phase platform of CFD. Typically, the CFD model simulates the fluid

and particles using Eulerian – Eulerian approach, which assumes both fluid and particle phases as two continuous phases. As a result, the default CFD-only approach can accurately simulate fluid flow but not a dense particle phase flow. To accurately model the particles, discrete element modeling (DEM), which uses a lagrangian approach to track the particles in space and time, can be coupled with the CFD software to obtain a holistic information.

1.2.1.5 Coupled PBM-DEM modeling

Due to the capability of DEM simulations to provide process information at particle-level scale, DEM approach has a great potential to assist the macro-scale modeling frameworks such as PBMs to become more mechanistic and accurate. As a result, multi-scale DEM-PBM coupled models can be applied to different unit operations including milling, granulation and drying processes where micro-behavior predominantly affect the bulk process. Since the tuned parameters in the PBMs rate kernels are empirical in nature, DEM data provides an opportunity to better tune these parameters by offering detailed information on collision velocity, frequency and shear force values on the particle that directly impact the mechanisms captured in PBM. For instance, Lee et al. (2010) correlates the information from DEM to the parameters of breakage determined by experiment in a vibrant mill. Gantt et al. (2006) studied the mechanistic aggregation kernel in PBMs by using a one way coupling PBM-DEM simulation. They extracted collision and velocity data from DEM and proposed a way to determine aggregation kernel β :

$$\beta(a, b) = C(a, b)\psi(a, b) \quad (1.8)$$

Where C is the collision rate which is the frequency of two types of particle (a and b) collide on a per particle. Collision efficiency ψ represents the probability of the collision between two types of particle leading to coalescence. The collision efficiency can be determined based on collision velocity and material properties. Gantt et al. (2006)'s work is a one-way coupled framework where the DEM simulation can't update itself with the new particle distributions. Other instances of two-way coupled framework are

also available in literature. In Barrasso and Ramachandran (2015), a two-way coupled DEM-PBM model was developed for granulation in a rotating drum system. In the study, the DEM model updates the particle generation at specified time intervals based in the particle distribution information generated by PBM. Figure 1.4 illustrates the two-way coupling framework.

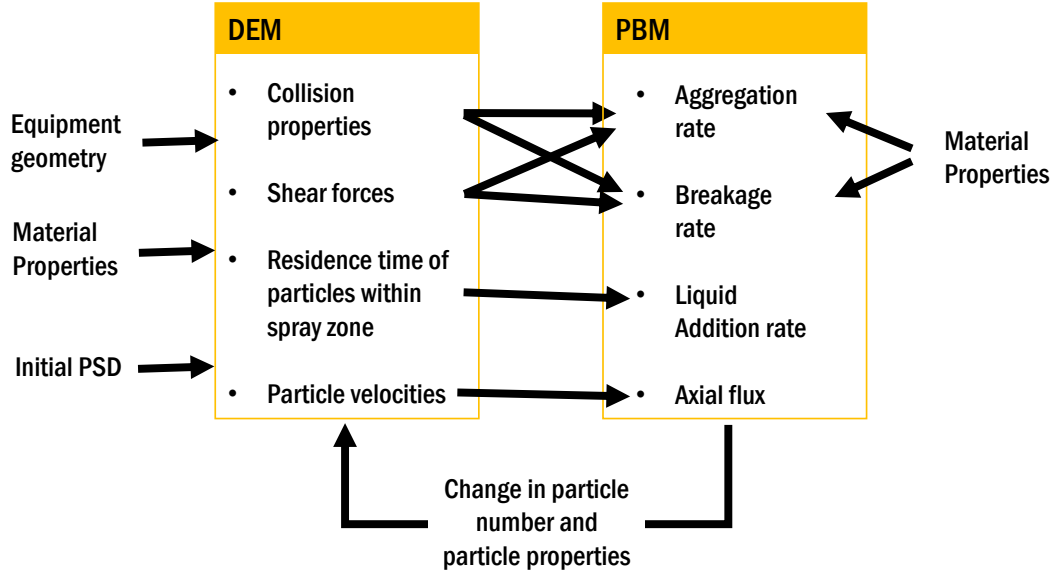


Figure 1.4: PBM-DEM coupled framework: Multi-scale model development through use of DEM feeding particle-level information to PBM which in turn provides the macroscopic data back to DEM.

1.2.1.6 Coupled CFD-DEM modeling

CFD and DEM are generally coupled to capture the fundamental dynamics of the fluid-particle system. Coupling between CFD and DEM can be a one-way or two-way coupling – similar to the DEM-PBM coupling approaches. In the one-way coupling approach, the fluid flow field calculated by CFD is exported and added as an external force field on the particles. A limitation here is that the effects of particles on the fluid flow are completely ignored; hence, they are only suitable for low solid density applications like a cyclone separator. In a two way coupling approach, the transfer of data between CFD and DEM is mutual, there is an exchange of mass, momentum and velocity between the solid phase and the fluid phase (Norouzi et al. (2016)). The

coupling process and the transfer of information is shown in the Figure below 1.5.

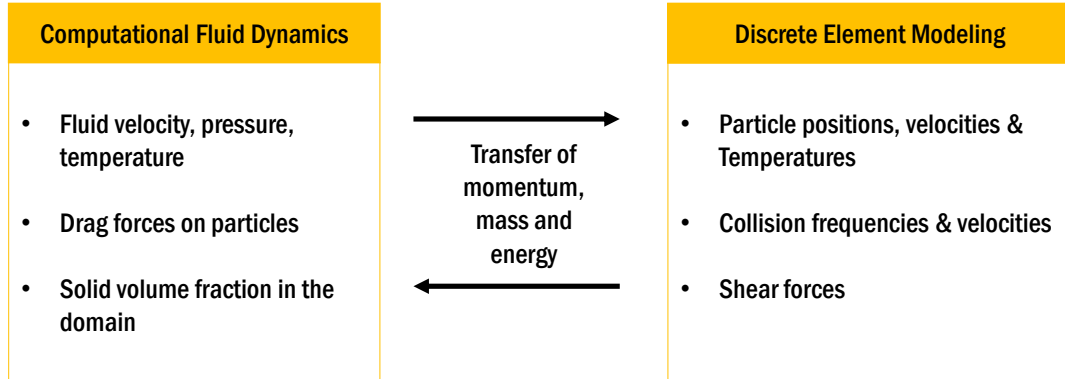


Figure 1.5: Two-way DEM-CFD coupled framework: Information about particle momentum, mass and energy is transferred between the two particle-level modeling techniques

1.2.2 Objectives of this work

The main objective of this dissertation work is to establish predictive frameworks that range from particle-level models to macroscopic models that can be efficiently used to model granular processes. The development, implementation and assessment of these frameworks are done through relevant case studies involving granule growth during agitated drying, wet granulation and fluidized bed granulation.

The use of dimensionless groups and regime maps to characterize granular process is the first step in developing efficient process models. Through careful process characterization through relevant dimensionless groups, reduced experimentation at all scales can be achieved. For practical purposes of quickly understanding process behavior and identifying critical process parameters, regime maps offer a guidance towards predicting granular process behavior. For instance, the use of granule growth regime map is a useful tool to understand the granule growth behavior through pore saturation of granules and the related wet granule deformability. In addition, these dimensionless groups also provide a criterion for scale-up.

Since the predictive value of regime maps is more qualitative in nature - especially with ambiguous demarcation of different regimes- a fundamental understanding of granular processes requires more advanced numerical techniques that can use a model-based

approach to describe the behavior of the process from a more scientific perspective. Particle-level models which account for the discrete nature of the granular processes offer better insight into the underlying mechanisms driving the process. High fidelity simulation tools such as Discrete Element Method (DEM) and Computational Fluid Dynamics (CFD) allow an in-depth examination of the effects of process variables, material properties and vessel geometries on granular and multi-phase flows and interactions. In addition, these models can be used to carry out virtual experimentation thus allowing for exploration of design space and consequently speeding up of the process development and scale-up of unit operations.

While these powerful modeling techniques do provide a greater awareness into the granular flow dynamics, the particle-level information obtained from these simulations do not readily translate into bulk process performance attributes. The information on individual particle collisions, for instance, offer an insight into agglomeration or attrition tendency within the system but on its own cannot be experimentally measured for validation nor does it predict subsequent particle size distributions. Development of hybrid multi-scale and multi-phase models thus becomes a necessity to relate particle-level dynamics with bulk properties. Such models can incorporate underlying mechanisms and allow for the development of a truly predictive granular process model that can be calibrated and validated with a limited number of experiments.

The specific aims of this thesis are:

- **Specific Aim 1:** Development, implementation and assessment of using dimensionless groups to predict granule growth behavior.
- **Specific Aim 2:** Development, implementation and assessment of using mechanistic Discrete Element Method (DEM) studies to understand underlying mechanisms of granular processes.
- **Specific Aim 3:** Development, implementation and assessment of using multi-scale hybrid models to relate particle-level mechanisms to bulk behavior.

Part I

Specific Aim I: Development, Implementation and Assessment of using Dimensionless Groups to Predict Granule Growth Behavior

1.3 Overview

In the specialty chemical industries such as pharmaceutical, agrochemical, cosmetics, etc. the agitated filter-dryer (AFD) is fast becoming the go-to alternative for performing filtration and isolation of active ingredients (AIs) and intermediates. Unfortunately, depending on the active ingredient (AI)-solvent system and the process parameters employed, AFD operations are often plagued with undesired agglomeration issues during the agitated drying cycles which necessitates additional processing steps to enable downstream formulation. Experimental analysis of the lumped powder formation at various operating conditions are now being used to gain insight into minimizing such activity; however, there is still a lack of understanding into the fundamental processes prompting such behavior and the effectiveness of suggested mitigation measures.

This study aims to investigate the applicability of using dimensionless groups to discern the underlying granulation mechanisms induced during the agitated drying phase of AFD operation. Through parametric study and granule growth regime map analysis, the dynamic drying and agglomeration profiles were studied for a model cohesive powder, micronized acetaminophen at various process conditions.

In Chapter 2, an experimental methodology to apply granule growth regime map analysis to the ever-changing system of agitated drying bed is presented. Using dimensionless groups, a novel technique is demonstrated to predict the granular growth processes occurring during different API-solvent combinations. In addition, parametric experimental analysis of the drying behavior over time as well as the agglomeration growth profile at various process conditions are examined. The parametric study aims to assess the validity of the regime map predictions.

1.4 Publications

The details of the discussions provided in this section were published in the following article/conferences:

- **A. Tamrakar**, A. Gunadi, P. M. Piccione, R. Ramachandran. Dynamic agglomeration profiling during the agitated drying phase in an agitated filter dryer: parametric investigation and regime map studies, Powder Technology 303 (2016) 109–123.

Chapter 2

Using dimensionless groups to predict undesired granule growth behavior during agitated filter drying

2.1 Background

2.1.1 Isolation and drying of particulate products

In general, isolation and drying of a solid/powder refers to the removal of relatively small amounts of liquid (water or other solvents) from the solid particle bed. The drying operation, which is usually the final step in a series of manufacturing operations, is performed to reduce the content of residual liquid to an acceptably low value. In pharmaceutical and specialty chemical industries, the isolation and drying of active ingredients (AIs) and drug intermediates are usually carried out upstream where the particulate product is purified from the residues of the crystallization step. Since the product quality cannot be compromised, gentle thermal treatment at low and moderate temperatures are mostly used during drying. In many cases, recovery of the expensive organic solvents (mother liquor) removed during drying is also desired. Unfortunately, the evaporation of solvents that have a high heat of vaporization, the condensation of the vapor with a refrigerant and/or compression of feed can significantly add to the total cost of the operation. Especially for several low value AIs, the high energy consumption of the drying operation means that the use of expensive drying techniques is simply not affordable. Tsotas and Mujumdar (2012) In such cases, the separation processes based on the use of barriers or solid agents are usually performed first through a filtration unit. Since the cost of recovering and purifying a chemical compound in a mixture is strongly dependent on the concentration of the chemical in the initial slurry as shown by Sherwood, Pigford, Wilke, Dwyer and Keller Seader and Henley (2001), the common

industrial practice is to reduce the solvent content as much as possible before proceeding with the drying phase.

Kudra and Majumdar Kudra and Mujumdar (2009) have shown that while mechanical dewatering processes such as filtration or centrifugation is more profitable for higher moisture content, using a thermal drying process is conventionally selected for finer particle sizes and lower moisture content. Usually coarser particles, where solvent can be removed by bulk or film drainage, have lower energy consumption while fine particles and pasty materials, as seen frequently in pharmaceutical and specialty manufacturing, need higher energy input. If filtration and drying were to be compared in terms of operational costs, due to the large latent heat of vaporization of some liquids, the mechanical solid-liquid separation is about 100-1000 times less energy intensive than thermal drying. Kudra and Hashmi (2010) Thus, over the recent decades, the new trend in isolating and drying of solids has become an innovative combination of mechanical dewatering and thermal drying processes that can reduce both the thermal load on the dryers as well as the production costs. Kudra and Mujumdar (2009)

2.1.2 Agitated filter drying

An agitated filter dryer (AFD) is an example of vertical filter dryer commonly used in chemical industries which involves isolating solutes from its mother liquor based on filtration and contact drying theories. In the agro-chemical industry, filter-dryers are used for sequestering AIs and key intermediates from the wet cake after the crystallization step. Traditionally, the filtration and drying of the crystallization product is carried out in separate equipment and thus, required considerable AI handling during product transfer (Sahni et al. (2013)). In order to minimize product loss/contamination as well as personnel exposure to hazardous media, manufacturers now use an AFD apparatus to contain the separation, washing and drying processes in a single vessel (Perlmutter (2007); Kudra and Mujumdar (2009)). Additionally, utilizing the integrated filtration and thermal drying unit offers manufacturer not only process flexibility and control but also compact design which allows for minimal space requirement and easy integration into existing facilities (Kudra and Mujumdar (2009)). Especially in process

plants where sterile environment needs to be maintained or frequent product changes are needed, AFDs have become particularly popular. Contact dryers, such as the AFD unit, have also become very popular in pharmaceutical industry lately due to two main reasons: improved containment and ability to operate under vacuum. Since most of the active ingredients and excipients are highly heat sensitive, strict temperature control is implemented to avoid any degradation.

Operationally, AFDs have three working stages: the filtration regime, the washing regime and finally, the drying regime (Figure 2.1). The filtration regime, which starts right after the slurry is charged into the AFD, can be distinguished into a deliquoring sub-process and a consolidation sub-process. Deliquoring involves the removal of the mother liquor either under pressure or vacuum while consolidation process involves cake smoothing. Essentially, the cake height which increases during the filtration time is consolidated by applying a mechanical force (Sören and Jürgen (2012)). The smoothening or compacting the cake's surface prior to applying spray wash allows for the entire bed to be washed evenly. During the second regime, wash solvents are sprayed on top of the solid cake to remove any remaining previous liquid and dissolved solutes. Since the trapped air/gas are removed during the compaction, the wash liquid displaces the mother liquor in the filter cake in a 'piston-like' manner (Sharratt (1997)). By systematic smoothening of the cake surface, the moisture content of the cake is decreased which in turn reduces the energy consumption during drying (Millennium (Accessed: 2014)). After desired number of washing (reslurrying) and smoothing cycles, the filter cake is dried under vacuum to remove the vapor.

Generally, most drying phases are initiated with a cold air or nitrogen blow-through step to reduce the pre-drying moisture content even further. The stirrer blades are subsequently lowered to start agitating the cake while it is drying. The use of low temperature during contact drying traditionally has lead this drying phase to be the bottleneck for the manufacture of AIs; however, with the opportunity to employ low pressure conditions in an enclosed AFD, a high driving force for heat and mass transfer is attainable even at relatively low temperatures (Kohout et al. (2005)) In most agitated drying operations, vacuum conditions are applied in order to lower the boiling point of

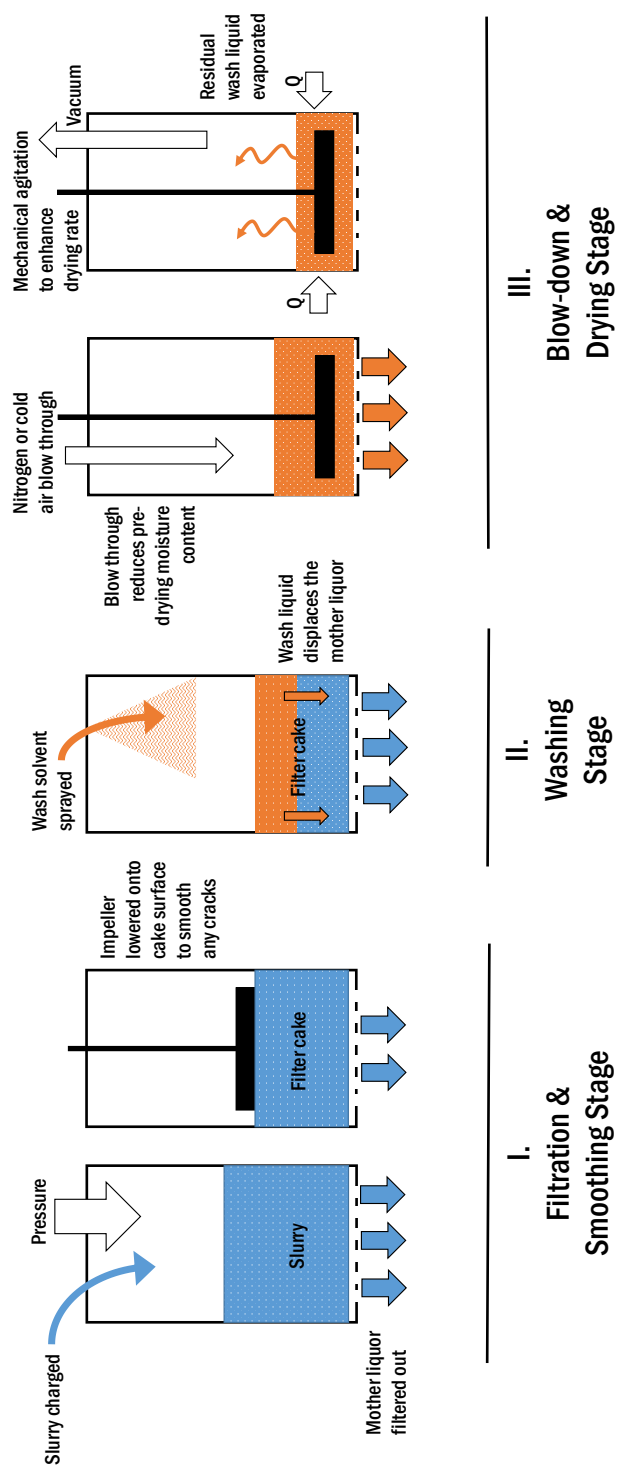


Figure 2.1: Schematic of different operating stages of agitated filter drying process.

solvent. Overall, several factors have a direct impact on the drying rate in an AFD. The liquid evaporation rate, for instance, can be enhanced by increasing the jacket temperature as well as by lowering the head-space pressure. Additionally, by amplifying the mechanical agitation of the powder bed, the driving force for heat transfer can be increased (Murru et al. (2011)). Aggressive drying conditions such as high agitation rate, as a result, are now being used to minimized drying times (Sahni et al. (2013)).

2.1.3 Particle Agglomeration Issues

In an agitated filter dryer due to the application of heat transfer coupled with simultaneous momentum and mass transfer within the bed, the microstructure and therefore the effective transport properties of wet granular medium are changing dynamically (Kohout et al. (2005)). Therefore, the extensive use of agitation during different stages of filter-drying processes when combined with the effects of moisture content of the cake can induce attrition (breakage) or agglomeration of powder particles (Kom et al. (2011)). If the powder bed has low moisture, the impact of collision with other particles, walls and the stirrer blades can result in particle attrition inside AFDs (Lekhal et al. (2003, 2004); Hare et al. (2011); Lamberto et al. (2011); Hamilton et al. (2013)). Attrition leads to formation of small fragments which can improve the bulk density of the product; nonetheless, in most cases, the generation of undesired fines causes a number of processing issues including dust explosion and poor flowability (Lekhal et al. (2003)). Contrastingly, if the residual moisture content of the particle is high, agglomeration or balling of overly wet or sticky cake can also occur which can lead to out-of-specification results.

Agglomeration behavior in terms of particle size enlargement occurs when smaller particles in the presence of residual solvent become cohesively bound to each other. As thermal energy is supplied, the free moisture from the wet cake evaporates first leaving a viscous film around the particles which is composed of dissolved AI in a thin layer of solvent. This residual moisture then behaves like as a binding agent forming liquid bridges with other particles which increases the overall cohesive strength of the bulk material (Pietsch (1969); Ende et al. (2013)). Due to poor mixing, the wet AI crystals

which are bound by these interparticle forces are not properly separated and when a non-uniform distribution of shear is applied in the drying chamber, uneven coalescence occurs (Lekhal et al. (2003)) As drying continues, the residual solvent within the thin liquid bridge is evaporated away, the particles come closer to each other, the soluble AI in the viscous film forms crystalline bridges that further strengthen the agglomerate (Pietsch (1969); Ende et al. (2013)).

Such agglomeration of particles in an agitated filter-dryer is undesired during isolation of powders for several reasons:

1. Due to agglomeration in AFD, the particle size distribution of the products is severely affected which can lead to content non-uniformity as well as variable or out-of-specification input for downstream blends.
2. Formation of large agglomerates is undesirable also because further size reduction steps are required to enable down-stream processing.
3. Agglomeration can also lead to difficulty in removing the batch from the processing equipment and can negatively impact cycle times.
4. In extreme cases the formation of hard agglomerates can also lead to equipment and agitator damage.

Over the last decade, several experimental investigations have been conducted to understand the operational parameters that lead to formation of undesired powder lumps in an AFD including Sahni et al. (2013); Lekhal et al. (2003, 2004); Hamilton et al. (2013); Ende et al. (2013); Birch and Marziano (2013); Sahni and Chaudhuri (2012); Lim et al. (2016). The most prominent hypotheses for the cause of agglomeration are summarized below:

1. Incomplete de-liquoring in presence of continuous agitation: Incomplete de-liquoring after the filtration step is believed to result in the presence of excess residual solvent in the cake, which in turn promotes the formation of liquid bridge and particle agglomeration. To quantify the potential for agglomeration, the rheological properties of the wet powder mass are usually monitored through mixer

torque rheometry data in combination with cake resistance and post-filtration moisture content. Ende et al. (2013), for instance, identified the potential risk zones of agglomeration in terms of the pre-drying moisture content by analyzing the mixer torque rheometry profile of proprietary compound in methanol. The authors found that the risk of agglomeration decreases drastically as the moisture content post-filtration (pre-drying) is reduced beneath 25 vol%.

2. Continuous agitation: Continuous agitation distributes the residual solvent present and reinforces agglomeration behavior. Experimental and modeling evaluations have shown that intermittent agitation can reduce the risk of agglomeration/attrition at the expense of drying rate (Hamilton et al. (2013); Michaud et al. (2008); Sahni and Chaudhuri (2012)).
3. Solubility of solids in the residual liquid: During the drying process, solvent evaporation can cause the dissolved solids in the liquid bridges to crystallize out and form solid bridges between the particles of bulk solid. Generally, the higher the solubility of the product in the wash solvent, the greater the chance solid bridge formation. In an experiment carried out by Birch and Marziano (2013), a proprietary compound A was washed in 4 different solvents: acetone/water in 1:1 v/v ratio, pure 2-methyl tetrahydrofuran (MeTHF), 2-MeTHF/water in 99:1 v/v ratio and 2-MeTHF/water in 96:4 v/v ratio. The respective solubility of A in the solvents are as follows: 2.0, 15.4, 6.4 and 14.5 g/L. Their results indicated strong impact of wash composition (solubilities) on the compound A agglomeration: at lower solubilities (i.e. for acetone/water system), the tendency to form agglomerates was much lower than for solvent systems with higher solubilities.

In a recent publication by Lim et al. (2016), the dripping of condensates formed on the vessel surface onto the filter cake during an AFD operation was investigated for its propensity to initiate agglomeration. The authors found that although drip-induced nucleation does significantly affect agglomeration growth for some model powders ($CaCO_3$ and $NaHCO_3$), for proprietary cohesive API (active pharmaceutical ingredient) under investigation, avoidance of condensates did not prevent agglomeration formation.

2.1.4 Objectives

This work investigates the applicability of using granule growth regime map to discern the underlying granulation mechanisms induced during the agitated drying phase of AFD operation. Although various investigations have been undertaken to minimize the formation of agglomeration in the past, there is still a lack of understanding in the fundamental agglomerate formation mechanisms, especially the dynamic subprocesses occurring during drying, and the effectiveness of different mitigation terms suggested for reducing agglomerates. The first aim of this work is to develop an experimental methodology to apply regime map analysis to the ever-changing system of agitated drying bed and implement the technique to predict the granular growth process occurring during different API-solvent combinations. Second, through parametric experimental analysis of drying behavior over time and agglomeration profiling at various process conditions, this study also aims to assess the veracity of the regime map predictions.

The objectives of this SPECIFIC AIM include:

- **Sub Aim 1:** [Development and Implementation] To investigate agglomerate growth behavior using regime map analysis and identify the granulation regimes encountered during the drying operation
- **Sub Aim 2:** [Assessment] To study the effect of operating conditions and material properties on dynamic agglomerate formation behavior and compare the findings with regime map predictions

2.2 Development and Implementation of Granule Growth Regime Map for Agitated Drying

2.2.1 Granule Growth Regime Map

The regime map for agglomerate growth during agitated drying used in this study is based on the granule growth regime map developed by Iveson et al. (2001); Iveson and Litser (1998). By quantifying the key parameters during the agglomerate formation through the use of dimensionless groups - Maximum Pore Saturation and Stokes deformation number, the regime map attempts to forecast the extent of undesired granule growth occurring during mechanical agitation of the wet filter cake. Although this study is the first time that regime map is being used to investigate agglomeration mechanisms during agitated drying, both dimensionless groups used in regime map are consistent with the before-mentioned causes of undesired agglomerate formation during AFD operation and offer an insight into the underlying subprocesses.

Mathematical expressions describing the key dimensionless groups are detailed in Equation 2.1 and 2.2.

$$\text{Maximum Pore Saturation, } s_{max} = \frac{\omega \cdot \rho_s \cdot (1 - \epsilon_{min})}{\rho_l \cdot \epsilon_{min}} \quad (2.1)$$

$$\text{Stokes deformation number, } St_{dev} = \frac{\rho_g \cdot U_c^2}{2 \cdot Y_g} \quad (2.2)$$

Where, ω is the liquid-to-solids ratio (L/S), ρ_s is the solid density, ρ_l is the liquid density and ϵ_{min} is the minimum porosity, ρ_g is the granule density, U_c is the particle velocity and Y_g is the dynamic yield stress of the granule. The relative particle velocity U_c , is determined from the rotational speed of the impeller (n , in RPM) and impeller radius (r) using Equation 2.3, where ω is the angular velocity of impeller.

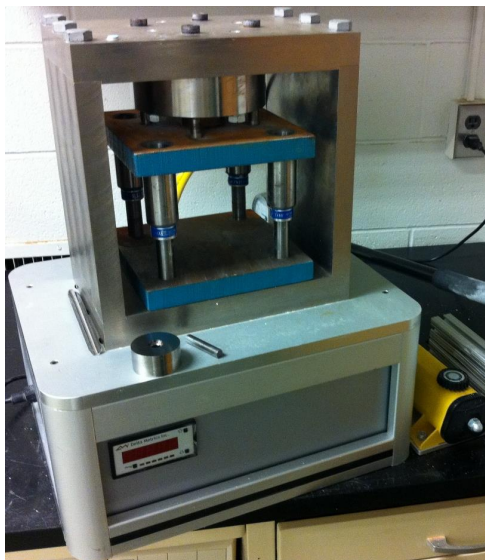
$$U_c = r * \omega = \frac{r * 2 * \pi * n}{60} \quad (2.3)$$

2.2.2 Granule Characterization Experiments

The dynamic yield stress values of the granules were obtained by deformation test carried out on pseudo-granules that were formed independently as pellets (Figure 2.2) similar to investigations by Iveson et al. (2001). Since stress-strain relationship for irregularly shaped granules are very difficult to measure experimentally, cylindrical pellets with uniform surface area for compression (circular-face with 10mm diameter) were used. These pseudo-granules were produced by mixing pure micronized Acetaminophen (APAP)(Mallinckrodt Inc, NC) powder and pure solvents at varying L/S ratios. The solvents used were: demineralized water, Methanol (Fisher Scientific, 99.9%) and Ethanol (Pharmaco-apper, 200 proof)). The reasoning behind powder and solvent choice are detailed in next section. The mixture was then compressed using a tablet compressor (ENERPAC by RothGreaves and Associates Inc.) at a constant force of 20N for 0.5s and multiple replicates of pellets were prepared (Figure 2.2a). Depending on the amount of powder and solvent used, the thickness of the pellet and the bulk density differs. To ensure accurate calculation of pore saturation and yield stress measurement, individual pellet dimensions, mass, stress and strain values were recorded. The dynamic yield stress (Y_g) component for the deformation was calculated from compression test of these pellets using INSTRON compressor(Figure 2.2b). Similarly, granule bulk density ρ_g , was obtained by mass and volume calculations of the pellet.

2.2.3 Granule Growth Regime Map Analysis

Figure 2.3 summarizes the characteristic properties of the pseudo-granules produced with different APAP-solvent combination in terms of maximum pore saturation achieved, dynamic yield stress of pellets and the bulk density of the pellets. In order to assess the baseline strength of granules formed from consolidation of just powder particles (without solvent), separate pellets were also created with the same compression force. The average yield stress and bulk pellet density for powder-only pellets was found to be 51.25 ± 13.2 KPa and 707.1 ± 12.9 kg/m³ respectively.



(a) Tablet compressor used to create pseudo-granules by compressing powder solvent mix with specified L/S ratio



(b) INSTRON Dynamite load frame used to measure stress vs. strain relationship



(c) Pellets or pseudo-granules developed were compressed at constant force for a constant time



(d) Close up of the pellet compression test

Figure 2.2: Experimental setup for granule yield strength test measurement.

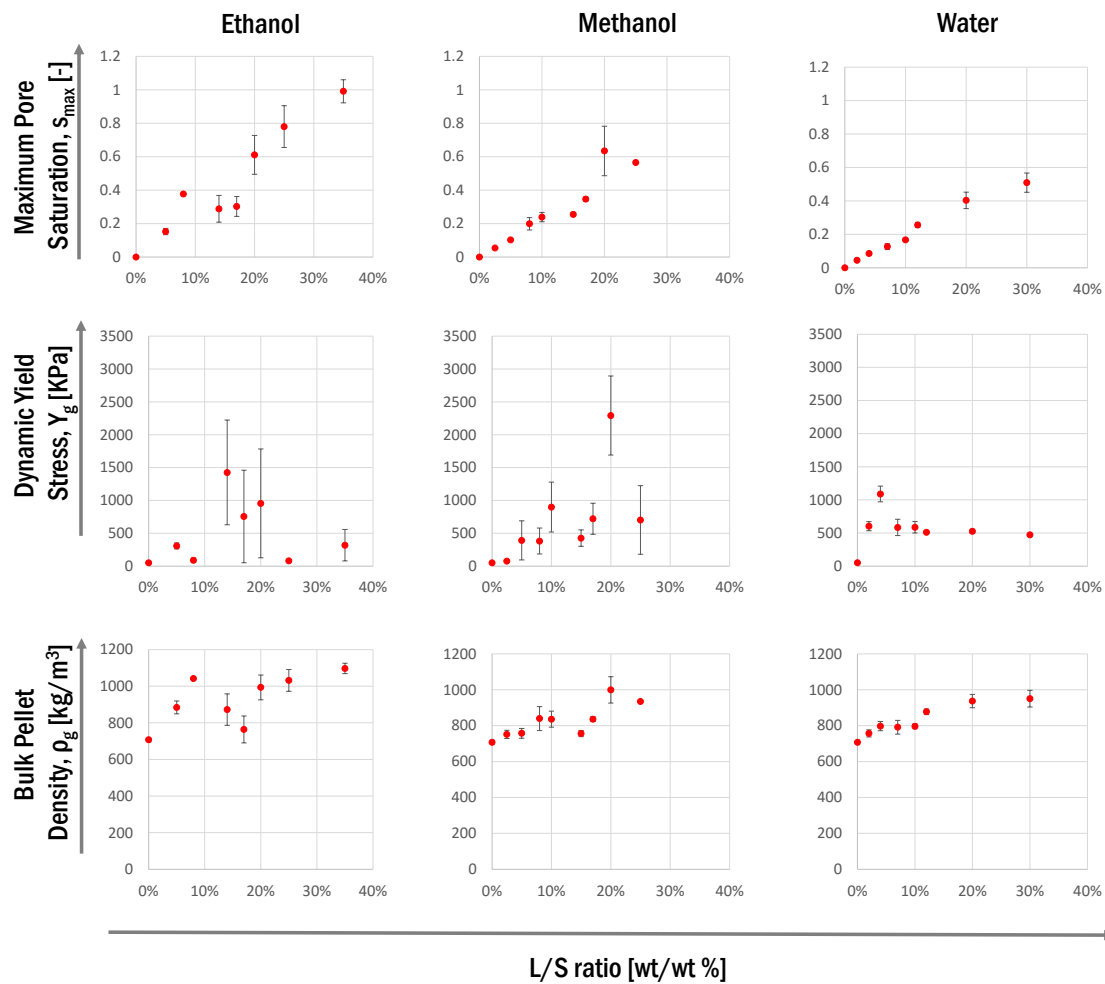


Figure 2.3: Characterization of pseudo-granules developed for regime map analysis.

The dependence of the parameters - maximum pore saturation, granule yield stress and bulk density- on the L/S ratio (or moisture content) of the granule is highlighted with the regression line (shown in blue). While the maximum pore saturation (s_{max}) values scale linearly with the liquid content of the pellet, distinct granule strength characteristic is noticeable for the three solvents used. The pellets formed with ethanol and methanol which progressively have higher solvent polarity and APAP solubility compared to water (see Table 1) are seen to have critical L/S ratios where the dynamic yield strength of the pellets peak. For APAP-ethanol granules, the critical moisture content appears to be around 15% L/S ratio whereas for APAP-methanol granules, the peak is closer to 20% L/S ratio. The yield stress value for APAP-water pellets seem to be highest around 5% L/S ratio.

The characterization of the pseudo-granules thus performed provides helpful insight into the underlying agglomeration behavior of different powder-solvent systems. The yield stress values of the granules obtained for each pellet represent the stress at which the structural breakdown of the granule occurs. Iveson et al. (2001) found that this dynamic yield stress values were significantly influenced by the liquid binder viscosity and to a lower extent by the liquid surface tension. In addition, decrease in the yield stress of the granules, correspond to increase in the strength of granules formed (Iveson et al. (2001); Nordstrom et al. (2008)). This is mathematically represented by the deformation number (see Equation 2.2) which hints at the deformability of the granule. Now taking into consideration that yield stress of different powder-solvent pellets peak at different critical L/S ratios, it becomes clearer that granules formed with solvents that have high viscosity - which is in turn increased by higher powder solubility - become strong or weak as moisture content changes. Thus, any agglomerates formed during agitated drying of such powder-solvent systems will experience high and low deformability over drying time. These trends also give an indication to the mechanism that will likely dominate agglomerate growth: for example, when the moisture content of the particular powder-solvent system is near its critical value, the mechanical strength of agglomerates is high (low-deformation system) which means that the agglomerates are slowly consolidating and exhibit induction growth behavior. If the moisture content

is higher or lower than the critical L/S ratio, then the yield stress is low, the agglomerate strength is low and depending on amount of moisture available may form weak nongranular material or over-wetted mass.

The projection of likely agglomerate growth mechanisms in these systems is better shown through the regime maps as illustrated below.

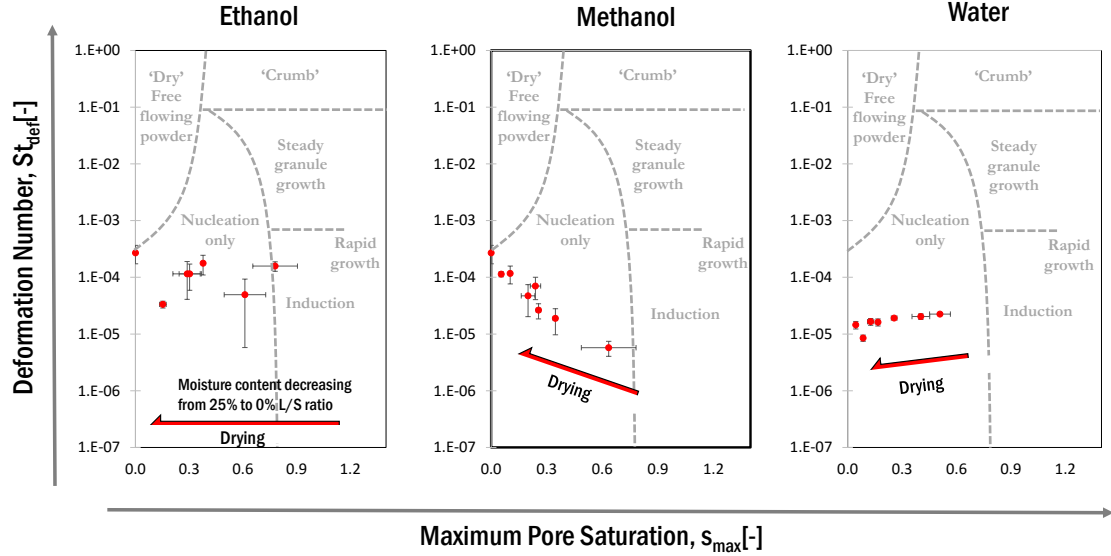


Figure 2.4: Prediction of granule growth mechanism using regime map analysis for different APAP-solvent systems.

Using the moisture content data from the bench scale drying experiments with 25% initial L/S ratio and 50 rpm agitation as the reference, dimensionless numbers St_{dev} and s_{max} were calculated for APAP-solvent systems. The regime map prediction for such systems are presented in Figure 2.4. It must be noted that although a time dimension is not shown explicitly, for each powder-solvent system, as drying proceeds, the moisture content and hence pore saturation value of the samples decreases. Thus, markers in the regime map successively move from right to left over drying time. Another important factor to consider is that during drying, due to the evaporation rate different solvents, the time dimension is not linear - i.e. solvents remain in the respective regime for variable amounts of time. For instance, for APAP-ethanol system, the experimental records show that the moisture content decreases sharply from 20 – 25% to less than 10% within the first 3 minutes and then it required more than 15 minutes for it to

decrease below 0.5%.

Predictions from the regime map presented strongly suggests that the growth of granules for APAP-solvent system is governed by induction-type growth at higher moisture content and nucleation (and likely layering) subprocesses at lower moisture content. Due to the low deformability of granules produced and the use of low agitation, the growth is restricted within these regime types and any steady granule growth behavior is not likely. The continued evaporation of liquid from the system also ensures that for most part of the drying time, the nucleation-only region is predominant where loose and weaker agglomerates are formed. On the flip side, if the moisture content remains high for a long time, there is a significant risk of undesired granulation occurring through induction behavior.

It must be noted that due to the obvious ambiguity of the demarcation lines between different regimes and the experimental errors inherent to the method of calculation of granule properties, the use of growth regime map is mostly used for guidance purposes only and not for quantitative prediction. Nevertheless, some insightful knowledge can be ascertained from such precursory experiments. Since the type of growth mechanism depends heavily on the amount and property of the solvent present in the system, the regime map clarifies the importance of selecting appropriate wash solvent before agitated drying of the system. If the wash liquid has high heat of vaporization and thus low drying rate, it remains in the system for a longer time than liquids that evaporate quickly. If such solvents were to also possess high viscosity and/or high solubility, then the agglomerates formed are much stronger and tougher to break. In another case, if the system has higher shearing rate then depending on whether the agglomerates are deformable or not, there is significant risk of undesired growth through steady coalescence.

2.3 Parametric Study to Assess the Granule Growth Regime Map Predictions

2.3.1 Parametric Study: Bench-scale Agitated Drying Experiments

Since the granule growth map only qualitatively suggests the possible agglomeration behavior, systematic bench scale experiments were carried out using a model AI wetted with pure solvents to investigate the dynamic nature of the agglomerate formation. Pure micronized acetaminophen (median diameter, d50: $30\ \mu m$) was used as the model powder due its highly cohesive and electrostatic nature which readily forms agglomerates of significant size. This behavior is evident in the agitated drying trials run with only dry micronized powder where agglomerates of sizes in millimeter range even without the presence of liquid (0% L/S ratio) were still formed. Literature compressibility studies performed on these needle-like micronized APAP have shown high Carr Index (CI) values which highlights the powder’s high packing tendency and poor flowability (Ghoroi et al. (2013)). Although secondary powder components are usually present in the bulk composition during industrial experiments, this work only employs a single powdered component to ensure that the observed agglomerate formation is not due to any interaction behavior of the excipients.

Four different solvents, that encompass a wide range of thermophysical properties, were investigated in this work: demineralized water (conductivity of $1\ \mu S.cm^{-1}$), Methanol (Fisher Scientific, 99.9%), Ethanol (Pharmaco-apper, 200 proof) and Acetone (Fisher Scientific, 99.8%). The physical and thermal properties of the solvents at different temperatures are listed in Table 2.1. APAP-Methanol combination was taken as the main powder-solvent system and the remaining solvents were tested to assess effect of solvent properties on agglomerate formation.

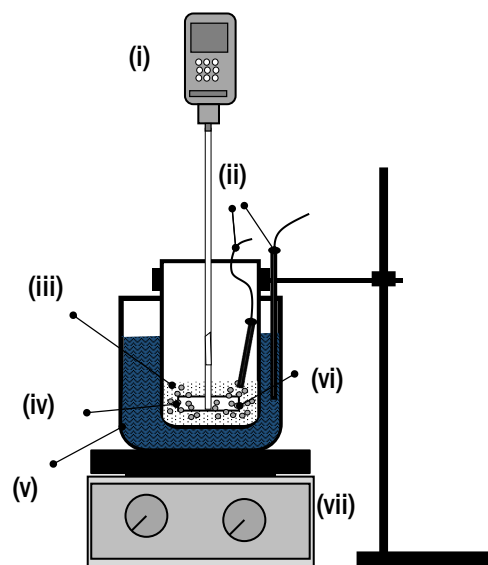
The agitated drying experiments were conducted in a bench-scale setup, shown in Figure 2.5, which is fitted with an over-head mechanical stirrer with a four-bladed steel impeller and thermocouples for temperature monitoring. At the start of each trial, 80g of the dry APAP powder was re-slurried with the desired solvent at a specific liquid to solid (L/S) ratio. The powder and solvent were mixed at various L/S ratios (0%, 5%,

Table 2.1: Thermophysical properties of the pure solvents used in parametric study

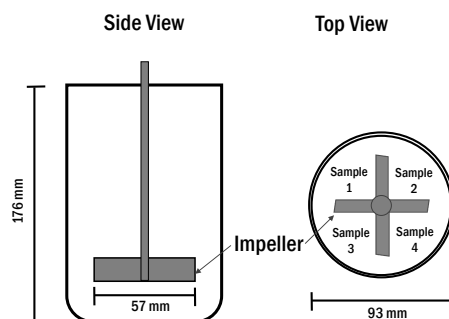
Solvent	Boiling point [C]	Density [kg/m ³]	Viscosity [mPa.s]	APAP solubility [mol/L]	Heat of va- porization [kJ/mol]	Surface tension [mN/m]	Polarity[-]
Methanol							
(at 25 °C)	64.6	787.87	0.53	1.73	37.44	22.62	0.762
(at 50 °C)		763.88	0.36	2.97	36.48	20.19	
Ethanol							
(at 25 °C)	78.5	784.07	1.06	1.09	42.37	22.23	0.654
(at 50 °C)		758.50	0.67	1.80	41.21	19.82	
Acetone							
(at 25 °C)	56.05	785.92	0.31	0.52	31.22	23.08	0.355
(at 50 °C)		757.51	0.25	0.87	29.69	19.36	
Water							
(at 25 °C)	100	999.04	0.90	0.10	43.94	72.67	1.000
(at 50 °C)		982.83	0.55	0.21	42.90	68.19	

Note:

1. Data for pure solvent density, viscosity, heat of vaporization and surface tension (at different temperatures) are calculated from DIPPR105 equation parameters, Vogel equation parameters, PPDS12 equation parameters and raw data regression respectively obtained from Dortmund Data Bank Software and Separation Technology (DDBST) thermophysical database. (DDB).
2. Solubility data at different temperatures extrapolated from Granberg and Rasmuson data for solubility of Acetaminophen in pure solvents Granberg and Rasmuson (1999).
3. Solvent polarity data were obtained from Reichardt, 2003. Reichardt (2003)



(a) Annotation: (i) Over-head stirrer with four-blade impeller (at 45° angle with respect to the bottom of dryer) (ii) Thermocouple (iii) Wetted APAP-solvent cake in a 600ml glass beaker (iv) Agglomerates (v) Water bath (vi) Four-bladed steel impeller (vii) Hot plate.



(b) The side and top views of the vessel illustrate the dimensions of the apparatus and the distinct areas from which samples were retrieved during specified time intervals.

Figure 2.5: Schematic of the bench-scale agitated drying apparatus.

15%, 25% and 50%) to simulate a wide range of pre-drying moisture content of the wet cake after the washing phase during the agitated filter drying operation (see Figure 2.1). Literature studies have shown that the amount of moisture (wash solvent) remaining after the washing and blow-down periods depend on the powder-solvent system such that different systems have different minimum achievable moisture content. Due to the powder-solvent interactions and the pore network distribution in the bed, some cakes make have high moisture content even after extended blow-down period (Lim et al. (2016)).

The vessel with the powder slurry was then immersed into the water bath which was maintained at 92°C. Since the apparatus is open to ambient pressure, a high temperature for the bath was chosen to ensure that pure solvent boiling points are reached. Table 2.2 details the experimental conditions explored when agitated drying were carried out by varying the L/S ratio, impeller speed and the solvent type. The height of the agitator was held constant over the drying period and the total drying time was kept same for all experiments (24 mins).

Table 2.2: Design space used in the parametric study of agitated drying

	Solvent choice	L/S ratio	Agitation at 50 rpm		Solvent choice	L/S ratio	Agitation at 50 rpm
1	Methanol	25%	Off	19	Ethanol	15%	On
2	Methanol	15%	Off	20	Methanol	25%	Off
3	Methanol	25%	On	21	Ethanol	25%	Off
4	Methanol	15%	Off	22	Ethanol	25%	On
5	Ethanol	5%	Off	23	Ethanol	15%	Off
6	Ethanol	5%	On	24	Methanol	5%	Off
7	Methanol	25%	On	25	None	0%	Off
8	Methanol	15%	On	26	None	0%	Off
9	Ethanol	25%	On	27	None	0%	On
10	Methanol	5%	On	28	None	0%	On
11	Methanol	5%	Off	29	Methanol	50%	Off
12	Ethanol	5%	Off	30	Methanol	50%	Off
13	Methanol	5%	On	31	Methanol	50%	On
14	Ethanol	5%	On	32	Methanol	50%	On
15	Ethanol	25%	Off	33	Water	15%	Off
16	Ethanol	15%	On	34	Water	15%	On
17	Ethanol	15%	Off	35	Acetone	15%	Off
18	Methanol	15%	On	36	Acetone	15%	On

For continuous agitation trials, the impeller speed was held constant at 50 rpm. The

choice of the rotation rate was determined from impeller tip speed scale-down from lab scale operation of various AFDs reported in literature (Sahni and Chaudhuri (2012); Lim et al. (2016); Lekhal et al. (2003)). An average of these values was selected so that industrially relevant agitation is used during the agglomeration profiling.

Regular samples were removed from the particle bed (at time 0, 3, 7, 13, 19 and 24 mins) to determine the variation of the moisture content in the bed and to study the changes in the agglomerate size distribution. In order to minimize the error in sampling, small amounts of powder (less than 2% of cake mass) were retrieved from distinct areas in the vessel and combined before further analysis. The moisture contents of the samples were determined by calculating the loss on drying (LOD) values after drying the sample in a hot-air convection oven at 90°C overnight. The particle size distributions of the samples were measured using *EYECONTM* particle sizer (operating range: 50-3000 μm). For this study, D_{10} , D_{50} and D_{90} diameters were recorded for each sample.

2.3.2 Parametric Study Analysis

A more thorough study of dynamic agglomeration profiles is presented in the following sections where the bench-scale agitated drying experiments are analyzed.

2.3.2.1 Influence of residual liquid amount (liquid to solid ratio)

Figures 2.6 below show the change in median particle diameter, D_{50} , of APAP-Methanol samples tested in the bench-scale setup. In order to distinguish the effect of the residual liquid content, the experimental trials where the other parameters - agitation and type of solvent - are held constant are chosen for analysis.

The dynamic agglomeration profile demonstrates the typical subprocesses involved in during wet granulation namely - wetting and nucleation, consolidation, and breakage. As can be seen from the sudden rise of particle size in the earlier time-steps, wetting and nucleation behavior where the liquid binder comes into contact with the powder bed to form initial particle agglomerates (or nuclei) is discernible. These soft/loose nuclei are created due to the formation of liquid bridges between the particles through mechanical dispersion of the solvent. The collision of these particles with each other

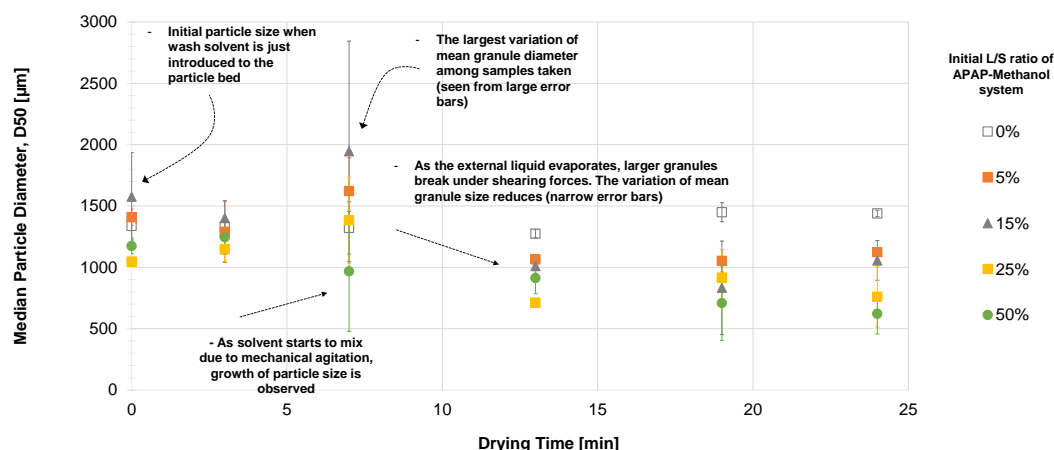


Figure 2.6: Mean particle diameter, D_{50} , dynamic agglomeration profile of APAP-Methanol samples over time. Solvent type and agitation (50 rpm) held constant while varying L/S ratio.

and the impeller blades result in the densification of granules. As drying continues, the moisture content decreases sharply which impedes any further growth (see Figure 2.8B). Due to the drying of liquid bridges and agitation of the bed, these granules tend to not survive the shearing forces which leads to granule breakage and reduction in the granule size. Similar breakage of nucleated granules has been observed in literature (Iveson et al. (2001); Tardos et al. (1997)). These trends are also visible in Figure 2.7 which exhibits images taken by the particle sizer.

Corresponding to the starting liquid level, the kinetics and impact of agglomeration processes also differ. At 0% L/S ratio, almost no granule growth is seen which characteristically emphasizes the absence of wetting and nucleation phase. Although no solvent is added, due to the cohesive nature of the powder particles itself, micronized APAP form millimeter-scale granules just from the inherent compression of the powder bed and impeller agitation. Granules formed in such a fashion maintain the granule size till the end. From 5% to 25% L/S ratio, the rise and fall pattern of granule size are almost identical. After the liquid disperses in the first few minutes, the wetted lumps formed most likely layers fine powders to grow to a certain size (and hence limits the span of particle size distribution seen in Figure 2.8a. As the drying proceeds, any free solvent present in the system quickly evaporates leaving only the moisture trapped

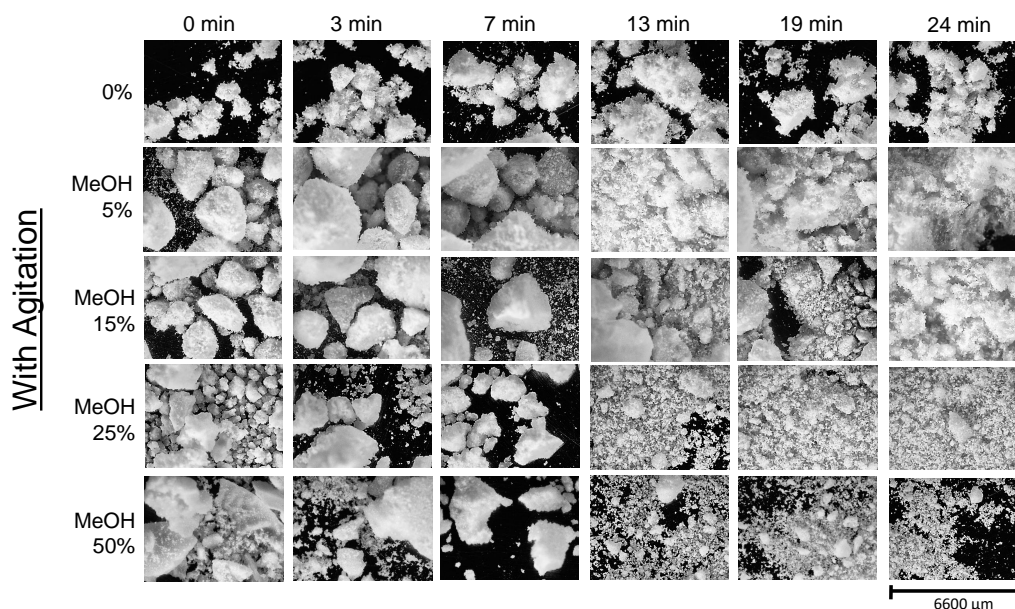
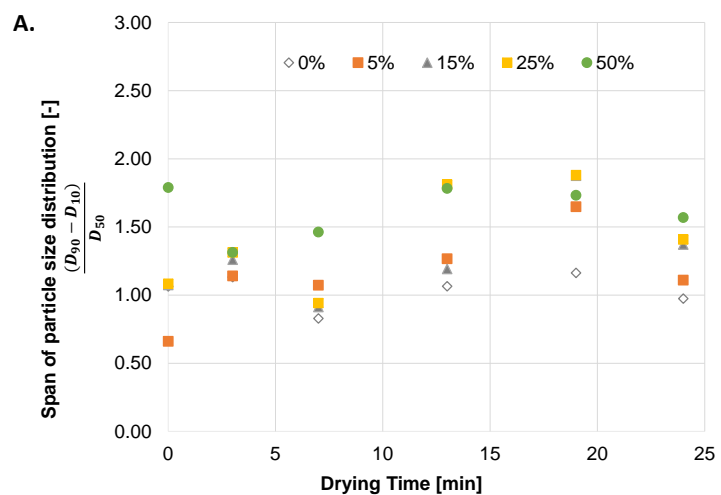


Figure 2.7: EYECON images of the particulate sample over time with different L/S ratio of APAP with Methanol. Solvent type and agitation (50 rpm) held constant.

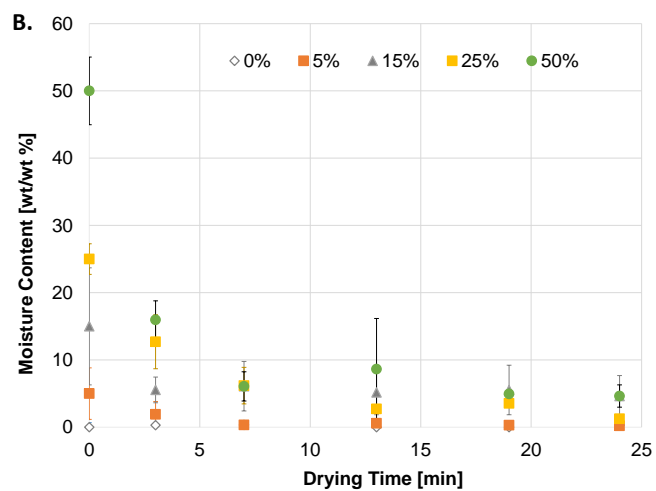
within these weak agglomerates. The increase in the PSD span towards the end of the drying period when the earlier-formed nuclei are starting to breakup also reaffirms the growth of weak agglomerates and subsequent breakage of such particles. In addition, the significant drop of the relative standard deviation of granule aspect ratio, shown in Figure 2.9, also indicates that most probably the irregularly shaped agglomerates start to break apart as drying proceeds. The aspect ratio of granules, generally, move closer towards 1 (spherical shape) over time.

The differences between the sizes of 5 to 25% L/S ratios is also distinctive. The largest agglomerates were produced when the starting L/S ratio was 15% rather than 25%. A probable reason for this is could be the amount of liquid contained in the agglomerates that are formed which reaches the critical L/S ratio levels that enhance the dynamic yield strength of agglomerates. From Figure 2.3, the high yield stress values for APAP-methanol granules are seen to peak around 10% and 20% L/S ratios. Due to the quick evaporation of free solvent from the system, it is more likely that more agglomerates formed with 15% initial L/S ratio had the critical moisture content.

At higher starting liquid levels (50% L/S ratio), however, relatively smaller granule



(a) Particle size distribution span



(b) Moisture content of samples

Figure 2.8: Dynamic profiles of APAP-Methanol samples over time with varying L/S ratio.

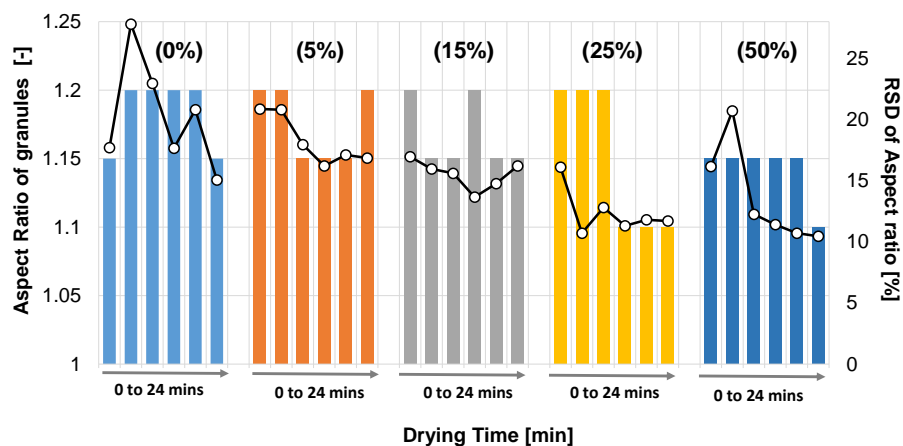


Figure 2.9: Aspect ratio of APAP-Methanol samples over time with varying L/S ratio. Bar plots represent aspect ratio values and overhead line plots outline the relative standard deviation of aspect ratio.

sizes are observed compared to lower liquid content runs. One reason for such behavior could be overwetting of powder: any agglomerates formed with excess liquid are highly deformable as seen from yield stress measurement experiments seen in previous section. These granules do not manage to retain any structural integrity and only reach a certain size before they are ultimately sheared.

2.3.2.2 Influence of agitation

In order to identify the effect of agitation on agglomerate growth dynamics, the experimental runs of APAP-Methanol wetted powder at varying L/S ratio were performed without mechanical agitation. Figure 2.10A below compares the change in D_{50} values over time.

One of the most distinguishable effect of employing continuous agitation is the destruction of nuclei over time due to the presence of shearing forces. When the agitation is removed, the granules that are formed at the start of the drying phase disintegrate slowly and thus, sharp rise and fall of granule size is absent. In Figure 2.10A, although the initial size of granules between runs with and without agitation are almost identical, the subsequent dynamics is very different. While the experiments with continuous agitation initiates dispersion of liquid and thus enables the early agglomeration formation, the agglomerate formation in trials without agitation do not show this type of

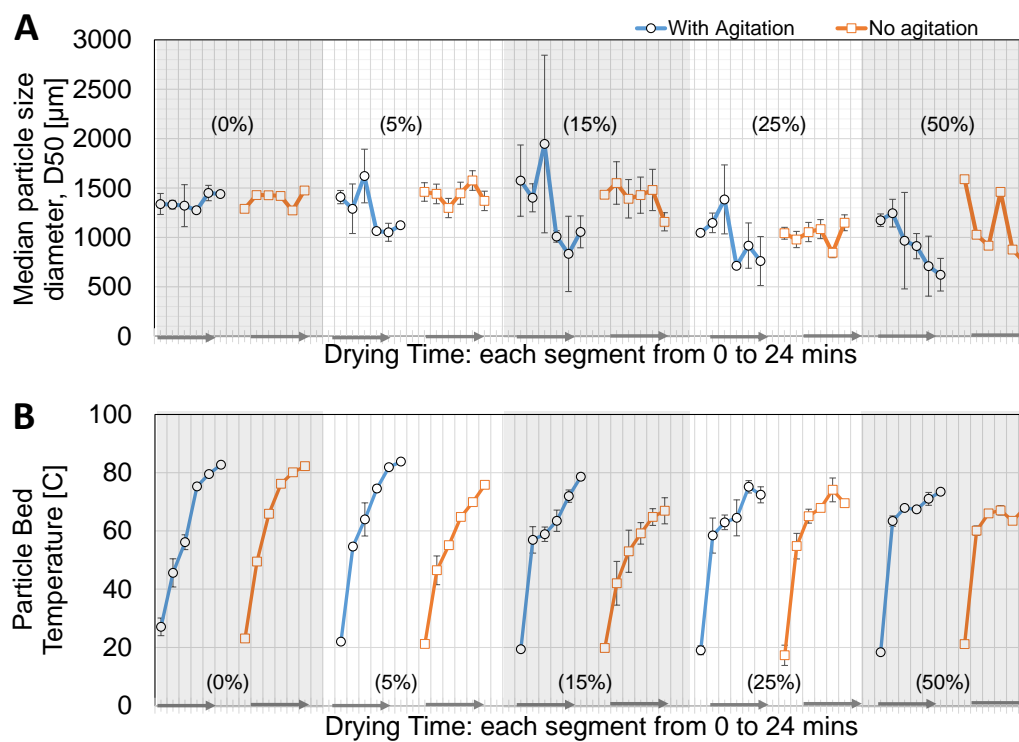


Figure 2.10: Comparison of **A.** Median particle diameter, D_{50} and **B.** Particle bed temperature profiles of APAP-Methanol samples over time with and without agitation.

growth. Although the liquid bridges formed in these agglomerates also dry over time, the hardening of agglomerates through recrystallization of solute in an un-sheared environment ensures that solid bridges maintain the granule structure. This pattern is clearly visible in the images taken from the particle sizer as shown in Figure 2.11. In terms of agitated drying operation, this finding re-emphasizes the need for agitation: the presence of moderate shearing helps enhance both drying rates (see Figure 2.10B) as well as in controlling agglomerate formation.

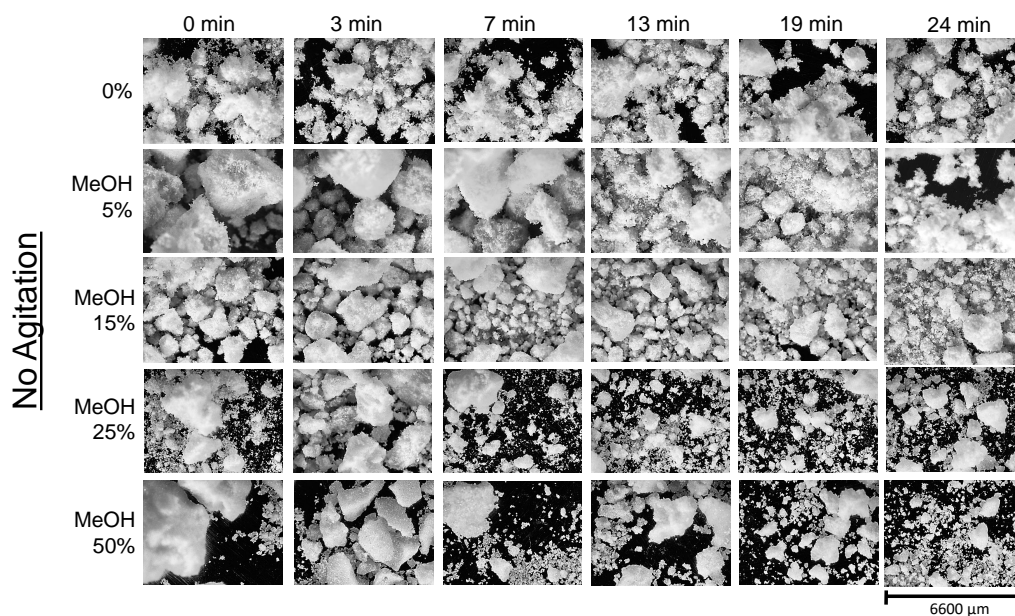


Figure 2.11: EYECON images of the APAP-Methanol samples over time with different L/S ratio and without agitation.

Similar comparison of experiments with and without agitation were also performed for other APAP-solvent combinations. In Figure 2.12, the median diameter of granules sampled over time are presented for methanol, ethanol, water and acetone solvents while keeping the L/S ratio constant at 15%. As mentioned earlier, the D_{50} values for trials without agitation are generally larger than those produced with continuous agitation. Further discussion on influence of solvent choice is presented in the following section.

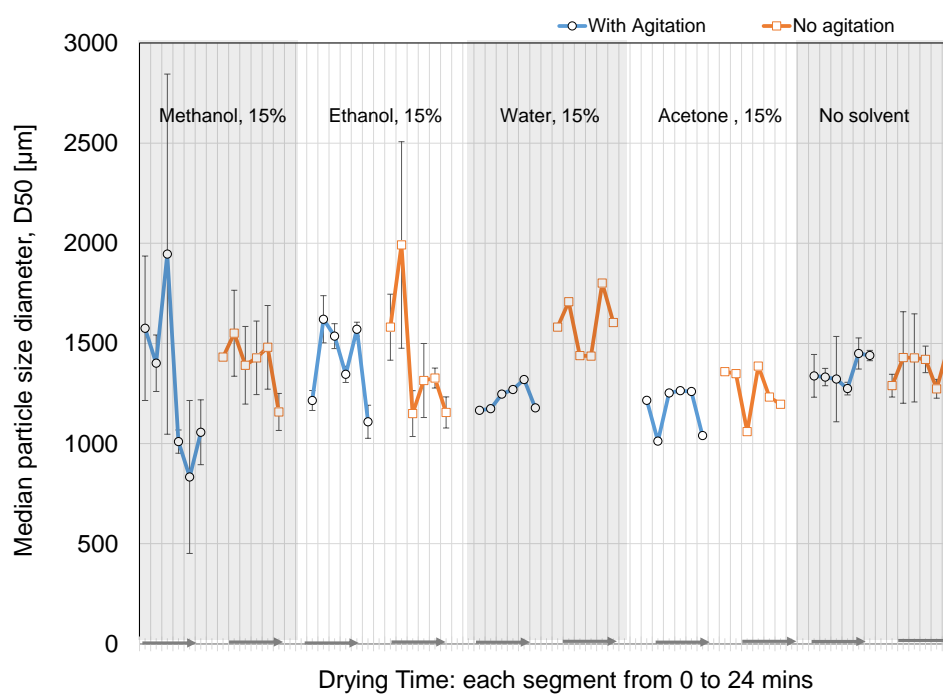


Figure 2.12: Mean particle diameter, D_{50} , profile of APAP-solvent samples over time with and without agitation. L/S ratio and impeller speed are held constant at 15% and 50 RPM respectively.

2.3.2.3 Influence of solvent choice

The dynamic effect of choosing different solvents as the residual wash liquid is presented in Figures 2.13A-C in terms of change in median particle diameter, moisture content of the samples and the aspect ratio of agglomerates respectively.

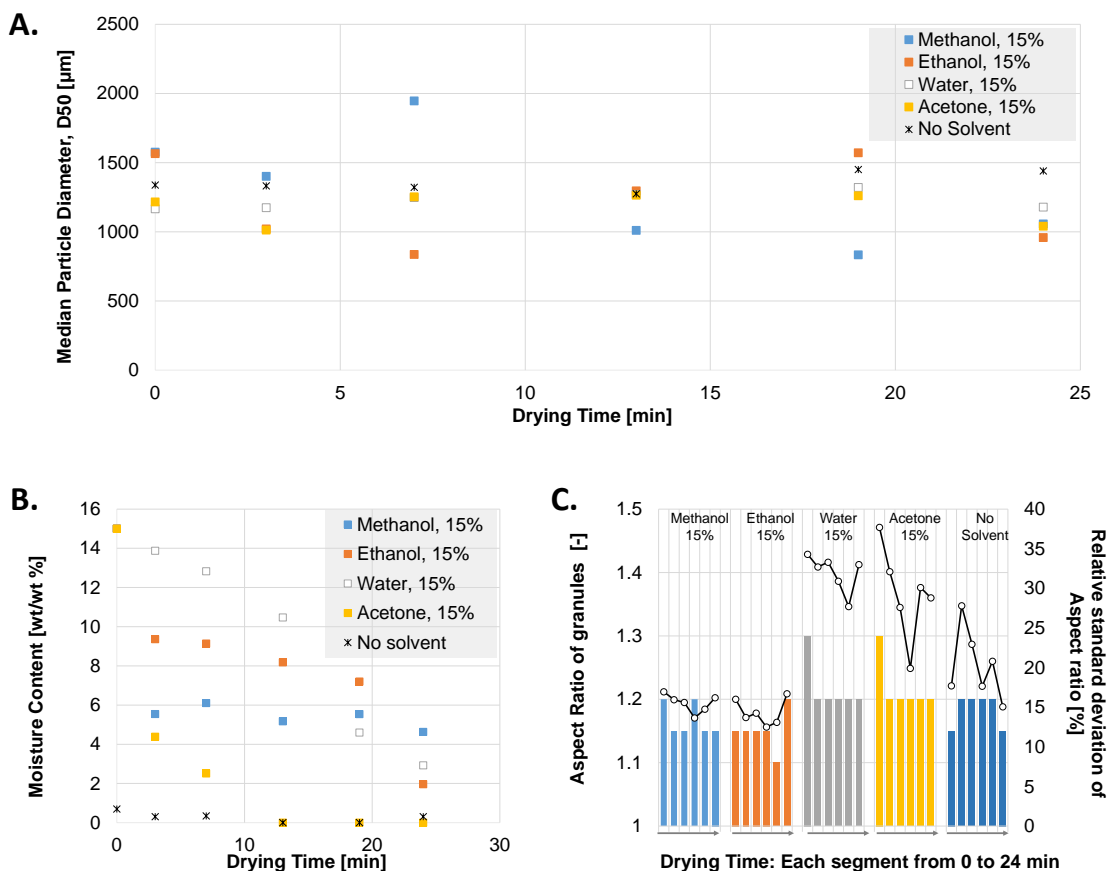


Figure 2.13: **A.** Mean particle diameter, D_{50} **B.** Moisture content and **C.** Aspect ratio (with RSD) of agglomerate samples over time with different residual solvents. Runs were performed at 15% initial L/S ratio and with agitation (50rpm). Note for **C.** Bar plots represent aspect ratio values and overhead line plots outline the relative standard deviation of aspect ratio.

From Figure 2.13A, the dynamic agglomeration profile for each solvent is discernable. While APAP-methanol and APAP-ethanol combinations show the rise and fall trend as discussed in earlier sections, the profile for using water and acetone differ drastically. The agitated drying experiments run with these low polarity solvents show very

minimal agglomerate growth behavior- similar to dry powder pattern. Any agglomerates formed with these solvents survive the shearing forces till the end of drying period. In contrast, experiments run with methanol and ethanol form larger but short-lived agglomerates which degenerate over time as can be seen from images in Figure 2.14.

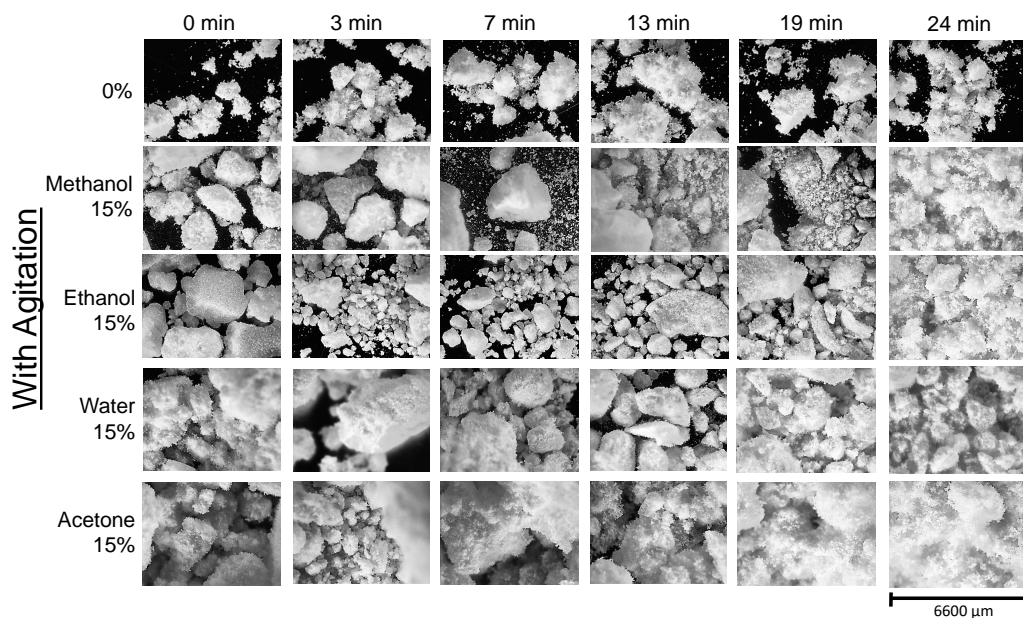


Figure 2.14: EYECON images of samples over time with different residual solvents. Runs performed at 15% L/S ratio and with agitation (50rpm)

The thermo-physical properties of the solvent, given in Table 1, provide an insight into this solvent-dominant behavior. First solvent property to note is the enthalpy of vaporization that directly affects the amount of liquid remaining in the powder bed (See Figure 2.13B). Solvents with low heat of vaporization such as acetone evaporates very rapidly than other solvents; hence, the wetted agglomeration behavior is minimal. This behavior is exacerbated due to the drastic decrease in boiling point of acetone when APAP is added to the solvent (see Figure 2.15A). As mentioned earlier, the agglomerate growth in general is instigated when the residual liquid present around the particles become more viscous as the solvent dries due the dissolution of solids. It is this viscous film which acts like the binding agent to enhance coalescence between wet particles. Solvents which evaporate quickly do not get an opportunity to undergo this process.

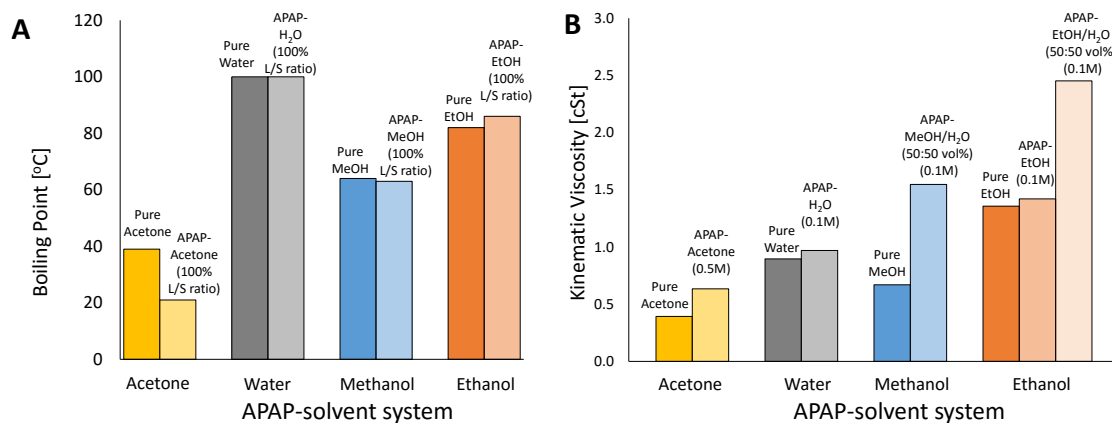


Figure 2.15: Effect of APAP concentration on **A.** Solvent boiling point (C) from McLoughlin et al. (2003) **B.** Solvent kinematic viscosity (cSt) calculated from data presented in Ålander and Å. C. Rasmuson (2005), Rajagopal and Renold (2015) and Shaikh et al. (2011)

Next solvent characteristic of importance while considering agglomeration is the wetting and spreading ability of solvents over the powder which is controlled by the polarity, viscosity and surface tension of the fluid (Parikh (2010)). APAP powder (crystals) have been investigated extensively in literature and are known to possess a strong negative (electron-donating) polar component (Ålander et al. (2003); Ålander and Å. C. Rasmuson (2005); Ålander and Rasmuson (2007)). For such a powder bed, a decrease in agglomeration is expected with increasing solvent polarity of protic solvents such as ethanol, methanol and water. This rationale explains why presence water as a binding liquid is weaker compared to methanol and ethanol solvents even though water remains in the system for the longest time (see Figure 14B). Another interaction at play could also be the extremely low solubility of APAP in water which means that the liquid film layer that lingers during drying phase likely has very low concentration of solid and hence low viscosity. Under such conditions, the agglomerates generated do not coalesce significantly.

For methanol and ethanol solvent runs performed with constant L/S ratio, the dynamic agglomeration profile differs in the degree of rise and fall of agglomerate size. While methanol agglomerates seem to disintegrate easily, the size of APAP-ethanol agglomerates seem to retain the size through the drying regiment. For a more detail comparison between methanol and ethanol, the agglomeration profile of APAP-ethanol

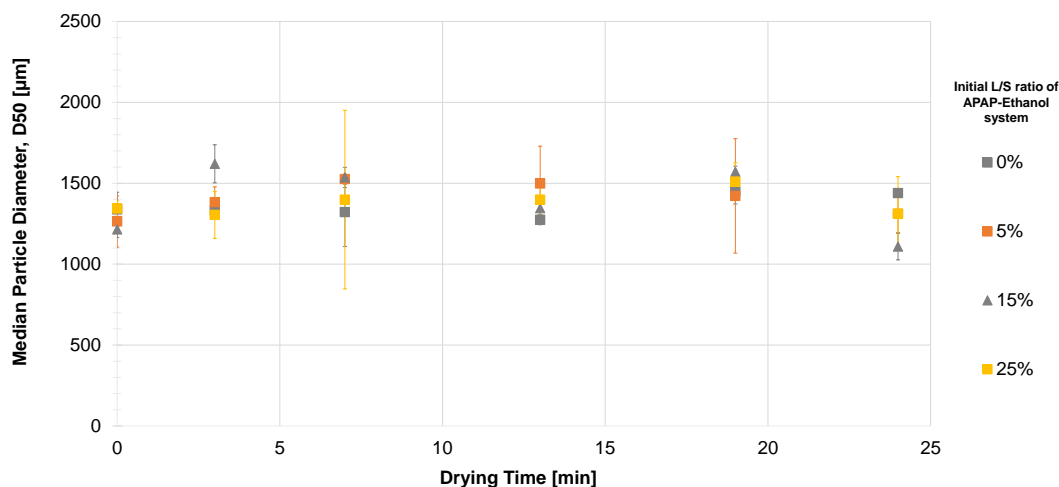


Figure 2.16: Mean particle diameter, D_{50} , dynamic agglomeration profile of APAP-Ethanol samples over time. Solvent type and agitation (50 rpm) held constant while varying L/S ratio.

experiments at different L/S ratio is shown in Figure 2.16. Even over different initial L/S ratio, this trend seems to be valid for ethanol runs. A possible explanation for such an agglomeration behavior could be the influence of ethanol's viscosity and heat of vaporization which is comparably higher than that of methanol. Firstly, ethanol seems to remain in the system at a higher moisture content due to its higher boiling point and heat of vaporization (See Figure 2.13B). From the granule growth regime map investigations carried out, the prolonged presence of high moisture content for APAP-ethanol runs means that induction-type of growth will most likely carry on for a longer time. The methanol runs which have faster drying rate, on the other hand, will remain in the induction growth regime for a short time and then proceed to nucleation-only regime. Additionally, ethanol possesses higher fluid viscosity which dominates over methanol's high APAP solubility levels. Figure 2.15B presents literature data (Ålander and Å. C. Rasmuson (2005); Rajagopal and Renold (2015); Shaikh et al. (2011)) on the effect of solute concentration on solvent kinematic viscosity. Although methanol has a higher solubility towards APAP powder than ethanol, it is still not able to overcome the difference in viscosity. As a result, the liquid bridges between particles that form due to the viscous surrounding film, thus is probably stronger for ethanol than methanol.

This trend can also be seen from the yield stress measurement carried out for APAP-ethanol runs. While the APAP-methanol pellets seem to have narrow peaks at which the granule yield stress is maximum, ethanol runs have a broader range of L/S ratios where the granules retain high yield strength values.

Figure 2.13C provides a further look at the nature of granules formed using different solvent choices in terms of aspect ratio and its RSD. As suggested earlier, experimental trials with acetone, water and dry powder, which primarily forms weak agglomerates have higher aspect ratio compared to granules formed using methanol and ethanol where coalescence also takes place. In addition, the higher RSD of water and acetone runs also hint at the wide distribution of such irregularly shaped lumps typical of weak nuclei formation behavior.

2.4 Conclusions

Through granule growth regime map investigation and parametric analysis of agitated drying behavior, dynamic agglomeration growth profile for a model cohesive powder, micronized acetaminophen at various process conditions were investigated in this study.

The granule growth regime map analysis generally concurs with the parametric studies performed and shows that induction and nucleation type of granule enlargement where the dynamics of wetting dictates the formation of granules is predominant during agitated drying. Depending on the amount of time the agitated drying experiment remains in the specific growth regime, the dynamic agglomeration profile differs drastically.

The three major causes for undesired lump formation during agitated drying- incomplete de-liquoring (high residual liquids), presence of continuous agitation and choice of wash solvent - all showed significant effect on increase in agglomerate formation. The thermo-physical properties of the wash solvents chosen seems to be most important factor that influences the dynamic agglomeration profile. Wash solvents which have high fluid viscosity seem to form stronger agglomerates that retain their structure through the drying process. Although higher solubility of the powder, which increases

the apparent viscosity of the thin liquid layer surrounding the particles, does elevate agglomerate formation, however, this effect was less dominant compared to the effects of liquid fluid viscosity levels- as seen from comparison with methanol and ethanol runs. In terms of the amount of residual moisture content, a critical L/S ratio range is noticeable for different wash solvents where the agglomerates formed possess superior strength. For prevention of agglomerates, such initial L/S ratios must be avoided. For use of agitation, the comparison between static runs without use of impeller and continuous agitated runs clarifies the importance of mechanical agitation to break any weak agglomerates formed in the system.

Part II

Specific Aim II: Development,
Implementation and Assessment
of using Mechanistic Studies to
Understand Underlying
Mechanisms of Granular Growth
Processes

2.5 Overview

Granule growth is a complex particle process often occurring intentionally or unintentionally during various granular processes. The change of particulate size, whether through controlled granulation operations or undesired agglomerate formation, are common granule growth processes that occur at various stages of particulate production in powder manufacturing industries. Typically, the desirable size enlargement of microscopic powders is carried out through wet granulation operations to improve flowability and handling of powder substances. During this unit operation, a mechanically stirred powder bed is introduced to dissolved binders through wet or dry addition to initiate granule growth. Conversely, a common industrial occurrence of unwanted granule growth occurs during the mechanical agitation of wet filter cake during filter-dryer operations. Enhanced process understanding of such granule growth phenomena are thus required to facilitate design, control, and optimization of such unit operations.

The simulation of agglomeration/attrition behaviors during granule growth, however, remains particularly challenging due to the simultaneous mass and momentum transfers occurring between particles in both environments. Moreover, due to the wide variety of physicochemical properties of the wet granular systems and complex interacting influence of operating conditions, there are no universal models available to understand the particle-level behavior inside the vessels. In this study two different case studies are investigated to develop and implement mechanistic studies to understand the underlying mechanism of granular processes.

In chapter 4, mechanistic simulations of agitated filter-drying operations, used in particulate industry for sequestering active ingredients and key intermediates from the wet cake after the crystallization step, are presented. In this study, Discrete Element Methodology (DEM) which simulates and tracks individual particles throughout the process are employed to gain particle-scale information. In general, DEM models have been used extensively in literature to simulate granular flow behavior since the algorithm can provide detailed profiles on forces, velocities and collisions experienced by particles. However, these DEM models have not incorporated a wet, cohesive granular flow with

heat transfer models which is the key mechanism in agitated drying. A novel DEM simulation which brings together capillary and viscous liquid bridge formation and, granular heat conduction and evaporation kinetics algorithms is presented in this study. Additionally, in-depth analysis of particle scale behavior which is responsible for drying and agglomerate growth kinetics are also studied with respect to different scaling criteria is also presented.

In Chapter 5, a mechanistic DEM model is presented which investigates the two kinds of binder addition approaches commonly used during wet granulation in a batch high-shear granulator: wet binder addition (WBA) and dry binder addition (DBA). To define the complex interactions in the systems, a novel integrated DEM algorithm that incorporates powder wetting behavior, capillary and viscous liquid bridge formation as well as binder dissolution was developed.

2.6 Publications

The details of the discussions provided in this section were published in the following article:

- **Tamrakar, A.**, Chen, S., Ramachandran, R. **2019**. A DEM model-based study to quantitatively compare the effect of wet and dry binder addition in high-shear wet granulation processes. *Chemical Engineering Research and Design*, 142, 307-326.
- **Tamrakar, A.**, Zheng, A., Piccione, P. M., Ramachandran, R. **2019** Investigating particle-level dynamics to understand bulk behavior in lab-scale agitated filter dryer (AFD) using Discrete Element Method (DEM) (*Manuscript in preparation*).

Chapter 3

Investigating particle-level dynamics in a lab-scale agitated filter dryer (AFD) using Discrete Element Method (DEM)

Agitated filter drying (AFD) is a complex physical-thermal separation process which involves isolating solutes from its mother liquor. In agro-chemical and pharmaceutical industry, filter-dryers are used for sequestering active ingredients (AIs) and key intermediates from the wet cake after the crystallization step. During the agitated drying phase, the mechanical agitation of the wet cake, implemented to enhance heat and mass transport, has been commonly observed to result in formation of undesired agglomerates that require further processing. Only relatively few experimental and computational studies of the effects of operating parameters and material properties on the drying and agglomeration growth kinetics have been described in the literature. In absence of robust predictive models, the go-to solution in order to avoid the agglomeration behavior of AIs has been to use minimal agitation which is not only suboptimal but also significantly increases the drying times.

The simulation of drying and agglomeration behaviors in AFD is particularly challenging because the agitated drying processes are mechanistically governed by simultaneous heat, mass and momentum transfer equations. In addition, the behavior of agglomeration growth and drying pathway varies significantly with the physical properties of the residual solvents in the cake as well as the operating conditions of the agitated dryer. A comprehensive modeling approach to simulate both drying and agglomeration behavior in AFDs through implementation of mechanistic Discrete Element Modeling (DEM) simulations with coupled granular liquid bridge cohesion model, heat

conduction model and evaporation kinetics is presented. Additionally, in-depth analysis of particle scale behavior which is responsible for drying and agglomerate growth kinetics are also studied with respect to different scaling criteria is also presented.

3.1 Background

3.1.1 Agitated filter drying

The AFD operation is a complex physical-thermal separation process which involves isolating solutes from its mother liquor. Through combination of the filtration and drying of the crystallization product into a single unit, AFD systems minimize solid handling - which leads to reduced product loss and contamination Perlmutter (2007); Kudra and Mujumdar (2009); Tsotas and Mujumdar (2012). In addition to improved containment, AFD units also offer manufacturers the ability to operate drying operations under low pressure/vacuum conditions. Since most active ingredients (AIs) and excipients are highly heat sensitive, strict temperature control is generally vital to avoid any degradation. Traditionally, the use of such low temperature has led to the crystal drying phase being the bottleneck for manufacturing Sahni et al. (2013); Murru et al. (2011); Mujumdar (2006). With the opportunity to employ low pressure conditions in an enclosed AFD system, however, a high driving force for heat and mass transfer is still attainable at relatively low temperatures. As a result, AFD systems are popular in various particulate industries including agro-chemicals, pharmaceuticals, biochemicals, fine chemicals, etc. for isolating AIs and key intermediates from slurries after the crystallization step.

One of the other main feature of an agitated filter dryer is the heated agitator with airfoil blades which not only provide an extended heat transfer area but also increase the stability at high torque levels Kudra and Mujumdar (2009). In essence by using heated agitation, AFD systems promote uniform drying through continuous exposure of particles to the heated surfaces (vessel walls, filter plates and the agitator itself). It is roughly estimated that the heat input contributions by the heated agitator is around 45% of the total energy input while the heat flux through the vessel walls and filter

plate are about 25% to 30% each Kudra and Mujumdar (2009). Thus, by amplifying the mechanical agitation of the powder bed, the driving force for heat transfer can be increased and the overall drying times minimized.

On the flipside, the use of aggressive drying conditions can have a major impact on the quality of dried materials. The physical properties of AIs have huge impact on the product performance: the particle size distribution, for instance, affects the stability, dissolution rate, content uniformity as well as the reproducibility of the manufacturing process Remy et al. (2015). Although the goal of the isolation and drying operations is to only separate the solids without affecting the particle size distribution, aggressive drying can lead to particle size alterations. In AFD systems, particles are often subjected to large compressive and shearing forces which can result in out-of-specification products which negatively affects the downstream operations Kougoulos et al. (2011); Lamberto et al. (2011). In particular, the extensive use of agitation during different filter-drying when combined with the effects of moisture content of the cake can induce undesired attrition (breakage) or agglomeration of particles.

In general, the experiments performed under agitated drying conditions indicate a competition between agglomeration and attrition phenomena. While agglomeration is usually dominant when the drying rate is high (i.e. at high moisture content), attrition is prevalent usually towards the end of the drying cycle when the drying rate is low and/or the shear rate is high Lekhal et al. (2003, 2004); Tamrakar et al. (2016); Birch and Marziano (2013); Zhang and Lamberto (2014). If the powder bed has low moisture, the particle breakage rate is enhanced due to the extended drying time which allows for particles to undergo several particle-particle/ particle-vessel collisions. The attrition of particles causes several manufacturing issues including generation of undesired fines, deviation from desired crystal size distribution, dust explosion, poor flowability, slow filtration as well as poor washing of subsequent lots Hare et al. (2011); Ende et al. (2013). It has been shown by Lekhal et al. (2003) that breakage during agitated drying is negligible until the critical moisture content (typically 2 – 4%) is reached. At moisture contents below this the breakage dramatically increases due to the increased shear stress. Contrastingly, for higher drying rates and high residual moisture contents,

the number of collision events decreases, and agglomeration becomes more dominant. Under such conditions, balling of overly wet or sticky cake can occur which can lead to undesired agglomeration Birch and Marziano (2013); Tamrakar et al. (2016); Lim et al. (2016). The formation of large agglomerates in an agitated filter dryer unit not only leads to product non-uniformity but can also negatively impact cycle times due to difficulty in removing the batch from the processing equipment and addition of further size reduction steps to enable down-stream processing.

In addition, the dynamic behavior of agglomerate growth and attrition varies significantly with the physical properties of the wet granular medium as well as the operating parameters of the agitated dryer. The solubility of powder in the solvent system chosen, for example, has a serious impact on the extent of agglomeration: higher solubility leads to greater concentration of solute in the liquid bridge between particles which can in turn lead to larger extent of agglomeration when dried Pietsch (1969); Ende et al. (2013); Tamrakar et al. (2016). In another case, the operating vessel-fill level has been observed to have a significant influence on the particle size distribution of the product: low fill depths ($\leq 25\%$ dryer load) enhanced attrition phenomena due to the increase in number of particle collisions as more of the powder bed were exposed to the shearing action of the impeller Sahni et al. (2013). As such, the particle flow dynamics and drying kinetics in an AFD is highly complex governed by a multitude of interacting parameters. The Ishikawa diagram in Figure 3.1 below highlights some of the major material and process parameters that influence agglomeration/attrition behavior in agitated filter-drying processes.

3.1.2 Modeling of agitated drying

The simulation of drying and agglomeration/attrition behaviors in an AFD is particularly challenging because the filter-drying processes are mechanistically governed by simultaneous heat, mass and momentum transfer equations. Moreover, due to a wide variety of physicochemical properties of the wet cake and complex interacting influence of operating conditions, there are no universal models available to understand both the drying kinetics and the macro-behavior of the powder bed in filter dryers Nere et al.

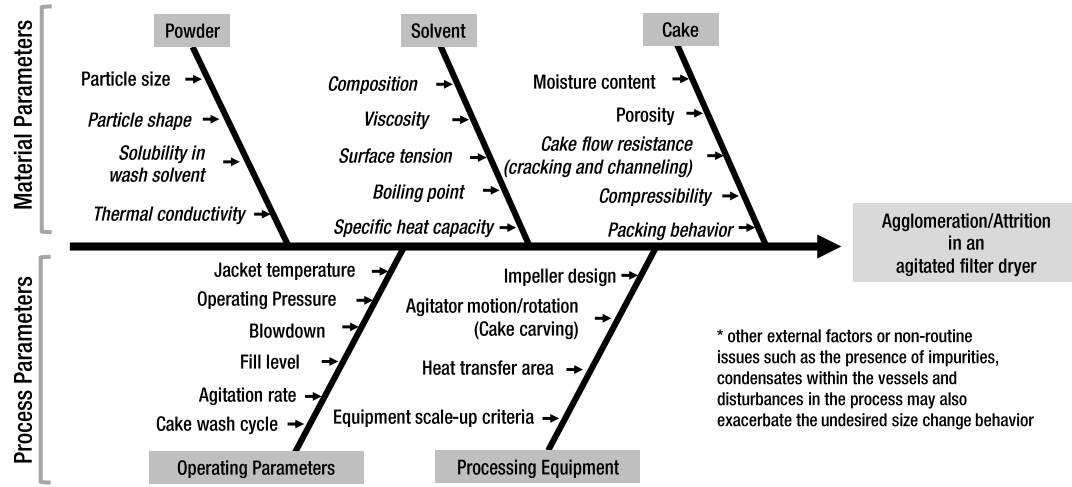


Figure 3.1: Multitude of interacting parameters that influence agglomeration/attrition in agitated filter dryers

(2012); Tsotsas et al. (2007). However, researchers are making progress, especially from two fronts: (A) continuum approach and (B) discrete particles approach.

A. Continuum approach: The continuum approach, based on the heat penetration theory through the particle bed proposed by Schlünder and colleagues Schlünder (1980, 1984); Schlünder and Mollekopf (1984); Tsotsas and Schlünder (1987, 1986a,b), considers the packed bed as a quasi-continuous phase and an effective heat transfer coefficient is then estimated by assuming that drying proceeds through alternating periods of contact drying and mixing. Here, the contact drying period (t_R) is a hypothetical time interval during which the agitated bed is considered static and a heat transfer from the heating wall to the stagnant bed occurs (Equation 3.1). The heat penetration through the bed during this period is then described as the movement of a distinct heating surface (termed drying front) parallel to the hot surface. Between the heating surface and the drying front, the particles are assumed to be drying - where a temperature profile exists between the heating wall at T_w and the drying front at T_s . Beyond the drying front, the particles are considered wet. The bed temperature here is assumed to be uniform and equal to the saturation temperature of the liquid at the operating pressure. Likewise, the mixing period t_{mix} is a time interval that is assumed to produce the perfect macro-mixing of the bed which levels out the temperature and moisture

content gradient (Equation 3.2). Thus, as drying proceeds, during every contact period the drying front penetration produces a drop in the bed moisture content and a rise in bed temperature. With every following mixing period, the front is then eliminated and both - the moisture content and the temperature of the bed - are spatially equalized to a mean value. Mathematically, the heat penetration across the bed (α_{bed}) during t_R is derived from the Fourier theory of conduction as shown in Equation 3.3.

$$t_R = \frac{1}{n} \cdot N_{mix} \quad (3.1)$$

$$t_{mix} = \frac{1}{n} \quad (3.2)$$

where n is the rotational frequency and N_{mix} is the dimensionless parameter *mixing number* which represents the number of revolutions needed for perfect mixing. N_{mix} is an empirically correlated value and depends on the type of dryer and its stirring device Schlünder and Mollekopf (1984); Tsotsas and Schlünder (1986b, 1987).

$$\alpha_{bed} = \frac{2}{\sqrt{\pi}} \sqrt{\frac{\rho c_p \lambda}{t_R}} \cdot \frac{1}{erf \zeta} \quad (3.3)$$

where ρ , c_p and λ are the density, heat capacity and thermal conductivity of the bed. The ζ term represents the reduced distance of the drying front which is estimated based on the *phase-change number* (Ph) Tsotsas et al. (2007). Ph is the reduced average moisture content of the bulk and is a measure of the intensity of heat sink.

Further extensions of this continuum approach are also available in literature. Over the years, the penetration theory has been broadened to include contact drying at various conditions including vacuum drying conditions Schlünder and Mollekopf (1984); Tsotsas and Schlünder (1986b, 1987), drying under atmospheric pressure Tsotsas and Schlünder (1986a); Gevaudan and Andrieu (1991); Blumberg (1994), drying of paste/sludge material Dittler et al. (1997); Arlabosse and Chitu (2007); Yan et al. (2009) as well as drying of solids wetted by multi-component mixtures Thurner and Schlünder (1986); Martinez and Setterwall (1991); Vidaurre and Martínez (1997).

Despite its prevalent use, one of the most important limitation of the continuum modeling approach is that the mechanics of particle motion is generally neglected in the model development. In fact, key parameters of the model including the duration of the fictitious static period, t_R , as well as the mixing number, N_{mix} do not have a theoretical basis but are empirically tuned. As a result, spatially correlated patterns are only observed due to the additional assumptions employed in the models and the particle property distribution profiles cannot be assessed accurately.

B. Discrete particle approach: While heat penetration models are numerical methods to estimate the heat transfer from hot walls to mechanically agitated powder beds by assuming a moving drying front, DEM methodology simulates individual particles in an AFD system and solves Newton’s equation of motion for each particle to account for their motion during the process. Particles are considered individual elements with sets of properties that influence its flow behavior (size, density, coefficient of restitution, etc.), and collision between particles or equipment and the resulting particle trajectories are determined for each time step. The key assumption in DEM is that the simulation time step can be chosen so small that the interaction force is applied only to immediately adjacent particles. Thus, DEM offers a more fundamental look into powder mixing and drying behavior. As a result, the limitations of continuum approach to account for granular motion and spatial inhomogeneity are overcome through DEM simulations. In general, DEM models have been used extensively in literature to simulate granular flow behavior since the algorithm can provide detailed profiles on forces, velocities and collisions experienced by particles Lian et al. (1998); Remy et al. (2010); Gantt et al. (2006); Barrasso et al. (2014); Sen et al. (2014); Kuo et al. (2004); McCarthy et al. (2000). However, these DEM models have not incorporated a wet, cohesive granular flow with heat transfer models which is the key mechanism in agitated drying. A novel DEM simulation which brings together capillary and viscous liquid bridge formation and, granular heat conduction and evaporation kinetics algorithms is presented in this study.

3.1.3 Objectives

In the past, several experimental/numerical investigations have been conducted to understand the key parameters that lead to formation of undesired powder lumps in an AFD Lekhal et al. (2003, 2004); Kim et al. (2005); Murru et al. (2011); Kougoulos et al. (2011); Lamberto et al. (2011); Nere et al. (2012); Sahni et al. (2013); Sahni and Chaudhuri (2012); Hamilton et al. (2013); Birch and Marziano (2013); Ende et al. (2013); Zhang and Lamberto (2014); Remy et al. (2015); Tamrakar et al. (2016); Lim et al. (2016); Adamson et al. (2015); Papageorgiou et al. (2016). However, it is generally understood that the suggested mitigation methods can be specific depending on the powder-solvent combination. In addition, much less is known on the particle-scale dynamics that is occurring during agitated drying. Therefore, there is a need to better understand the relationship between the material properties, process conditions as well as equipment scale as it relates to the agglomeration behavior.

The main objective of this work is to develop a mechanistic model of particle-level dynamics in a filter dryer system through implementation of DEM simulations. Custom-made particle contact models with coupled granular liquid bridge (capillary and viscous force), cohesion model and heat conduction model are integrated to simulate the various wet granular flow dynamics. An in-depth analysis of the drying and granulation behavior is studied with respect to particle shape (aspect ratio), particle size, impeller design and rotation rate, filter cake smoothing and cake carving phase, fill level as well as residual wash liquid type and moisture content. Finally, a discussion on appropriate scaling criteria to ensure consistent particle velocities, compressive and shearing forces at different vessel scales is also presented. The scale up investigation assess the usability of common dimensionless number (such as Froude number, Reynolds number, Powder number, etc.) in scaling the particle-level dynamics of AFD operation. Different scaling indices are compared on their ability to maintain internal particle flow (i.e. particle velocities), dynamic similarities (in terms of compressive forces and cumulative collision energies) as well as thermal similarities (in terms of average particle temperature) at different vessel scales.

3.2 Model Development

DEM simulations follow a fixed algorithm to track the particles within its system (see Figure 3.2). Details regarding each stage of the DEM algorithm and the unique features incorporated in this study to recreate agitated drying processes are provided in the following sections.

In this work, the agitated filter dryer system was modeled after a lab-scale 2-L agitated filter dryer (ProCept nv, Belgium). The simplified DEM geometry based on the equipment design is illustrated in Figure 3.3. In the DEM geometry, the walls of the vessel as well as the impeller are considered as heat sources at a fixed temperature to simulate the jacketed wall/ heated impeller design used in the equipment. Table 3.1 below lists the key variables used in the setup of DEM simulation. In this study several designs of the system including impeller design, particle shape, size, equipment scaling, etc. were investigated; hence, the values given in Table 3.1 refer only to the base case scenario.

Table 3.1: Design and operation variables in base case DEM simulation

Parameter	Units	Values
Geometry		
Vessel volume (V)	L	2.3
Vessel height (H)	mm	174
Vessel diameter (D)	mm	130
Impeller diameter (D_i)	mm	125
Density	kg/m^3	7850
Poisson's ratio	-	0.3
Shear Modulus	Pa	1×10^{10}
Particle		
Particle diameter	mm	4
Total number of particles	-	12,500
Total mass of particles	kg	0.528
Density	kg/m^3	1260
Poisson's ratio	-	0.25
Shear Modulus	Pa	1×10^6
Thermal conductivity	W/m.K	0.12
Specific heat capacity	J/kg.K	1235
Operating Conditions		
Geometry temperature	K	365
Initial particle temperature	K	293
Fill level	%	18.14
Rotation Rate	RPM	30
Impeller tip speed	m/s	0.182

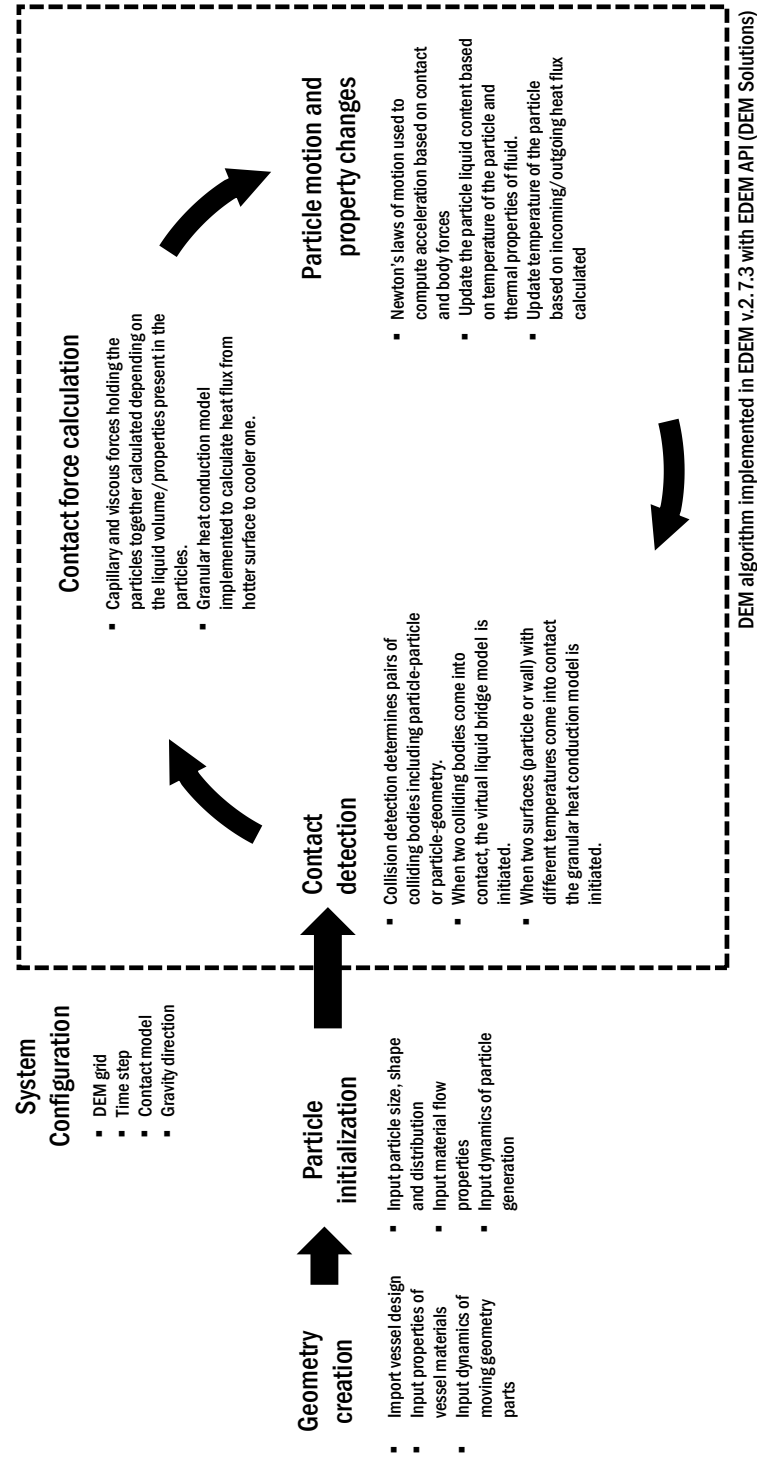


Figure 3.2: Discrete Element Method (DEM) algorithm implemented in this study. In order to simulate the wet granular flow and heat transfer mechanics in the agitated drying system, a virtual liquid bridge model and a heat conduction contact models were integrated into the DEM algorithm (added steps highlighted)

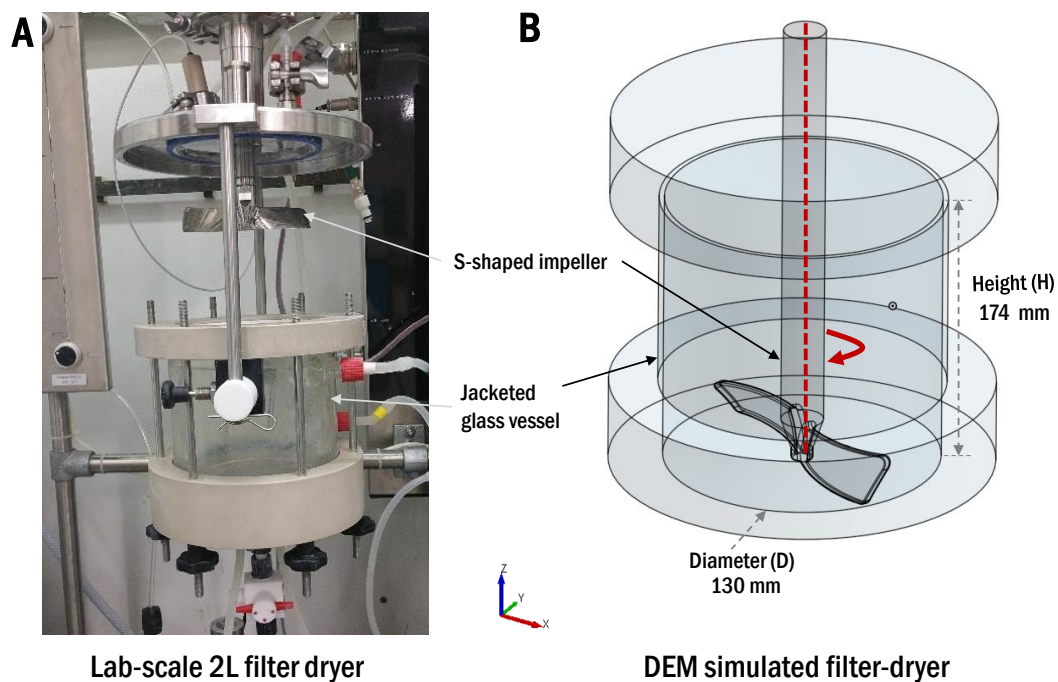


Figure 3.3: Geometry of the 2L lab-scale agitated filter dryer. **A.** Experimental Agitated filter dryer setup (ProCept, Belgium) **B.** CAD drawing used in the DEM simulation of 2L lab-scale agitated filter dryer.

3.2.1 Contact force calculations

The DEM algorithm calculates the collision events in every time step - events when particle-particle or particle-geometry have sufficient overlap - based on the velocity and position profiles of the particles in the previous time step. The overlap threshold is satisfied for particle-particle collisions if the distance between the centers of the particles is smaller than the sum of their radii; for particle-geometry collisions, the distance between the particle center and the point of contact needs to be smaller than the radius of the particle for successful contact detection.

Once a collision event is detected, the DEM algorithm then implements a particle contact force model to calculate the forces and energies experienced by the colliding particles. In the broadest sense, two types of contact models are available in DEM: the soft sphere model and the hard sphere model Mikami et al. (1998). The hard particle approach assumes that the particles collide with each other instantaneously while the

soft particle approach considers collisions as a continuous process that occurs over a period of time. In soft particle approach, the interactive forces are treated as continuous functions of the distance between particles Lian et al. (1998). Normally for application in powder process research where particles are very deformable in nature, soft particle approach is applicable.

In addition, there are a number of different types of soft particle contact models that are run after every collision detection - the common contact models available in commercial DEM software include Hertz-Mindlin model, the linear spring and dash-pot model etc. Comparisons between these models can be found in the review paper of Zhu et al. (2007).

In this framework, a simplified Hertz-Mindlin no-slip contact DEM phase interaction model was used to calculate the contact forces. The contact forces in the normal and tangential direction (\vec{F}_n and \vec{F}_t) determine how particles behave when they encounter each other or solid boundaries. The general expression for the Hertz-Mindlin model, which is a variant of the non-linear spring-dashpot contact model, are provided in Table 3.2.

3.2.2 Cohesion force calculation

In order to account for the wet granular flow in DEM, liquid bridge models - capillary liquid bridge model and viscous liquid bridge model - were used to determine the inter-particle cohesive forces between particles in contact. These models use the fluid volume on granules as well as fluid properties such as viscosity, surface tension and contact angle to calculate the cohesion forces. In addition, a critical separation distance based on fluid properties is also computed for each contact to determine a bridge rupture distance - if particles in contact move beyond the rupture distance, the liquid bridge is broken. Thus, the cohesion model used in this work simulate dynamic bonding between wetted granules which takes viscous forces into account.

The application of capillary or viscous bridge model can be determined through calculation of the dimensionless group capillary number (Ca) (Equation 3.14) for the contact between each wetted particle Ennis et al. (1990).

Table 3.2: Mathematical expressions for particle force calculation in DEM Particles model*

Parameter	Equation
Normal contact force (F_n)	$F_n = -K_n x_n - \eta_n \frac{dx_n}{dt} \quad (3.4)$
Normal spring stiffness coefficient (K_n)	$K_n = \frac{4}{3} E_{eq} \sqrt{x_n R_{eq}} \quad (3.5)$
Normal damping coefficient (η_n)	$\eta_n = \sqrt{5 K_n M_{eq}} \left[\frac{-\ln e_r}{\sqrt{\pi^2 + (\ln e_r)^2}} \right] \quad (3.6)$
Tangential contact force (F_t)	$\vec{F}_t = \begin{cases} -K_t x_t - \eta_t \frac{dx_t}{dt} & \text{if } K_t x_t \leq e_{sf} K_n x_n \\ -e_{sf} x_t \left \frac{K_n x_n}{x_t} \right & \text{if } K_t x_t > e_{sf} K_n x_n \end{cases} \quad (3.7)$
Tangential spring stiffness coefficient (K_t)	$K_t = 8 G_{eq} \sqrt{x_n R_{eq}} \quad (3.8)$
Tangential damping coefficient (η_t)	$\eta_t = \sqrt{5 K_t M_{eq}} \left[\frac{-\ln e_r}{\sqrt{\pi^2 + (\ln e_r)^2}} \right] \quad (3.9)$
Equivalent particle radii (R_{eq})	$R_{eq} = \frac{1}{\frac{1}{R_a} + \frac{1}{R_b}} \quad (3.10)$
Equivalent particle mass (M_{eq})	$M_{eq} = \frac{1}{\frac{1}{M_a} + \frac{1}{M_b}} \quad (3.11)$
Equivalent Young's modulus (E_{eq})	$E_{eq} = \frac{1}{\frac{1-\nu_a^2}{E_a} + \frac{1-\nu_b^2}{E_b}} \quad (3.12)$
Equivalent Shear modulus (G_{eq})	$G_{eq} = \frac{1}{\frac{2(2-\nu_a)(1+\nu_a)}{E_a} + \frac{2(2-\nu_b)(1+\nu_b)}{E_b}} \quad (3.13)$

* Equations sourced from: Tsuji et al. (1993); Di Renzo and Di Maio (2004),

Johnson and Johnson (1987); Verkoijen et al. (2002); CD-adapco (2016)

Subscripts a and b denote the two colliding particles

e_r and e_{sf} represent the coefficient of restitution and static friction.

x_n , x_t are the overlaps in normal and tangential directions at contact point.

Particle radius, mass, Young's modulus and Poisson's ratio are given by R , M , E and ν respectively

$$Ca = \frac{\mu U}{\gamma} \quad (3.14)$$

where μ is the average viscosity of fluid, U is the relative particle velocity and γ is the fluid surface tension present in the liquid bridge.

The Ca value of the liquid bridge generated describes the dominance of viscous forces (F_{vis}) relative to capillary forces (F_{cap}) (i.e. surface tension) across the bridge. Generally, for low capillary numbers ($Ca < 0.001$), the magnitude of the liquid bridge force is dominated by capillary forces, whereas for high capillary numbers, the capillary forces are negligible compared to the viscous forces. In the DEM simulation for this work, where the viscosity of the fluid is changing over time due to solvent evaporation, two cases of liquid bridge formation were implemented: $Ca < 0.001$ and $Ca > 0.001$. For $Ca < 0.001$, the capillary force model is used as the only liquid bridge force ($F = F_{cap}$). On the other hand, when Ca becomes larger than 0.001, both capillary and viscous force model are implemented ($F = F_{cap} + F_{vis}$).

Capillary force: The capillary force between particle-particle (F_{cap}^{p-p}) and particle-wall (F_{cap}^{p-w}) contact can be computed using Equation 3.15 and 3.16 respectively Lian et al. (1993, 1998); Lambert et al. (2008); Rabinovich et al. (2005); Liu et al. (2011); Washino et al. (2016).

$$F_{cap}^{p-p} = \frac{4\pi\tilde{r}\gamma\cos\theta}{1 + \frac{1}{\sqrt{1 + \frac{1}{V_{liq}} - 1}}} \quad (3.15)$$

$$F_{cap}^{p-w} = \frac{4\pi r\gamma\cos\theta}{1 + \frac{S}{\sqrt{\frac{\pi\tilde{r}}{V_{liq}}}}} \quad (3.16)$$

where \tilde{r} is the equivalent radii of the particles involved in the contact (see Equation 3.10), γ and θ are the surface tension and contact angle of the bridge fluid, V_{liq} is the volume of the liquid involved in the formation of bridge and S is the distance between two objects (particle or wall).

The V_{liq} value is calculated using the volume of liquid contributed by each wetted particle ($particle_i$ and $particle_j$) using Equation 3.17, 3.18 and 3.19 Shi and McCarthy (2008).

$$V_i = \frac{L_i}{2} \times \left(1 - \sqrt{1 - \frac{r_j^2}{r_i + r_j^2}} \right) \quad (3.17)$$

$$V_j = \frac{L_j}{2} \times \left(1 - \sqrt{1 - \frac{r_i^2}{r_i + r_j^2}} \right) \quad (3.18)$$

$$V_{liq} = V_i + V_j \quad (3.19)$$

where V_i and V_j are the liquid volume contribution of $particle_i$ and $particle_j$ for formation of liquid bridge respectively, L_i and L_j are the total liquid volume on the two particles and r_i and r_j are the respective particle radius.

In order to avoid the capillary forces going into infinity when two objects are attached to each other (i.e. $S = 0$), an important part of this bridge model is the forced damping of capillary forces by setting a minimum separation distance S_{min} Anand et al. (2009). S_{min} is usually determined based on the roughness of the particle; in this study an arbitrary S_{min} of $1 \mu m$ is used to limit the capillary forces.

In addition, a bridge rupture mechanism is also implemented when the separation distance S between particles is larger than a critical separation distance (S_c) which is dependent on liquid bridge properties. The estimation of S_c proposed by Lian et al. Lian et al. (1993) is used for both particle-particle and particle-wall bridge rupture (Equation 3.20).

$$S_c = \left(1 + \frac{1}{2}\theta \right) V_{liq}^{\frac{1}{3}} \quad (3.20)$$

Viscous force: The viscous forces (\vec{F}_{vis}) of the liquid bridge consist of normal and tangential components calculated using Equation 3.22 and 3.23 respectively Lian et al.

(1998); Goldman et al. (1967). The normal viscous force is derived from the Reynolds lubrication theory Lian et al. (1998):

$$\vec{F}_{vis} = \vec{F}_{vis}^n + \vec{F}_{vis}^t \quad (3.21)$$

$$\vec{F}_{vis}^n = \frac{6\pi\mu\tilde{r}v_r^n}{S} \quad (3.22)$$

$$\vec{F}_{vis}^t = \left(\frac{8}{15} \ln \frac{\tilde{r}}{S} + 0.9588 \right) 6\pi\mu\tilde{r}v_r^t \quad (3.23)$$

where μ is the fluid viscosity, \tilde{r} is the equivalent radii of the particles involved in the contact (see Equation 3.10), v_r^n and v_r^t are the relative velocities between two particles in normal and tangential direction and S is the separation distance. In the case of particle to geometry interactions, \tilde{r} is replaced by r radius of the particle.

3.2.3 Heat Conduction calculation

In order to simulate the heat transfer from the walls and impeller to a wet cake (high solid concentration phase), a conductive heat transfer model between particles developed by Chaudhuri et al. Chaudhuri et al. (2006) is used in this study. The heat flux (Q) between particles i and j is defined as a product of the inter-particle conductance (h_c) and the temperature gradient between the particles - given mathematically as:

$$Q_{i,j} = h_c \Delta T_{i,j} \quad (3.24)$$

The heat transfer coefficient, h_c value is estimated using Equation 3.25 and 3.26.

$$h_c = \frac{4k_i k_j}{k_i + k_j} A \quad (3.25)$$

$$A = \left[\frac{3F_N \tilde{r}}{4E^*} \right]^{1/3} \quad (3.26)$$

where k is the thermal conductivity of the colliding particles, A is the contact area, F_N is the normal force during the contact, \tilde{r} is the equivalent radii of the particles involved in the contact and E^* is the effective Young's modulus for the two particles.

3.2.4 Particle Motion and Temperature analysis

Besides the contact forces (\vec{F}_C^N and \vec{F}_C^T) which are only calculated upon contact detection, DEM algorithm also take into account other body forces (\vec{F}_B) such as gravity, drag forces, electrostatics, etc. which can act on particles at every time step. The final step in the DEM algorithm is the determination of new particle velocities and position due to the changes in contact and body forces. The total force (\vec{F}_T) which is a summation of contact forces (\vec{F}_C^N and \vec{F}_C^T) and body forces (\vec{F}_B) is then used to calculate the acceleration of the particle by Newton's 2nd law to compute the new velocity and position profile.

$$\vec{F}_T = \vec{F}_C^N + \vec{F}_C^T + \vec{F}_B \quad (3.27)$$

In addition, the change in the temperature of the particle i due to the heat flux in a single time step is then calculated by summing all the heat fluxes for the specific particle as follows:

$$\Delta T_i = \left[\frac{\Sigma Q_i}{\rho_i C p_i m_i} \right] \quad (3.28)$$

where ρ_i , $C p_i$ and m_i are the density, mass-averaged solid and solvent specific heat capacity and mass of the particle respectively.

3.2.5 In-silico scale-up design

In order to investigate the effect of scaling during agitated drying, a set of virtual experimentation using the DEM model developed were carried out by developing geometrically similar AFD vessels by enlarging the ProCept vessel design shown in Figure 3.4. Using a high-fidelity, first-principle based model such as DEM, a comprehensive scaling criterion can be investigated by analyzing dimensionless similarities. By investigating the scale-independence of granular flow under various scaling criteria such as keeping impeller Reynolds number, Froude number, Power number and impeller tip speed constant, the effectiveness of using such scaling indices can be observed. In the following study, the granular flow performance of a 2L agitated drying vessel was compared with enlarged vessels of sizes 5L and 15L designed in SolidWorks™CAD software. Table 2 below shows the parameters used in these scaled simulations in terms of particle diameter (D_p), vessel height (H), vessel diameter (D).

For these simulations, mono-sized spheres were used as the model particles and the fill level ($V_{particle}/V_{vessel}$) was kept constant at 18.14%. In order to assess the distribution of particle dynamics, two regions of the vessel - (i) Lower section of vessel where the impeller is rotated and (ii) upper section of the vessel towards the top layer of the particle bed were analyzed for any differences (see Figure 3.5).

The scaling indices (n) examined in this study are listed below:

1. **Constant Froude Number (n=0.5):** Generally used as a criterion for kinematic similarity in powder blending. Relates the inertial forces to gravitational forces. Given mathematically as:

$$Fr = \frac{v^2}{gR} = \frac{R\omega^2}{g} \quad (3.29)$$

where v is the impeller tip speed, R is the impeller radius, ω is the angular velocity and g is the gravitational constant. For constant Froude number scaling, the associated scaling expression used is given as follows:

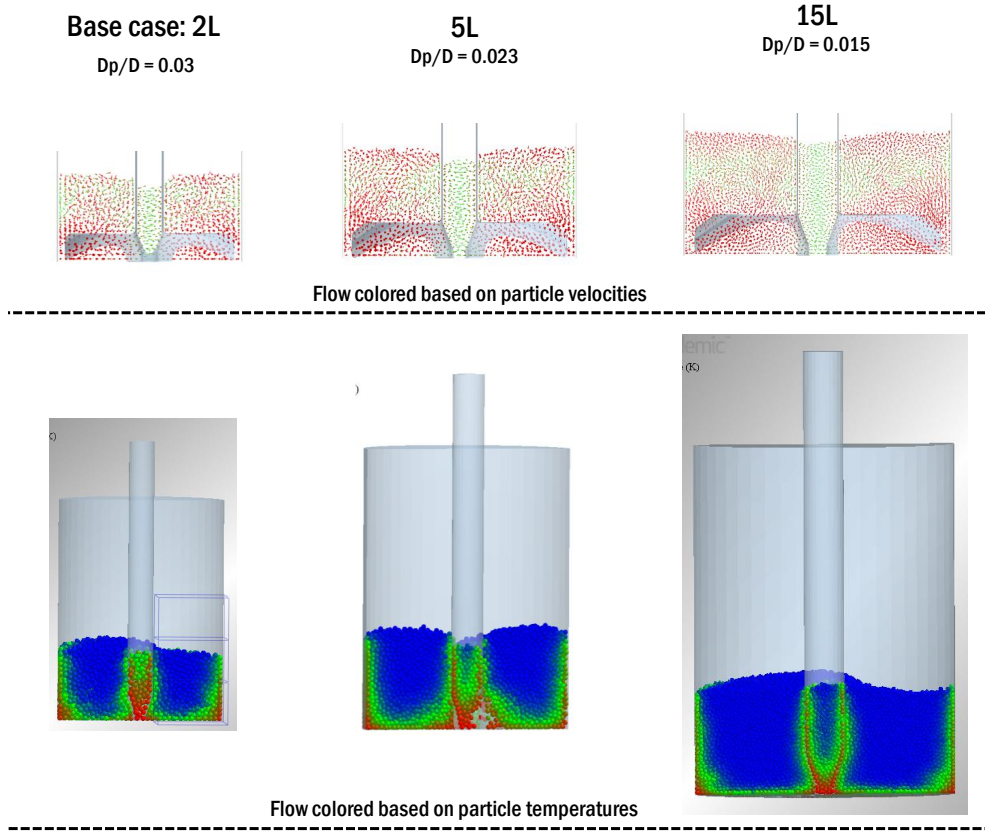


Figure 3.4: Illustration of the internal particle flow and temperature distribution. Figures not to scale **Top** Flow colored based on particle velocities: lower velocity (in green), higher velocity (in red). **Bottom** Flow colored based on particle temperatures: Low temp (in blue then green), high temp (in red)

$$\frac{N_{base}}{N_{scaled}} = \left[\frac{R_{scaled}}{R_{base}} \right]^{0.5} \quad (3.30)$$

2. **Constant Powder Number (n=0.66):** Relates the drag forces acting on a unit area of the impeller and the inertial stress and is thus a measure of the power required to overcome friction in powder flow. Mathematically -

$$Ne = \frac{2\pi\tau}{\rho N^2 d^5} \quad (3.31)$$

where τ is the impeller torque, ρ is the specific density of particle and d is the impeller diameter. For constant power per unit volume number scaling, the associated scaling expression used is given as follows:

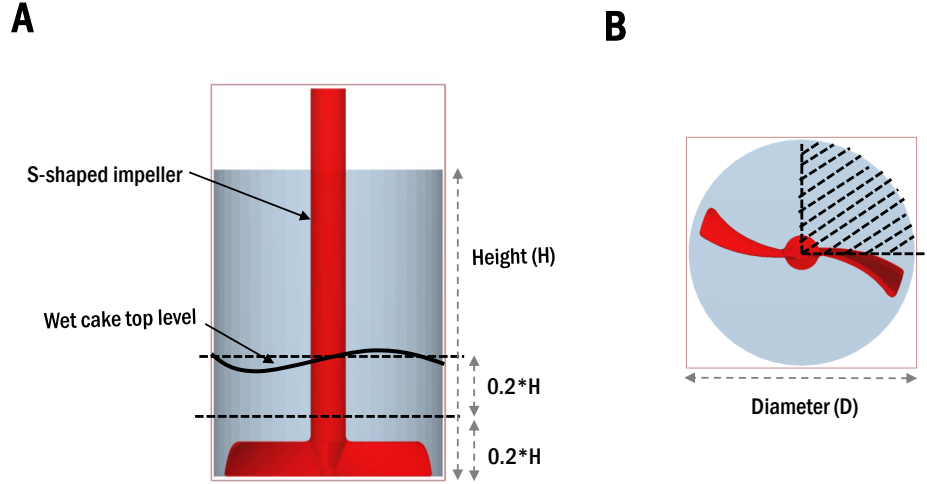


Figure 3.5: DEM data sampling schematic. **A.** DEM data obtained from 2 levels of the particle bed. **B.** Data extracted from one quarter of the vessel

$$\frac{N_{base}}{N_{scaled}} = \left[\frac{R_{scaled}}{R_{base}} \right]^{0.66} \quad (3.32)$$

3. **Constant Tip Speed (n=1):** Most commonly used to relate the impeller rotation to the velocities of particle within mixers. The scaling expression used for constant tip speed is given as:

$$v = R\omega = R.(2\pi N/60) \quad (3.33)$$

$$\frac{N_{base}}{N_{scaled}} = \left[\frac{R_{scaled}}{R_{base}} \right]^1 \quad (3.34)$$

4. **Constant Impeller Reynolds Number (n=2):** Relates the inertial forces to the viscous forces. For agitated mixers, impeller Reynolds number or mixing Reynolds number is used:

$$Re_N = \frac{d^2 N \rho}{\mu} \quad (3.35)$$

where μ is the effective viscosity of powder bed. For constant impeller Reynolds number scaling, the associated scaling expression used is given as follows:

$$\frac{N_{base}}{N_{scaled}} = \left[\frac{R_{scaled}}{R_{base}} \right]^2 \quad (3.36)$$

Although other indexes have also been used for scaling up of particulate operations - e.g. Tardos et al. Tardos et al. (2004) found $n = 0.8 \pm 0.01$ to be best to preserve magnitude of stress in larger high-shear mixer granulators. However, the applicability of the scaling criteria depends heavily on the system under consideration. The four scaling criteria used in this study were chosen due the popularity of these indices in literature.

Table 3.3: Parameters used in scaled AFD simulations

Volume	D_p	H	D	D_p/D	Fill
5L	4 mm	229.5 mm	171.4 mm	0.023	18.14
15L	4 mm	328.5 mm	215.4 mm	0.016	18.14

The associated impeller rotation rates and impeller tip speeds for the 2L, 5L and 15L vessels according to each of the four scaling indices (constant Froude number, constant Power number, constant tip speed and constant particle Reynolds number) are illustrated in Figure3.6 below:

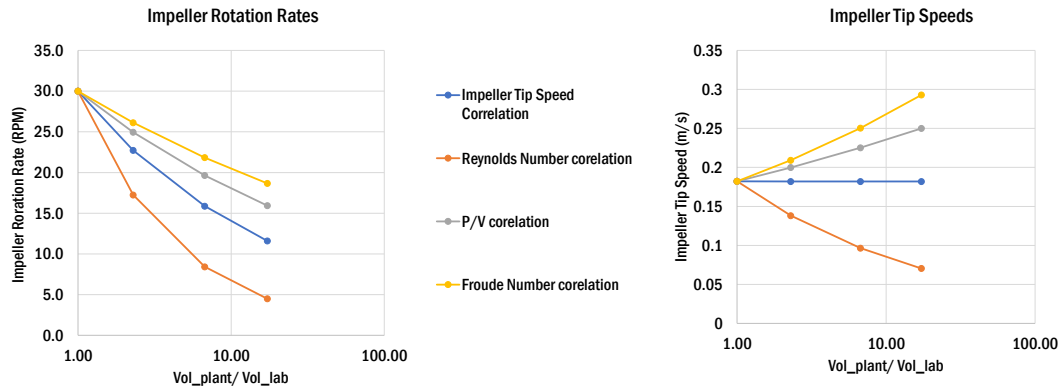


Figure 3.6: Different scales of filter dryer investigated in the DEM simulations (Top). The corresponding impeller rotation values and tip speed used according to different scaling indices (Bottom)

In order to comprehensively capture the particle-scale behavior of the DEM simulations, key representative variables that impact the internal particle flow, collision & shear dynamics as well as forces & energies experienced by the particles within the system were recorded at each scale. A successful scale-up operation thus ensures that all these critical dynamics are maintained over the different size scales.

3.2.6 Normalized parameter approach

By normalizing the time-averaged flow properties of particles including particle velocities in radial and axial direction, angular velocity, relative collision velocity, number of collisions, average kinetic energy as well as rate of temperature increase in the particle bed, a critical insight into the effect of scale up on particle-scale dynamics can be observed.

A schematic of the procedure used to normalize the particle scale information collected from the upper and lower section of the vessel for easier comparison is illustrated in Figure 3.7. For the standardization process, information on the key variables per revolution values were first converted to a single point for each scale of the vessel and for each scaling index by averaging the data over the period of 1 revolution for each simulation. The information is then normalized with respect to the base case simulation to examine the impact of scaling on the specific parameter. For instance, in the Figure 3.7, the particle velocities in X-direction for each of the 2L (base case), 5L and 15L scaled using constant Reynolds number were averaged over one revolution generated and plotted separately for the lower and upper section of the vessel.

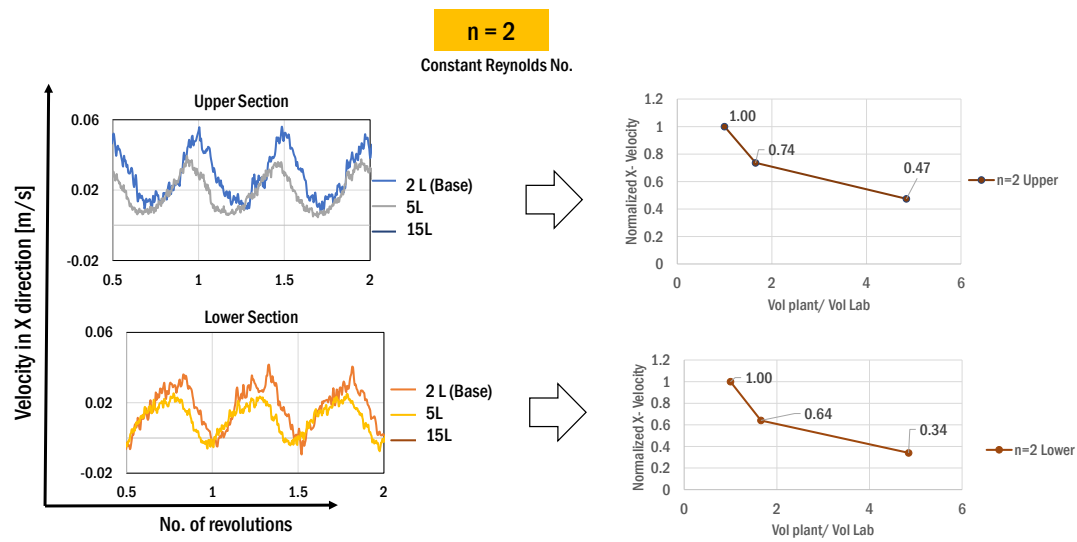


Figure 3.7: Schematic for the normalization procedure used for comparing key particle-scale variables using a scaling index. An example of particle velocity information obtained from simulating the different scales of filter dryer using constant Reynolds number criteria is presented.

3.3 Effect of Material Parameters on the particle-scale dynamics

3.3.1 Primary particle shape

The shape of the primary particle plays a critical role in the packing and flow of granular material. Experimental agitated drying results conducted by Tamrakar et al. Tamrakar et al. (2016) have shown that agglomerates of different shape (aspect ratios) are created during the agitated drying process. In the experimental results presented in Specific Aim I, AR values from 1.1 to 1.3 were observed as shown in Figure 3.8 below. In order to investigate the effect of particle shape, four different particle types created by merging spherical surfaces were developed in DEM as shown in Figure 3.9A to represent the range of AR values seen in experiment.

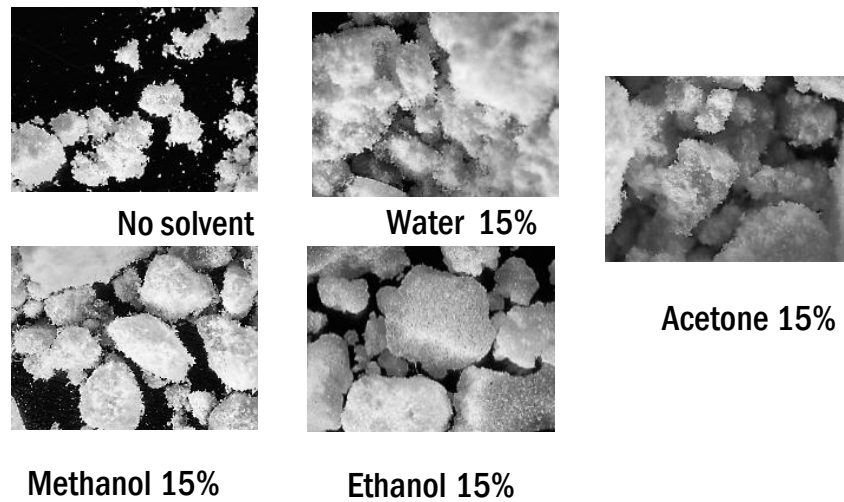


Figure 3.8: Various shapes of granules formed during the bench-scale study of the AFD

A drastic difference in the powder flow behavior - in terms of the average particle velocity and average compressive forces - is observable from agitated drying DEM simulation with equivalent fill level of particles (Figure 3.9B). Spherical particles show higher particle velocity and compressive forces compared to non-spherical particles. The presence of irregularly shaped and coarse particles can increase the internal friction of packed bed (i.e. force resisting motion between particles) which can lead to less flowability and poor mixing of the granular bed. This in turn can affect moisture and heat

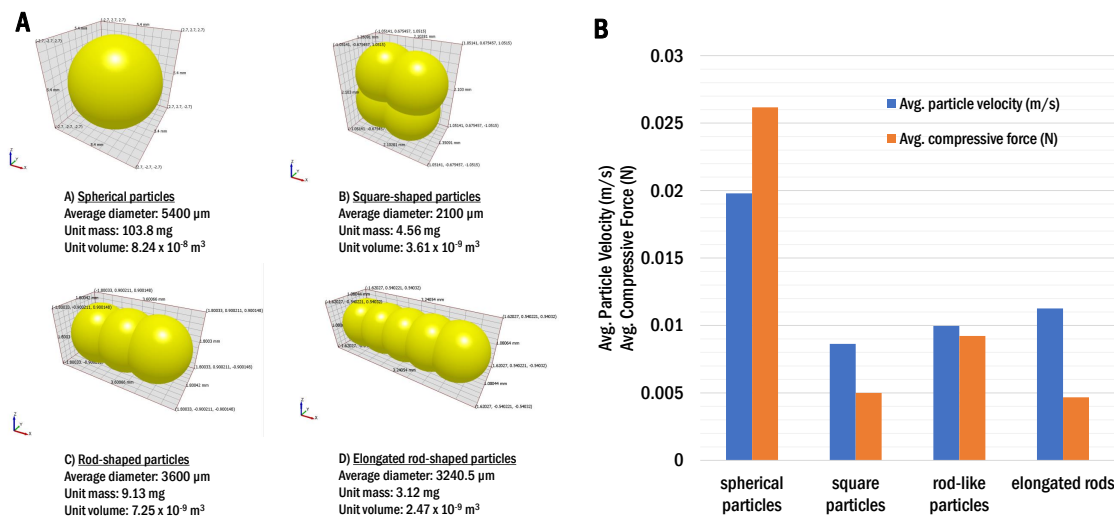


Figure 3.9: A. Different types of particle shapes simulated in DEM. The aspect ratio of particles and the principal diameter are provided. **B.** Effect of the particle shape on the average particle velocities and compression forces

dispersion within the bed. Among the non-spherical particles, changing the shape from square to elongated rod doesn't seem to affect particle velocities significantly. Although, rod-like particles show greater compressive forces among the rest.

The results from the DEM simulation indicate that the particle shape affects the mobility and therefore can cause segregation within the vessel. This in turn can affect moisture and heat dispersion. The particle shape, thus, is an important factor in designing the DEM system. Especially if the granule aspect ratio diverges significantly from 1.

3.3.2 Primary particle size

Primary particle size is an important property which can not only affect the flow pattern of particles within the mechanically agitated vessel but can also impact the compression forces experienced by agglomerates. In order to investigate the effect of particle size on AFD operation, two different sized primary particles (2.7 mm and 5.4 mm diameters) were simulated with a constant total mass (894 g) in the DEM algorithm developed in this study. The setup of the DEM simulation is shown in Figure 3.10A where the fill level and mass of the particle bed is kept same. The total number of particles simulated

for the 2.7 mm particles was 76,812 while for the 5.4 mm particles were 9,601.

The effect of simulated particle size on the average particle velocity, average compression forces and the impeller torque are illustrated in Figure 3.10B, 3.10C, and 3.10D below. Results show that smaller particle size generally have lower avg. velocities and compressive forces experienced than larger particle powder bed under same Froude number. In addition, the impeller torque recorded were lower for smaller particle sizes. A common practice for DEM simulations is using larger particles to relieve computational burden of the simulation. However, such scaling can affect the estimates of both particle velocities and compressive forces: DEM simulations with larger particles will tend to overpredict the degree of mixing.

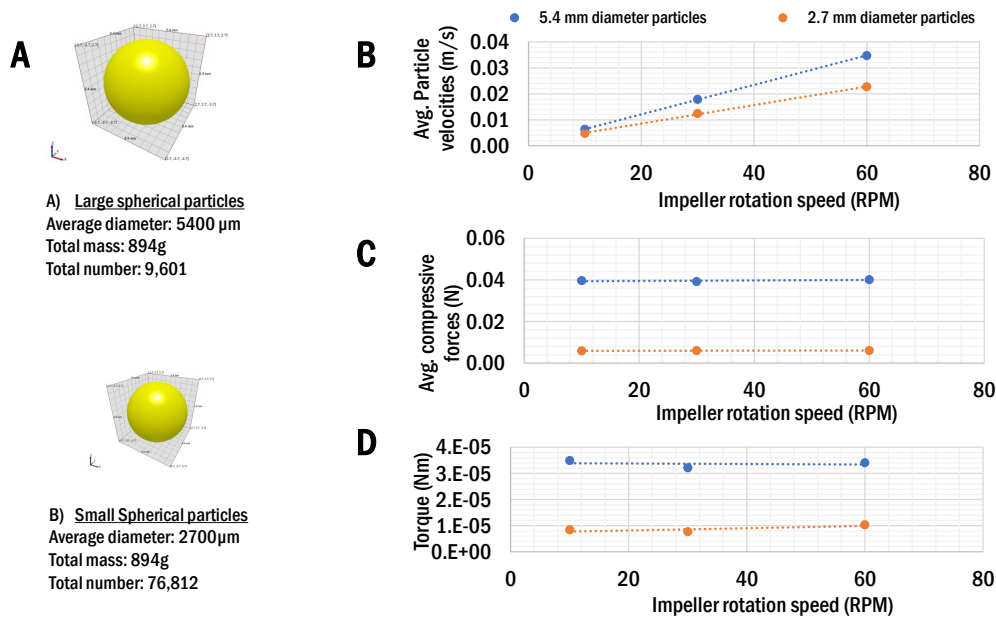


Figure 3.10: **A.** Two different particle size distributions with average diameter of 5.4 mm and 2.7 mm were investigated in DEM. The effect of these particle size distribution on **B.** Average particle velocities, **C.** Average compression forces and **D.** Torque experienced by the impeller are provided.

3.3.3 Effect of moisture content

The amount of liquid present in the powder bed affects the number of instances of liquid bridge formation in the particle bed which in turn affects the velocity of particles in

motion. Three different residual liquid content (using properties of water) were tested in the DEM simulation.

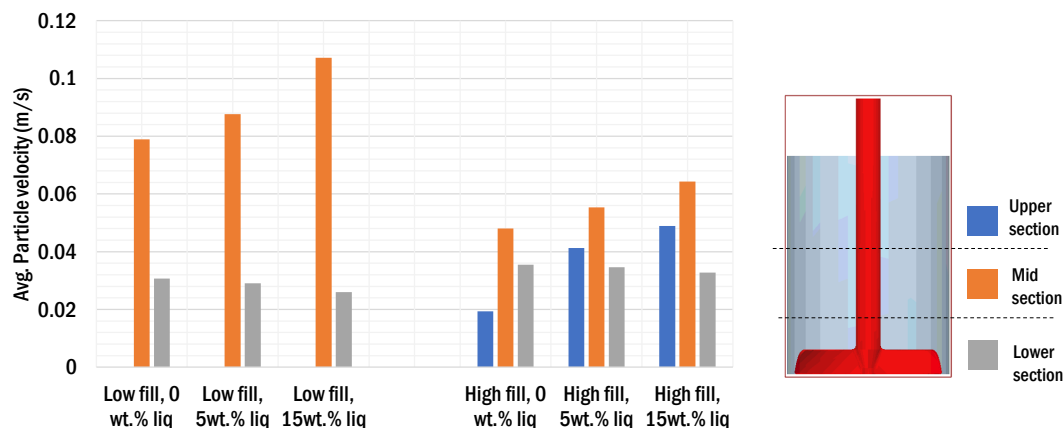


Figure 3.11: Effect of moisture content of the powder bed (0, 5 and 15 %wt./wt. liquid) on the average particle velocities within the filter dryer. Six independent DEM simulations were performed at 3 different liquid content levels and 2 different fill levels (low fill: 65 vol% loading and high fill: 95 vol% loading). The average particle velocities were extracted at 3 layers within the filter dryer (as shown on the legend)

DEM results in Figure 3.11 indicate that wetter particles in general have larger average particle velocities than drier particles. A possible explanation could be the formation of liquid bridge between particles and with the impeller. With more residual moisture content, particles agglomerate and move as a clump due to which the average particle velocities is observed to increase. In addition, with higher moisture content, more particles are likely to form liquid bridge bonds with the impeller blade - i.e. powder particles stick to the blades - which also increases the average particles velocities of particles near the impeller (lower section of the vessel).

3.3.4 Effect of wash liquid type

Thermo-physical properties of residual liquid affect the heat transfer within the packed bed. Properties of Methanol and Ethanol solvents were used for liquid bridges force calculations in the DEM algorithm to investigate the effect of solvent type.

As seen from Figure 3.12, the thermo-physical properties of residual liquid affect the heat transfer within the packed bed.

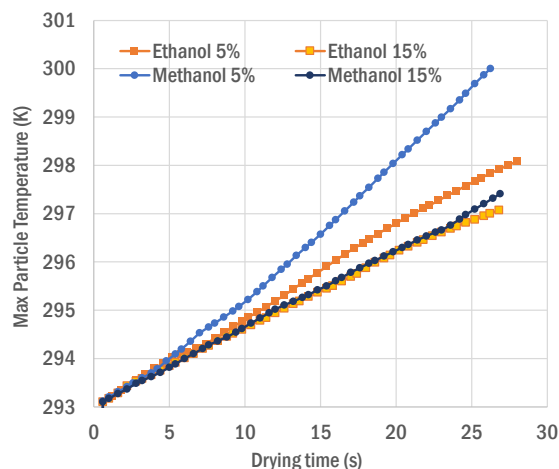


Figure 3.12: Effect of solvent properties – specific heat capacity and boiling point – on the maximum particle temperature observed in the filter cake. Two levels of solvent volume are investigated (at 5 and 15 %wt./wt. liquid) using values of pure Methanol and pure Ethanol solvents.

3.4 Effect of Operating Parameters on the particle-scale dynamics

3.4.1 Effect of agitator design

Agitated filter dryer vessels usually come with a number of designs of the impeller that can be used in the equipment. The shape and design of such impellers directly affects the mixing dynamics. In order to assess the granular flow using the S-shaped Procept AFD impeller, comparisons were carried between the AFD impeller and other standard impeller types as shown in Figure 3.13A.

Figure 3.13B and 3.13C illustrate the magnitude of average particle velocity as well as the axial-directional velocity of using the three impeller designs. The impeller design drastically affects the velocity profile of the agitated system. In general, the average particle velocity is highest for the ProCept blade; however, the degree of mixing with respect to the velocity in axial-direction is the lowest. This result indicates that particle mixing in axial direction is likely insufficient for the ProCept design if the impeller is kept at a fixed height over the course of the drying. Thus, impeller movement up and down is likely necessary to ensure good mixing.

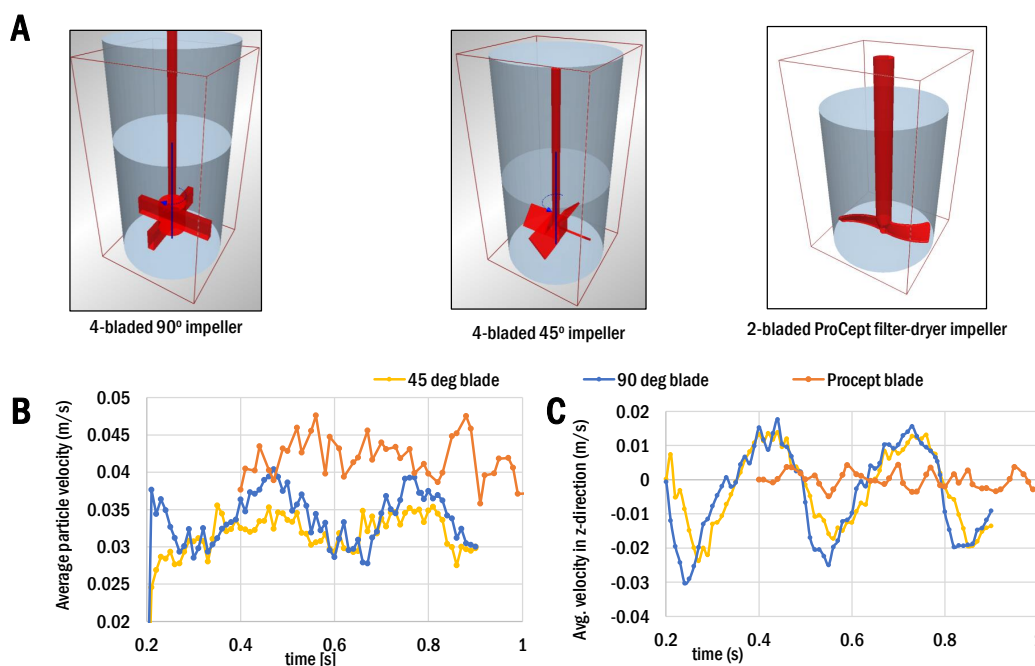


Figure 3.13: **A.** Three different impeller designed were simulated in DEM with a constant rotation rate of 50 RPM. The effect of impeller design on **B.** Average particle velocity magnitude, **C.** Average axial particle velocities.

3.4.2 Effect of impeller movement

During the cake compression phase of AFD operation as well as to enhance the drying of the cake, the impeller in filter dryers are often lowered or removed from the cake. In addition, most filter dryers have an option to rotate the impeller in both Clockwise (CW) and anti-clockwise (ACW) directions. In order to investigate the impact of this impeller movement and its potential effect on the particle-scale dynamics, independent DEM simulations were performed. Figure 3.14 and 3.15 illustrate the effect of impeller motion when it is lowered into the cake and removed from the cake respectively.

The DEM results show that when the impeller is lowered into the cake in ACW direction, the impeller motion produces significantly faster growth in the average particle velocities to reach quasi steady state values. In addition, the ACW rotation down also greatly aids in the compaction of the filter cake necessary for cake smoothing as seen from the average compression forces experienced by the particles as well as the bed voidage profile.

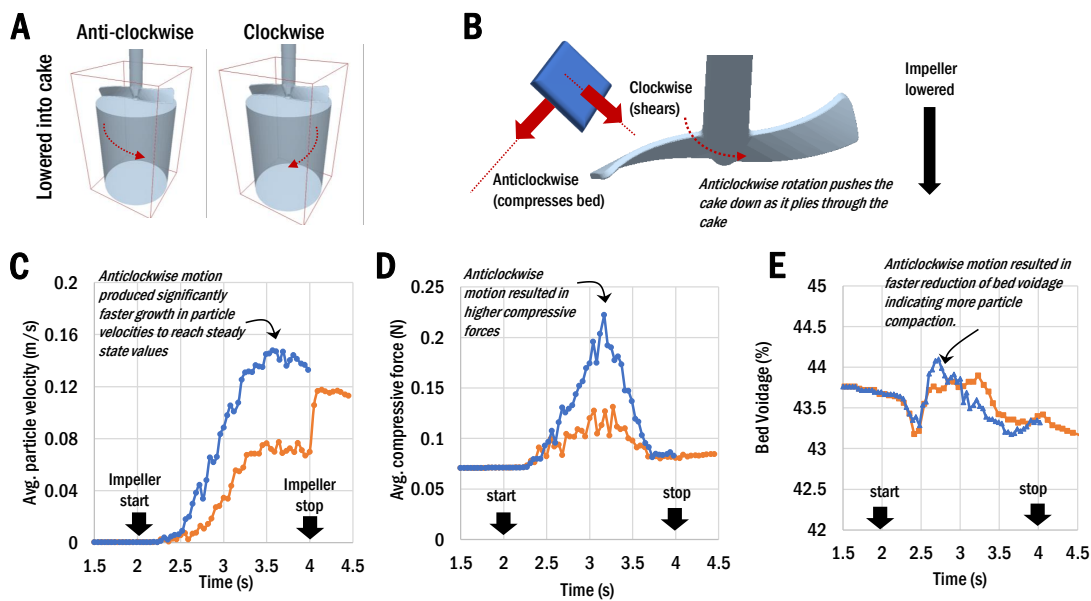


Figure 3.14: **A.** The rotational directions of the impeller as it is lowered into the cake (in 2s time interval) **B.** Schematic of the impeller as it plies through the powder bed. The effect of CW and ACW rotation of the impeller as it is lowered on **C.** average particle velocities **D.** average compressive forces and **E.** bed voidage

When removing the impeller from the filter cake, the DEM results show that operating the impeller in CW direction greatly aids in circulating the particles in the bed. Since the CW rotation not only increases the average particle velocities but also increases the bed voidage as it is removed, better turnover of particles within the cake is more likely. This results in better distribution of heat transfer within the bed.

3.4.3 Effect of agitation rate

Impeller speed directly relates to particle velocity and hence collision velocity profile of the system which is an important factor to consider for agglomeration tendency. Collision velocity affects whether particles stick together after collision or bounce back (i.e. rate of aggregation). Different impeller speeds were investigated for their effect on the average particle velocities.

The DEM findings of the study are illustrated in Figure 3.16. In general, higher rotation rate relates directly with higher particle velocities and thus, average particle velocity can be observed to scale linearly with Froude number.

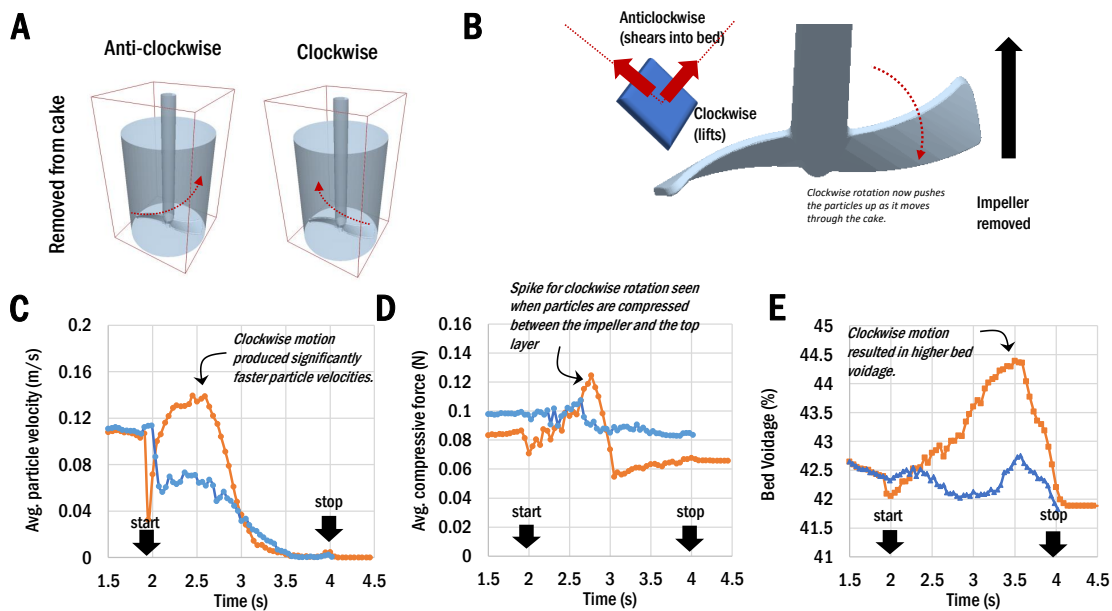


Figure 3.15: **A.** The rotational directions of the impeller as it is removed from the cake. **B.** Schematic of the impeller as it plies through the powder bed. The effect of CW and ACW rotation of the impeller as it is removed on **C.** average particle velocities **D.** average compressive forces and **E.** bed voidage

3.4.4 Effect of fill level

Fill level or vessel loading directly relates to particle velocity and compressive forces experienced by the particle bed. In order to investigate its effect on granular flow, two different levels were tested at the same impeller speed.

DEM results (Figure 3.17) show that fill level does not significantly affect average particle velocities. However, higher fill level demonstrates higher compressive force regardless of Froude number.

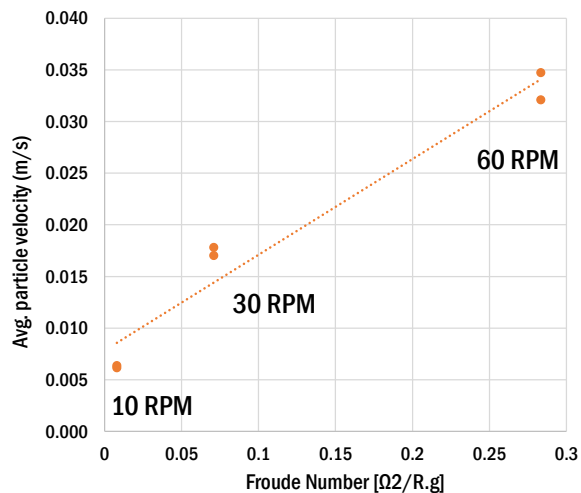


Figure 3.16: Effect of impeller speed on the average particle velocities. Three impeller rotation rates at 10 RPM, 30 RPM and 60 RPM were investigated in DEM.

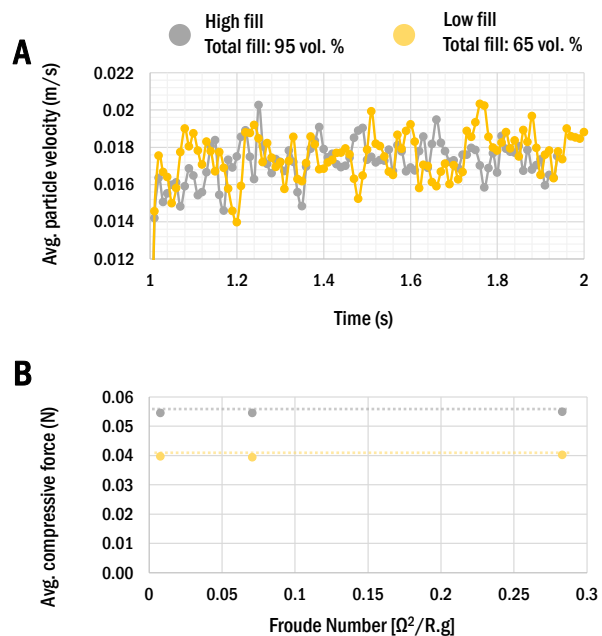


Figure 3.17: Two different particle fill levels at 65 vol% and 95 vol% were investigated in DEM. The effect of powder loading on **A.** Average particle velocities, **B.** Average compression forces are provided.

3.5 Effect of Scale-up using different scaling constants on particle-scale dynamics

The effect of scaling criteria on the internal particle flow, collisions, shear, forces and energies experienced by particles in an agitated drying vessel using the normalized parameter approach was investigated in this study. The results of the DEM simulation are presented in Figures 3.18, 3.19 and 3.20 below.

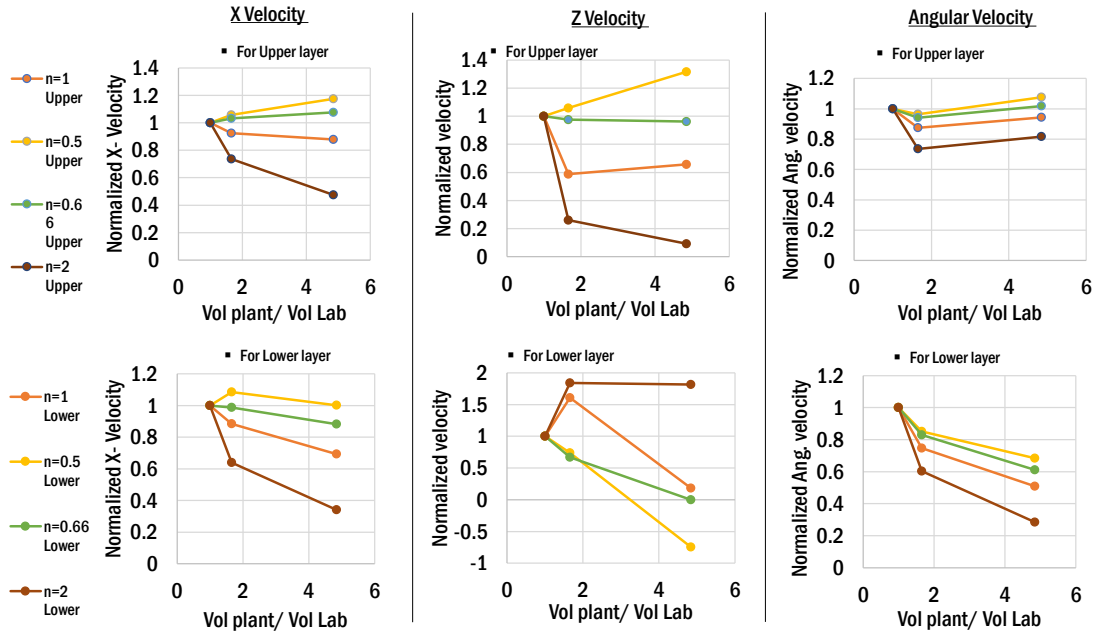


Figure 3.18: Effect of scale-up on the internal particle flow dynamics: X-, Z- and Angular velocity

The normalized plots in Figure 3.18, 3.19 and 3.20 were further reduced to a succinct color chart by fitting a linear regression for each scale. The absolute value of the slope of these fitted lines were then used as metrics to determine if the scaling criteria employed produced scale-independent dynamics. Since impeller torque and average compressive forces were clearly not scale-independent from Figures 3.18 and 3.19, they are omitted in the color map.

The particle-level dynamics color map representing the effect of scale up on the particle-scale dynamics is presented in Figure 3.21 below. In the figure, the color of each square indicates the scale independence of the particular key variable when using

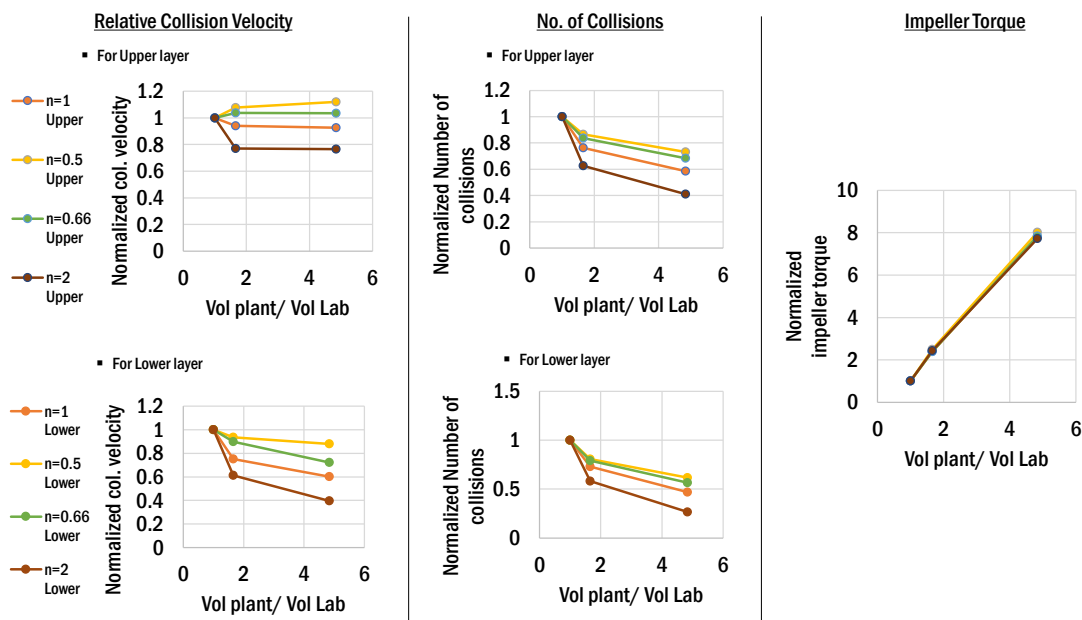


Figure 3.19: Effect of scale-up on the collision and shear dynamics: relative collision velocity, no. of collisions and impeller torque

the chosen scaling index. As the color goes towards blue, the scaling index selected maintains the dynamics of the variable over the three vessel sizes examined. Conversely, if the color is more red, the scaling index fails at keeping the critical variable dynamics constant over the different scales.

The main conclusion from this study shows that constant Power/Volume ratio ($n=0.66$) gives the closest process similarity at different scales using the normalized parameter metric approach. However, using constant Froude number ($n=0.5$) shows better scaling of collisions dynamics, and using the constant impeller tip speed criteria ($n=0.1$) shows better scaling of particle temperature increase. Maintaining a constant Reynolds number ($n=2$) over the different scales, on the other hand, shows the lowest scale independence.

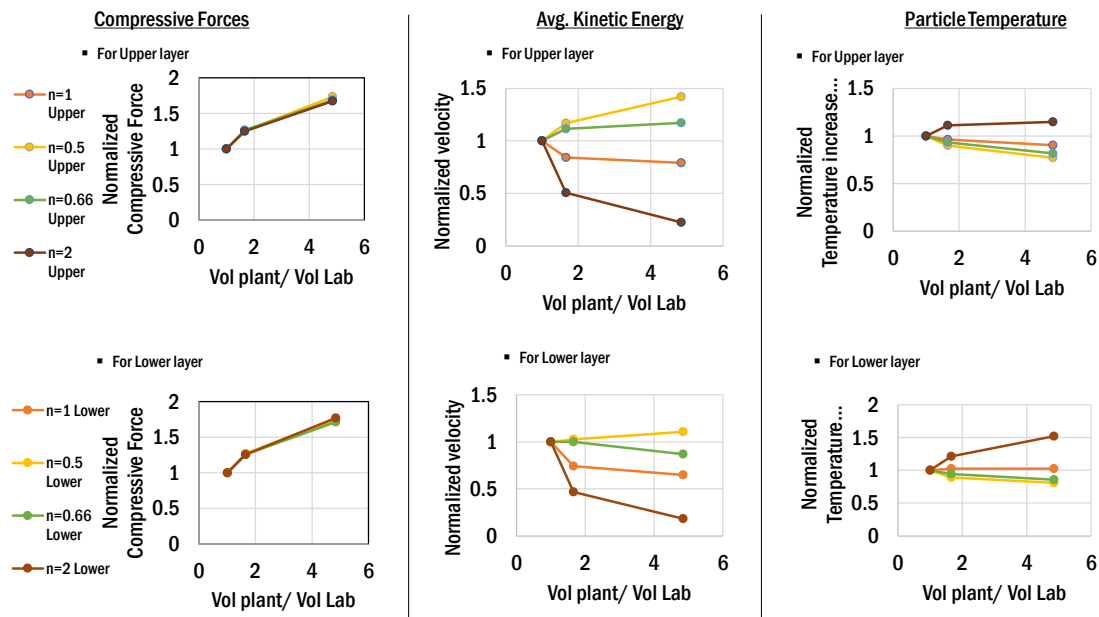


Figure 3.20: Effect of scale-up on the forces and energies dynamics: compressive forces, avg. kinetic energy and particle temperature

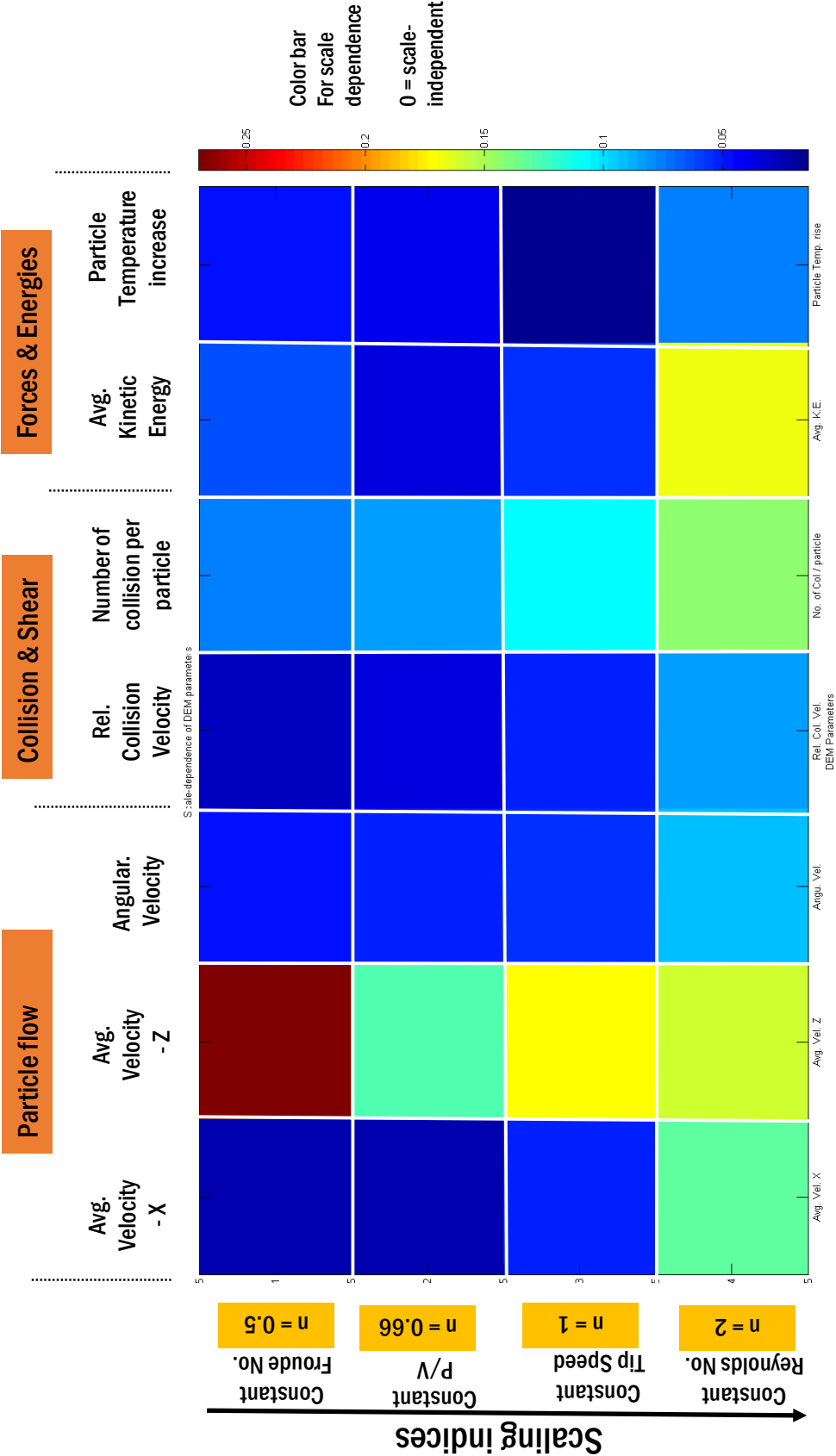


Figure 3.21: Scaling map for normalized granular flow parameters based on different scaling indices

Chapter 4

Using DEM to quantitatively compare the effect of wet and dry binder addition in high-shear wet granulation processes

Wet granulation is widely used in many particulate industries for its capability to improve flowability and handling of powder substances. A mathematical model using Discrete Element Methodology (DEM) was developed to study two kinds of binder addition approaches commonly used during wet granulation in a batch high-shear granulator: wet binder addition (WBA) and dry binder addition (DBA). To define the complex interactions in the systems, a novel integrated DEM algorithm that incorporates powder wetting behavior, capillary and viscous liquid bridge formation as well as binder dissolution was developed. DEM simulation results show a significant difference between the viscous regions in the particle bed for the two systems: the WBA approach quickly wets the majority of the particle bed with a low viscosity fluid, while in the DBA approach fewer particles with higher viscous surface liquid are generated that are responsible for a delayed but faster granule growth rate. The difference in the viscosity of the surface liquid in the two systems lead to varying strengths and numbers of the liquid bridge formed between particles as well as particle velocities. In general, the high viscous areas are dependent on the binder and liquid dispersion which are affected by the mechanical agitation.

4.1 Background

4.1.1 Wet granulation process

Due to the difficulty of handling fine/poor-flowing powder, wet granulation processes where a liquid solution is sprayed onto a particle bed are widely used in the pharmaceutical/particulate industries to initiate size enlargement of fine particles. Traditionally, batch wet granulation operation is carried out in a high shear mixer which consists of a metallic bowl with impellers at the bottom that can rotate at very high rpm, a spray nozzle at the top to introduce the solution and, in some cases, choppers on sides of the vessel to break down large agglomerates. This type of granulator is popular in pharmaceutical industry since it has advantages in short processing time, less binder required compared to fluidized bed granulation, and the ability to handle highly cohesive material. In presence of liquid and mechanical agitation, micronized powders coalesce together to form larger granules that not only flow better but have superior compressibility and dissolution characteristics Parikh (2010).

Because of its widespread use, the last few decades have seen enormous research invested into understanding this complex granulation behavior specially to predict and control the granule growth rate. Although this task is still challenging, it has been approached in many ways: starting primarily from investigating the effect of material properties and process parameters on final product to now more focused research on understanding fundamentals of granulation from a mechanistic perspective Iveson et al. (2001); Agrawal and Naveen (2011); Leuenberger et al. (1981); Rowe and Sadeghnejad (1987); Sastry and Fuerstenau (1973); Green and Perry (1999). In general, the granulation process occurs in three stages: (a) Wetting and Nucleation, (b) Consolidation and Growth, and (c) Attrition and Breakage Green and Perry (1999). During the first stage, the wetting thermodynamics and kinetics of nucleation govern the initial wetting of the fine powder which creates soft nuclei. Hapgood et al. Hapgood et al. (2002) investigated the wetting properties of powder through droplet penetration experiment and, by relating the ability of powder bed to absorb different kinds of droplets, they developed a method to quantify the wettability of the powder. Rowe et al. York and Rowe (1994)

defined the spreading coefficient by the surface free energy of the material and related it to the kinetics of nucleation. These works were combined into a nucleation regime map by Lister and Hapgood Hapgood et al. (2003) which postulated that the interaction between drop penetrating time and the dimensionless spray flux would determine the nucleation behavior. After the nuclei are formed, granules undergo consolidation and growth. During consolidation, the compaction of granules due to mechanical agitation and collision with other particles/wall result in internal liquid or air being squeezed out from the granular pores resulting change in porosity and liquid content on the surface. The effect of consolidation on granule yield strength was studied by Rumpf and Knepper Rumpf and Knepper (1962); Ennis et al. Ennis et al. (1990) implemented the viscous Stokes number to account for the effect of binder viscosity. Once sufficient liquid film forms on the surface of granules, these particles coalesce due to the formation of liquid bridges between them. Depending on the volume and viscosity of the liquid available for formation, these bridges are held together by capillary pressure and viscous forces Hotta et al. (1974); Lian et al. (1993); Adams and Edmondson (1987); Mazzone et al. (1987); Ennis et al. (1990). During the breakage and attrition stage, the agglomerates subject to shear forces from the mechanical agitation break down into smaller fragments. Depending on the magnitude of shear and the liquid content of the granules, they may even undergo attrition to form fines. Numerous investigations into breakage behavior are also available in literature Reynolds et al. (2005); Ramaker et al. (1998); Tardos et al. (1997).

4.1.2 Modes of binder addition

One of the most essential formulation elements in wet granulation products are binders which add cohesiveness to powders thereby providing the necessary bonding to form granules. Although wet granulation operations can be carried out by using pure solvents such as water as a binder fluid, in majority of the cases, polymeric binders are added to enhance the granulation process Dürig (2016). Several articles are already available in literature regarding the role of binders in wet granulation Rajniak et al. (2007); Parker et al. (1990); Tardos et al. (1997); Hancock et al. (1994). Typically, these binders are

added to the system in one of two ways Dürig (2016); Chaturbedi et al. (2017):

- **Wet Binder Addition (WBA)** - where the binder is pre-dissolved in a suitable granulating fluid to form a "fully activated" binder solution which is then sprayed onto the particles, or
- **Dry Binder Addition (DBA)** - where solid binder particles are blended in with the drug and excipient mass and a solvent (usually water) is sprayed onto the particle bed to dissolve these binders

Traditionally, the wet granulation in a high shear mixer is performed through a WBA approach while DBA is the mode of choice for dry granulation processes such as roller compaction or hot melt granulation Larsson et al. (2008); Cavinato et al. (2010a); Kayrak-Talay and Litster (2011). Recently, however, investigations into the effect of binder addition method have become popular with granulation researchers primarily due the differences observed experimentally on the final size of the granules. D'alonzo et al. D'alonzo et al. (1990) examined the effect of method of binder addition in a high intensity mixer and concluded that the growth of granules prepared by WBA approach are generally smaller than granules prepared with corresponding concentrations of dry binder. Similar results were also observed by Osborne et al. Osborne et al. (2011) and Chaturbedi et al. Chaturbedi et al. (2017) in high shear granulator experimentation.

4.1.3 Objectives

Although the DBA approach of binder addition is getting popular in the industry due to its simplicity (and avoidance of viscous solution delivery which tends to clog the liquid delivery pipeline) from a manufacturing point of view, there haven't been many mathematical models and simulations developed to study the differences between the WBA and DBA systems. A preliminary model development work to compare WBA and DBA system was conducted in author's previous paper - Chaturbedi et al. Chaturbedi et al. (2017) - using compartmental population balance models with integrated binder dissolution mechanism (see Section 5.3). The study indicated the possibility of in-homogeneously distributed high-viscous and low-viscous regions within

the DBA system which significantly influence the rate of granule growth compared to a WBA system. In order to investigate this phenomenon, a more mechanistic simulation is required which can provide insight into the formation of these viscous regions (via liquid bridges between particles) and its effect on the process dynamics. In this study, discrete element methodology (DEM) which simulates and tracks individual particles throughout the process are employed to gain particle-scale information. In general, DEM models have been used extensively in literature to simulate (wet and dry) granular flow behavior since the algorithm can provide detailed profiles on forces, velocities and collisions experienced by particles Lian et al. (1998); Remy et al. (2010); Gantt et al. (2006); Barrasso et al. (2014); Sen et al. (2014); Kuo et al. (2004); McCarthy et al. (2000). However, these DEM models have not incorporated the liquid addition stage which is the key difference between WBA and DBA systems. A novel DEM simulation which brings together liquid addition, liquid bridge formation, and binder dissolution mechanism to augment the simulation of wet granulation process is presented in this study. The primary objectives of this work are listed below:

- Develop an integrated contact model for the DEM which incorporates capillary and viscous liquid bridge formation as well as binder dissolution and liquid penetration mechanisms.
- Implement the custom-built contact model in the DEM algorithm to simulate WBA and DBA wet granulation processes in a high shear granulator
- Identify the high viscous regions in both systems and compare its effect on process dynamics including particle velocities, particle collision frequencies as well as number of liquid bridges between particles.

4.2 Mathematical Model Development

Due to the wide variety of complex mechanisms inherent in granulation processes as mentioned earlier, developing a model to predict granule growth is still an open area of research. However, researchers are making progress, especially from two fronts: population balance model (PBM) and discrete element method (DEM). While PBMs are mesoscopic models that attempt to capture the bulk dynamics of granulation processes through granule growth and breakage rates, DEM methodology simulates individual particles in a system and solves Newton's equation of motion for each particle to account for their motion during the process. Particles are considered individual elements with sets of properties that influence its flow behavior (size, density, coefficient of restitution, etc.), and collision between particles or equipment and the resulting particle trajectories are determined for each time step. The key assumption in DEM is that the simulation time step can be chosen so small that the interaction force is applied only to immediately adjacent particles. Thus, DEM offers a more fundamental look into powder mixing and wetting behavior. The general DEM algorithm to track the particles within its system are illustrated in Figure 4.1. Details regarding each stage of the DEM algorithm and the unique features incorporated in this study to recreate WBA and DBA granulation are provided in the following sections.

4.2.1 DEM Configuration

The first steps in the development of a DEM algorithm are the geometry creation and particle initialization stages where the system vessel and particles to be simulated are generated. In this work, the experimental setup used in Chaturbedi et al. Chaturbedi et al. (2017) was used as the foundation to create the vessel design, process dynamics and approximate particle properties. Details of the experimentation and conclusions are summarized in Section 5.3. In this DEM model, the geometry of the particular high-shear granulator used in the experiment is re-created and the powder properties of microcrystalline cellulose (MCC) and hydroxypropyl cellulose binder (HPC) powders are simulated as "Primary particles" and "Binder particles" respectively.

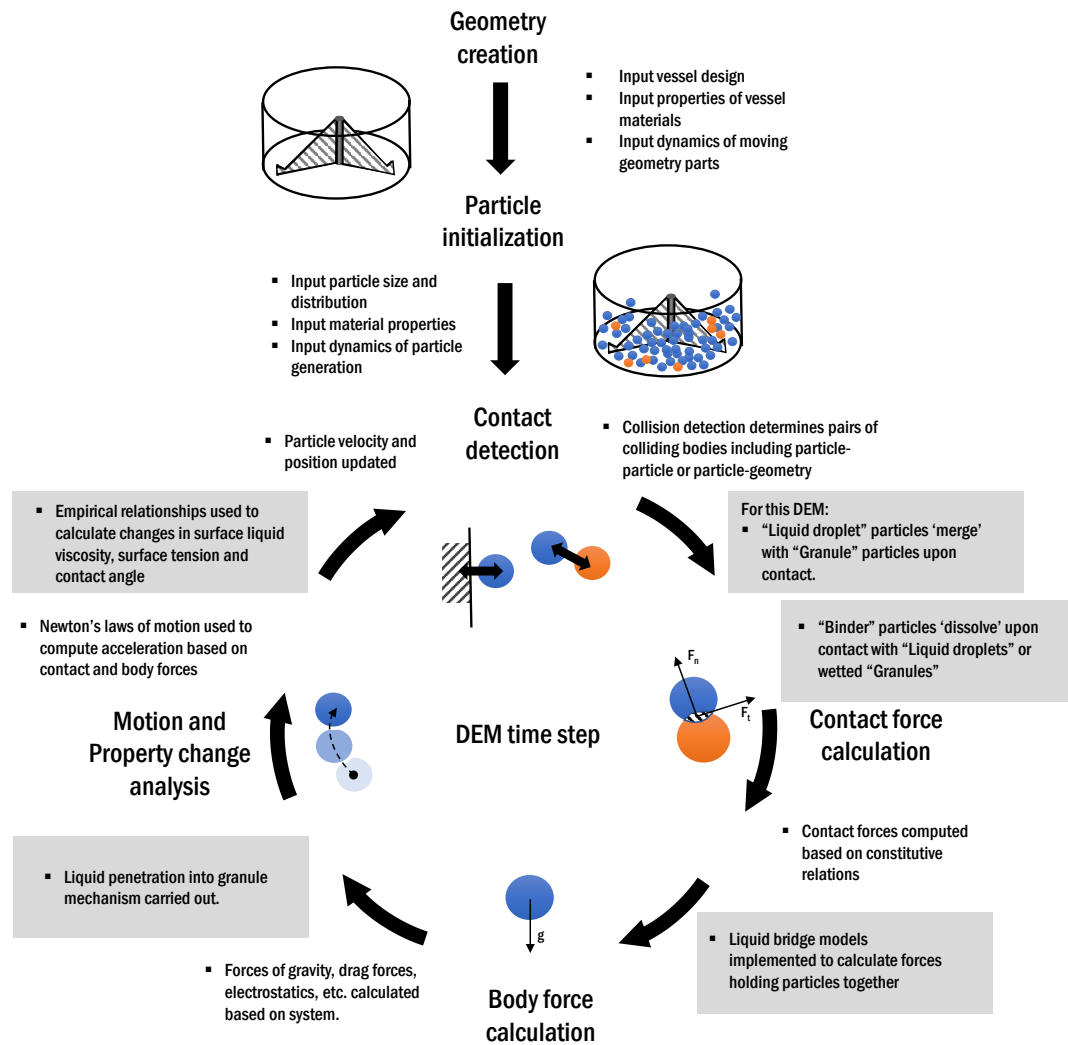


Figure 4.1: Discrete Element Method (DEM) algorithm used in the study. The implementation of liquid addition, binder dissolution and liquid bridge forces unique to this work are highlighted.

4.2.1.1 DEM system design

Due to the computationally taxing nature of DEM simulations, a number of virtual scaling operations - particle size enlargement, vessel scale-down, process condition and spray rate scaling - were performed to ensure that the simulations were carried out within a reasonable amount of time. A particle scaling (i.e. enlargement of the size of the simulated particles compared to original size distribution of powder particles) was first performed to ensure that a computationally viable number of particles were generated in the system. The primary and binder particles were enlarged to a radius of 2 mm such that the total batch size of 1.6 kg powder fit realistically within the 10-L granulator. This particle scaling, however, proved to be insufficient to curtail the computational load and hence a secondary scale down of the vessel was required to reduce the DEM simulation time. The 10-L high shear mixer geometry was then scaled down to a 1-L system under geometric similarity conditions. The fill level in both systems were kept constant. In addition, in order to maintain the dynamics (similar force and flow profile) of the system in line with the 10-L vessel, the process parameters were similarly scaled down for the 1-L system using dimensionless numbers. Although several dimensionless numbers - including Powder number, Reynolds number, constant tip speed, relative swept volume, etc. - have been recommended in literature to perform such scaling of high shear granulation Cliff and Parker (1990); Ramaker et al. (1998); Landin et al. (1996); Yadav et al. (2010), Froude number (expressed mathematically in Equation 4.1) gave the most similar flow pattern, in terms of average particle velocities and collision frequencies, between the 10-L and the 1-L vessel for the DEM simulations performed in this study. Thus, for the WBA and DBA systems simulated in this work, the scaled-down operating condition for impeller speed was computed by keeping the Froude number constant using Equation 4.2.

$$Fr = \frac{DN^2}{g} \quad (4.1)$$

where D is the impeller diameter, N is the impeller speed and g is the gravitational acceleration.

$$\frac{N_2}{N_1} = \sqrt{\frac{D_1}{D_2}} \quad (4.2)$$

where N_1 and N_2 are the impeller speed of the system before and after scaling down respectively; D_1 and D_2 are the lengths of the original and scaled down impeller blade respectively.

Besides the force and the flow profile, spraying is another key factor that should be considered in scaling wet granulation processes. A change in spraying dynamics results in differences in binder dispersion which can lead to further alterations in granulation mechanisms Litster et al. (2002). In order to maintain similar liquid addition pattern, the volumetric spray rate (\dot{V}) for the 1-L system was calculated through the conservation of the dimensionless spray flux number (ψ_a) (Equation 4.3) developed by Lister et al. Litster et al. (2001) between scales. The area flux of the powder traversing the spray zone (\dot{A}) was estimated using the impeller speed and the nozzle diameter (d_n). In the scaled-down system, the diameter of the droplet (d_{drop}) and the total liquid to solid mass ratio (L/S) was also kept constant between scales.

$$\psi_a = \frac{3\dot{V}}{2\dot{A}d_{drop}} \quad (4.3)$$

Table 4.1 below lists the variables changed in the scale-down operation for the DEM simulations carried out in this study. The operating conditions from the original 10-L granulator experiment are listed in the 'original' column. The geometry of the 1-liter high shear granulator is shown in Figure 4.2.

4.2.1.2 Particle types and interaction

In order to simulate the wetting and dissolution behavior in a discrete element environment of DEM, three different types of particles namely - *Granule* particles, *Binder* particles and *Liquid droplets* were generated to recreate the MCC powder, HPC binder and water droplets respectively. The material and flow properties of these particle types - based on the literature data available for the materials - are listed in Table 4.2. The

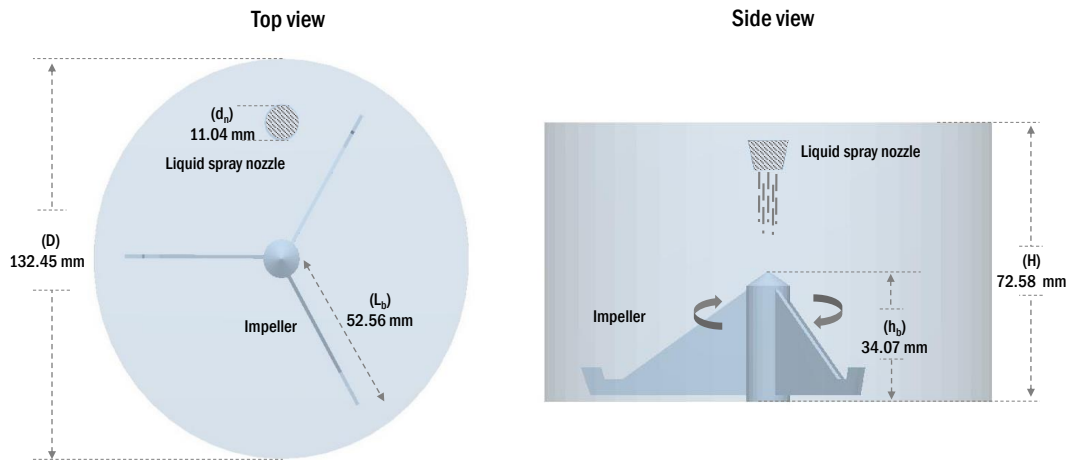


Figure 4.2: DEM geometry of the 1-liter high shear granulator.

Table 4.1: Operation variables changes before and after scale-down.

Parameter	Units	Original (10L)	Scaled down (1L)
Design parameters			
Granulator volume (V)	L	9.16	1
Vessel height (H)	mm	151.88	72.58
Vessel diameter (D)	mm	277.18	132.45
Impeller length (L_b)	mm	110.00	52.56
Impeller height (h_b)	mm	71.30	34.07
Nozzle Spray diameter (d_n)	mm	16.00	11.04
H/D ratio	-	0.55	0.55
2L/D ratio	-	0.79	0.79
Initial parameters			
Fill level (F)	mm	52.83	25.25
Fill fraction (F/H)	-	0.348	0.348
Ratio of Primary: Binder particle mass	-	96:4	96:4
Total batch size	kg	1.664	0.281
Liquid to solid mass ratio (L/S)	-	0.721	0.721
Total number of Primary particles	-	30,623	5,180
Total number of Binder particles	-	1,642	278
Total number of droplet particles	-	286,479	48,455
Operating parameters			
Froude number (Fr)	-	0.58	0.58
Impeller speed	<i>RPM</i>	306	443
Spray flux (ψ_a)	-	1.22	1.22
Liquid addition rate	g/min	400	276.77
Liquid addition time	s	180	44
Area flux through spray zone (\dot{A})	m^2/s	4.10×10^{-3}	2.82×10^{-3}

Note: The original operational variables are based on experiments detailed in Section 5.3

granule and binder particles are generated randomly within the granulator at the start to avoid segregation while the liquid droplets are generated based on the liquid addition rate calculated through scale-down criteria.

Table 4.2: Input variables for the DEM simulation.

Granule Particle[‡]		Binder Particle[*]	
Particle radius	2 mm	Particle radius	2 mm
True Density	1557 kg/m ³	True Density	1210 kg/m ³
Porosity	0.1	Washburn Constant	3.65 × 10 ⁻¹⁷
Washburn Constant	3.65 × 10 ⁻¹⁷	Poisson's ratio	0.33
Maximum liquid retention	0.45 wt/wt	Shear Modulus	1 × 10 ⁶ Pa
Poisson's ratio	0.3	System Properties	
Shear Modulus	1 × 10 ⁶ Pa	Time step	2.71 × 10 ⁻⁶ s
Coef. of Restitution	0.575	Total time	44 s
Coef. of Static Friction	0.176	Mesh size	4 mm
Coef. of Rolling Friction	0.01	Droplet Particle (WBA)[×]	
Droplet Particle (WBA)[×]		Droplet Particle (DBA)[×]	
Particle radius	1 mm	Particle radius	1 mm
Density	1000 kg/m ³	Density	1000 kg/m ³
Washburn Constant	3.65 × 10 ⁻¹⁷	Washburn Constant	3.65 × 10 ⁻¹⁷
Poisson's ratio	0.25	Poisson's ratio	0.25
Shear Modulus	1 × 10 ⁸ Pa	Shear Modulus	1 × 10 ⁸ Pa
Binder concentration	0.055 wt/wt	Binder concentration	0 wt/wt
Contact angle	1.048 rad	Contact angle	1.048 rad
Surface tension	0.041	Surface tension	0.041
Solubility	0.12 wt/wt	Solubility	0.12 wt/wt

[‡]: Properties of granule particle based on Avicel PH102.

Data obtained from Rojas et al. (2011); Ganderton et al. (1995); Roberts et al. (1994) and Luukkonen et al. (2001)

^{*}: Binder particle properties based on HPC EXF binder obtained from Ashland (2012); Picker-Freyer and Dürig (2007)

[×]: Droplet properties based on HPC-water systems obtained from Chang and Gray (1978); Mezdoor et al. (2007); Pelofsky (1966)

Beside the differences in the material and flow properties, the three particle types also interact differently at contact to mimic solid and liquid characteristics. The liquid droplet particles, for instance, are programmed to disappear on contact with granule particles to simulate liquid absorption by powder; the granule particles then gain the corresponding liquid mass to become wetted granules. Similarly, when liquid droplets encounter binder particles, a size change in binder particles is initiated to account for binder dissolution - the liquid droplet then gains binder mass value proportional to the dissolved binder. A list of different combination of particle type interaction is explained in Table 4.3. Note that in the WBA system, only liquid droplet and granule particles are present while in DBA system all three particle types are generated.

Table 4.3: Customized combinations of interactions between different particle types in DEM

$Particle_i$	$Particle_j$	Interaction
Liquid droplet	Liquid droplet	No interaction
Liquid droplet	Binder	<ul style="list-style-type: none"> • If liquid droplet is unsaturated with binder: binder particle reduces size proportional to binder dissolution, liquid particle gains dissolved binder mass • If liquid droplet is saturated with binder: binder dissolution does not take place
Liquid droplet	Granule	<ul style="list-style-type: none"> • If granule is not at its maximum liquid retention point: liquid particle disappears, granule particle gains liquid mass to become wetted granule • If granule is at maximum liquid retention limit: no absorption
Granule	Binder	<ul style="list-style-type: none"> • If granule has liquid not saturated with binder: binder particle reduces size proportional to binder dissolution, liquid in granule particle gains dissolved binder mass • If granule does not have liquid or, liquid is saturated with binder: no dissolution
Granule	Granule	No interaction
Binder	Binder	No interaction

4.2.2 Contact force calculations

The DEM algorithm calculates the collision events in every time step - events when particle-particle or particle-geometry have sufficient overlap - based on the velocity and position profiles of the particles in the previous time step. The overlap threshold is satisfied for particle-particle collisions if the distance between the centers of the particles is smaller than the sum of their radii. For particle-geometry collisions, the distance between the particle center and the point of contact needs to be smaller than the radius of the particle for successful contact detection. Note, the particle type interactions listed in Table 4.3 only takes place once a contact is detected between specific particle types.

Once a collision event is detected, the DEM algorithm then implements a particle contact force model to calculate the forces and energies experienced by the colliding particles. In the broadest sense, two types of contact models are available in DEM: the soft sphere model and the hard sphere model Mikami et al. (1998). The hard particle approach assumes that the particles collide with each other instantaneously while the soft particle approach considers collisions as a continuous process that occurs over a period of time. In soft particle approach, the interactive forces are treated as

continuous functions of the distance between particles Lian et al. (1998). Normally for application in pharmaceutical process research where particles are very deformable in nature, soft particle approach is applicable. In general, there are several different types of soft particle contact models that are run after every collision detection - the common contact models available in commercial DEM software include Hertz-Mindlin model, the linear spring and dash-pot model etc. Comparisons between these models can be found in the review paper of Zhu et al. (2007).

In this study, the simplified Hertz-Mindlin no-slip model was used to determine how particles behave when they meet each other or solid boundaries. The general expression for this contact model, which is a variant of the non-linear spring-dashpot contact model, are provided in Equation 4.4, 4.5 and 4.6 Tsuji et al. (1993). This contact force formulation considers both forces in normal (\vec{F}_C^N) as well as tangential (\vec{F}_C^T) direction with respect to plane of contact between particles. The model uses equivalent radii (\tilde{r}) and mass (\tilde{m}) to calculate the forces; the formulation for equivalent radii and mass are shown below in Equation 4.7 and 4.8 Vercoeijen et al. (2002).

$$F_n = -kx_n - \eta \frac{dx_n}{dt} \quad (4.4)$$

$$F_t = \begin{cases} -kx_t - \eta \frac{dx_t}{dt} & \text{if } |F_t| \leq \mu |F_n| \\ -\mu |F_n| \frac{x_t}{|x_t|} & \text{if } |F_t| > \mu |F_n| \end{cases} \quad (4.5)$$

$$\eta = \frac{-2 \ln e_r}{\sqrt{\pi^2 + (\ln e_r)^2}} \quad (4.6)$$

where k is the spring stiffness, x_n and x_t the normal and tangential displacement, η is the damping coefficient, μ is the coefficient of static friction and e_r the coefficient of restitution.

$$\tilde{r} = \frac{1}{\left(\frac{1}{r_i} + \frac{1}{r_j}\right)} \quad (4.7)$$

$$\tilde{m} = \frac{1}{\frac{1}{m_i} + \frac{1}{m_j}} \quad (4.8)$$

Where, r_i, r_j are the radii of the colliding particles and m_i, m_j are the masses of the colliding particles.

4.2.3 Cohesion force calculations

In order to account for the wet granular flow in DEM, liquid bridge models - capillary liquid bridge model and viscous liquid bridge model - were used to determine the inter-particle cohesive forces between particles in contact. These models use the fluid volume on granules as well as fluid properties such as viscosity, surface tension and contact angle to calculate the cohesion forces. In addition, a critical separation distance based on fluid properties is also computed for each contact to determine a bridge rupture distance - if particles in contact move beyond the rupture distance, the liquid bridge is broken. Thus, the cohesion model used in this work simulate dynamic bonding between wetted granules which takes viscous forces into account.

The application of capillary or viscous bridge model can be determined through calculation of the dimensionless group capillary number (Ca) (Equation 4.9) for the contact between each wetted particle Ennis et al. (1990).

$$Ca = \frac{\mu U}{\gamma} \quad (4.9)$$

where μ is the average viscosity of fluid, U is the relative particle velocity and γ is the fluid surface tension present in the liquid bridge.

The Ca value of the liquid bridge generated describes the dominance of viscous forces F_{vis} relative to capillary forces F_{cap} (i.e. surface tension) across the bridge. Generally, for low capillary numbers ($Ca < 0.001$), the magnitude of the liquid bridge force is dominated by capillary forces, whereas for high capillary numbers, the capillary forces are negligible compared to the viscous forces. In the WBA and DBA simulation for this work, where the viscosity of the fluid is changing over time due to binder dissolution

mechanism, two cases of liquid bridge formation were implemented: $Ca < 0.001$ and $Ca > 0.001$. For $Ca < 0.001$, which happens during early stage of the process when minimal low viscous liquid is present in the system, the capillary force model is used as the only liquid bridge force ($F = F_{cap}$). On the other hand, when Ca becomes larger than 0.001, both capillary and viscous force model are implemented ($F = F_{cap} + F_{vis}$).

Capillary force: The capillary force between particle-particle (F_{cap}^{p-p}) and particle-wall (F_{cap}^{p-w}) contact can be computed using Equation 4.10 and 4.11 respectively Lian et al. (1993, 1998); Lambert et al. (2008); Rabinovich et al. (2005); Liu et al. (2011); Washino et al. (2016).

$$F_{cap}^{p-p} = \frac{4\pi\tilde{r}\gamma\cos\theta}{1 + \frac{1}{\sqrt{\frac{1}{1 + \frac{1}{\pi\tilde{r}S^2}} - 1}}} \quad (4.10)$$

$$F_{cap}^{p-w} = \frac{4\pi r\gamma\cos\theta}{1 + \frac{S}{\sqrt{\frac{\pi r_i}{V_{liq}}}}} \quad (4.11)$$

where \tilde{r} is the equivalent radii of the particles involved in the contact (see Equation 4.7), γ and θ are the surface tension and contact angle of the bridge fluid, V_{liq} is the volume of the liquid involved in the formation of bridge and S is the distance between two objects (particle or wall).

The V_{liq} value is calculated using the volume of liquid contributed by each wetted particle ($particle_i$ and $particle_j$) using Equation 4.12, 4.13 and 4.14 Shi and McCarthy (2008).

$$V_i = \frac{L_i}{2} \times \left(1 - \sqrt{1 - \frac{r_j^2}{r_i + r_j^2}} \right) \quad (4.12)$$

$$V_j = \frac{L_j}{2} \times \left(1 - \sqrt{1 - \frac{r_i^2}{r_i + r_j^2}} \right) \quad (4.13)$$

$$V_{liq} = V_i + V_j \quad (4.14)$$

where V_i and V_j are the liquid volume contribution of *particle_i* and *particle_j* for formation of liquid bridge respectively, L_i and L_j are the total liquid volume on the two particles and r_i and r_j are the respective particle radius.

In order to avoid the capillary forces going into infinity when two objects are attached to each other (i.e. $S = 0$), an important part of this bridge model is the forced damping of capillary forces by setting a minimum separation distance S_{min} Anand et al. (2009). S_{min} is usually determined based on the roughness of the particle; in this study an arbitrary S_{min} of 1 μm is used to limit the capillary forces.

In addition, a bridge rupture mechanism is also implemented when the separation distance S between particles is larger than a critical separation distance (S_c) which is dependent on liquid bridge properties. The estimation of S_c proposed by Lian et al. Lian et al. (1993) is used for both particle-particle and particle-wall bridge rupture (Equation 4.15).

$$S_c = \left(1 + \frac{1}{2}\theta\right) V_{liq}^{\frac{1}{3}} \quad (4.15)$$

Viscous force: The viscous forces (\vec{F}_{vis}) of the liquid bridge consist of normal and tangential components calculated using Equation 4.17 and 4.18 respectively Lian et al. (1998); Goldman et al. (1967). The normal viscous force is derived from the Reynolds lubrication theory Lian et al. (1998):

$$\vec{F}_{vis} = \vec{F}_{vis}^n + \vec{F}_{vis}^t \quad (4.16)$$

$$\vec{F}_{vis}^n = \frac{6\pi\mu\tilde{r}v_r^n\tilde{r}}{S} \quad (4.17)$$

$$\vec{F}_{vis}^t = \left(\frac{8}{15} \ln \frac{\tilde{r}}{S} + 0.9588\right) 6\pi\mu\tilde{r}v_r^t \quad (4.18)$$

where μ is the fluid viscosity, \tilde{r} is the equivalent radii of the particles involved in the contact (see Equation 4.7), v_r^n and v_r^t are the relative velocities between two particles in

normal and tangential direction and S is the separation distance. In the case of particle to geometry interactions, \tilde{r} is replaced by r radius of the particle.

4.2.4 Body force calculations

Besides the contact forces (\vec{F}_C^N and \vec{F}_C^T) which are only calculated upon contact detection, the DEM algorithm also take into account other body forces (\vec{F}_B) such as gravity, drag forces, electrostatics, etc. which can act on particles at every time step. In this study, the DEM body force algorithm, which can be set to act on particles when a specified condition is met, was also used to setup the binder dissolution and the solution penetration mechanisms.

Liquid penetration: In order to account for the distinction of internal liquid (in pores) and external liquid (on surface) in the granules, a binder solution penetration mechanism is also integrated in the body force algorithm. In general, this algorithm ensures that when a liquid droplet meets a granule particle, the droplet will continuously penetrate the pores of the particle until pore volumes are fully saturated. This leads to the change in the available amount of granule surface liquid which critically affects both dissolution and liquid bridge formation mechanisms. To determine the mass of liquid penetrating from the external liquid into the pores of the granules, concepts and mathematical correlations developed by Hapgood et al. Hapgood et al. (2002) and Siebold et al. Siebold et al. (1997) - which are derived from Washburn equation - were used (see Equation 4.19). In this mechanism, an assumption is made that liquid on the surface of a spherical granule particle will penetrate the pores in the same fashion as liquid droplets penetrate a powder bed.

$$m_{liq}^2 = w_c \left(\frac{\rho^2 \gamma \cos \theta}{2\mu} \right) t \quad (4.19)$$

where m_{liq} is the mass of liquid penetrating into the pores and w_c is the Washburn constant (i.e. geometric factor which is constant if the packing of the bed and particle size remains same). ρ , γ , θ and μ are the fluid density, surface tension, contact angle and viscosity respectively. t is the time period of observation (i.e. DEM time step).

Binder dissolution: When a successful dissolution event occurs between a liquid droplet or a granule with unsaturated surface liquid and a binder particle, a binder dissolution mechanism is triggered in this DEM model (see Table 4.3). In this mechanism, the amount of binder mass that can get dissolved into the available liquid volume without exceeding the max saturation limit of the droplet (12 % wt/wt) is then transferred from the binder particle to the liquid droplet. This dissolution rate is derived from the Noyes-Whitney correlation Noyes and Whitney (1897); Hattori et al. (2013) and is directly proportional to the concentration difference between maximum solubility and the bulk concentration of binder in liquid (Equation 4.20):

$$\frac{dm_d}{dt} = \frac{D\rho_l A}{L}(C_s - C_b) \quad (4.20)$$

where m_d is the mass of dissolved binder, D is the diffusion coefficient of HPC binder ($8.66 \times 10^{-9} \text{ m}^2/\text{s}$), A is the surface area for dissolution, ρ_l is the density of liquid, L is the diffusion layer thickness, C_s is the maximum solubility and C_b is the bulk binder concentration in the liquid volume. For the purposes of this study, the entire binder particle surface area is assumed to be in contact with the liquid volume during dissolution - i.e. the binder particle is entirely engulfed by a thin layer of liquid spread from the droplet. The dissolution surface area A is then calculated from the binder particle size and the L value is assumed to be a fraction (20%) of the thickness of liquid shell layer (L^*) given by Equation 4.21. Once the dissolution occurs, the binder particle loses mass proportional to the dissolved quantity and a corresponding binder particle size reduction takes place (Equation 4.22).

$$L^* = \left[\frac{3V_l}{4\pi} + r_b^3 \right]^{1/3} - r_b \quad (4.21)$$

$$r_b^* = \left[r_b^3 - \frac{3m_d}{4\pi\rho_b} \right]^{1/3} \quad (4.22)$$

where V_l is the total volume of the liquid droplet, r_b is the initial radius of the binder particle, r_b^* is the reduced binder particle radius and ρ_b is the density of binder particle.

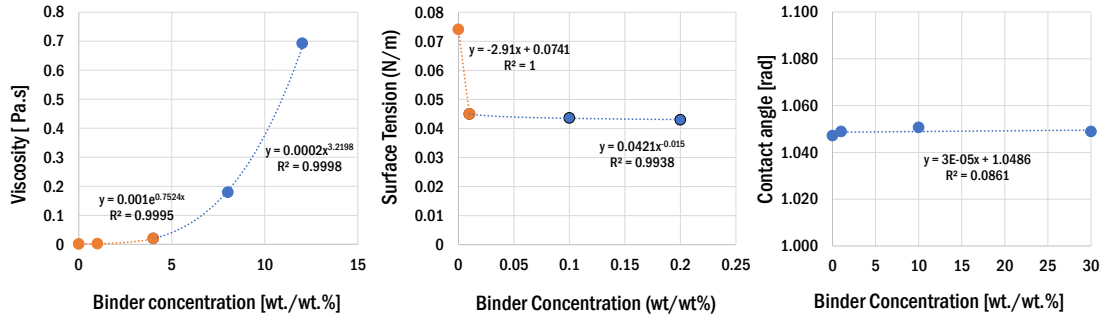


Figure 4.4: Effect of binder concentration on the viscosity, surface tension and contact angle of the solution. Data based on properties of hydroxypropyl cellulose binder obtained from literature Ashland (2012); Chang and Gray (1978); Mezdoor et al. (2007); Pelofsky (1966).

4.2.5 Particle motion and position analysis

The final step in the DEM algorithm is the determination of new particle velocities and position due to the changes in contact and body forces. The total force (\vec{F}_T) which is a summation of contact forces (\vec{F}_C^N and \vec{F}_C^T) and body forces (\vec{F}_B) is then used to calculate the acceleration of the particle by Newton's 2nd law to compute the new velocity and position profile.

$$\vec{F}_T = \vec{F}_C^N + \vec{F}_C^T + \vec{F}_B \quad (4.23)$$

In the DEM simulations carried out in this work, the particles generated for the batch all settle down completely (i.e. average particle velocity = 0) by 0.2 seconds after which the impeller motion is activated. Once the particle flow/velocity profile reach a steady state, liquid addition is started (around $t = 2$ s). The spraying continues throughout the whole simulation for 44 seconds and stops when the all the liquid amount is introduced to the system. DEM simulations for the WBA and DBA system were performed separately to compare the differences in the dynamics of the two binder addition approaches.

4.2.6 DEM model limitations

In the current DEM framework, the wet granulation behavior in both DBA and WBA are simulated only based on the agglomeration kinetics via liquid bridge connection between particles and breakage via rupture of these liquid bridges. While impact breakage of granules and attrition of particles are also important mechanisms occurring during high shear granulation, these processes have been omitted in this framework to focus on the distribution of viscous regions within the two systems.

In order to expand the model to account for impact breakage and attrition of particles themselves, there are a few methodologies that have been implemented in literature. One of the possible methods is coupling the current DEM model with a PBM breakage kernel. Several population balance breakage kernels have already been published including works by Pandya and Spielman Pandya and Spielman (1983), Pinto et al Pinto et al. (2007) and Ramachandran et al Ramachandran et al. (2009). The other popular method is to incorporate a breakage mechanism within the DEM algorithm. Generally, the impact breakage is embedded into DEM in one of two ways: **(a)** A bonded particle method – where particles held together with an adhesive force or surface energy values is used as the initial particle design and impact force is applied to study breakage behavior Kafui and Thornton (2000), or **(b)** A particle replacement method – where the primary particle is replaced entirely with smaller daughter particles with volume conservation Metta et al. (2018); Capece et al. (2014).

4.3 Experimental data

The high-shear granulation setup simulated in this work is based on the experimental work carried out in Chaturbedi et al. Chaturbedi et al. (2017). In the experiment, microcrystalline cellulose (MCC), (FMC Co., Philadelphia, PA) was granulated with hydroxypropyl cellulose (HPC EXF), (Ashland Specialty Ingredients, Wilmington, DE) as one of the binders tested and with water as the dissolving medium. The total granulation batch size of 1.664 kg with 96 wt./wt. % of MCC and 4 wt./wt. % HPC was used during both WBA and DBA experiments. For wet binder addition, a

5.547 wt./wt.% binder solution was prepared by dissolving all the binder particles in water while in dry binder addition, the binder particles were pre-blended with primary particles and then pure water was added to the mixture during liquid addition stage. A 10-liter PMA high shear granulator operated at 306 RPM was utilized as the granulating vessel.

The authors compared the average diameter of granules obtained from DBA and WBA experiments and found that the dissolution of dry binder during DBA gives rise to a dynamic viscosity environment in the granulator which promotes faster growth of granules in DBA system versus traditional wet addition method. A representative result plot from the investigation is provide in Figure 4.5. Two main differences are observable for the DBA and WBA systems:

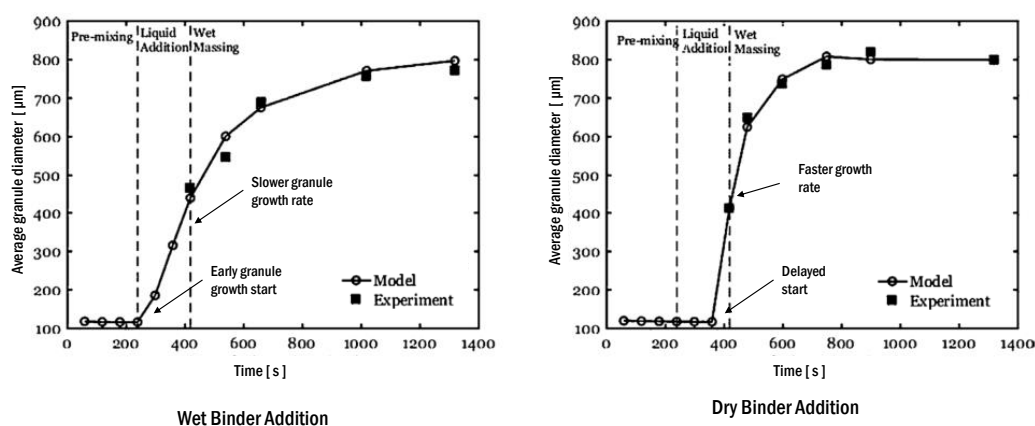


Figure 4.5: Comparative differences between WBA and DBA system seen through experiment and numerical model developed by Chaturbedi et al. (2017). (Re-printed with permission of the author)

- The granule growth in wet binder addition method starts earlier than the DBA system. In the figure, the granule growth in WBA system starts as early as 200s when the liquid addition phase starts; while in DBA system, the growth of granule size is only noticeable well into the liquid addition phase.
- The granule growth rate for the DBA system is significantly faster than the WBA method wherein the granules reach their maximum size early in the wet massing period.

4.4 Comparative analysis between wet binder addition and dry binder addition

The main difference between the WBA approach and the DBA approach is the mechanism by which dissolved binder solution is introduced onto the particles during granulation which ultimately affects the viscosity of the surface liquid present on granules. While a binder solution is sprayed directly onto the particle bed in WBA thus giving granules the viscous surface liquid needed for agglomeration, in a DBA system, the granules obtain a viscous film only after binder particles have been dissolved by the pure liquid sprayed onto the bed. This variability in how the binder is present in the surface liquid significantly alters the properties of the external liquid present on the granules for the two system (see Figure 4.4). For instance, the binder solution added in WBA has a constant viscosity due to the fixed amount of binder dissolved in the solution while for the DBA system the viscosity content is dynamic due to the progress of binder dissolution over time.

Figure 4.6 illustrates this concept through snapshots of the DEM simulation at various time points. Note that in the figure the maximum viscosity values of wetted granules in the two system are not same: the similarly colored dark blue particles in the DBA system are a magnitude of order more viscous than the WBA system. In both systems, as liquid is sprayed onto the dry particle bed, the un-wetted granules gain liquid and hence taken on the viscosity of the liquid absorbed.

In the WBA approach, since the binder concentration of the sprayed solution is fixed at 5.547 wt./wt.% (in accordance with experimental data), the concentration of binder in the surface liquid of the granules can only be two levels: 0% (unwetted) or 5.547% (wetted). Even when the granules absorb more liquid droplets - till its maximum liquid retention limit - the binder concentration doesn't go beyond that of the liquid droplet since it takes up proportional amount of liquid and binder. As a result, the snapshots of granules in the figure display only two levels of viscosity - grey (no liquid, no viscosity) and dark blue (viscosity of 5.547 wt.% binder solution = 0.0497 Pa.s).

In the DBA system, however, as the un-wetted granules take up pure liquid droplets,

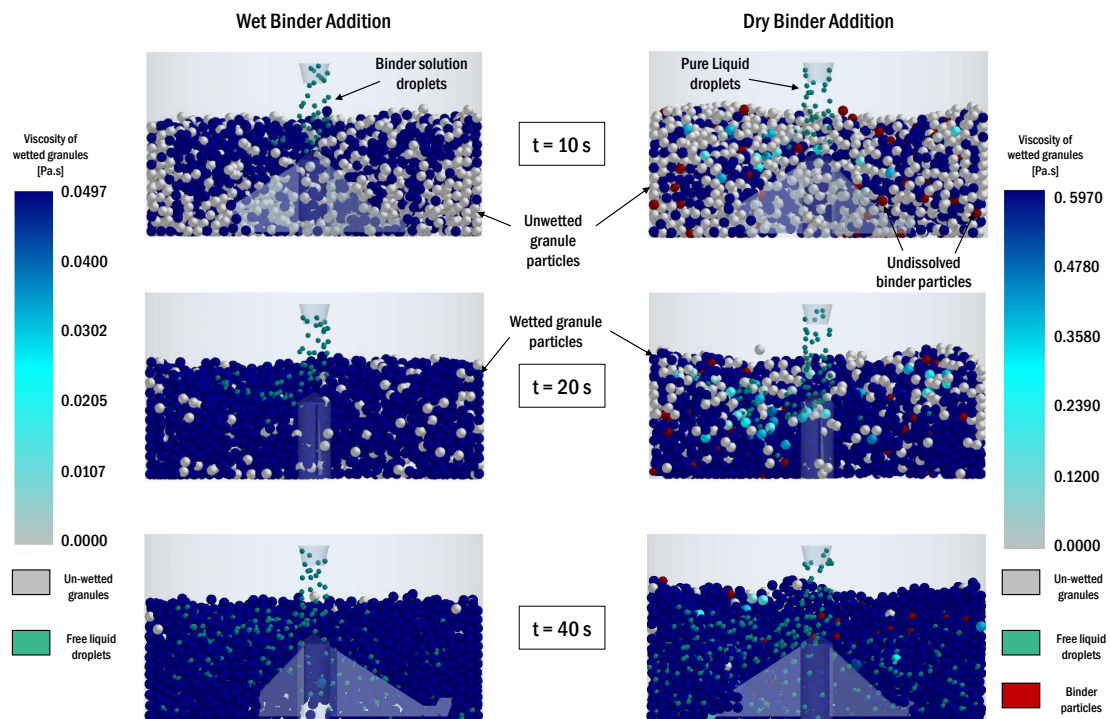


Figure 4.6: DEM snapshot of simulations with Wet Binder Addition (WBA) and Dry Binder Addition (DBA) systems colored by the viscosity value of the fluid in the particles. Note: the un-wetted particles are a fixed color of grey, the binder particles are fixed color of red, the free liquid droplets are a fixed color of green and only wetted granule particles vary in shades of blue.

the granule surface liquid viscosity is essentially that of pure water at 0.001 Pa.s (grey in color scale). As these wetted granules and free liquid droplets encounter binder particles (colored red), binder dissolution occurs till the solubility saturation point (12 wt./wt.%) is reached. At this binder saturated liquid state, the viscosity of the surface liquid attains a maximum value of 0.597 Pa.s (dark blue color) based on the material property of the HPC EXF. In Figure 4.6, the presence of light blue particles thus indicates that there are an intermediate levels of binder concentration present in the surface liquid of granules - i.e. when granules absorb more pure liquid droplets than dissolved binder.

Qualitatively, when the two systems are compared over time, several differences can be observed.

1. At the early time points ($t = 10$ s): the distribution of the viscous particles (blue) in the system for the WBA are at the top layer of the bed where particles meet the binder solution from the nozzle; while for DBA system, the viscous particles are more concentrated around binder particles wherever they are spread. This phenomena in the DBA method can be attributed to the two binder dissolution mechanisms employed: the granule particles obtain viscosity in two kinds of interactions between particles: granule-free droplet and granule-binder interactions. In the granule-droplet case, if a granule meets a liquid droplet with some dissolved binder, the granule absorbs the droplet and gains binder concentration. In the granule-binder case, the granule can itself dissolve binder particles if there is unsaturated external liquid present in the granule. Thus, both the distribution of solid binders and the position of the nozzle determines the viscous regions in the DBA system at the early stages.
2. At the intermediate stage ($t = 20$ s): Due to the mechanical mixing of particles, most granules in WBA system are wetted and attain some liquid viscosity which will immediately initiate granule growth. Meanwhile, a significant portion of the granules in DBA system are still unwetted or wetted only by pure water - which does not have enough viscosity to result in successive agglomeration.

This phenomenon confirms the dynamic differences observed between WBA and DBA system observed in experimental trials as seen in Figure 4.5. The DEM simulations in this work recreate the pre-mixing and the liquid addition time frames of the wet granulation process.

3. At the end of liquid addition time ($t = 40$ s): Continued spraying of liquid and mechanical mixing results in almost all granules in both systems attaining surface liquid with high viscosity (darker blue color). As opposed to the WBA system, the DBA system achieves higher viscosity surface liquid (a magnitude of order higher) for its granules. This means that the granule growth phenomena are probably faster for DBA system since most collisions will result in successful agglomeration.

An interesting thing to note is the presence of free binder particles in the DBA system even at the end of the liquid addition stage. Although two systems possess the same ratio of binder mass to granule mass, the undissolved binder particles in the DBA system can mean that binder dissolution can take place even after liquid addition time and possibly faster granule growth rate will be observed during wet massing time as well. Figure 4.7 quantitatively shows the presence of solid binder particles at the end of the simulation – note the black dashed line which represents the total mass of undissolved binder particles normalized by the total mass of the binder added to system at the start. Due to dissolution, binder particles are losing mass and by the end of the simulation (i.e. liquid addition stage) about 10 wt.% remains undissolved. These particles are supposed to dissolve further with a longer period of mixing since there are liquid droplets accumulating in the system. The presence of free liquid droplets is seen in the liquid balance of the two systems depicted in Figures 4.7 and 4.8. In Figure 4.8, granules are seen to be taking up all the liquid added to the system in the initial stages of the simulation. This absorption slows down considerably around 25 s and almost reaches a plateau. This saturation indicates that the bed is reaching a collective maximum liquid retention capability of its individual granules as seen in Figure 4.7 in the end of the liquid addition. The penetration of surface liquid on the granule into

the pores of granule particles is also verified by the internal liquid content curve in Figure 4.7 which shows that the internal liquid content can only reach the amount of maximum pore volume (porosity) of granules.

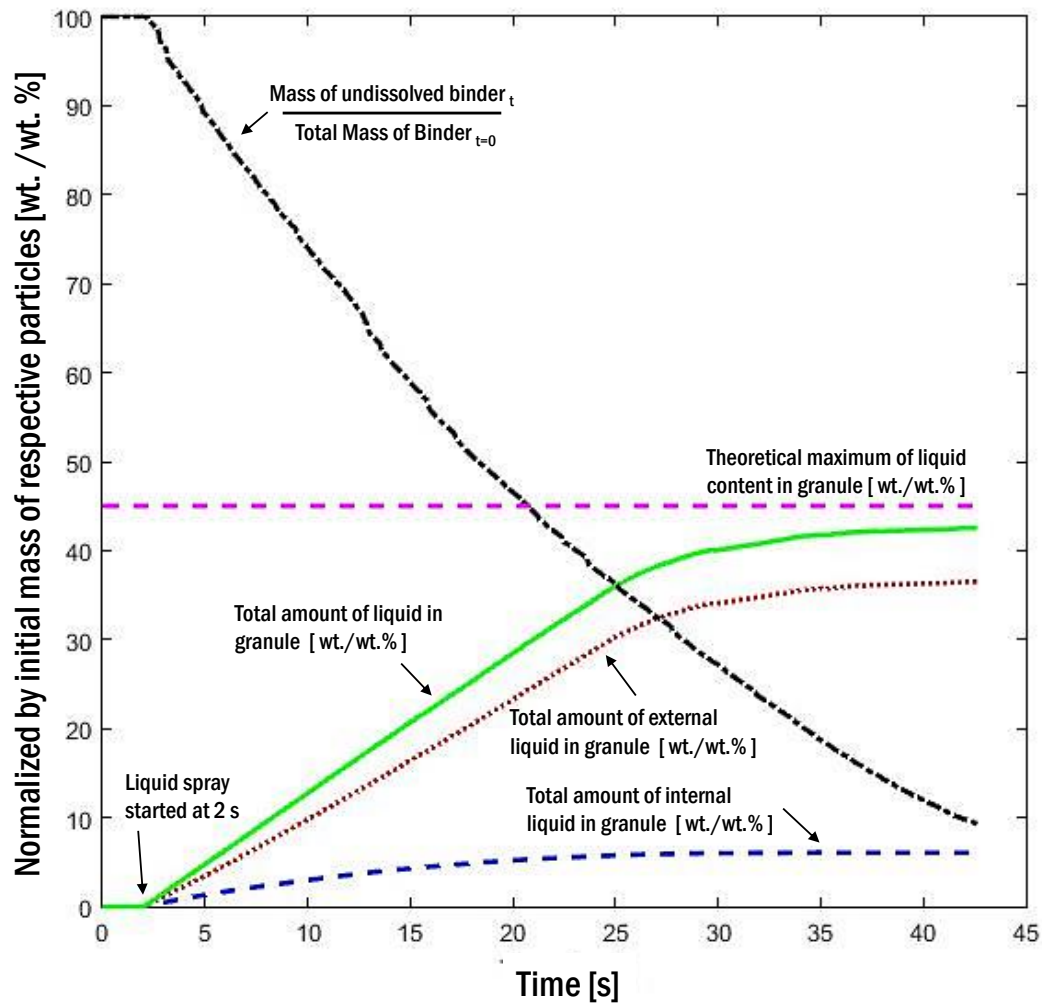


Figure 4.7: The liquid content and binder dissolution curves in the Dry Binder Addition (DBA) system.

In order to quantitatively compare the systemic differences between the WBA and the DBA method, the dynamics of the system with respect to key process parameters - viscosity of the surface liquid on granules, magnitude of the liquid bridge forces, particle velocities, collision frequency of granules as well as the dynamic number of contacts between particles are presented in detail below.

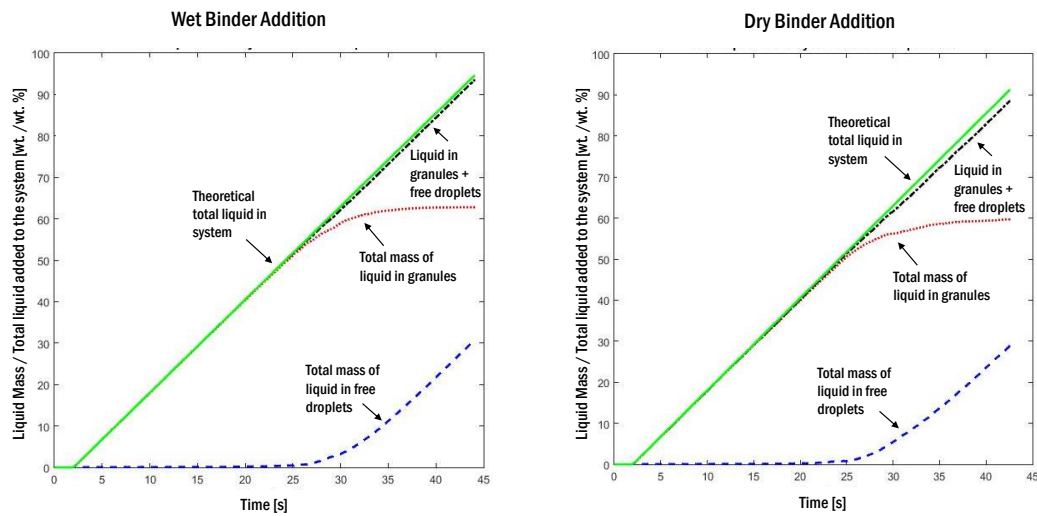


Figure 4.8: The liquid balance in WBA and DBA systems.

4.4.1 Differences between distribution of surface liquid viscosities

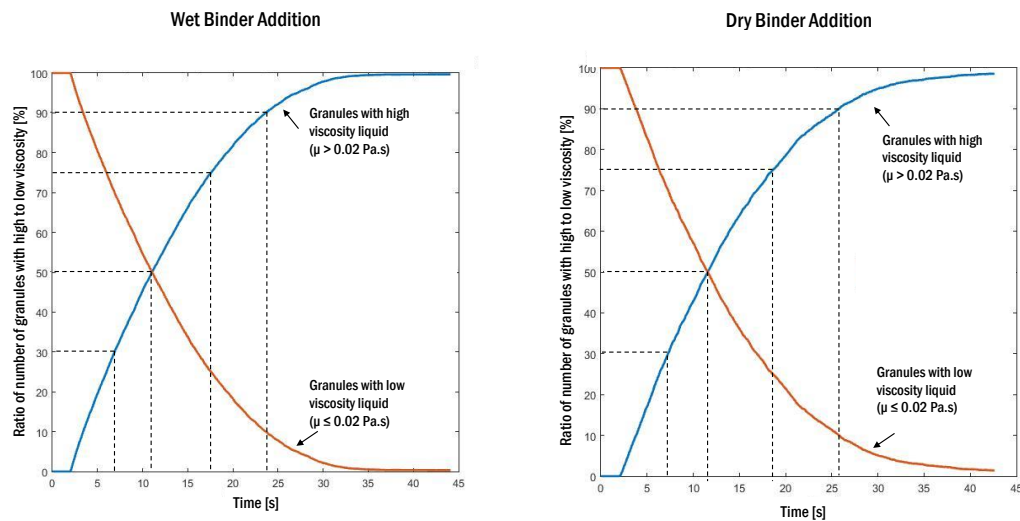


Figure 4.9: Distribution of granules with high ($\mu > 0.02 \text{ Pa.s}$) and low ($\mu \leq 0.02 \text{ Pa.s}$) viscosity of external liquid.

With the help of a particle-scale DEM simulation, an interesting distribution to observe - which is not readily possible through experimentation - is the location of high viscous regions during the granulation with the WBA and the DBA approaches. In order to help differentiate the high viscous regions, the DEM simulated particles were classified into: (a) granules with low surface liquid viscosity and (b) higher surface liquid

viscosity. A value of viscosity 0.02 Pa.s - which is 20 times more viscous than pure water - was chosen as an arbitrary cut off point. Thus, granules with surface liquid viscosity more than 0.02 Pa.s were classified as 'high viscosity particles' and those lower than cut off value were considered 'low viscosity particles'. Figure 4.9 illustrates the growth in percentages of high and low viscosity particles for both approaches. In both systems, low viscosity particles slowly turn into high viscous particles during the liquid addition phase. It is interesting to note here that the conversion of low viscosity particles to particles with at least 0.02 Pa.s viscosity is slower in the DBA approach. For instance, the 90% of particles reach 0.02 Pa.s viscosity for the WBA system by 24 s while the same of the DBA takes 2 s longer (which is about 15 more blade passes at the chosen impeller speed).

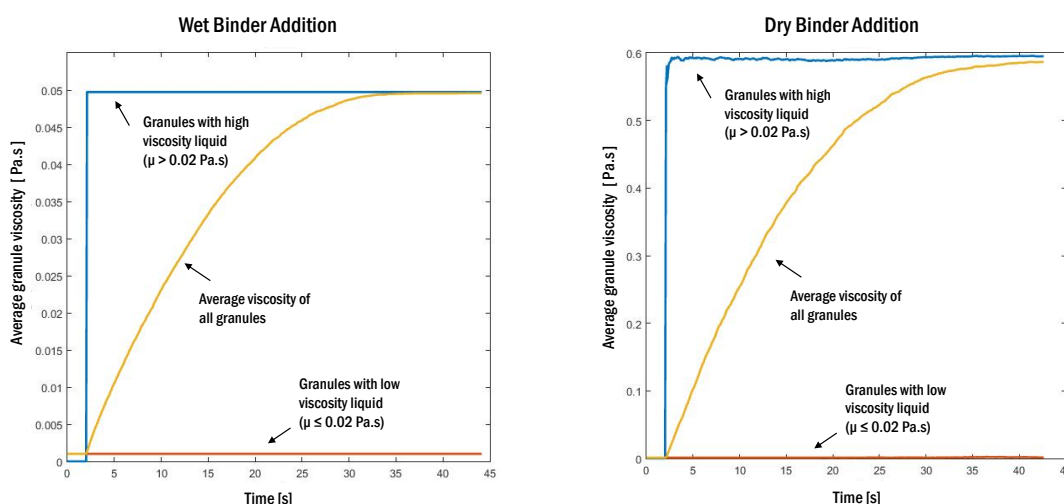


Figure 4.10: Average viscosity of high/low viscosity particles in the two systems.

It must, however, be noted that although the ratio of low to high viscous particles look somewhat similar in the two systems, the average viscosity values of these particles groups are drastically different in the two systems as seen in Figure 4.10. In the WBA system, the high viscosity particles have viscosity around 0.05 Pa.s, while in the DBA system, the value is closer to 0.59 Pa.s (quantitative depiction of snapshots in Figure 4.6).

In terms of the location of these viscous regions, viscosity distribution profiles of the two systems in Y direction (height-wise) and R-direction (radial) are illustrated in

Figures 4.11 and 4.12.

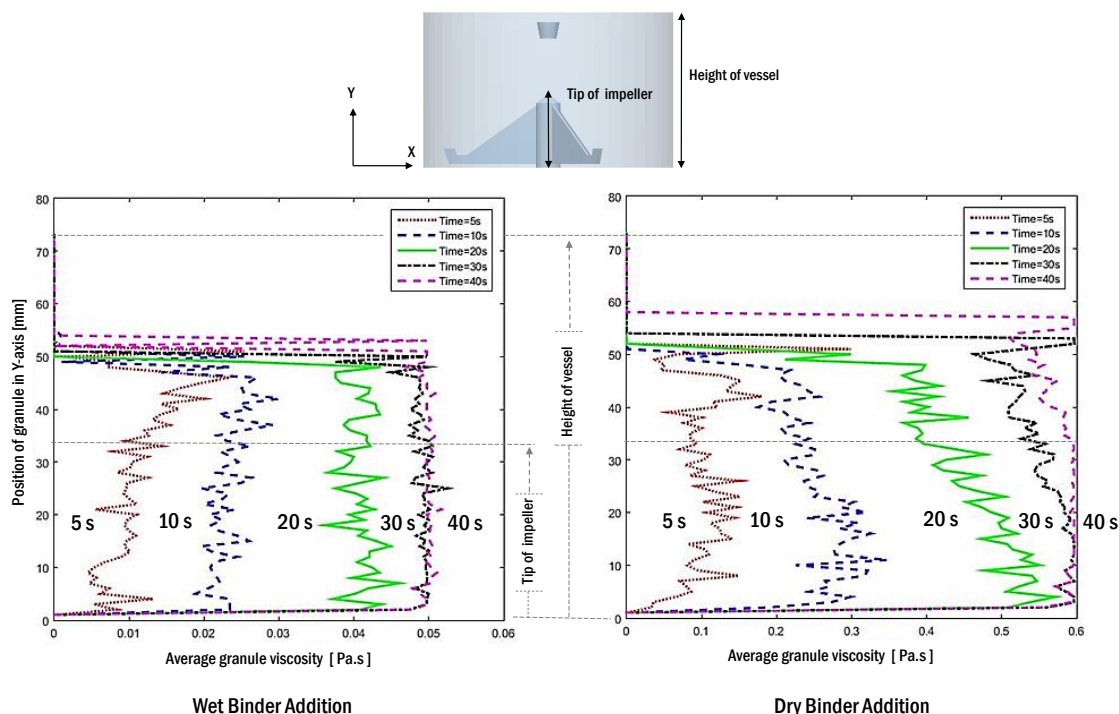


Figure 4.11: Average viscosity of liquid in granules over the granulator height. The viscosity distribution profile at different time points (5s, 10s, 20s, 30s and 40s) are plotted in the same graph. The height of the vessel as well as height till the tip of the impeller are annotated.

In Figure 4.11, the average viscosity distribution of granules over the depth of the particle bed is shown at different time points for both systems side by side. In the WBA system, at early time points (5 s and 10 s), the high viscous particles are seen at the top of the particle bed which receives the most liquid from the spray nozzle at the top of the granulator. As the liquid addition and mixing proceeds, the average granule viscosity homogenizes over the bed depth. On the other hand, for the DBA system, the lower depths of the particle bed (below the tip of the impeller annotated in the figure) seem to consistently be at a higher average viscosity than the top. A possible explanation for this behavior could be the efficient circulation/mixing of particles in this region near the impellers which results in more wetted-granules and free liquid droplets encountering binder particles. This leads to more dissolution of binders, and thus more viscous particles.

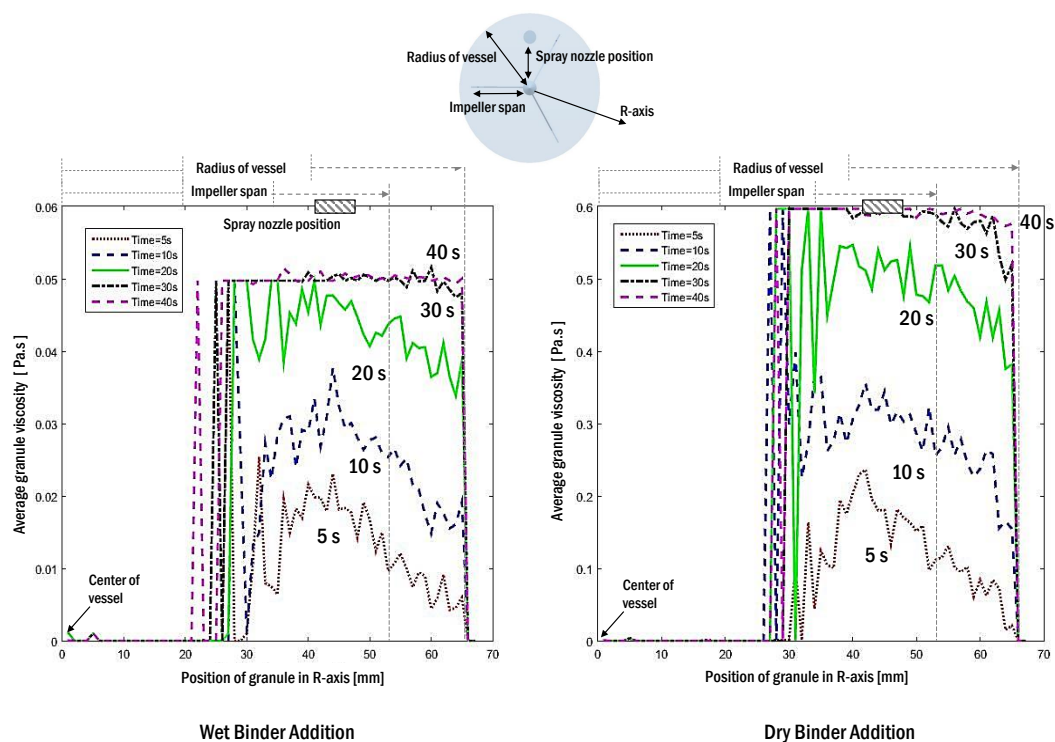


Figure 4.12: Average viscosity of liquid in granules at different distance from the center of the granulator. The viscosity distribution profile at 5s, 10s, 20s, 30s and 40s time points are plotted in the same graph. The span of the impeller, the radius of the vessel as well as the position of the liquid spray nozzle area annotated.

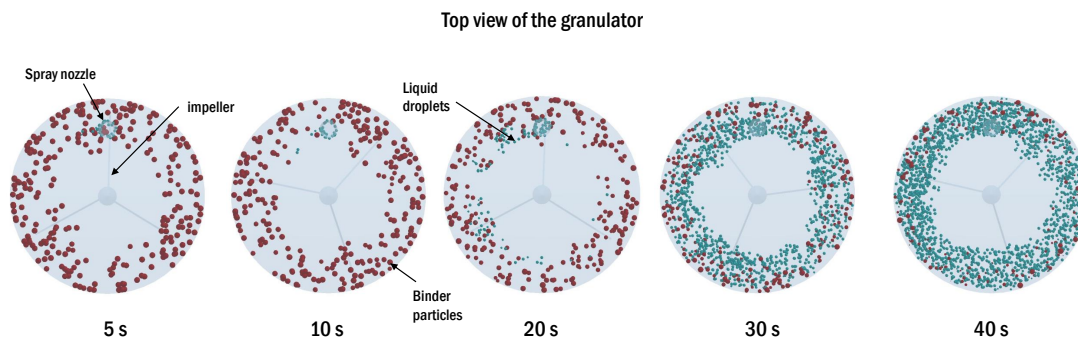


Figure 4.13: Distribution of binder particle and liquid droplets seen from a top view of the granulator for a DBA system over time.

In Figure 4.12, the average viscosity distribution of granules at different distances from the center of the granulator is shown at different time points for both systems. A clear trend that can be seen immediately for the two systems is the influence of the impeller. In the region between the wall of the vessel and the tip of the impeller, the average viscosity of the surface liquid in the granules drops significantly. This trend can be seen for both systems. The influence of the impeller on system is visually supported by Figure 4.13. In the figure, the granule particles are rendered invisible while only solid binder particles and free liquid droplets are colored. The shrinkage in the size of binder particles (i.e. dissolution of the binders) can be seen in areas where it meets liquid droplets - mostly towards the center of the granulator. In the regions near the wall, most of the binder particles are still intact and thus have experienced very little dissolution. Thus, granules near this region have low viscosity surface liquid.

In addition to the impeller, the spray nozzle position is also seen crucial to the viscosity profile at the early stages of liquid addition in Figure 4.12. The positions right below the nozzle (gray patterned square on the top of the plots) correspond to peaks with the highest average viscosity since this band has the largest concentration of liquid droplets (as can be seen in Figure 4.13).

4.4.2 Differences between the magnitude of liquid bridge forces

The impact of the heterogeneous viscosity distribution observed for the two systems has several consequences on the granulation behavior. As the viscosity of the surface liquid changes, the liquid bridges made from these fluid (which hold the agglomerates together) are directly impacted. The two types of liquid bridge forces implemented in the system - capillary forces (Equation 11 and 12) and viscous forces (Equation 18 and 19) - both are impacted by the viscosity of the liquid present in the bridges. For the viscous forces, the impact of viscosity is more prominent since the magnitude of the viscous bridge force is directly proportional to the viscosity of the liquid in the bridge. For capillary forces, the impact of viscosity is subdued since the values of the surface tension and contact angles do not vary as drastically with increase in liquid viscosity (this relationship is indirect through change in binder concentration, which is

proportional to viscosity, see Figure 4.4). As seen in the plot of Capillary number in Figure 4.14, both WBA and DBA system operate at viscous force dominating regime ($Ca > 0.001$) after the liquid addition starts; thus, the impact of viscosity will be more pronounced. Moreover, the capillary number of DBA system is about 100 times larger than that of the WBA system due to the higher viscosities present.

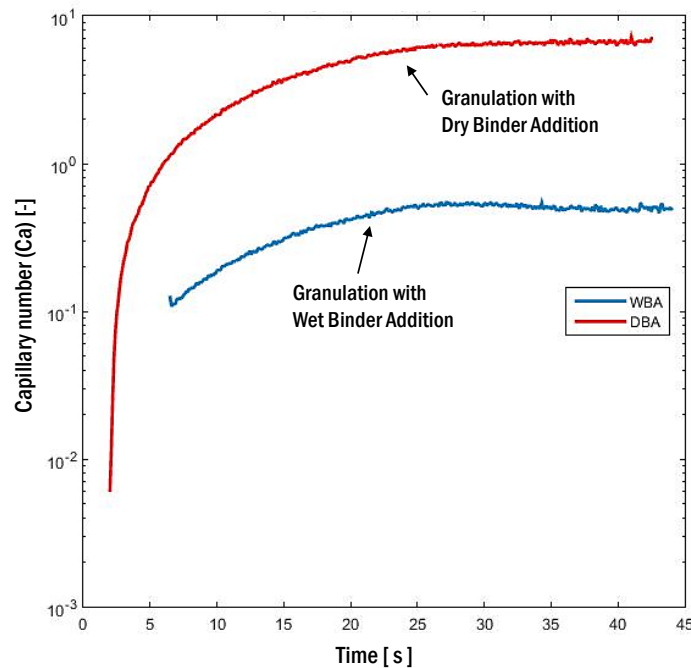


Figure 4.14: Capillary number (Ca) of the two systems over time.

This difference in the viscosity of the surface liquid drastically alters the strength of the liquid bridge force keeping particles together and ultimately the dynamics of the granulation. Figure 4.15 plots the average magnitude of these liquid bridges for both systems over time. The results show that the granules in the DBA system which have high viscosity surface liquids form liquid bridges which are approximately 5 times stronger than those made in the WBA system.

4.4.3 Differences between distribution of average particle velocity

Figure 4.16 illustrates the average particle velocities of high and low viscous granules for the two system over time. Although the impeller speed for both systems are kept

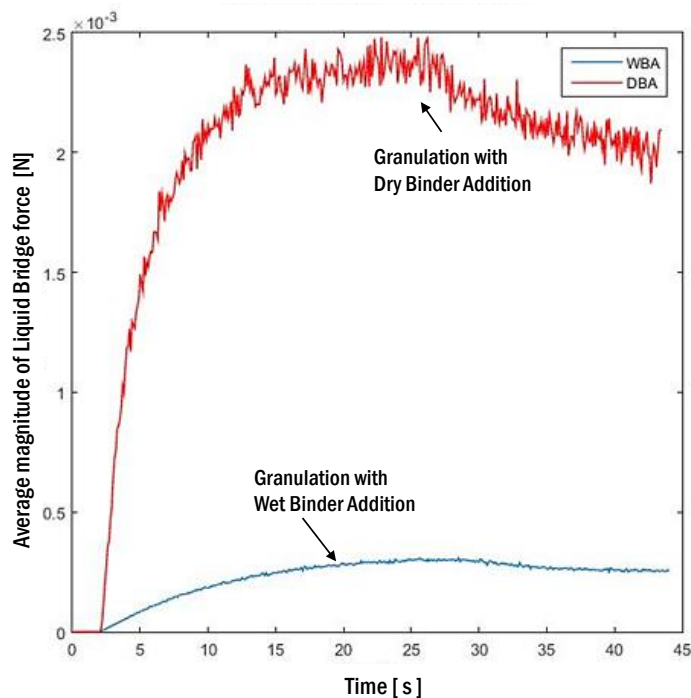


Figure 4.15: Average magnitude of the liquid bridge force holding granules together in the two systems over time.

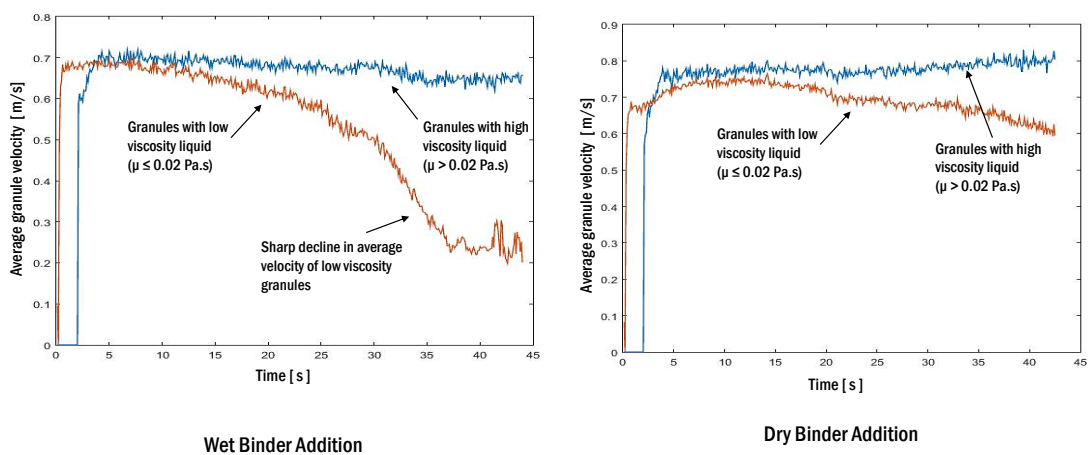


Figure 4.16: Average velocity of granules in the two system. Granules with high viscosity surface liquid and low viscosity surface liquid are differentiated.

constant at 443 RPM, several clear distinctions between WBA and DBA systems can be observed. First, the average velocity of the high viscous granules in the dry binder addition approach is observed to be higher than the counterparts for the wet binder addition approach. This is very likely due to the difference in the absolute viscosity of the high viscous granules for the DBA and WBA system (viscosity in DBA a magnitude of order higher than WBA) which results in more particles sticking together and moving at a faster pace for DBA system - rendering the average to be higher.

The second and most important difference is seen in the average velocities of the low viscosity granules in both systems. Although the average velocities of these granules decline over time for both systems, the fall in the curve for the wet binder addition approach is very drastic compared to the dry binder addition approach. The decline in the speed of these granules with low viscosity is primarily due to the influence of the impeller mixing. As liquid addition and mixing proceeds, granules near the impeller receive more efficient circulation of liquid droplets while those towards the wall receive fewer (see Figure 4.13). This causes granules beyond the reach of impellers to have lower viscosity surface liquids. Moreover, these same granules may also be stuck in the dead zone (poorly mixed) regions (see Figure 4.17) which means they do not get circulated around the bed. Thus, particles near the wall are likely to have both lower velocities and low viscosity surface liquids. The sharp decline in the velocity for the WBA system is again due to the relative viscosity values of the surface liquids between DBA and WBA. While DBA system with highly viscous particles maybe able to stick to particles from the poorly mixed areas (see Figure 4.18) and get them into circulation, the granules in WBA system with low viscosity granules are unable to stick to the particles in the poorly mixed area essentially rendering these locations as dead-zone pockets. As more particles get wetted during the granulation process, the only remaining low viscosity granules are present in these pockets and thus shows a sharp decline in average velocity.

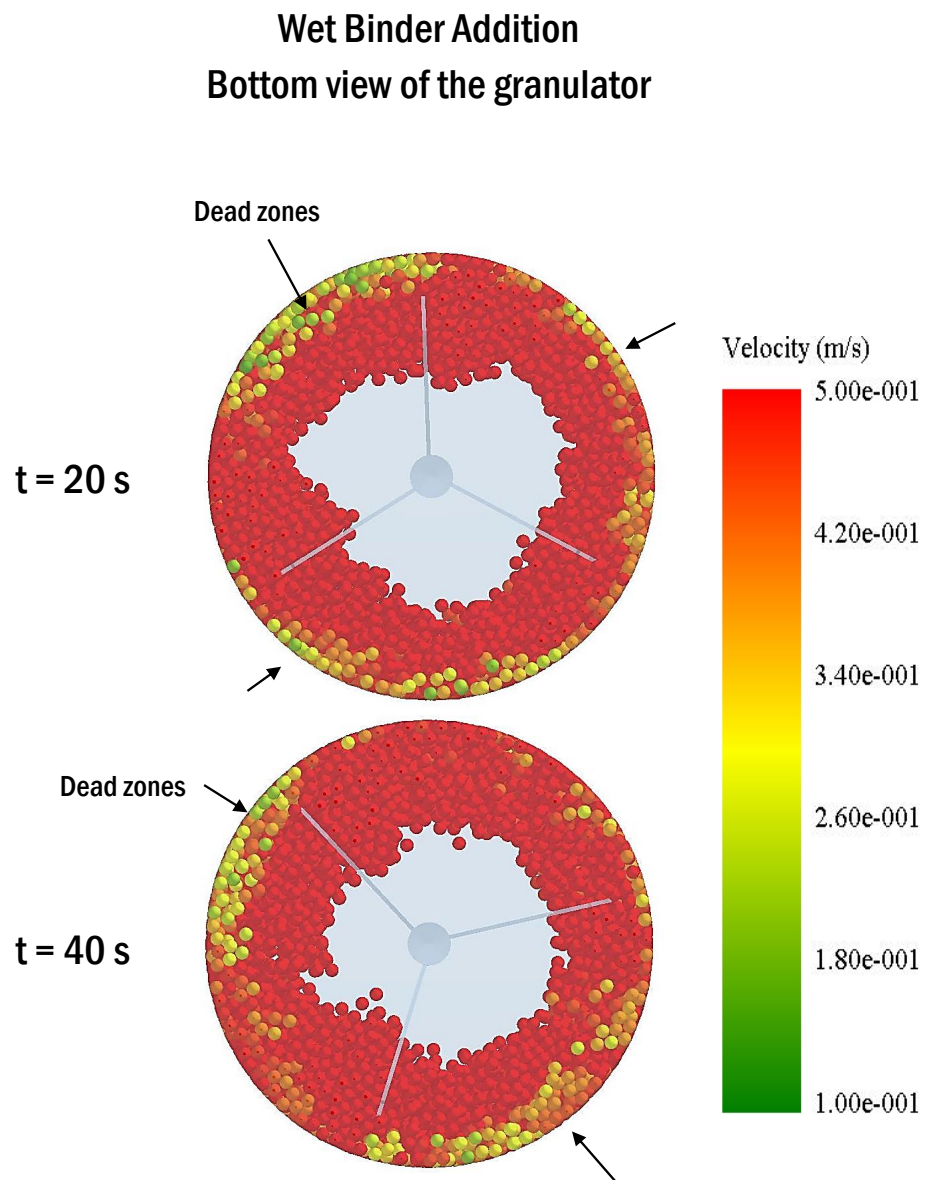


Figure 4.17: Velocity profile of granules in Wet Binder Addition system showing dead zones with lowest particle velocities. Note: Snapshots are taken from the bottom of the granulator.

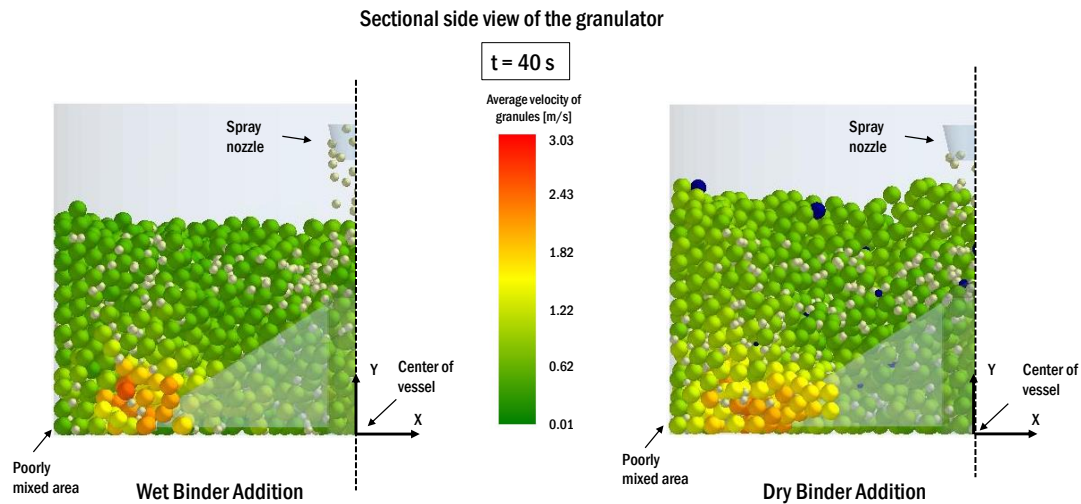


Figure 4.18: Sectional view of the granulator for both systems at $t = 40$ s. Particles are colored based on individual particle velocities.

4.4.4 Differences between particle collision frequencies and size of agglomerates

In wet granulation, collision frequency of particles - calculated by dividing the total number of collisions by total number of particles per time step - is an important parameter since it provides an insight into how often particles with viscous liquid layer meet each other to form liquid bridges. Higher collision frequencies are usually attributed for facilitating coalescence mechanism in granulation Gantt et al. (2006). Figure 4.19 illustrates the collision frequency profiles for the two systems; in order to differentiate the impact of high and low viscosity granules, the collision frequencies for the two categories of granules are plotted separately.

The impact of surface liquid viscosity on the collision frequency is significant: particles with high viscosity ($\mu > 0.02 \text{ Pa.s}$) in both systems have higher collision frequencies than particles with low viscosity liquid ($\mu < 0.02 \text{ Pa.s}$). This may be due to the fact that higher viscosity particles in both systems are generally present near the impellers while the low viscosity granules are mostly in the poorly mixed regions (see Section 3.3). In addition, the collision frequency values for the WBA system are seen to be slightly higher than the DBA system which may be due to the fact that the granules with lower absolute viscosity surface liquid in WBA system form and break liquid bridges more

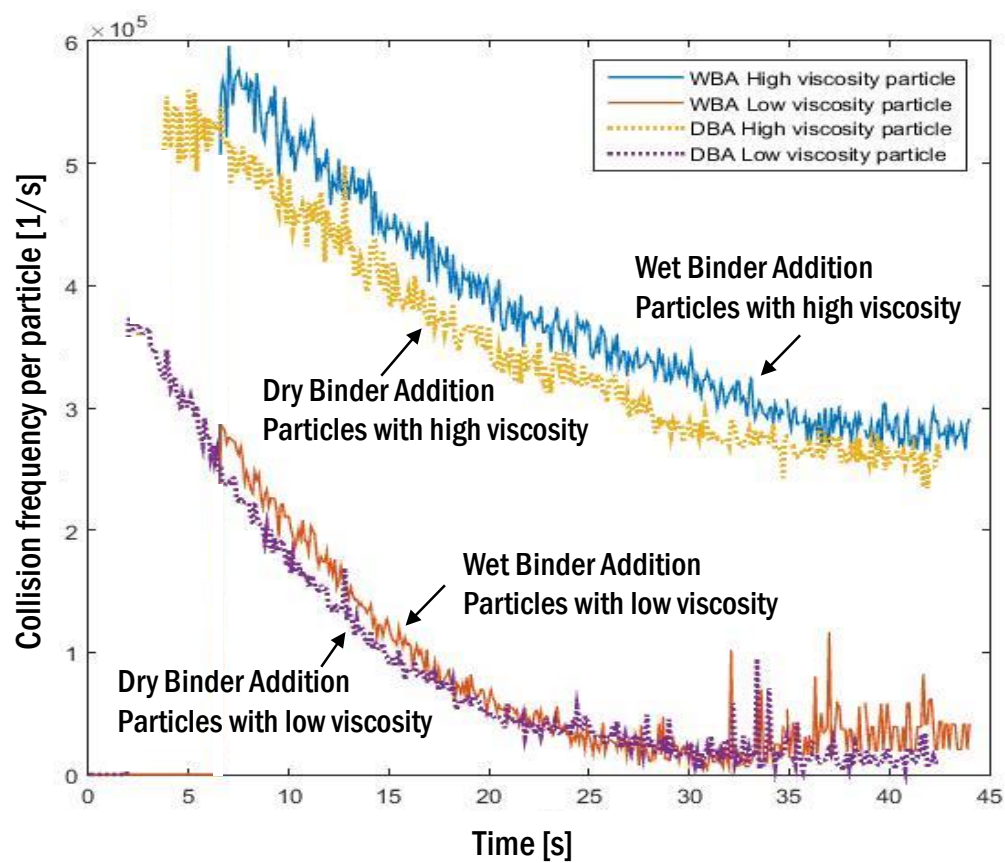


Figure 4.19: Collision frequency profiles of the two systems over time. Collision frequency of high/low viscosity granules in both systems are separated.

often and thus have a higher probability of colliding with other particles than those in DBA system which have stronger liquid bridge forces. Nonetheless, for both systems the collision frequency declines over time as the granulation progresses since granules start agglomerating and moving together which reduces the chance of colliding with other particles.

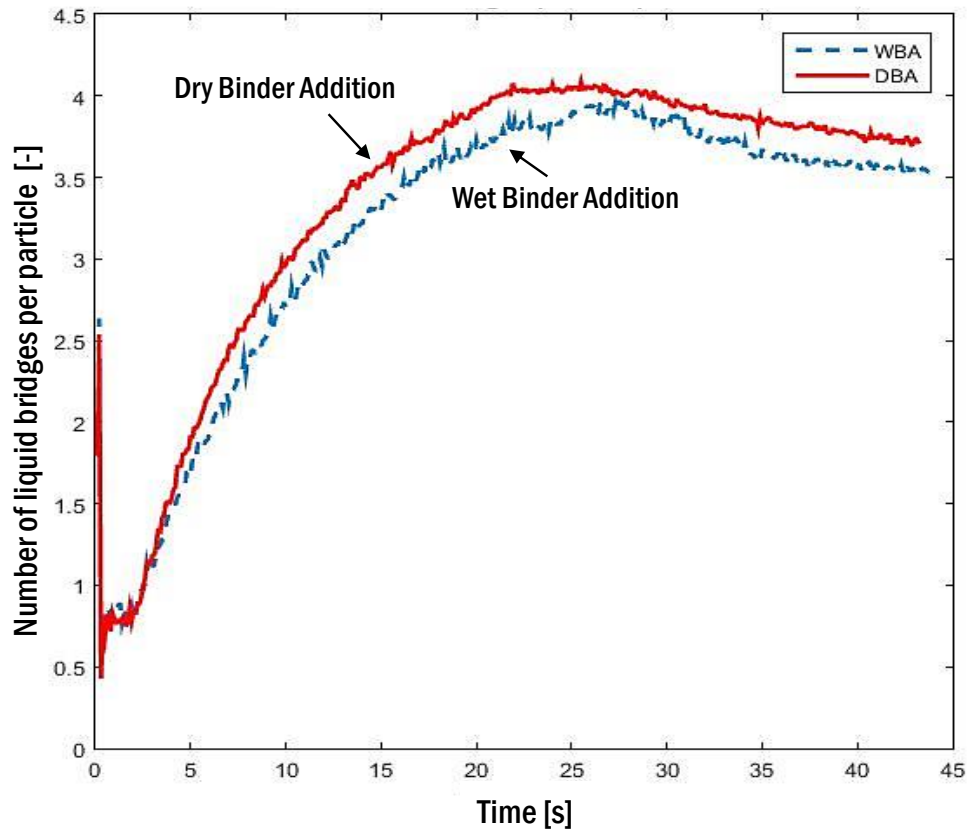


Figure 4.20: Average number of liquid bridges in place for a single granule over time.

This increase in the number of liquid bridges formed is illustrated in Figure 4.20 where the number of intact liquid bridges per particle is seen to be increasing over time. The curve plateaus after 25 s for both system which corresponds to the time when the number of free liquid droplets in the system are seen to increase in Figure 4.8. Realistically this depicts the scenario where liquid droplets have not met with dry particles yet and would need more wet massing time to be spread around the particle bed.

Another insight that can be gained from Figure 4.20 is the approximate size of agglomerates in the two system. The average number of liquid bridges on a single granule is the number of other granules attached to the chosen particle - thus this value can be used as an indicator of the size of granules in the system. In Figure 4.20, the DBA system is seen to have both a higher number and a faster rate in increase of liquid bridges on average than the WBA system. This indicates that the agglomerates in the DBA system may be larger than those in the WBA system and/or maybe be growing at a faster rate. This trend seems to match with the experimental results and model predictions published by Chaturbedi et al. Chaturbedi et al. (2017). The reason for this phenomenon lays in the fact that high viscosity in DBA system forms stronger liquid bridges between particles (explained in Section 3.2) that may be able to resist shear forces of the impeller to stick more particles to itself.

4.5 Conclusion

During wet granulation process, binders which are crucial for the coalescence of the particles can be introduced to the system in two ways – through traditional wet binder addition (where a solution with dissolved binder is sprayed onto the particle bed) or through dry binder addition (where binder particles are mixed in with the particle bed and a pure liquid is sprayed to dissolve the binder in place). This work employs discrete element methodology to differentiate between the two approaches by simulating a 1-liter high shear granulator. A custom-built contact model was developed for the DEM to define the interactions between different types of particles in the system including liquid droplets, granule particles representing mixed drug and excipients composition and solid binder particles. The contact model integrates two types of liquid bridge force models - capillary forces and viscous forces- as well as binder dissolution and liquid penetration mechanism. The simulation results were extracted and post-processed to observe the effect of the two binder addition approaches on granulation mechanism through key system parameters including viscosity of surface liquid on granules, magnitude and number of liquid bridge forces, collision frequency of particles and the average velocities of particles.

The DEM simulation points out several differences between the WBA and DBA system. Primarily, due to the dynamic dissolution of binder in the DBA system, distinct viscosity distribution profiles are observed in the two system. For the WBA system, the high viscous regions are generally found at the top layer of the particle bed and around the band below the nozzle while the low viscous regions are near the vessel wall where poorly mixed dead zones are observed. On the other hand, for DBA systems, high viscous regions are generally around the lower portion of the particle bed where the mixing of binder and liquid droplets is efficient. The low viscous regions in DBA system also occur near the vessel walls; however, due to the stronger liquid bridge forces of high viscosity particles, the size of poorly mixed region is smaller compared to WBA system. Comparative differences are also observable regarding the size of these viscous regions. For WBA, the liquid droplets are quickly spread around the particle bed since the liquid bridge forces are significantly weaker; thus, most of the particle bed are wetted by the end of liquid addition time. Meanwhile for DBA system, only granules near binder particles gain viscous liquid layers and hence only fewer number of particles with highly viscous surface liquid are generated. The presence of these agglomerates also limits the distribution of liquid throughout the system hence a significant number of granules remain unwetted for a longer time. Thus, even though there is a faster agglomerate growth, it is delayed by the liquid mixing and binder dissolution time. For both systems, the high viscous areas are dependent on the binder and liquid dispersion which are affected by the mechanical agitation.

Part III

**Specific Aim III: Development,
Implementation and Assessment
of using Multi-scale Hybrid
Models to Relate Particle-level
Mechanisms to Bulk Behavior.**

4.6 Overview

In pharmaceutical manufacturing, fluidized bed granulation is one of the common processing options available to achieve better flowability of powders through size enlargement of primary particles. In fact, over the last 50 years, various fluidized bed operations including freezing, drying, impregnation, coating, etc. have become a common place in the chemical processing industry due to the high level of contacts between fluids and solids attainable in a fluid bed system. These complex interactions between the fluid and particles also mean that simulating fluidized beds are still a challenging endeavor. Generally, Computational Fluid Dynamics (CFD) packages are employed to model the pressure drops in fluids; however, the presence of high concentration of solids and the complexity of granulation behavior require more advanced particle models than are available with CFD software. As a result, coupled frameworks that utilize the strength of particulate simulations such as Discrete Element Method (DEM) and bulk granulation modeling such as Population Balance Model (PBM) in conjunction with CFD information are the next steps to developing practical fluid bed granulation models.

As the pharmaceutical industries are transitioning towards implementation of US Food and Drug Administration (FDA) recommended Quality by Design (QbD) guidelines, there is a growing effort in development of practical and predictive models of particulate processes over the last decade to incorporate discrete particle simulations in the study of particle and particle-fluid flow. Since the behavior of bulk material in powder processing units are dictated by the microscale interactions of the particles with surrounding particles, fluid or equipment, fundamental modeling approaches such as discrete element modeling (DEM) and computational fluid dynamics (CFD) have become exceedingly popular in capturing particle level physics. However, employing such computationally complex simulation requires the model to solve a set of differential equations for each and every particle being handled in the system for very small time intervals (around 10^{-6} s scale) while also tracking their interactions and spatial movements. The high computational cost incurred for implementing a computationally

complex model such as DEM-CFD renders it grossly inefficient while developing models for real scale geometries and for simulating actual time length of unit operations. Another significant challenge in the implementation of mechanistic DEM-CFD model arises from its inability and inefficiency to simulate particle size and property changes resulting from the subprocesses in wet granulation. Since these mechanistic models do not directly relate the captured particle-scale properties back to mesoscopic quality attributes traditionally utilized by the pharmaceutical standards (such as changes in particle size distribution, average liquid content, etc.), there is a disparity between the needs of the industry and the aims of academic projects.

In order to deal with these limitations, two multi-scale hybrid models are presented in this SPECIFIC AIM which can be utilized to both build scientific understanding into the process through discrete particle simulation and also connect mesoscopic dynamics through bulk granulation modeling. Chapter 6 introduces a proof-of-concept hybrid model development of a fluidized bed granulation process implemented through coupling of ANSYS Fluent CFD software and EDEM DEM algorithm. In this chapter, the effect of operating parameters on the granule size enlargement as well as wetting of particles is demonstrated using a simplified miniature fluidized bed system. Chapter 7, on the other hand, presents the implementation and validation of a lab-scale fluidized granulation system and assess the quality of hybrid model framework against experimental data. In this study, a different CFD-DEM coupling package using STARCCM+ is used to demonstrate the feasibility of using the framework across platforms.

4.7 Publications

The details of the discussions provided in this section were published in the following article/conferences:

- **Tamrakar, A.**, Ramachandran, R. **2019**. CFD-DEM-PBM coupled model development and validation of a 3D top-spray fluidized bed wet granulation process, *Computers and Chemical Engineering*, 125, 249-270.
- **Tamrakar, A.**, Devarampally, D.R., Ramachandran, R. **2018**. Advanced multi-phase hybrid model development of fluidized bed wet granulation processes. *Book chapter in Process Systems Engineering for Pharmaceutical Manufacturing, Computer Aided Chemical Engineering*, 41, 159-187.
- **Tamrakar, A.**, Barrasso, D., Cruz, C.N., Ramachandran, R. **2015**. Multi-scale modelling of fluid bed granulation processes through a coupled PBM-DEM-CFD framework to facilitate QbD in pharmaceutical drug product manufacturing, *In conference proceedings: 7th International Granulation Workshop*.

Chapter 5

Multi-scale framework development of a fluidized bed wet granulation process

A novel proof-of-concept framework is presented that couples compartment-based population balance modeling (PBM), discrete element methods (DEM) and computational fluid dynamics (CFD). The main goal of the framework is to incorporate CPPs (e.g. liquid spray rate, airflow rate) and formulation properties of both liquid and powder particles (e.g. solid density and liquid-particle contact angle) to predict their effects on granule CQAs (e.g. particle size distribution, average liquid content). The framework relies on the PBM to simulate the changes in the particle size distribution (PSD) due to rate processes including aggregation, liquid addition and consolidation, and on DEM-CFD simulations to provide dynamic mechanistic information such as flux data, collision frequencies and drag forces needed to evaluate the rate kernels involved. The heterogeneity of liquid distribution and particle collisions as the system is fluidized and sprayed with binder is captured and embedded into PBM calculations via associated rate kernels which are functions of PSD and liquid content changes. Initial results are promising and demonstrates that the proposed multi-scale model can be successfully coupled as described.

5.1 Background

5.1.1 Fluidized bed granulation

Granulation systems where the agglomerated granules are produced by spraying a binder solution onto a bed of powder suspended by a fluid flow are termed as fluidized bed granulation (FBG) processes. Due to the wetting of the particles by the sprayed liquid and the collisions of circulating particles, size enlargement of primary powder takes place within the fluid bed chamber. Such a controlled granulation of fine powders enhances the flowability of the powders, reduces particle segregation, improves blend uniformity as well as powder compressibility. FBG systems are thus widely used in pharmaceutical industry since the mixing, wetting, and drying of the granules can be achieved in a single operation which helps avoid transfer losses, enables dust containment, and saves labor costs and time Burggraeve et al. (2005). In addition, since the fluid flow within the FBG system undergoes extremely turbulent motion which introduces eddies and velocity fluctuations, fluidized bed granulators also provide good heat transfer and overall high mixing capability Parikh (2016). Over the last 50 years, various fluidized bed operations including freezing, drying, impregnation, coating, etc. have also become a common place in the chemical processing industry due to this high level of contacts between fluids and solids attainable in a fluidized bed system.

5.1.2 Fluidized bed granulation models

Due to the complex interactions between the fluids and solids in an FBG system, understanding fluidized bed mechanisms and developing systematic methodology for a better control of product quality is challenging. The underlying mechanisms which dictate the quality and rate of granulation in an FBG system are not only dependent on the pressure drop across the bed, but also on the inter-particle collisions and the wetting/drying behavior occurring within the system. The particle wetting rates in an FBG is highly dependent on the particle flow pattern which in turn is affected by the flow field of the fluidizing gas (Fries et al. (2011)). Granule product size and moisture

content are, thus, highly dependent on particle circulation patterns and on particle-level interactions which in turn are affected by the material properties of solids and fluids in the vessel as well as the operating conditions and the design of the vessel. Due to such inherent complexity, there has been no fundamental mathematical model that can be applied to better design and operate FBG processes at scale-up (Lourenco et al. (2012)). The traditional approach to rely heavily on experimentation programs for product and process design can thus be costly and time consuming, and lengthen the time-to-market.

To tackle this issue, several attempts are being made to develop *in-silico* models of the fluidized bed granulation systems. Different investigators have used different frameworks to simulate fluidized bed systems including using fluid flow simulations through Computational Fluid Dynamics (CFD) packages, meso-scale numerical methods such as population balance models (PBM) or a combination of methodologies including CFD-Discrete Element Method (DEM) coupling as well as CFD-PBM integrations Rajniak et al. (2009, 2006); Drumm et al. (2009); Yan et al. (2011); Tan et al. (2004); Yuu et al. (2000); Bokkers et al. (2004); Muddu et al. (2018); Dosta et al. (2010); Fries et al. (2011, 2013); Sen et al. (2014); Dosta et al. (2012, 2013); Tamrakar et al. (2015, 2018).

The CFD models are generally used to simulate the flow of fluidizing air and the associated pressure drops across the FBG bed. In fact, CFD-based simulations have been used in various fields of science and engineering to optimize fluid flow process/equipment design and operating parameters. In pharmaceutical industry, CFD has been used to model fluid flow in several processes such as mixing, separation, and fluidized bed granulation. Ierapetritou and Ramachandran (2016); Lyngberg et al. (2016) These simulations calculate the fluid flow field by solving the volume averaged Navier – Stokes energy and mass conservation equations over the region of interest. The use of CFD provides a distinct advantage of getting the data of the complete flow field within the domain. This is done through discretization of the region into individual cells over which volume averaged conservation equations of mass, momentum and energy are solved.

For pharmaceutical operations involving high solid concentrations such as the fluid bed granulation system, CFD packages on its own does not provide robust models

to estimate particles dynamics. Traditionally, two-fluid CFD models have been used to model multiphase fluid-particle systems using Eulerian – Eulerian approach. This strategy simulates both the fluid air phase and the solid particle phase as two interpenetrating continua and, resolves the conservation of mass, momentum and energy equations for both Hoomans et al. (1996); Ding and Gidaspow (1990); Kuipers et al. (1993). However, the presence of large amounts of particles in the FBG system means that complex, often turbulent flow patterns and interactions between the fluid and particles need to be accounted for - which may not be possible through Eulerian multiphase particle models built into the CFD packages.

To accurately model the particle flow behavior, DEM - which uses a Lagrangian approach to track the particles in space and time - can be implemented in a Eulerian-Lagrangian approach. In this approach, the fluid phase is treated as a continuum by solving the time-averaged Navier Stokes equations, while the dispersed phase is solved by tracking a large number of particles through the calculated flow field. Proposed first by Cundall and Strack (1979) in 1979, DEM modeling technique simulates the particle motion in a closed domain by individually solving the Newton's equation of motion for all particles present. In DEM methodology, particles are considered individual elements with sets of properties that influence its flow behavior (size, density, coefficient of restitution, etc.), and collision between particles or equipment and the resulting particle trajectories are determined for each time step. DEM algorithms, which were built to handle solids-based interactions, are thus often coupled with the CFD software to account for the particle dynamics. In the coupled Eulerian- Lagrangian approach, the dispersed phase can exchange momentum, mass and energy with the fluid phase. In literature, several authors have developed coupled CFD-DEM models to study the effect of process parameters in fluidization operations. Yuu et al. (2000) modeled a fluid bed using 100,000 particles of 310 microns diameter using coupled CFD-DEM simulations to study the bubble formation, coalescence and disruption behavior during fluidization. The model accurately describes the hydrodynamic behavior of the particles observed in the experiment trails, obtained through instantaneous particle positions and velocities. Other authors have similarly developed and validated the CFD-DEM models of powder

beds in different fluidization regimes with experimental results Bokkers et al. (2004). Fries et al. Fries et al. (2011) used similarly coupled CFD-DEM studies to compare the spray wetting dynamics of powders between a top spray fluid bed granulator and a Wurster coater. The authors investigated the residence time distributions of particles in the spray zone for both systems and found that the Wurster coater provided a narrower residence time distribution whereas a wide distribution was observed for a top spray fluid bed granulator. Such studies demonstrate the advantage of coupled CFD-DEM models in not just simulating gas and solid flows but also developing insight into heterogeneity of liquid distribution occurring under different fluidization conditions.

In addition, meso-scale numerical methods such as population balance models (PBMs) have also been used extensively in order to model FBG processes Cryer (1999); Heinrich et al. (2002); Tan et al. (2004, 2006); Vreman et al. (2009); Chaudhury et al. (2013b); Muddu et al. (2018). PBM relies heavily on the different aggregation, breakage, consolidation, etc. rate expressions - also called rate kernels- which describe the sub-mechanisms involved in the size enlargement phenomena during granulation. By summing the effect of different sub-mechanisms for individual size class of particles, PBM can offer a net change information on the size of granules within the system in response to different operating conditions. PBMs are thus used to gain insight into the underlying granule growth/attrition rate processes. Dosta et al. (2010), for instance, used a one-dimensional PBM to mathematically model FBG where simple fluid bed dynamics were coupled with heat and mass transfer. Traditionally, however, stochastic PBM methods model processes without particle transport, implying that the system is perfectly mixed. Tan et al. Tan et al. (2004), on the other hand, developed kinetic energy (EKE) kernel for PBM to describe the evolution of granule size distributions in fluidized bed melt granulation from kinetic theory of granular flow (KTGF). For heterogeneous granulation behaviors observed in fluidized beds, where all powder particles are not wetted to the same degree, the assumption of uniformity breaks down. In such circumstances, compartmental PBMs have been proposed to account for the heterogeneous nature of liquid addition and powder mixing Börner et al. (2013); Liu and Li (2014).

While different modeling frameworks are extensively reported in the chemical engineering literature, as seen in above examples, one of the more promising hybrid frameworks to describe a granulation phenomenon has been to extract particle kinetics information in terms of velocities and collision data from particle-level simulations (e.g. CFD, DEM) and thereafter, use these results in bulk-level growth rate kernels (e.g. PBM) to forecast the particle size changes. Freireich et al. (2009) and Gantt et al. (2005); Gantt et al. (2006) have demonstrated the use of this strategy to model high shear granulation processes. For fluidized bed granulation, this strategy needs to be updated to account for the fluid phase. An approach for combined theoretical and experimental study of a fluid bed granulation using coupled CFD-PBM strategy, for instance, was demonstrated by Rajniak et al. (2009) which combines the hydrodynamic modeling of gas-solid mixture with CFD and the population balancing of granule growth. Similarly, to comprehensively study the agglomeration of particles into granules, Sen et al. (2014) used a hybrid CFD-DEM-PBM model which incorporates PBM algorithm within the CFD-DEM simulations. Dosta et al. (2012, 2013) have also implemented multi-scale framework by transferring micro-scale data from CFD-DEM to macroscopic one-dimensional PBM algorithm.

5.1.3 Objectives

The main purpose of this study is to introduce a multi-scale hybrid framework of fluidized bed granulation model which utilizes a compartment-based PBM coupled with mechanistic DEM-CFD simulations that can capture spatial inhomogeneities present during granulation. In this model, the CFD simulation calculates the fluid flow-field while the DEM adds force-field calculation including development of capillary forces relevant for granulation systems with low moisture content. Additionally, the spray nozzle setup in the model's DEM portion accounts for the uneven distribution of liquid which is reflected through particle transfer rates and collision frequencies values. The two-compartment based PBM obtains the various mechanistic information required to calculate the rate processes from DEM-CFD to quantify the size change and update the particle size distribution (PSD).

The objectives of this specific aim include:

- To develop a proof-of-concept CFD-DEM-PBM hybrid framework to relate particle-level data with macroscopic properties of a fluid bed
- To investigate the effect of process parameters on the performance of the fluid bed granulator

5.2 Hybrid model development

The formulation and solution of a multi-scale model for any process is complex due to the different length and time scales involved. Moreover, various model forms and scales must be efficiently integrated to relate formulation/material properties, processing conditions (CPPs) and equipment geometry at the micro/meso scale to the macro/application (CQAs) scale to extract maximum benefit and applicability of the model. Figure 5.1 illustrates the schematic for the proposed multi-scale approach to FBG. First, the geometry of the lab-scale FBG was constructed in *SolidWorks*TM and loaded into the coupled CFD-DEM software (ANSYS Fluent 14.5.0TM linked with *EDEM Academic* 2.5TM interface, both of which are validated commercial packages widely used in many process industries).

At the initial time step (i.e. $t=0$), the CFD model based on the operating air flow rate computes the drag force (fluid force) term required by DEM to compute the various forces/velocities/collisions experienced by the particles in the granulation chamber (Figure 5.1). These terms extracted from the DEM calculations are then delivered into the two-compartment based PBM as process inputs to the different sub-processes such as aggregation, liquid addition and consolidation within the PBM framework. The PBM then computes the new particle number distributions with respect to particle size and liquid content for the required granulation time period. Since the computational demand of running CFD-DEM calculations are astronomical, a short time period (in the order of magnitude of the PBM time step) was simulated in CFD-DEM to characterize particle scale behavior. The meso scale process model (PBM) then uses this mechanistic data to simulate the full duration of process.

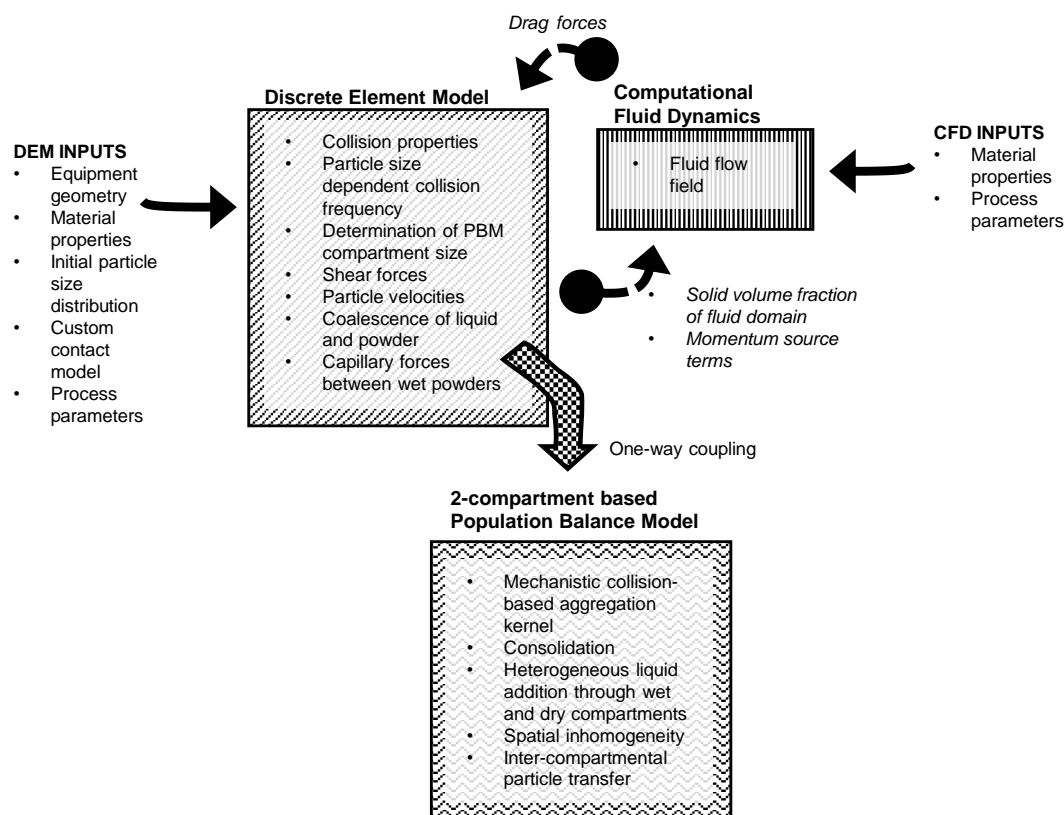
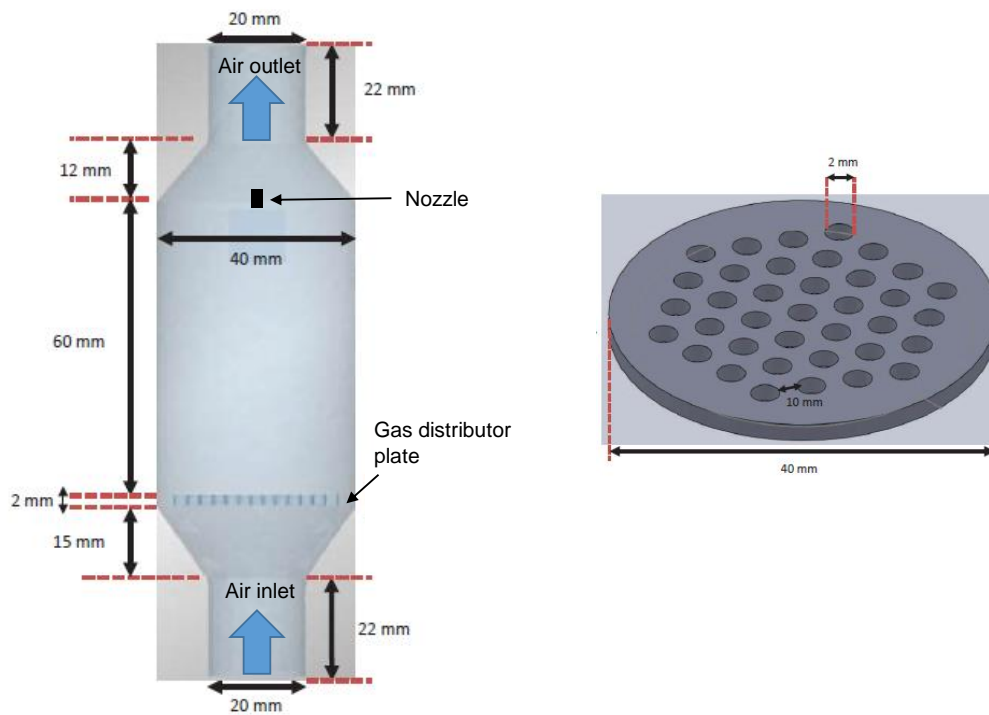


Figure 5.1: Schematic of PBM-DEM-CFD multi-scale approach.

5.2.1 Particle-scale: CFD-DEM simulations

In order to capture the fundamental dynamics of the fluidized bed system, a coupled relationship between CFD-DEM is critical. In this framework, the mechanistic information needed for PBM calculations, as shown in Figure 5.1, are obtained from the CFD-DEM model of the granulator. Information such as the delineation of the compartments in the compartmental PBM development as well as collision frequencies as function of particle size can be ascertained using high fidelity CFD-DEM approach. Since the collision frequency is related to the packing of the particles and the interstitial space between large particles, the size distribution will affect the collision rate and its dependence on particle size. In addition, it is important for the PBM rate kernels to account for both collision frequency and collision efficiency to capture more accurate granulation dynamics.



(a) Geometry of the fluidized bed granulator (b) Geometry of the gas distributor plate

Figure 5.2: Schematic showing the equipment setup in the DEM-CFD model

Figure 5.2a and 5.2b below illustrates the geometry of the fluidized bed granulator and the distributor plate used in this framework. Since gas distributor plates play a critical role in the design of fluidized bed systems, a gas distributor plate with 9.25% opening has been used in the model.

For the CFD simulations, the geometry has been meshed using the polyhedral domain in the FLUENT software and then coupled with EDEM. The CFD-DEM coupling allows for data transfer between the two software such that every time the simulation converges in CFD, relevant drag forces within the time interval are supplied for DEM calculations. For fluid flow calculations, a transient CFD simulation was performed assuming a viscous laminar flow. The minimum fluidization velocity (u_0) was analytically estimated (roughly to be 8 m/s) through the Ergun equation using gravitational acceleration (g), density of powder (ρ_p) and air (ρ), viscosity of air (μ), minimum porosity (ϵ_M), average diameter of particles (D_p) and the sphericity of particle (ϕ_s) (McCabe et al. (2005))

$$u_0 = \frac{g(\rho_p - \rho)}{150\mu} \frac{\epsilon_M^3}{1 - \epsilon_M} \phi_s^2 D_p^2 \quad (5.1)$$

In order to differentiate the CFD-DEM implemented in this project with previously developed models, two novel, mechanistic features were included within the developed CFD-DEM framework to capture realistic fluidization dynamics as presented below:

1. One of the major components of the DEM-CFD framework is the implementation of a top-spray nozzle in the DEM simulations that can be deliver binder solution at desired volume rate and velocity as per the operating conditions of the FBG process. For the base case framework 0.07 ml/s of water was sprayed to the particle bed at an average speed of 10 m/s. Furthermore, the liquid wetting of the powder particles was achieved by modeling the liquid droplets as solid particles with properties similar to the powder but with 100% liquid volume instead of solid volume. Using custom built DEM contact model (Barrasso and Ramachandran (2015)), the liquid droplets were designed such that they would disappear from the simulation on collision with solid particles. The powder particle would in turn collect the liquid volume of the colliding liquid droplet. In addition, in case of two liquid particle collision, a larger liquid particle with conserved total volume would be formed.
2. Another feature implemented in the CFD-DEM simulations is the custom liquid bridge contact model. Since the presence of moisture content in the real fluidized bed leads to cohesion due to capillary forces, a custom DEM contact model to represent the liquid bridge forces was implemented using the liquid bridge model approach developed by Remy et al. (2014). By enforcing capillary forces, this approach ensures natural wet granular behavior (which are not captured by Hertz-Mindlin contact model) such as formation of soft agglomerates, wet particles sticking to the wall, etc. which enhances the fluidization dynamics.

In the coupled CFD-DEM framework developed, air was chosen as the fluidizing medium and different air flow velocities near the u_0 estimated using Equation 5.1 were

used in the simulation to observe the effect of air flow on compartment size and collision rates. The air flow was started at $t=0$ while particle generation in DEM were initiated at 0.03s. With regards to the fluid flow boundary conditions, the flow near wall was assumed to be laminar with no slip conditions at the wall. In addition, the velocity was selected to vary linearly with the distance from the wall.

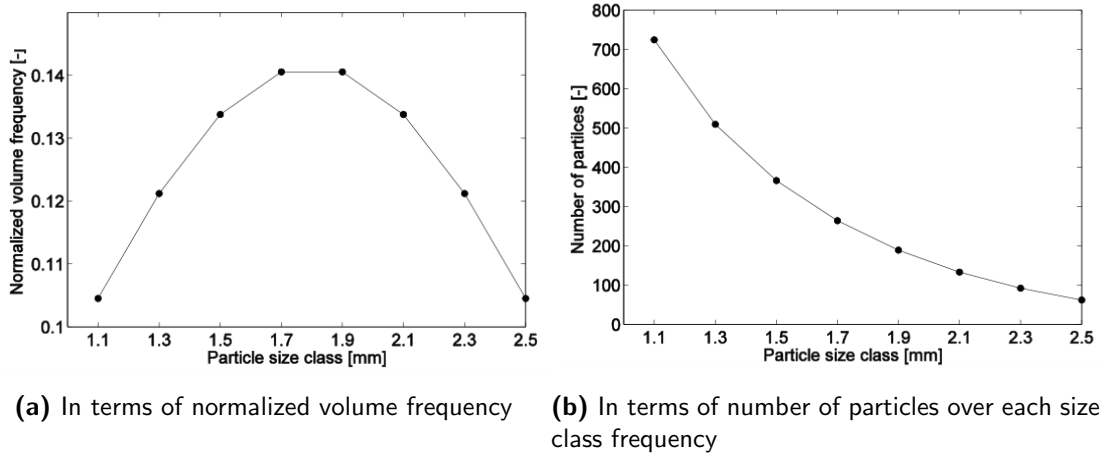


Figure 5.3: Particle size distribution used in DEM-CFD simulations

The initial particle size distribution used in the DEM factory, shown in Figure 5.3, was selected by calculating a volume normal distribution of particles with a mean diameter of 1.8 mm. Although in real granulation operations, the powder particles are much finer (around microns in diameter), much larger size classes were used for this simulation to conserve computational efficiency. An initial liquid content of 4 v/v% was charged into each particle to simulate a PSD condition that would better represent a granulation that has proceed for a while.

The properties of materials and geometry used in the DEM-CFD simulation are provided in Table 5.1. The time steps chosen for PBM, CFD and DEM are: 0.1s, 2.2×10^{-4} s and 2.2×10^{-6} s.

5.2.2 Meso-scale: Two compartment PBM

A multi-dimensional PBM was used to track critical granule CQAs such as particle size and liquid content. Compared to the CFD-DEM simulations, the PBM is computationally efficient and is able to account for spatial heterogeneities within the FBG geometry.

Table 5.1: Physical properties of particles and equipment used in DEM-CFD simulation

	Particle	Equipment
Material	Acetaminophen	Steel
Density [kg/m^3]	1030	7800
Shear Modulus [N/m^2]	1×10^6	7.6×10^8
Poisson's ratio	0.25	0.25
Coefficient of restitution	0.2	
Coefficient of static friction	0.5	
Coefficient of rolling friction	0.01	

In order to specifically address the inhomogeneities present during fluidized granulation, a compartment-based approach was implemented in this framework. Previous studies have utilized similar compartment-based PBM approach to model fluid bed coating or granulation processes where the geometry is divisible into distinct compartments such as active spray zone, active drying zone and non-active domain. Compartmental PBM based approaches by Freireich et al. (2011) and Li et al. (2012) use DEM simulations to identify the particle flow information and residence time distribution within each compartment of a particle mixer coater. Liu and Li (2014), on the other hand, have utilized exclusively CFD based simulations to determine the flow properties and distribution of particles which were then used to develop two-compartmental population balance model for pulsed top-spray fluidized bed granulation.

For this framework, a three-dimensional two-compartmental PBM was developed to represent the spray zone and the dry zone in the granulator, as illustrated in Figure 5.4. In order to identify the spatial compartments and assign particle transfer rates between the two well-mixed regions, mechanistic information such as liquid distribution and particle flux data was extracted from CFD-DEM simulations.

In each compartment, a multi-dimensional PBM was then implemented that accounts for aggregation, liquid addition and consolidation mechanisms that are predominant in each of those regions. The 3-D PBM describing the granulation process within a fluidized bed compartment can be written as:

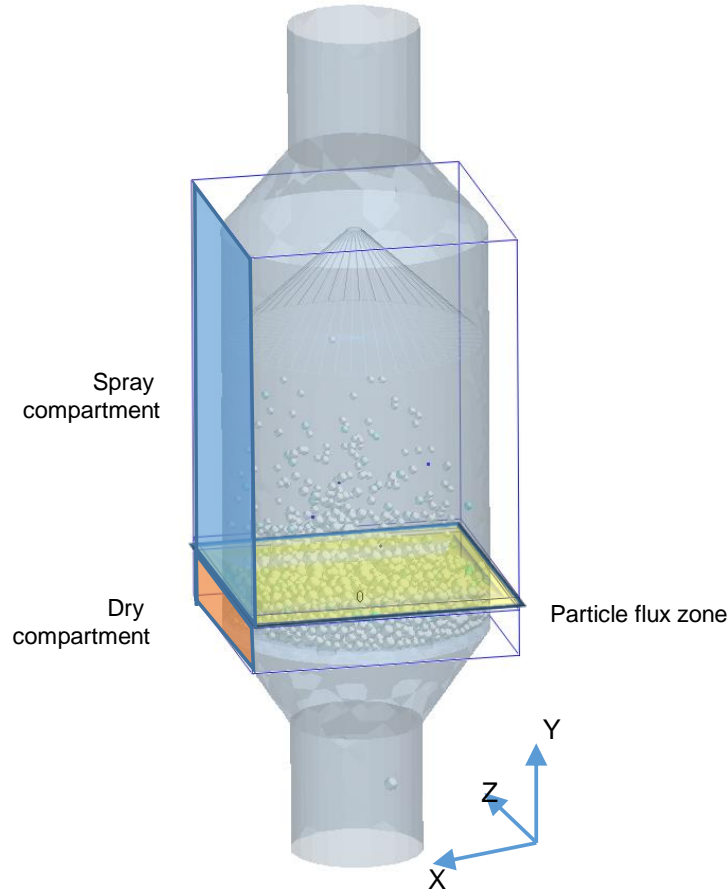


Figure 5.4: Schematic diagram of the two compartments in fluidized bed granulation.

$$\frac{\partial}{\partial t} F(s, l, g, t) + \frac{\partial}{\partial l} \left[F(s, l, g, t) \frac{dl}{dt} \right] + \frac{\partial}{\partial g} \left[F(s, l, g, t) \frac{dg}{dt} \right] = \Re_{aggregation} \quad (5.2)$$

Here, $F(s, l, g, t)$ represents the population density function in terms of the solid (s), liquid (l) and gas (g) volumes. The partial derivative terms with respect to l and g represent the growth terms-liquid addition and consolidation respectively. The consolidation and liquid addition rate expressions developed by Chaudhury et al. (2015a,b, 2013b) were implemented in the model. Since the DEM-CFD simulations were carried out without drying kinetics, the breakage subprocesses which depends on the rupture of solidified binder bridges from fluidized bed agitation was not considered in this study.

The mechanistic information for the fluidized bed granulation is captured by the $\beta(s', s, l', l, g', g)$ term which represents the size-dependent aggregation kernel which

incorporates the product of collision frequency (C) and collision efficiency (ψ) between two particle size classes (Equation 5.3) (Barrasso et al. (2013)) Since particles in PBM can only exist within a fixed number of size classes spaced with respect to volume bins, this simplified version of aggregation assumes that the rate change of number of particles in (s, l, g) and (s', l', g') classes are dependent on the number of collisions occurring between these particle types and a tuned collision efficiency term.

$$\beta(s, s', l, l', g, g', t) = C(s, s', l, l', g, g', t)\psi(s, s', l, l', g, g', t) \quad (5.3)$$

Details of the collision frequency and efficiency calculations using number of collisions between particle types over a time interval and number of particles is presented in detail in authors previous work (Barrasso and Ramachandran (2015)). Estimations of the collision frequencies are carried out through extraction of collision numbers from the coupled DEM-CFD simulations.

During fluidization, particles are continuously moving from the dry compartment to the spray compartment and vice versa which causes the inhomogeneity in liquid distribution. In order to effectively capture this behavior in the two compartmental PBM, a transfer rate between the two compartments must be established. Moreover, since the transfer rate of each size class of particles can be drastically different from others due to the varied drag forces experienced by the powder, a size dependent transfer rate was implemented for each compartment. Equation 5.4 and 5.5 were used to calculate the updated number of particles in each compartment (F_1 for spray zone and F_2 for dry compartment) using transfer rates from lower to upper (φ_1) and from upper to lower compartment (φ_2) rates. The units of the transfer rates are in particles/particle-s.

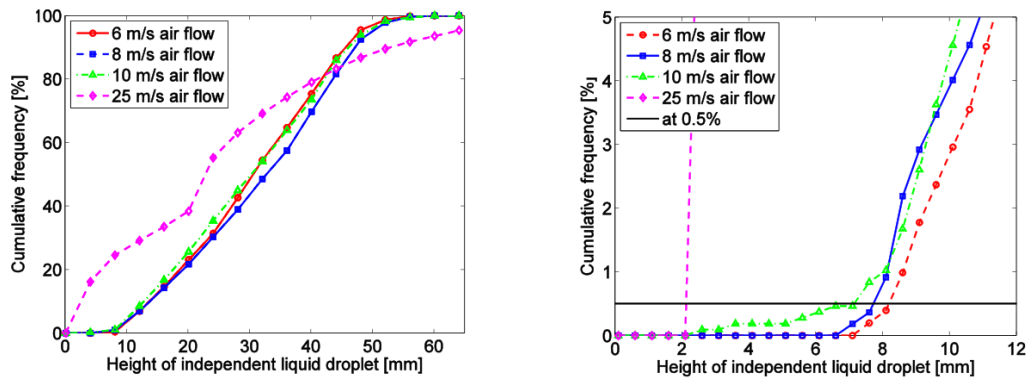
$$\frac{dF_1}{dt} = \varphi_1 F_2 - \varphi_2 F_1 \quad (5.4)$$

$$\frac{dF_2}{dt} = \varphi_2 F_1 - \varphi_1 F_2 \quad (5.5)$$

5.2.3 Coupling of CFD-DEM outputs into PBM

In this framework several mechanistic data including liquid distribution, particle flux, collision information as well as spatial location of particles were extracted from CFD-DEM simulations and coupled appropriately with PBM calculations. Broadly there are four major coupling operations performed: liquid distribution was analyzed to determine the spray compartment volume, particle velocity data was investigated to estimate inter-compartmental particle transfer rate, spatial location of particles were utilized to calculate fraction amount of particles in each zone, and finally, particle-particle collision information was extracted to measure the size dependent collision frequency values.

Utilizing the DEM's custom built liquid droplet model, the separation between the active sprayed compartment and the dry compartment was determined by analyzing free liquid droplets present in the system. Since the liquid droplets were custom coded to disappear upon collision with a solid particle, the presence of independent liquid droplets provides good insight into the penetration capability of the liquid spray. By temporally marking the lowest height at which free liquid droplets are present, the partition of active spray zone and dry zone was established. A representative schematic of the spray and dry compartment in DEM is illustrated in Figure 5.4.



(a) Entire plot of liquid distribution

(b) Rescaled plot to determine the separation between the compartments

Figure 5.5: Determination of height of dry compartment using position of free liquid droplets from DEM-CFD simulation.

In this study, the dry compartment was specified as the zone in which only 0.5% of

the total free liquid droplets are present. Due to the scaled-down number of particles present in the DEM-CFD simulations (around 7000 individual particles) and the height at which the nozzle is located (60mm above distributor plate), the fluidized powder bed simulated in this project are rendered very porous and thus spray compartments are much larger than dry compartments. Figure 5.5a shows the plot of cumulative frequency (which indicates fraction of liquid droplets) versus height (in +Y direction) of the droplet in the granulator. The results for different air flow rates show that as the fluid flow increases, more liquid droplets can reach lower heights. This behavior matches expectation since with increase in air flow, the fluidization of bed increases which leads to a drastic increase in bed void space. This allows more liquid droplets to pass through compared to under-fluidized beds which have a more compact bed structure. This is clarified in the rescaled plot of Figure 5b where the height at which only 0.5% of the sprayed liquid droplet remains is large (for 8.2 mm) for 6 m/s (i.e. under-fluidized bed) and gets narrower for higher flow rates. For 25 m/s air flow rate, which is a more turbulent type of fluidization, liquid droplets almost reach the bottom of the particle (2 mm above distributor plate). The height of the lowest free liquid droplet, thus obtained, can then be directly used to estimate reasonable compartment sizes for the PBM processes. By accounting for the effect of air flow rate on spray zone location, a mechanistic information is supplied through CFD-DEM simulations to PBM.

Another important PBM-DEM-CFD coupling operation carried out was to specify the fraction of total particles in each individual compartment. This information is critical in calculations for the total number of particles in spray and dry zone i.e. F_1 and F_2 values as well as the transfer rates (φ_1 and φ_2) between compartments.

Since CFD-DEM simulations keep track of the spatial location of every particle, the fraction data can be readily ascertained from these simulations, as shown in Figure 5.6. After setting up the boundary between the two zones using the liquid distribution data, the number of particles in each compartment can be extracted and forwarded to PBM calculations. In the figure, the number of particles in the upper spray zone is seen decreasing with time due to the randomized positioning of initial particles during

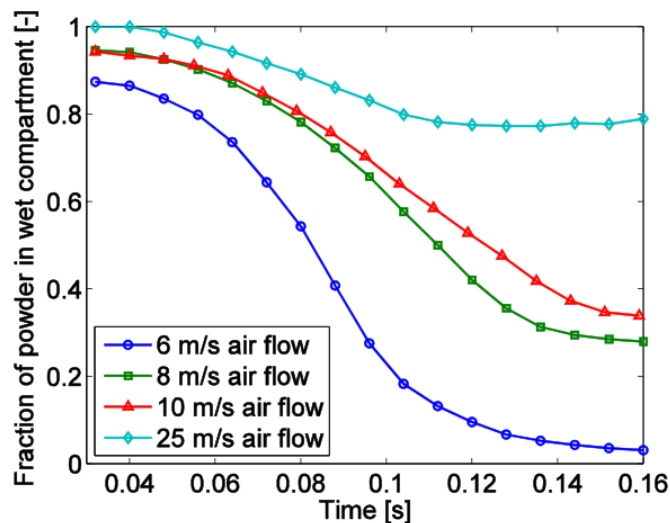


Figure 5.6: Fraction of total powder particles in spray/wet zone over time.

the start-up of the DEM simulation. When particles are first introduced in DEM (at $t=0.3s$), they are randomly distributed over the granulation chamber. As gravitational forces and fluid field forces balance out to reach fluidization, a steady level of powder fraction in wet compartment is observed after some time. This steady level of powder fraction data was used to confirm whether the particle bed had fluidized or not. As expected, with higher air flow rate, the fluidization state is achieved at a higher fraction of powder in the spray compartment than for lower air flow rates.

Additionally, the fraction of particles in each compartment data was also used to calculate the transfer rates between the two regions. The φ_1 and φ_2 values were evaluated using the particle velocity information from the DEM-CFD simulations and the total number of particles in each compartment. By recording the number and velocity of particles in the particle flux zone (which is the boundary between the two compartments; see Figure 5.4) during the steady fluidization period, an estimation of the transfer rate values can be made. The total number of particles with $+Y$ and $-Y$ velocities in the particle flux zone for a time interval chosen for PBM (0.1s). The φ_1 and φ_2 values are then determined by dividing them by total number of particles in dry compartment and wet compartment respectively.

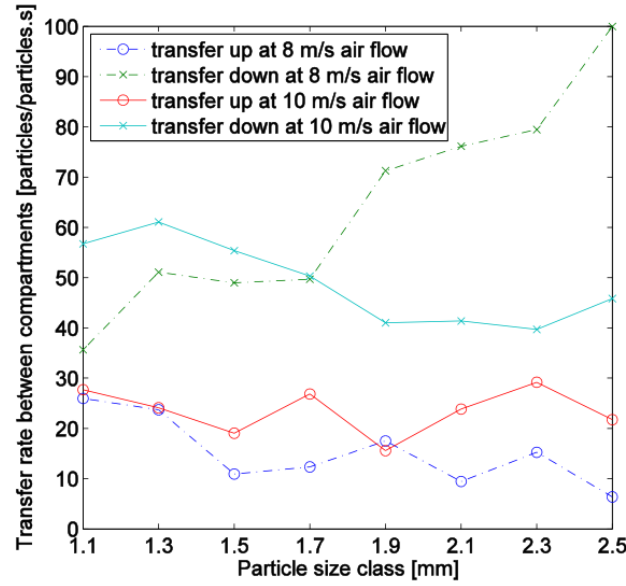


Figure 5.7: Size-dependent transfer rate of particles between the two compartments.

Figure 5.7 shows the size dependent transfer rates for two different air flow conditions: 8m/s and 10m/s. Results show that transfer down rate (i.e. from top to bottom compartment) is generally larger than the transfer up rate (i.e. from dry to wet compartment). A possible explanation for this is the increasing volume of particles as liquid is sprayed; the constant air flow cannot support the increasingly heavier particles and thus they fall more rapidly than dry particles can be lifted. The values obtained from CFD-DEM also capture the size-dependent nature of transfer rate as smaller particles have higher transfer up rate than larger particle. Additionally, a distinct effect of air flow on transfer rate is also observed: at air flow rates close to estimated minimum fluidization velocity (8 m/s) the turnover rate of particles is high indicated by the large gap between transfer up and transfer down values. This trend indicates that a majority of the particles that were wetted in the spray compartment are transferring to the drying compartment. For the larger air flow rate condition, the turnover rate is less pronounced suggesting that fewer wet and dry particles are moving between the compartments. This transfer rate discrepancy has a significant role in the granulation behavior as discussed in the results section.

Finally, CFD-DEM simulations were also used to enumerate the collision events during the granulation process. Figure 5.8 below illustrates the collision frequencies

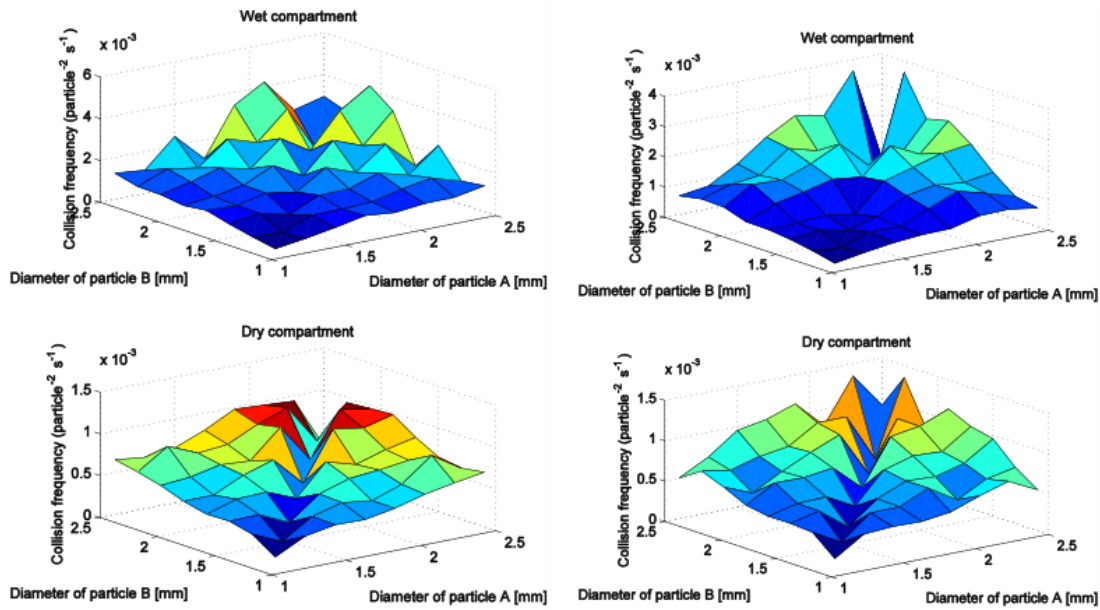


Figure 5.8: Collision frequency plot for 8m/s air flow rate (left column) and 10m/s (right column). Spray or wet compartments are illustrated in top row and the dry compartment are shown in the bottom row.

observed for 8 m/s and 10 m/s air flow rate conditions. Since the collision frequency is related to the packing of the particles and the interstitial space between particles, the colliding particle sizes and air flow rate (which affects apparent bed height) have a discernible impact on the frequency values. Results indicate that the frequency of particle collisions is generally 2 to 4 times larger in the spray(wet) compartment than in the dry compartment. This disparity can be attributed to the differences between the sizes of the spray and dry compartments: since the spray compartment is much larger, a significantly large number of collisions is stochastically observed in this region. Another important trend discernible in the collision frequency plot is the augmented frequencies for larger particle collisions, as shown by peaks in the rear portion of the surface plots. This trend is also expected since larger particles with larger surface areas are likely to collide more often with surrounding particles than fine powder. These size-dependent collision frequency values were used in the aggregation kernel (Equation 5.3) where the

aggregation rate (β) is a product of collision frequency and collision efficiency.

5.3 Model Results and Discussion

The multi-dimensional coupled PBM-DEM-CFD framework thus developed was used to simulate 15 seconds of granulation for two levels of CPPs: air flow rates (8m/s and 10m/s) and liquid addition rates (0.07 ml/s and 0.036 ml/s). CFD-DEM simulation of 7000 particles were performed for 0.25s, which requires approximately 15h of computational time on a Dell Precision T1650 computer with Intel Core i7-3770 CPU (3.4GHz and 32 GB RAM) using 8 processors. The computation time of simulating 15s of PBM is approximately 6 min. The main CQAs obtained from the model are PSD, median diameter (d_{50}) and the average liquid content of particles in each compartment.

5.3.1 Effect of liquid addition and air flow on particle diameter

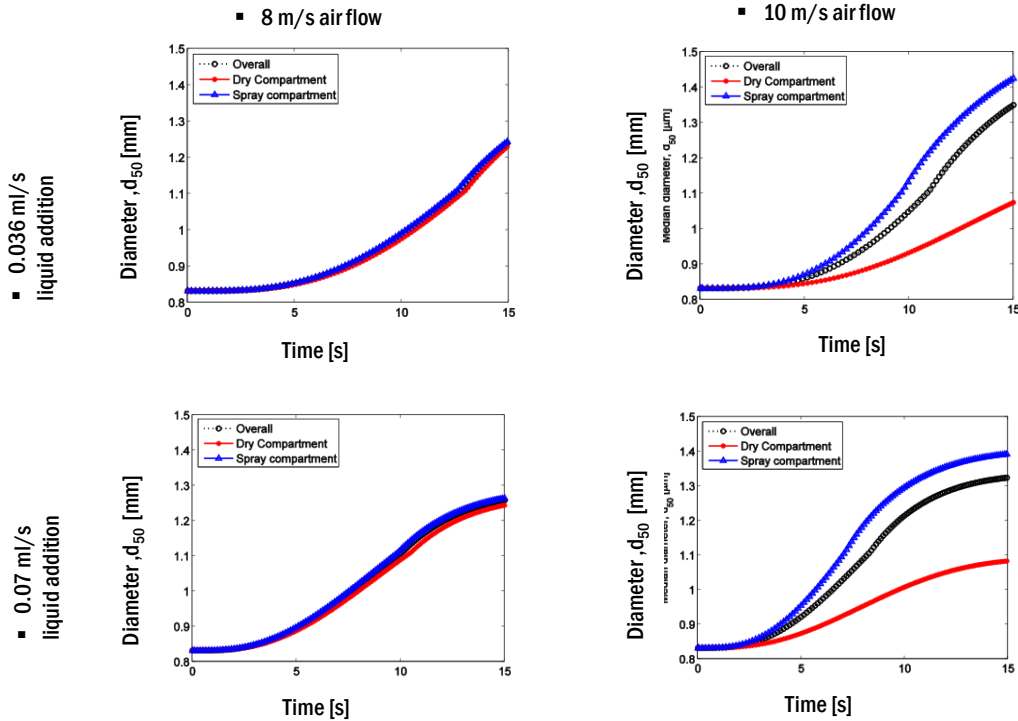


Figure 5.9: Median particle diameters (d_{50}) for different process parameters over time. Air flow rates are separated through columns and liquid addition rate are divided into different rows.

Figure 5.9 highlights the effect of liquid addition and air flow rate conditions on the d_{50} values for each compartment as well as an overall value. One of the most obvious trends seen in the figure is the inhomogeneous mixing of particles in the two compartments for the 10m/s air flow rate. This contrast is very likely due to the difference in particle transfer rates observed for the two air flow rate conditions: with the increased fluid flow, the turnover rate between the compartments is reduced (as shown in Figure 5.7) causing a segregation of particles in the wet and dry zones. The particles that remain in the spray compartment thereby receive larger amount of binder and aggregate actively. For 8 m/s airflow rate, on the other hand, due to the increased turnover rate, the difference in the mean diameter values for the two compartments are negligible. The effect of increasing the liquid spray rate can be seen only on the initial growth rate of particles. In Figure 5.9, for lower liquid spray rate (top row), the d_{50} values at $t=5s$ is about 0.85 mm while the same for higher liquid spray rate (bottom row) is approximately 0.9 mm to 0.95 mm depending on the air flow rate. With larger binder addition rate, the moisture content of the particles in the spray compartment increases rapidly. Thus, more collisions of these wetter particles end successfully in agglomeration leading to faster granule growth.

5.3.2 Effect of liquid addition and air flow on average liquid content

The effect of process parameters on the average liquid content of particles is shown in Figure 5.10. The inhomogeneous compartmental distribution observed for higher air flow rate in terms of particle diameter is also apparent in average liquid content values. Results show that increasing the air flow rate from 8 m/s to 10 m/s starts to split the amount of binder liquid accessible by each compartment. As the miniscule water droplets are dragged along by the strong bulk air motion, the amount of liquid available for solid particles in the underlying dry compartment decreases. This difference continues to increase as granulation proceeds further since the turnover rate of wetted particles between compartment decreases for the higher air flow. In terms of liquid addition rates, as expected, increasing the liquid spray rate shows proportional increases to the average liquid content over the entire size classes. For instance, the

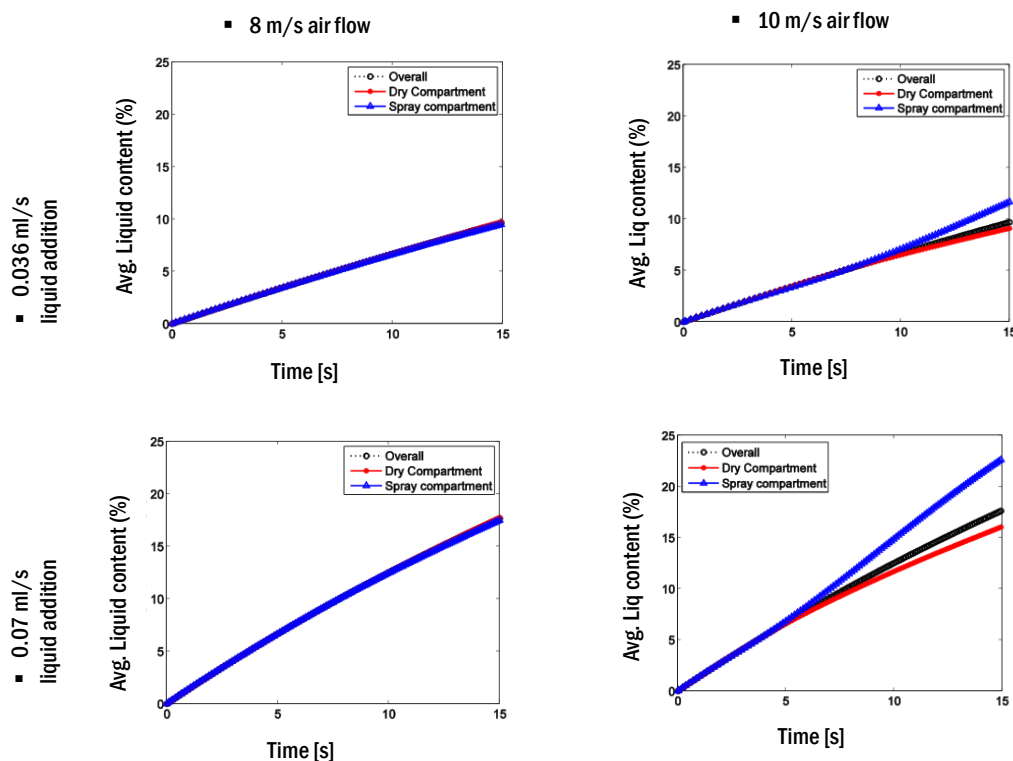


Figure 5.10: Average liquid content in each compartment for different process parameters over time. Air flow rates are separated through columns and liquid addition rate are divided into different rows.

average liquid content for 0.036ml/s liquid addition rate (top row) at $t=15s$ is around 10% while that for 0.7ml/s rate is above 15%.

5.3.3 Effect of liquid addition and air flow on particle size distribution

The effect of CPP on the liquid content and d_{50} values are coupled in the PBM outputs of fluidized bed granulation PSDs. As mentioned earlier, with the increase in air flow rate, the transfer rates of particles between compartments decreases significantly leading to inhomogeneous particle size distribution. This phenomenon is observable in the differences between PSDs with 8m/s and 10m/s air flow rate shown in Figure 5.11. The size distribution of particles for 8 m/s almost overlap each other while those of the 10m/s air flow rate are distinct. The particle size distribution for the 10m/s flow rate (right column in Figure 5.11) shows greater presence of larger particles in the spray compartment. Additionally, the effect of increasing liquid addition rate is also

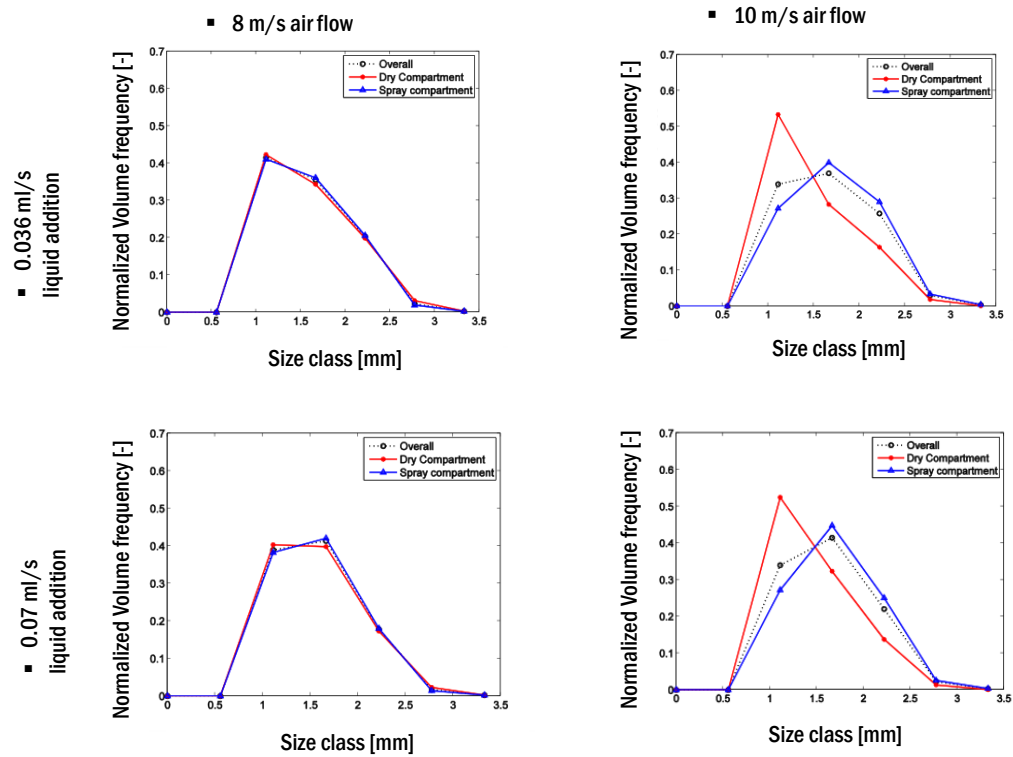


Figure 5.11: Final particle size distribution for different process parameters. Air flow rates are separated through columns and liquid addition rate are divided into different rows.

distinguishable in the PSD in terms of elevated volume frequency values for the larger particle sizes. As the moisture content increases in the particle bed, more collisions end successfully into agglomeration which leads to granule growth. When comparing the top row of PSDs in Figure 5.11 with the ones in the bottom with a larger liquid rate, the total amount of larger particles (1.5mm and above) present in the final powder bed are increasing while the fine powder amount is shrinking.

5.4 Conclusion

This paper exhibits a hybrid, mechanistic methodology to capture the granulation dynamics in a fluidized bed using multi-dimensional two compartmental PBM which has been coupled with DEM-CFD. Using DEM-CFD simulations not only allows for better reproduction of the inhomogeneities in liquid distribution, but also provides a plethora of mechanistic data such as collision frequencies, particle velocities, etc. that are not

inherent in the stochastic PBM kernels. The DEM-CFD model implemented in this framework utilizes liquid spray dynamics to divide the wet and dry compartments in the PBM; critical particle transfer rate values between the compartments are also obtained from these simulations. Additionally, inclusion of custom DEM contact models that simulate liquid absorption into solid particles and mimic the capillary forces between wet particles further reinforces the mechanistic nature of the model. Initial results of the framework are promising and demonstrates that the proposed multi-scale hybrid model can be successfully coupled as described.

The main objective of this work was to provide a proof-of-concept and basis of comprehensive model development for fluidized bed operation; hence the size and scale of the simulations were contracted for computational efficiency. Future work includes scale up of the model to manufacturing level and subsequent validation of the model through corroboration with industrial data. Industrial experimental methodology which are conventionally organized as factorial forms of Design of Experiments (DoE) need levels of CPPs as dependent variables and CQAs as process outputs. The current framework has proven to be able to establish a design space linking these key parameters as well as to take in the geometry and formulation effects into consideration.

Another major future work for the framework could be development of efficient reduced order models (ROMs) from the DEM-CFD data to substantially decrease the simulation time. Previous studies by the authors Barrasso et al. (2014) have verified the effectiveness of reduced order models in capturing high-fidelity of DEM simulations. Development of ROMs for the PBM-DEM-CFD framework should allow for iterative calculations required during parameter estimation and validation.

Chapter 6

Implementation and validation of a 3D CFD-DEM-PBM coupled top-spray fluidized bed wet granulation model

This chapter aims to provide a comprehensive description of the implementation and validation of a coupled CFD-DEM-PBM framework for a fluidized bed wet granulation operation. A two-way coupled CFD-DEM model is developed for a 3-dimensional, lab-scale, top spray fluid bed granulator to study the effects of process parameters such as inlet air flow rate and inlet air temperature on the particle flow dynamics and the residence time in the spray zone. A one-way transfer of data from CFD-DEM to PBM is then applied to relate the effects of particle-fluid interactions to granulation behavior occurring within the fluidized bed system. Mechanistic rate expressions were developed in the PBM to create links between CFD-DEM results and PBM rate kernels which can express the effect of critical process parameters (CPPs) such as air flow rate, inlet air temperature, binder spray rate, etc. to experimentally measured critical quality attributes (CQAs) including granule size distribution and liquid content values. From comparison with experimental results, the framework presented shows good accuracy at capturing the dynamics of the system. The presented framework demonstrates a practical process model development methodology by efficiently coupling multi-phase simulation techniques which can be used for effective process design, development and scale-up purposes.

6.1 Objectives

Recent investigations into developing modeling framework for an FBG have aimed at capturing the particle flow and aggregation mechanisms during the granulation process, however, not much attention is paid in linking critical process and formulation parameters to quality attributes. In Chapter 6, the development of a simplified hybrid CFD-DEM-PBM framework is presented to assess the feasibility of relating particle-level information to bulk particle properties. In this study, the development and validation of CFD-DEM-PBM multi-scale mechanistic framework of an FBG process is taken to a more advanced level. A realistic lab-scale fluidized bed system is used as a benchmark to simulate experimental conditions and assess the validity of model outputs. Similar to the simplified hybrid model, this study also utilizes a compartment-based PBM coupled with multi-phase CFD-DEM simulations to relate the effect of operating conditions to the granulation process. The main objectives of this work are summarized below:

1. Implement mechanistic rate expressions by creating links between CFD-DEM results and PBM rate kernels which can express the effect of critical process parameters (CPPs) such as air flow rate, inlet air temperature, binder spray rate, etc. to experimentally measured critical quality attributes (CQAs) including granule size distribution and liquid content values.
2. Validate the framework by quantitatively assessing the simulation results against experimental data

6.2 CFD-DEM-PBM Model Development

In this study, a hybrid framework to understand the fluid-particle dynamics of a fluid bed granulation system is presented. The formulation and solution of a multi-scale model for any process is complex due to the different length and time scales involved. Moreover, various model forms and scales must be efficiently integrated to relate formulation/material properties, processing conditions (CPPs) and equipment geometry at the micro/meso scale to the macro/application (CQAs) scale to extract maximum

benefit and applicability of the model. In this study, a two-way coupled CFD and DEM model is developed for a top-spray fluid bed granulator to study the effects of operating parameters on the particulate flow dynamics. A one-way transfer of data from particle-level CFD-DEM models to meso-level PBM is then applied to relate the effects of particle-fluid interactions to macro properties of the unit operation. The CFD-DEM simulations were developed in StarCCM+ ver. 11.06.010 (CD-adapco®), Siemens PLM Software, Inc) and the PBM calculations were performed using Matlab R2017b (The MathWorks, Inc). Figure 6.1 illustrates the schematic for the proposed multi-scale approach to FBG.

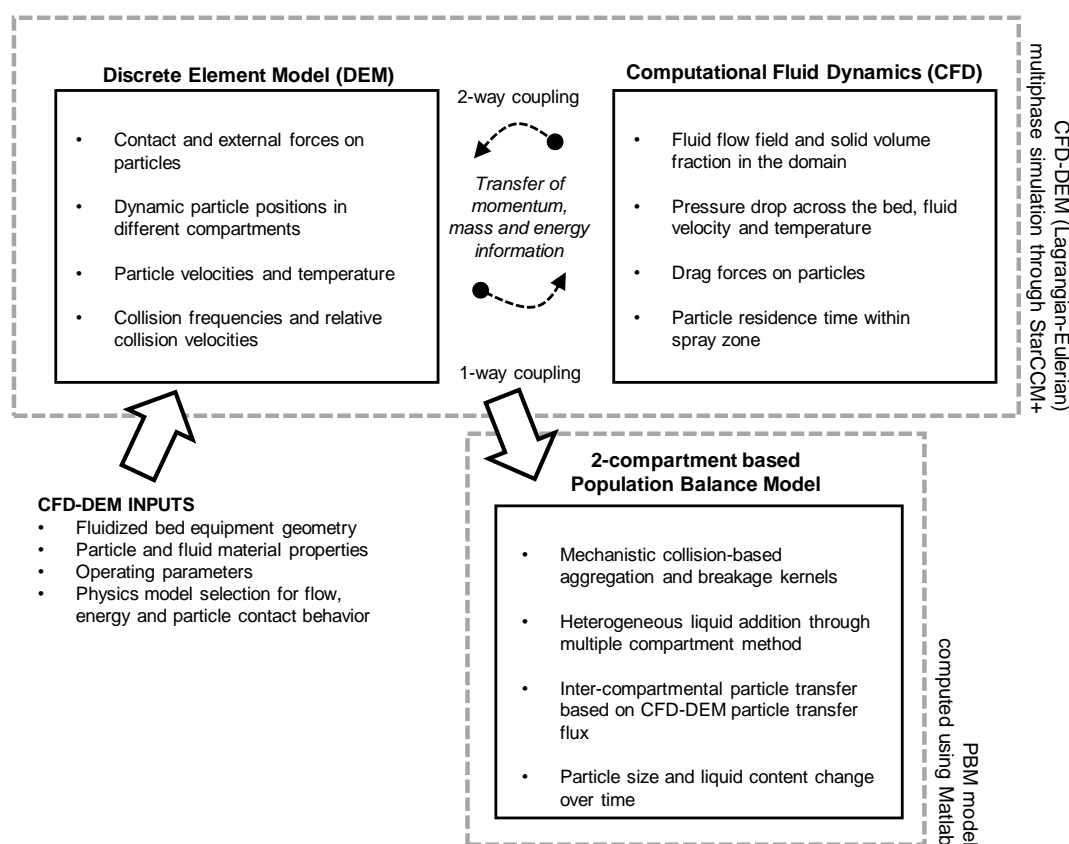


Figure 6.1: Schematic of the PBM-CFD-DEM multi-scale hybrid framework. Data transfer between Computational Fluid Dynamics (CFD) and Discrete Element Method (DEM) are coupled using a two-way approach while data from CFD-DEM are transferred one-way to a 2-compartmental Population Balance Model (PBM).

In the CFD-DEM simulations, the DEM calculates the position and velocity data

for each individual particle at each time step and the CFD provides the fluid flow profiles over fluid cells for the next time step. In general, the fluid phase is usually defined in CFD by the distribution of pressure, velocity, temperature and species concentration in the flow field. The dispersed solid phase is described in DEM by size, position, linear and rotational velocities, temperature and species concentration of each particle type. The inputs for the CFD-DEM simulation thus are the equipment geometry, material properties of the solid and fluid phases as well as the operating parameters. Different sub-models for particle contact behavior, fluid flow and energy transfer models are also selected. The fluid-particle interaction for the fluid phase is based on the total interactions per unit volume of the fluid cells, while the fluid-particle force for the solid phase is based on each individual particle. In the two-way coupled CFD-DEM approach used in this framework, the transfer of data between CFD and DEM goes both ways. As shown in Figure 6.1, there is an exchange of mass, momentum, and energy information between the solid phase and the fluid phase. The outputs of CFD-DEM simulations are particle positions, velocities, temperatures, collision events, inter-particle forces, and fluid flow field parameters at any moment of the simulation. Although these variables enable an in-depth investigation into the overall and local phenomena in the system, they are not easily accessible or relatable to experimental measurements. Thus, these simulation data are transferred to population balance models through mechanistic kernels that describe mixing and circulation of particle bed, aggregation and breakage of granules and liquid distribution profiles that can be used to compute experimentally measurable properties such as granule size growth.

6.2.1 System configuration

Figure 6.2 illustrates the equipment design for the CFD-DEM simulation - the geometry of the system is modeled after a top-spray fluid bed granulator, GPCG Fluid bed Dryer (Glatt Air Techniques Inc., Ramsey, NJ, USA). The 3D vessel design was created using the CAD module available in STAR-CCM+. The positioning and the angle of the spray zone cone were determined from the high-resolution spray zone pictures obtained from the FBG experimentation. For a tapered fluidized bed design, as shown in the figure,

the fluidization of granules can generally be divided into two regions: a dilute fluidized region (where bed expansion and mixing take place) and a dense lower region Sau and Biswal (2011). Since the particle flow, circulation, collision and wetting dynamics differ drastically within these two regions, a demarcation of the *Top* and *Bottom* compartments, as illustrated, were also carried out during post-processing. Mechanistic data regarding fluid flow and particle interactions were individually collected from the two compartments. These CFD-DEM results are used in the similarly-configured two compartmental population balance model to incorporate the rate processes in granulation as well as the particle transfer between the two regions.

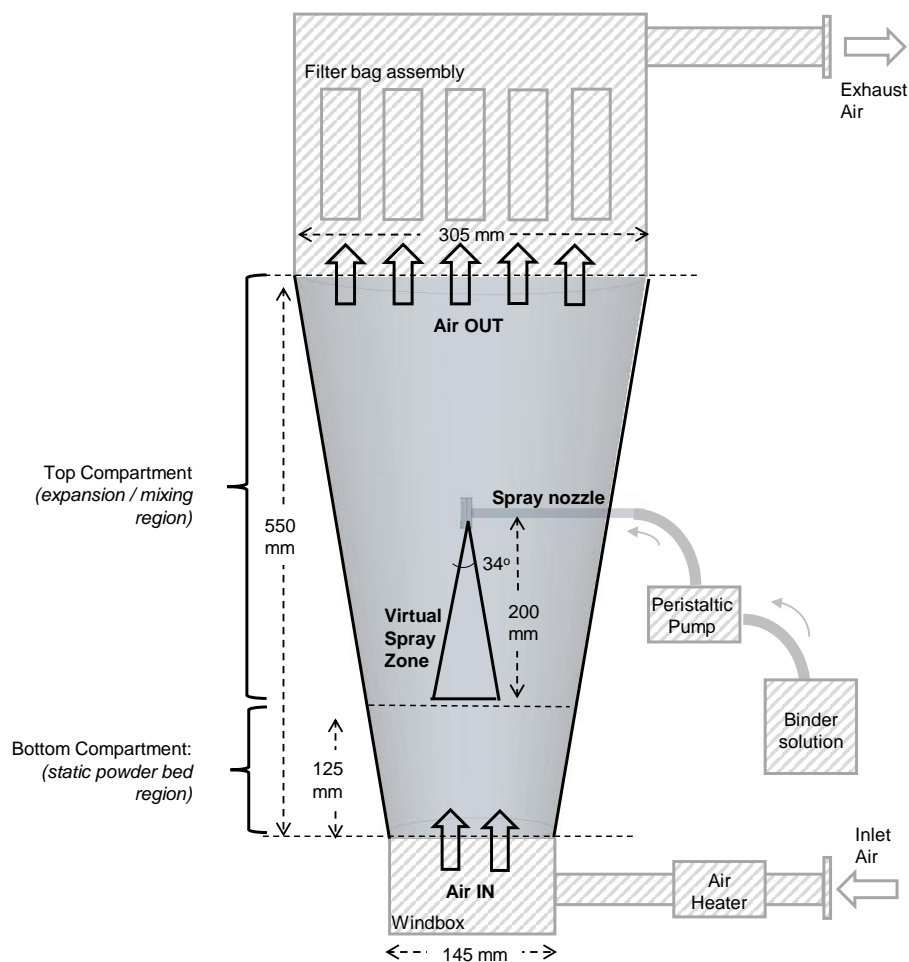


Figure 6.2: Geometry of the simulated fluidized bed granulator. The position of the virtual spray zone as well as the demarcation of the two PBM compartments are differentiated. For the CFD-DEM simulations, only the shaded portion of the schematic were rendered as the domain region.

Table 6.1 lists the system mesh, boundary and time-step configuration for the CFD-DEM simulations performed.

Table 6.1: Overview of CFD-DEM simulation configuration

Parameter	Value/Type
Mesh	
Type	Trimmer and Prism mesh
Total number of grid cells	84,830
Total number of interior faces	246,518
Total number of vertices	98,431
Boundary conditions	
Domain inlet - Fluid	Uniform mass flow inlet
Domain inlet - Solids	Phase impermeable
Domain outlet - Fluid	Constant atmospheric pressure
Domain outlet - Solids	Phase impermeable
Domain walls - Fluid	No-slip
Domain walls - Solids	stationary wall; zero stress
System	
Initial air velocity	0 m/s
Initial air temperature	293.15 K
Particle type	Spherical, mono-dispersed
Initial particle temperature	293.15 K
Initial static bed height	0.125 m
CFD time step	2×10^{-4}
DEM time step	1×10^{-6}
Total simulation time	10 s
Convergence criterion	10^{-3}

In terms of the CFD flow calculations, mesh independence and convergence stability test were performed at the start of the CFD design by running several trial simulations to ensure that the convergence of residual error as well as the CFD solution (pressure drop, particle velocities, collision frequencies) between multiple mesh sizes and time-steps were comparable. In the simulations presented, Trimmer volume mesh scheme with a base size of 5 mm has was used. For a better resolution of flow field near the walls, a Prism layer mesh - which decreases the cell size at the walls - was also added to the domain. The final meshing and time step configuration were selected to keep the computational load low.

At the start of each simulation, the air inside the fluidized bed domain were set to an initial velocity of 0 m/s and an initial temperature of 293.15 K. The particles generated within the system were also set at temperature of 293.15 K and allowed to completely settle down. Once the kinetic energy of the particles reached zero, air flow

was initiated at the target flow rate to fluidize the bed.

6.2.2 System scaling

The computational load of high-fidelity simulations such as CFD-DEM increase drastically with the increase in the number of particles Börner et al. (2017); Amritkar et al. (2014); Alobaid et al. (2013); Gopalakrishnan and Tafti (2013). This inflation in the computational complexity is generally due to the calculation of computationally expensive contact detection algorithm, and the solid-phase time step limitations to resolve the particle interactions via collisions. As a result, it is generally understood that a system scaling approach must be undertaken to render the simulations feasible and within a reasonable time scale. One of the most promising methods of reducing the computational load of the system is the *similarity model* approach which entails reducing the total number of particles within the system while maintaining the process dynamics. In this approach, in order to ensure that similarity in fluid mechanics is maintained, critical dimensionless numbers such as particle Reynolds number (Re_p) and Archimedes number (Ar) are kept constant across the system scales. Similar scaling methods have been successfully adapted in literature by Börner et al. (2017) and Link et al. (2009) where comparison of experimental results agree with the particle hydrodynamics in the scaled systems.

For this study, a similarity model scaling of the system was carried out by keeping the minimum fluidization velocity, particle Reynolds number and Archimedes number as constants while scaling the granule size. The original system scale is derived from the experimental conditions with batch size of 2 kg, particle diameter of 885 μm and particle density of 1670 kg/m^3 . In order to reduce the computational time to a reasonable limit, the number of particles required for the simulation was reduced from 3.3 million to 40,000 while keeping the total particle volume constant. The similarity scaling approach is summarized as follows:

1. The Archimedes number (Ar) for the original system, which is used to describe the motion of fluid due to density differences, is first calculated using the ratio of

gravitational forces to viscous forces using Equation 6.1 Rhodes (2008):

$$Ar = \frac{gd_p^3(\rho_p - \rho_g)}{\gamma_g^2 \rho_g} \quad (6.1)$$

where g , d_p , ρ_p , ρ_g and γ_g are respectively gravity, particle diameter, particle density, gas density and gas kinematic viscosity.

2. For gas fluidization with granules larger than $100 \mu m$, the particle Reynolds number Re_p at minimum fluidization velocity can be calculated using the Wen and Yu empirical correlation Wen and Yu (1966):

$$Re_p = 33.7 [(1 + 3.59 \times 10^{-5} Ar)^{0.5} - 1] \quad (6.2)$$

3. The minimum fluidization velocity (U_{mf}) can then be determined by rearranging the particle Reynolds number expression at minimum fluidization velocity as follows:

$$Re_p = \frac{d_p U_{mf} \rho_g}{\mu_g} = \frac{d_p U_{mf}}{\gamma_g} \quad (6.3)$$

where μ_g is the dynamic viscosity of gas. Thus,

$$U_{mf} = \frac{Re_p \gamma_g}{d_p} \quad (6.4)$$

4. In order to maintain similar bed height between systems, the total volume of particles was kept constant while increasing the particle size. For the new system, the scaled diameter of the particles can then be derived from total volume conservation as follows:

$$d_{p,2} = \left[\frac{6 \cdot m_{bed,1}}{\rho_{p,1} \cdot N_2 \cdot \pi} \right]^{\frac{1}{3}} \quad (6.5)$$

where $m_{bed,i}$, N_i , $\rho_{p,i}$, $d_{p,i}$ denote total mass of particle bed, number of particles, particle density and particle diameter respectively. The subscript i can be 1 or 2 representing the original and scaled systems respectively.

5. The scaling factor between the two systems is represented by k_c :

$$k_c = \frac{d_{p,2}}{d_{p,1}} \quad (6.6)$$

6. For both systems, the gas density ρ_g and the gravity term g are held constant.
7. The scaled kinematic viscosity of gas ($\gamma_{g,2}$) can then be calculated from the conservation of U_{mf} and Re_p :

$$\gamma_{g,2} = \left(\frac{d_{p,2}}{d_{p,1}}\right)\gamma_{g,1} = k_c\gamma_{g,1} \quad (6.7)$$

8. The reduced density of particle $\rho_{p,1}$ derived from the conservation of Ar is given by:

$$\rho_{p,2} = \left(\frac{1}{k_c}\right)(\rho_{p,1} - \rho_g) + \rho_g \quad (6.8)$$

Overall, the particle diameters in the new simulation system are scaled up roughly 4.5 times than actual size to reduce the computational load of the simulation while also making sure that the grid size for the CFD calculations is small enough to get an accurate solution. The system parameters in the original and scaled system are provided in Table 6.2.

The validity of the scaling approach was further examined by investigating the dimensionless Stokes number (St) and drag coefficient (C_D) of the particle-fluid flow. At low Reynolds number, the St value is given by Equation 6.9 Börner et al. (2017). The C_D parameter was calculated using the Gidaspow drag coefficient model given by Equation 6.11 with the void fraction (ϑ_f) assumed as 0.8 (low concentration) Gidaspow

Table 6.2: Particle and fluid properties used for the scaled system in the CFD-DEM simulations

Parameter	Original	Scaled
Number of particles (N_p)	3,299,781	40,000
Scaling factor (k_c)	1	4.35
Particle diameter (d_p), [m]	8.85×10^{-4}	3.85×10^{-3}
Particle density (ρ_p), [kg/m ³]	1670	385
Gas kinematic viscosity (γ), [m ² /s]	1.60×10^{-5}	6.97×10^{-5}
Mass of bed (m_{bed}), [kg]	2	0.46
Total particle volume (Vol), [m ³]	1.20×10^{-3}	1.20×10^{-3}
Gravity (g), [m/s ²]	9.8	9.8
Gas density (ρ_g), [kg/m ³]	1.184	1.184
Archimedes number (Ar)	3.74×10^4	3.74×10^4
Minimum fluidization velocity (U_{mf}), [m/s]	0.323	0.323
Particle Reynolds number (Re_p)	17.88	17.88
Stokes number (St)	44.42	44.42
Drag coefficient (C_D)	6.33	6.33
Terminal velocity (u_t), [m/s]	4.538	4.538
Drag Force (F_D^*), [N]	2.41×10^{-7}	4.56×10^{-6}

(1994). The corresponding drag forces (F_D^*) are calculated from Equation 6.10 where A_p is the projected area of the spherical particle calculated as $\frac{\pi d_p^2}{4}$ McCabe et al. (2005). As shown in Table 2, the independently calculated theoretical values of St and C_D for the two scales show a close match: St for both systems are around 44.42 and similarly, drag coefficients are around 6.33.

$$St = \frac{F_D^*}{\gamma \rho_g d_p U_{mf}} \quad (6.9)$$

$$F_D^* = \frac{1}{2} C_D \rho_g A_p U_{mf}^2 \quad (6.10)$$

$$C_D = \begin{cases} \frac{4}{3} \left(150 \frac{1-\vartheta_f}{Re_p} + 1.75 \right) & \text{if } \vartheta_f < \vartheta_{min} \\ \frac{(24+3.6+Re_p^{0.687})}{Re_p} \cdot \vartheta_f^{-3.65} & \text{if } \vartheta_f \geq \vartheta_{min} \end{cases} \quad (6.11)$$

where, ϑ_{min} is the cutoff void fraction (typically 0.8).

In addition, the flow dynamics away from U_{mf} were also compared by determining the theoretical terminal velocity of the particles (u_t) using Equations 6.12. Calculations

show that both in original and scaled system, the theoretical terminal velocity for particles is around 4.53 m/s .

$$u_t = \frac{gd_p^2(\rho_p - \rho_g)}{18\gamma\rho_g} \quad (6.12)$$

6.2.3 CFD-DEM model equations

In the CFD-DEM two-way coupled framework, the CFD algorithm solves the volume averaged conservation equations in all the cells in the fluid flow domain while the coupled DEM algorithm solves the conservation of particle momentum equations. The conservation of energy equation is solved by both DEM and CFD to resolve the temperature of both the continuous (fluid) and discrete (particle) phase. The volume-averaged equations solved by the flow and energy model over the fluid domain cells are provided in Equations 6.13, 6.14 and 6.15.

The continuity equation (conservation of mass):

$$\frac{\partial(\rho_f \varepsilon_f)}{\partial t} + \nabla \cdot (\rho_f \varepsilon_f \vec{u}_f) = 0 \quad (6.13)$$

where ρ_f is the fluid density, ε_f is the volume fraction of fluid in the cell and \vec{u}_f is the average velocity of the fluid phase.

The general Navier-Stokes equation (conservation of Momentum) for fluid phase:

$$\frac{\partial(\rho_f \varepsilon_f \vec{u}_f)}{\partial t} + \nabla \cdot (\rho_f \varepsilon_f \vec{u}_f \vec{u}_f) = -\varepsilon_f \nabla p - \varepsilon_f \nabla \cdot \overleftrightarrow{\tau}_f + \rho_f \varepsilon_f \vec{g} - \vec{S}_p \quad (6.14)$$

where $\overleftrightarrow{\tau}_f$ is the fluid phase stress tensor and \vec{S}_p is the sink term which denotes the volumetric mean of all the forces acting on the particle by the surrounded fluid in a fluid cell. The sink term here thus achieves the two-way coupling between the fluid and particle phase by including the drag force, fluid pressure force, shear stress forces and other possible fluid-particle interaction forces.

The conservation of energy equation for the fluid phase is provided in Equation 6.15:

$$\frac{\partial(\rho_f \varepsilon_f C_{p,f} T_f)}{\partial t} + \nabla \cdot [\vec{u}_f \varepsilon_f \rho_f C_{p,f} T_f] = \nabla \cdot (\varepsilon_f k_f^{eff} \nabla T_f) + E_f \quad (6.15)$$

where, $C_{p,f}$ is the specific heat capacity of fluid at constant pressure, T_f is the temperature of the fluid, k_f^{eff} is the effective thermal conductivity of the fluid, and E_f is the net rate of heat transferred to the fluid per unit volume, which includes rate of heat exchanged between fluid and particles, fluid and wall, heat generated through friction and from viscous forces.

In terms of the solid phase, the equations of motion for individual spherical particles are given by Equations 6.16 and 6.17 while the conservation of energy for a particle is provided in Equation 6.18:

$$m_i \frac{\partial(\vec{v}_i)}{\partial t} = \vec{F}_T \quad (6.16)$$

$$I_i \frac{\partial(\vec{\omega}_i)}{\partial t} = \vec{M}_T \quad (6.17)$$

$$m_i C_{p,i} \frac{\partial T_i}{\partial t} = E_p \quad (6.18)$$

where, m_i , \vec{v}_i , I_i , $\vec{\omega}_i$, $C_{p,i}$, T_i are respectively the mass, velocity, moment of inertia, angular velocity, specific heat capacity and temperature of the i^{th} particle. Similarly, the \vec{F}_T , \vec{M}_T and E_p terms are the net forces (contact, drag and body forces), the net torque (tangential, rolling and fluid rotational resistance torque) and the net rate of energy transferred to the particle i . It should be mentioned that in Equation 6.18 the inner thermal resistance of particles is neglected, and a uniform temperature is assumed within the particle (i.e. Biot number $\ll 1$).

DEM Particles Model: In terms of simulating the solids, the dispersed Lagrangian phase particles are modeled as soft spheres (where particle overlap is allowed) by using the *DEM Particles* model. The DEM here is implemented within the Lagrangian framework and uses Lagrangian phase model to define the particles. In this approach, the net force acting on the particles are first accounted for by a summation of contact forces (particle–particle and particle–wall contacts) and external forces (gravity,

drag force) acting on individual particles (Equation 6.19). The net force is then used to calculate the acceleration of the particle by Newton's 2nd law and compute the new velocity and position profile. Mathematically:

$$\vec{F}_T = \vec{F}_n + \vec{F}_t + \vec{F}_g + \vec{F}_d \quad (6.19)$$

where, \vec{F}_T is the net total force on the particle; \vec{F}_n and \vec{F}_t are the contact forces in normal and tangential direction, \vec{F}_g is the gravity force and \vec{F}_d is the drag force acting on the particle.

The contact forces \vec{F}_n and \vec{F}_t determine how particles behave when they encounter each other or solid boundaries. In this framework, a simplified Hertz-Mindlin no-slip contact DEM phase interaction model was used to calculate these forces. The general expression for the Hertz-Mindlin model, which is a variant of the non-linear spring-dashpot contact model, are provided in Chapter 3, Table 3.2.

To calculate the F_d due to the viscosity-induced fluid resistance, the *Gidaspow* correlations (Equation 6.11) were used in this framework to calculate the drag coefficient (C_D). In fluidized beds, the flow of spherical particles can transition from the initial dense packing to low-volume fractions through the fluid phase. The *Gidaspow* method, which is a combination of Wen and Yu, and Ergun equations, provides a suitable approach to switch between low- and high-concentration flows *Gidaspow* (1994).

In order to incorporate the heterogeneity of particle wetting behavior during the binder spray, the residence time distribution of particles inside the virtual spray zone were also investigated in the CFD-DEM simulations via a *Passive Scalar* model approach. In this model methodology, a user-defined scalar variable of arbitrary value can be assigned to individual particles at each time step under the fulfillment of defined conditions CD-adapco (2016). To account for the residence time, particles passing through the mathematically defined space of the spray zone were tagged with the number of timesteps these particles were within the zone as the scalar value in this framework. Thus, if a particle stays inside the spray zone for 10 iterations, for instance, then the passive scalar model adds a 10 x DEM time step value to the residence time

of that particle. Moreover, if the same particle passes through the spray zone again, additional time steps are similarly added to its passive scalar value representing the residence time. It must also be mentioned that these passive scalar parameters do not affect the physical properties of the simulation and only track how long particles have passes through a specified region. The mean residence time of particles within the spray zone (τ_{spray}) was calculated using Equation 6.20.

$$\tau_{spray} = \int_0^{\infty} tE(t)dt \quad (6.20)$$

where, t is the time spent by the particle within the spray zone and $E(t)$ is the fraction of particles with the residence time t .

6.2.4 PBM model equations

A multi-dimensional PBM was used to track critical granule attributes such as granule size and liquid content. In order to specifically address the inhomogeneities present during fluidized granulation, a two-compartmental PBM was developed to represent the expansion/mixing zone (Top compartment) and the powder bed zone (Bottom compartment) in the granulator, as illustrated in Figure 6.2. The distribution of particles among the compartments is based on the average particle number information extracted from the CFD-DEM simulations. In addition, other mechanistic information such as particle flux between compartments, collision frequencies, collision energies, particle wetting, etc. were also calculated from the CFD-DEM simulations for each compartment. The general 3-D PBM equation is provided in Equation 6.21.

$$\begin{aligned} \frac{\partial}{\partial t} F(s, l, g, t) + \frac{\partial}{\partial l} \left[F(s, l, g, t) \frac{dl}{dt} \right] + \frac{\partial}{\partial g} \left[F(s, l, g, t) \frac{dg}{dt} \right] \\ = \mathfrak{R}_{aggregation} + \mathfrak{R}_{breakage} \end{aligned} \quad (6.21)$$

where $F(s, l, g, t)$ represents the population density function in terms of the solid, liquid and gas volumes represented with the variables s, l and g . As particles agglomerate, gain liquid content or compact over time, the changes to the granules' solid, liquid

and gas content are reflected through these 3-D bins. The partial derivative terms with respect to l and g represent the growth terms - liquid addition and consolidation. The $\mathfrak{R}_{aggregation}$ and $\mathfrak{R}_{breakage}$ are the source terms representing aggregation and breakage mechanisms respectively.

For each compartment, Equation 6.21 were run independently to calculate the population density functions, F_1 and F_2 for the top and bottom compartment respectively. At initial time point, the division of total particle mass between the top and bottom compartment were carried out based on average number of particles in each compartment spatially from the CFD-DEM simulations. In each compartment, the associated PBM accounts for the aggregation, breakage, liquid addition and consolidation mechanisms that are predominant in each of those regions.

Particle transfer: During fluidization, granules are continuously moving from the top compartment to the bottom compartment and vice versa which causes the inhomogeneity in liquid distribution. In order to effectively capture this behavior in the two compartmental PBM, a particle transfer rate between the two compartments was also determined by analyzing the CFD-DEM results regarding the particle flux at the interface between the compartments. Equation 6.22 and 6.23 were used to calculate the updated number of particles in each compartment (F_1 and F_2) using particle transfer rates from lower to upper (ψ_1) and from upper to lower compartment (ψ_2) respectively. The units of the transfer rates are in particles/particle-s.

$$\frac{dF_1}{dt} = \psi_1 F_2 - \psi_2 F_1 \quad (6.22)$$

$$\frac{dF_2}{dt} = \psi_2 F_1 - \psi_1 F_2 \quad (6.23)$$

Aggregation: During granulation, the principle size enlargement of particles occurs due to the aggregation of two or more particles to form a larger granule. Thus, the rate of change in number of granules in different size bins can be divided into (a) rate of formation of the particle from aggregation of smaller particles ($\mathfrak{R}_{agg}^{form}$), and (b) rate of depletion of smaller particles that were combined to make the larger granule (\mathfrak{R}_{agg}^{dep}). Mathematically, it can be expressed as:

$$\mathfrak{R}_{aggregation}(s, l, g, t) = \mathfrak{R}_{agg}^{form}(s, l, g, t) - \mathfrak{R}_{agg}^{dep}(s, l, g, t) \quad (6.24)$$

$$\mathfrak{R}_{agg}^{form}(s, l, g, t) = \frac{1}{2} \int_0^{s_{max}} \int_0^{l_{max}} \int_0^{g_{max}} \beta_{agg}(s', s - s', l', l - l', g', g - g') F(s', l', g', t) F(s - s', l - l', g', g - g') ds' dl' dg' \quad (6.25)$$

$$\mathfrak{R}_{agg}^{dep}(s, l, g, t) = \int_0^\infty \int_0^\infty \int_0^\infty \beta_{agg}(s, s', l, l', g, g') F(s', l', g', t) F(s, l, g, t) ds' dl' dg' \quad (6.26)$$

$$\beta_{agg}(s, s', l, l', g, g') = \beta_0 \cdot \theta_{cf} \cdot C_{P,1}(s, s', l, l', g, g', t) \cdot E_c(s, s', l, l', g, g', t) \cdot \eta_p(s, s', l, l', g, g', t) \quad (6.27)$$

where the two colliding particles are described by (s, l, g) and (s', l', g') . The particle-scale information for the fluidized bed granulation is captured by the aggregation kernel (β_{agg}) term which incorporates the product of collision frequency ($C_{P,1}$), collision energy (E_c) and the collision efficiency (η_p) between two particle size classes (Equation 6.27). The $C_{P,1}$ value, with units in collisions/particle.particle.s is extracted from the CFD-DEM data by dividing the total number of collisions (N_{col}) by the total number of particles in each compartment (F_i) in every time step (Equation 6.28). For the E_c term, a kinetic energy value is calculated based on the mass of the colliding particles (\hat{m}) and the relative collision velocity (\hat{v}) as shown in Equation 6.31. Since the aggregation rate is known to depend on the liquid binder content of the particles, a simplified η_p probability of either 0 or 1 based on a threshold liquid content value of the colliding particles is implemented in the system. As shown in Equation 6.32, the collision efficiency is 1 (successful agglomeration) only if either of the two colliding particles have minimum liquid content required for coalescence (LC_{min}).

$$C_{P,1}(s, s', l, l', g, g', t) = \frac{N_{col}(s, s', l, l', g, g', t)}{F(s, l, g, t) \cdot F(s', l', g', t) \cdot \Delta t} \quad (6.28)$$

$$\hat{m}_p(s, s', l, l', g, g', t) = \frac{m_p(s, l, g, t) \cdot m_p(s', l', g', t)}{m_p(s, l, g, t) + m_p(s', l', g', t)} \quad (6.29)$$

$$\hat{v}_p(s, s', l, l', g, g', t) = v_p(s, l, g, t) + v_p(s', l', g', t) \quad (6.30)$$

$$E_c(s, s', l, l', g, g', t) = \frac{1}{2} \cdot \hat{m}_p(s, s', l, l', g, g', t) \cdot \hat{v}^2(s, s', l, l', g, g', t) \quad (6.31)$$

$$\eta_p(s, s', l, l', g, g', t) = \begin{cases} 1, & \text{if liquid content of either particle} \geq LC_{min} \\ 0, & \text{otherwise} \end{cases} \quad (6.32)$$

Since the experimental data which is used to validate the framework also consists of additional experimental factors such as super-disintegrant amount and atomization air pressure (see Section 7.4) which is not modeled mechanistically in the CFD-DEM simulations, a correlation coefficient (θ_{cf}), is included in the β_{agg} term to account for the limitations in simulation data. The θ_{cf} coefficient is developed from the analysis of the experimental factors impacting the size growth (Pandey et al. Pandey et al. (2018)) as well as mechanistic information from CFD-DEM simulations as provided in Equation 6.33.

$$\theta_{cf} = 0.8 - 0.25 \cdot \hat{A} + 0.01 \cdot \hat{D} - 0.2 \Re_{Tp} + 0.2(\tau_{spray} * \dot{u}_{spray}) - 0.1(\Re_{Tp} - 1.01) \\ (\tau_{spray} * \dot{u}_{spray} - 4.68) \quad (6.33)$$

where \hat{A} is the nozzle atomization pressure (in *bar*), \hat{D} is amount of super disintegrant (in *wt%*), \Re_{Tp} is rate of change of particle temperature at a given inlet air condition (in *K/s*), τ_{spray} is the mean residence time of particles in the spray zone (*s*), and \dot{u}_{spray} is liquid addition rate (in *g/min*). Besides the \hat{A} and \hat{D} term, all other variables are extracted directly from the CFD-DEM simulations (more details in Results and Discussion section).

Breakage: When particles disintegrate due to collision impact or attrition under process conditions, granule breakage occurs. Very similar to the aggregation mechanism, the rate of change of number of particles due to breakage is composed of two terms: rate of depletion of larger granules ($\mathfrak{R}_{break}^{dep}$) and the rate of formation of smaller particles ($\mathfrak{R}_{break}^{form}$).

$$\mathfrak{R}_{breakage}(s, l, g, t) = \mathfrak{R}_{break}^{form}(s, l, g, t) - \mathfrak{R}_{break}^{dep}(s, l, g, t) \quad (6.34)$$

$$\mathfrak{R}_{break}^{form}(s, l, g, t) = \int_0^\infty \int_0^\infty \int_0^\infty \beta_{break}(s', l', g') \cdot b_{uni}(s', l', g', s, l, g) F(s', l', g', t) ds' dl' dg' \quad (6.35)$$

$$\mathfrak{R}_{break}^{dep}(s, l, g, t) = \beta_{break}(s, l, g) F(s, l, g, t) \quad (6.36)$$

$$\beta_{break}(s, l, g) = \beta_1 \cdot C_{P,2}(s, l, g) \cdot E_c(s, l, g) \cdot V(s, l, g) \cdot \left(\frac{1}{\theta_{cf}} \right) \quad (6.37)$$

Here, the (β_{break}) term represents the breakage kernel which incorporates the collision frequency ($C_{P,2}$), collision energy (E_c) and the size of the particles (V) to calculate the rate at which particles break. The collision frequency parameter for breakage ($C_{P,2}$) here is in units of collisions/particle-s. The $b_{uni}(s', l', g', s, l, g)$ term is the uniform probability distribution function which determines the volume bin for the broken particles. With the uniform probability distribution assumption, a parent particle is equally likely to break into sizes that can be described by each smaller bin size. Mathematically, the b_{uni} function for all for all $(s, l, g) < (s', l', g')$ is expressed as:

$$b_{uni}(s', l', g', s, l, g) = \frac{1}{(i-1)(j-1)(k-1)} \quad (6.38)$$

where i , j and k are the solid, liquid and gas bin numbers of the parent particles respectively. Similar to the aggregation constant, in order to account for other

experimental factors that can account for the granule size change in the system, the correlation coefficient (θ_{cf}) was also used in the breakage calculations.

Liquid addition: The liquid addition mechanism represents the spraying of the liquid binder through the top-spray nozzle during the wet granulation process. In this framework, a simplified assumption is made such that the total amount of liquid added to the compartment is distributed uniformly to all the particles within the same compartment. If spray rate of the binder solution is represented by \dot{u}_{spray} , the amount of liquid received by each particle will depend on the total number of particles within the system as given by Equation 6.39. In addition, an inhomogeneity in liquid spray rate for the two compartments is also integrated in this framework. Since the spray zone in the CFD-DEM simulation were present exclusively in the Top compartment, the total u_{spray} rate is assumed to be present only in the Top compartment. Thus, the amount of liquid gained by the Bottom compartment depends exclusively on the particle transfer between the two regions.

$$\frac{dl}{dt}(s, l, g, t) = \frac{\dot{u}_{spray} F(s, l, g, t)}{\int_0^\infty \int_0^\infty \int_0^\infty F(s, l, g, t) ds dl sg} \quad (6.39)$$

Consolidation: The compaction of the granules due to different process conditions results in the decrease of the porosity (ϵ) of the particles. In this study, the exponential decay of porosity developed by Verkoeijen et al. (2002) is used to calculate the rate of change of gas volume in the granules. The consolidation term $\frac{dg}{dt}$ is calculated as below:

$$\frac{dg}{dt}(s, l, g, t) = -\beta_{con} \left[\frac{(s + l + g)(1 - \epsilon_{min})}{s} \right] \left[l - \frac{\epsilon_{min} \cdot s}{(1 - \epsilon_{min})} + g \right] \quad (6.40)$$

It must be noted that other granule growth mechanisms such as nucleation and layering of fines do occur during the fluidized bed granulation. However, at the air flow rates being investigated in this framework – which are about 4-7 times larger than the minimum fluidization velocity – it can be assumed that these subprocesses are not going to be as dominant as the aggregation and breakage of granules. In addition, for the nucleation mechanism to occur the powder particles must meet droplets to form

nucleates. At high flow rates, droplets are most likely already deposited on particles (low droplet concentration) within the spray location thus limiting the nucleation rate. Literature studies such as Grünewald et al. (2007) have also shown that at high fluidization rates, the fines/dust residence time in fluidized bed are greatly reduced (larger entrainment in filters) thus limiting the solids layering rate.

6.3 CFD-DEM-PBM simulation design:

6.3.1 CFD-DEM simulations

In order to study the effect of fluidized bed operating parameters on the particle flow dynamics during granulation, multiple CFD-DEM simulations recreating the liquid addition phase of the experimental trials described in *Section 7.4* were carried out. The main goal of these simulations is to extract particle-level information during the binder spray phase of granulation which can be imported into PBM equations to link processing parameters to the dynamic granule size distribution. For the CFD-DEM simulations, 3 levels of inlet volumetric air flow rates (Q_g): $80 \text{ m}^3/h$, $110 \text{ m}^3/h$ and $130 \text{ m}^3/h$ spanning the range of experimental gas velocities used as well as 2 levels of inlet air temperatures (T_g): $303K$ and $323K$ were chosen in line with the experimental parameters. A total of six simulations were performed; the design space is presented in Table 6.3. The superficial gas velocity (V_0) for the corresponding Q_g are also provided. Other process factors including the binder spray rate, the nozzle pressure and the amount of super-disintegrant investigated in the experimental trials were not directly simulated in the CFD-DEM; an empirical relationship between these parameters and the granule growth mechanisms are implemented in the PBM portion of the framework.

Table 6.3: Design space for the CFD-DEM simulations

<i>Sim. #</i>	Q_g [m^3/h]	T_g [K]	V_0 [m/s]
1	80	303	1.3
2	80	323	1.3
3	110	303	1.9
4	110	323	1.9
5	130	303	2.2
6	130	323	2.2

Every CFD-DEM simulation in this study were performed in the transient mode for a total simulation time of 10s each. To ensure that all simulations were run under a quasi-steady state - in which the fluid/particle flow dynamics are time independent - the pressure drop across the FBG bed were monitored and compared with theoretical pressure drops expected. The theoretical pressure drops across the bed a fluidized bed system is given by McCabe et al. (2005):

$$\Delta P = (\rho_p - \rho_g) \cdot (1 - \epsilon_{mf}) \cdot g \cdot L \quad (6.41)$$

where ρ_s and ρ_g are the density of particle and gas respectively, ϵ_{mf} is the bed voidage at minimum fluidization and L is the height of the particle bed.

The CFD-DEM ΔP value for all inlet air flow rates are shown in Figure 6.3. The pressure drop across the bed for all trails are seen to be stably oscillating around the theoretically ΔP of 223.4 Pa - exhibiting a bubbling fluidization process. This is in agreement with the Geldart's group B classification of particles Geldart (1973). As seen in the simulation snapshots over time (Figure 6.4), gas bubbles are observable as soon as the fluidization occurs. Moreover, the bubbles are small at the bottom of the bed and grow with bed height. The simulation results, in addition, show that the particle bed expands roughly 1.8x to 2x to 2.5x fold from 80 to 130 m^3/h . This expansion comes mainly from the space occupied by the gas bubbles.

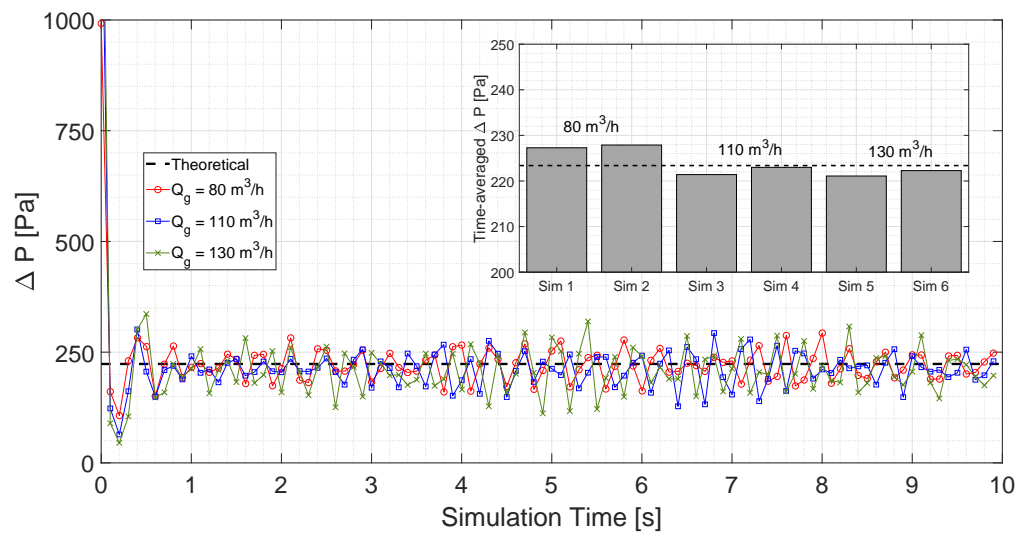


Figure 6.3: Pressure drop across the fluidized bed for different inlet air flow rates. The theoretical ΔP expected for the system is shown in black dashed line. **Inset view:** Comparison of time-averaged pressure drop across all simulated conditions.

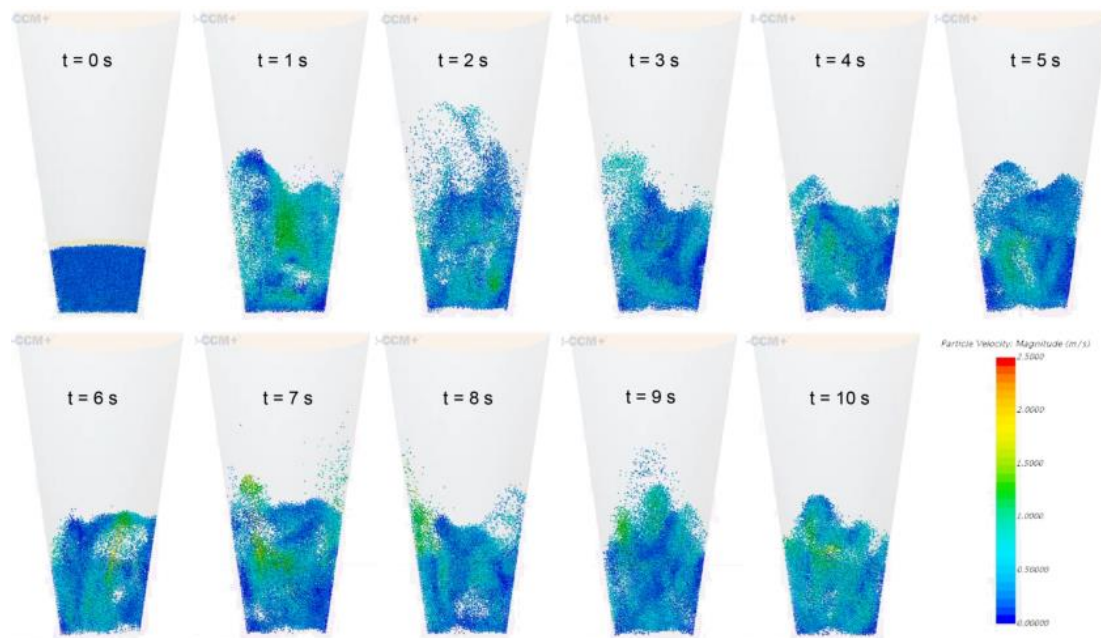


Figure 6.4: Snapshots of the CFD-DEM simulation captured every 1s for Sim# 3 showing bubbling fluidization. The snapshots are sliced along the X-Z plane and colored according to instantaneous particle velocities.

For the output of the simulations, mechanistic particle data were recorded every

0.004 seconds for a total simulation time of 10s. Particle and gas properties that were saved include: particle number, particle velocities, particle temperature, particle transfer rate, number of collisions, gas velocities, gas temperatures, and the residence time of particles in spray zone. Detailed discussion on the effect of operating parameters on the flow, collision and wetting dynamics within the system are described in preceding sections.

The CFD-DEM simulations were performed using Star CCM+ v11.04 (CD-adapco) on an Intel dual Xeon E5-2630 v3 CPU processors (2.4 GHz) with 64 GB of RAM.

6.3.2 PBM calculations

The population balance models developed for this framework utilize the particle-scale information from the CFD-DEM simulations to calculate the dynamic granule size distributions during the liquid addition phase of the FBG process. In order to simulate the experimental granule sizes observed, an 8 x 8 x 8 array of s, l and g volumes bins were used to define each particle class in the population density F function (Equation 6.21). Since a linear grid would require a very large number of bin size to cover the size range observed experimentally, a non-linear grid - mathematically expressed in Equations 6.42 to 6.44 - were used to define the grid array. Table 6.4 below details the configuration of the PBM granule size grid which was used in this framework.

$$s_i = s_{coef} \cdot (s_{base})^{(i-1)} \quad (6.42)$$

$$l_i = l_{coef} \cdot (l_{base})^{(i-1)} \quad (6.43)$$

$$g_i = g_{coef} \cdot (g_{base})^{(i-1)} \quad (6.44)$$

The values of s, l, g coefficients and bases used to calculate the non-linear grid array to cover the experimental granule size distribution range are provided in Table 6.5.

Table 6.4: PBM granule size grid configuration

Grid bin	Solid Volume		Liquid Volume		Gas Volume		Volume	Diameter
no. (<i>i</i>)	(m^3)	(%)	(m^3)	(%)	(m^3)	(%)	(m^3)	(μm)
1	1.92e-13	95.24	7.66e-15	3.81	1.92e-15	0.95	2.01e-13	72.7
2	5.56e-13	92.21	3.83e-14	6.36	8.62e-15	1.43	6.03e-13	104.8
3	1.61e-12	87.49	1.92e-13	10.40	3.88e-14	2.11	1.84e-12	152.1
4	4.67e-12	80.49	9.58e-13	16.50	1.75e-13	3.01	5.81e-12	223.0
5	1.36e-11	70.85	4.79e-12	25.04	7.86e-13	4.11	1.91e-11	331.8
6	3.93e-11	58.84	2.40e-11	35.86	3.54e-12	5.29	6.68e-11	503.4
7	1.14e-10	45.66	1.20e-10	47.97	1.59e-11	6.37	2.50e-10	781.2
8	3.31e-10	33.02	5.99e-10	59.82	7.16e-11	7.15	1.00e-09	1241.4

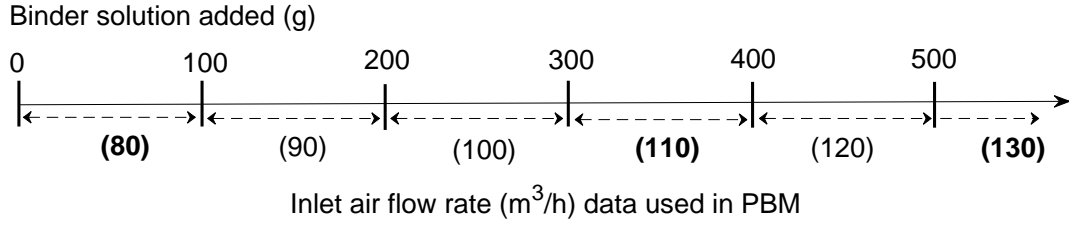
The process parameters and initial conditions used with the population balance model equations are presented in Table 6.5.

Table 6.5: Process parameters and initial conditions used in PBM calculations

Parameter	Value
Total number of bins in each dimension	8
Minimum solid volume of particles, (s_{coef})	$1.92 \times 10^{-13} \text{ m}^3$
Minimum liquid volume of particles, (l_{coef})	$7.66 \times 10^{-15} \text{ m}^3$
Minimum gas volume of particles, (g_{coef})	$1.92 \times 10^{-15} \text{ m}^3$
Exponentiation base for solid volume grid, (s_{base})	2.9
Exponentiation base for liquid volume grid, (l_{base})	5
Exponentiation base for gas volume grid, (g_{base})	4.5
Initial particle count F	1.8874×10^{10}
Density of solid in particle	512 kg/m^3
Density of liquid in particle	1000 kg/m^3
Density of gas in particle	1.225 kg/m^3
Total liquid binder spray amount	667 g
Aggregation constant, (β_0)	8.5
Breakage constant, (β_{break})	1×10^6
Consolidation constant, (β_{con})	$1 \times 10^{-25} \text{ m}^3$
Minimum porosity of granules, (ϵ_{min})	0.03 wt/wt
Minimum liquid content for aggregation, (LC_{min})	8 %wt/wt
Concentration of binder in liquid, (c_{binder})	0.06 wt/wt

In addition, the PBM model in this framework has been tailored to replicate the experimental procedure during the liquid addition phase of the granulation (when experimental sample measurements were conducted). During the validation experiment, the inlet airflow velocity was increased according to the bed behavior in order to maintain vigorous fluidization. As a result, for every 100 g of binder solution added, the air flow rate was manually increased by roughly $10 \text{ m}^3/\text{h}$. This process phenomenon is integrated into the PBM algorithm by updating the mechanistic information provided from the DEM-CFD simulation to change with the amount of liquid added to the system as illustrated in Figure 6.5.

The mechanistic parameters updated include the collision frequencies ($C_{P,1}$ and $C_{P,2}$), the particle collision energy (E_c), the inter-compartmental particle transfer rate (ψ), Mean residence time in spray zone (τ_{spray}) and the rate of change of particle



→ The mechanistic parameters used in PBM algorithm include the collision frequencies ($C_{P,1}$ & $C_{P,2}$), the particle collision energy (E_c), the inter-compartmental particle transfer rate (ψ), Mean residence time in spray zone (τ_{spray}) and the rate of change of particle temperature (R_{Tp}) for the Top and Bottom compartments.

→ Inlet air flow rates in bold were simulated in CFD-DEM and the rest were interpolated from the simulation results.

Figure 6.5: PBM update schematic. The mechanistic parameters in PBM were updated every 100g of binder added to match with the experimental methodology.

temperature (R_{Tp}) for the Top and Bottom compartments. The information for the various flow rates were interpolated from the CFD-DEM simulations performed with 80, 110 and 130 m^3/h flow rates as shown in Figure 6.6.

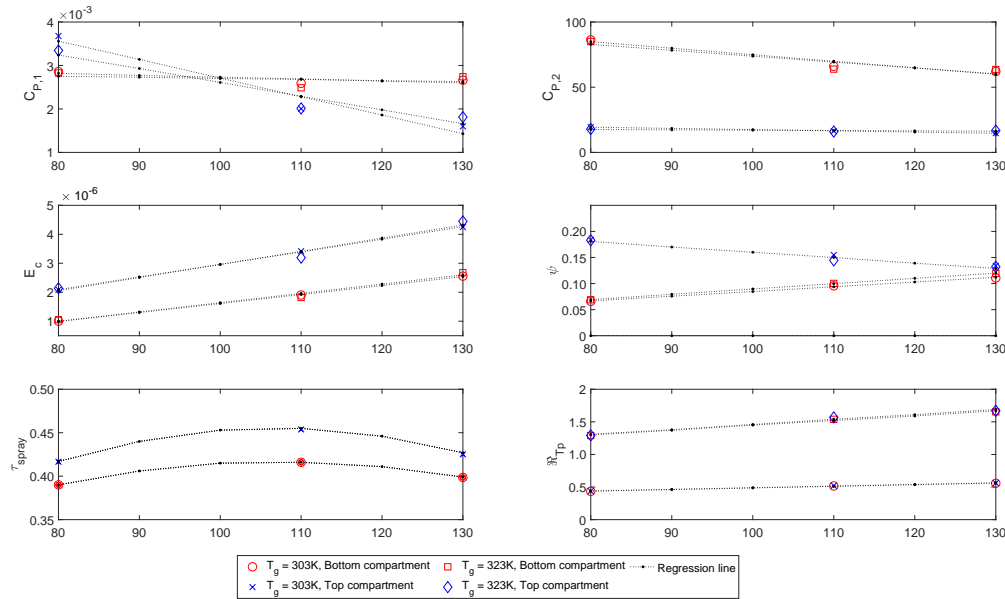


Figure 6.6: Mechanistic data used in the PBM rate kernels. Results from the CFD-DEM simulations performed with 80, 110 and 130 m^3/h flow rates were interpolated.

The resulting 3-D, two compartmental population balance equation was solved numerically using Matlab 2017b (The Mathworks Inc.) on an Intel Core i7-3770 CPU

processor (3.4 GHz) with 32 GB of RAM. The numerical integration of the PBM equations was performed using the finite difference method to reduce the equations to a set of ordinary differential equations; first order explicit Euler integration was performed to track the population distribution (F) over time. An adaptive time-step size calculation was computed at the end of each time step to satisfy the Courant-Friedrichs-Lewis (CFL) condition. In addition, the cell average method developed by Chaudhury et al. Chaudhury et al. (2013a) was also used to distribute particles with volumes that remained between the bin sizes into the surrounding population bins.

6.4 Validation experimentation

Experimental investigation of the fluidized bed granulation performed by Pandey et al. Pandey et al. (2018) at Drug Product Science and Technology, Bristol-Myers Squibb, New Brunswick, NJ, USA was used as the numerical benchmark to quantitatively assess the CFD-DEM-PBM framework results.

6.4.1 Experimental method

The experimental data were collected from granulation performed in a top-spray GPCG fluidized bed (Glatt Air Techniques Inc., Ramsey, NJ, USA). The binder solution was sprayed onto the fluidized bed using an integrated peristaltic pump and 1-mm spray nozzle positioned in the lowest port of the top spray configuration (7-8 inch distance to static bed). In each granulation trial, a 2 kg batch size of pre-mixed blend was used to charge the fluid bed and the concentration of binder in the sprayed liquid was kept constant for all batches (at 6 %wt/wt). In addition, the total mass of binder solution delivered to the bed was kept constant at 667 g (Liquid to solid ratio of 0.3335) with the binder spray rate being varied according to the DoE. Thus, the total liquid addition time for the trials vary accordingly. Initially, the powder bed was pre-warmed using inlet air at the target temperature for 5 min at an initial air flow velocity of 40 m^3/h . During the further granulation stages, the air flow rate was varied manually based on the bed behavior within the range of 80-130 m^3/h . Once the total binder solution amount

was sprayed, the inlet air temperature was increased to 60 °C to facilitate drying of the granulation. In the experimental design, a $2^{(4-1)}$ fractional factorial design with two center points (10 experiments) was used to study the effect of one formulation factor (amount of super-disintegrant, M_{sd}) and three process factors (inlet air temperature T_g , spray rate u_{spray} and nozzle atomization air pressure P_{spray}) on the moisture profile and granule growth rates of the FBG batches. The complete study design is listed in Table 6.6.

Table 6.6: Design of experiments for the fluidized bed granulation experiments

Batch No.	T_g [°C]	u_{spray} [g/min]	P_{spray} [bar]	M_{sd} [%wt/wt]
1	30	16	1	10
2	30	8	1	5
3	40	12	2.5	7.5
4	50	8	4	5
5	50	16	4	10
6	30	16	4	5
7	50	16	1	5
8	40	12	2.5	7.5
9	30	8	4	10
10	50	8	1	10

6.4.2 Response variables

The main response variable recorded during the study was the granule size distribution of granules during the liquid addition period. Approximately 5 g of granule samples were taken at different time points - based on the amount of binder added (after 200 g, 400 g and 667 g solution) - during granulation to quantify the granule growth progression as a function of processing parameters. The granule size distributions were measured by sieve analysis using a Sonic Sifter (Advantech, New Berlin, WI) operated at a constant pulse-and-sift setting of 5 with a total sifting time of 5 minutes. Six screens and a fines collection pan were used during the measurement: 590 μm (#30), 420 μm (#40), 250 μm (#60), 177 μm (#80), 105 μm (#140) and 53 μm (#270). Mass percentages of material retained on each of the meshes were recorded. The geometric mean diameter

(D_p) and corresponding standard deviation (σ_p) calculated using Equations 6.45 and 6.46 are reported in Table 6.7. The D_p and σ_p values for the batch pre-blend were 72.70 μm and 1.91 μm respectively.

$$D_p = \exp \left[\frac{\sum (W_i \cdot \ln(d_i))}{\sum W_i} \right] \quad (6.45)$$

$$\sigma_p = \exp \sqrt{\frac{\sum (W_i (\ln(d_i) - \ln(GMD))^2)}{\sum W_i}} \quad (6.46)$$

where i represents the corresponding size class, d_i is the midpoint of granule size class and W_i is the mass of particles per size class retained.

Table 6.7: Geometric mean diameter and standard deviation of unmilled samples collected during granulation

Batch	<i>Sample_a</i> [*]		<i>Sample_b</i> [*]		<i>Sample_c</i> [*]	
#	D_p [μm]	σ	D_p [μm]	σ	D_p [μm]	σ
1	290.30	1.74	348.86	1.57	368.85	1.46
2	354.44	1.50	380.37	1.46	393.56	1.46
3	220.85	1.64	240.73	1.67	190.60*	2.06
4	178.70	1.60	165.36	1.62	142.00	1.62
5	194.00	1.94	215.30	1.71	222.30	1.67
6	274.30	1.58	277.70	1.64	326.50	1.47
7	296.10	1.62	362.40	1.53	462.10	1.48
8	245.31	1.65	285.07	1.53	317.50*	1.52
9	199.55	1.73	219.00	1.80	242.00	1.62
10	267.30	1.61	337.10	1.57	383.30	1.59

* *Sample_a*, *Sample_b* and *Sample_c* were collected immediately after 200 g, 400 g and 667 g of binder solution were added

* Some error in dynamic data of batch 3 and 8 observed due to caking of samples

The dynamic granule size data (Table 6.7) collected during the binder spray phase of the FBG granulation were used as the validation set to assess the quality of the proposed framework.

6.5 Results and discussion

6.5.1 Impact on particle flow and circulation dynamics

Air flow rate and solid volume fraction: The fluid flow and voidage profiles of the fluidized bed CFD-DEM simulations investigated at different inlet air flow rates are reported in Figure 6.7. As expected for gas-solid systems under bubbling fluidization, the air flow rate increment beyond the minimum fluidization velocity (U_{mf}) is accompanied by the formation of rising bubbles or voids with minimal solid particles inside them. For all three Q_g flow rates examined (all flow rates well above the U_{mf} value), distinct regions of air bubbles with high fluid velocity are observable in the snapshots taken at $t = 10s$. In addition, the gas velocity through the surrounding dense continuous phase is seen to remain essentially low implying that the excess gas flow (beyond that of minimum fluidization) goes through the bed in the form of bubbles.

The solid volume fraction snapshots in Figure 6.7 also illustrate a significant expansion of bed with increase in the inlet air velocity. From 80 to 130 m^3/h , the particle bed expands roughly $1.8\times$ to $2.5\times$ compared to the static particle bed denoted by the dashed line in the illustration. This expansion in bed height comes mainly from two sources: first, the space occupied by the gas bubbles adds to the overall bed height, and secondly, the increased drag force created by the higher air velocities can support a larger mass of particles. As a result, the solid concentration over the Top compartment is generally much lower compared to the lower dense region.

Particle velocities: Figure 6.8 illustrates the impact of inlet air flow rate on the instantaneous velocities of particles captured at $t = 10s$ from the CFD-DEM simulations. In the figure, particles colored in darker shades of represent granules with low velocity (0 to 0.5 m/s) while those colored in shades of green/yellow represent granules with higher velocity (1 to 2 m/s) as indicated through the color bar. Dashed lines separating the Top and Bottom compartments are also provided in the figure. A clear increase in the average particle velocity is seen when the flow rate Q_g is raised from 80 to 130 m^3/h .

A quantitative comparison of the effect of the operating parameters on the average

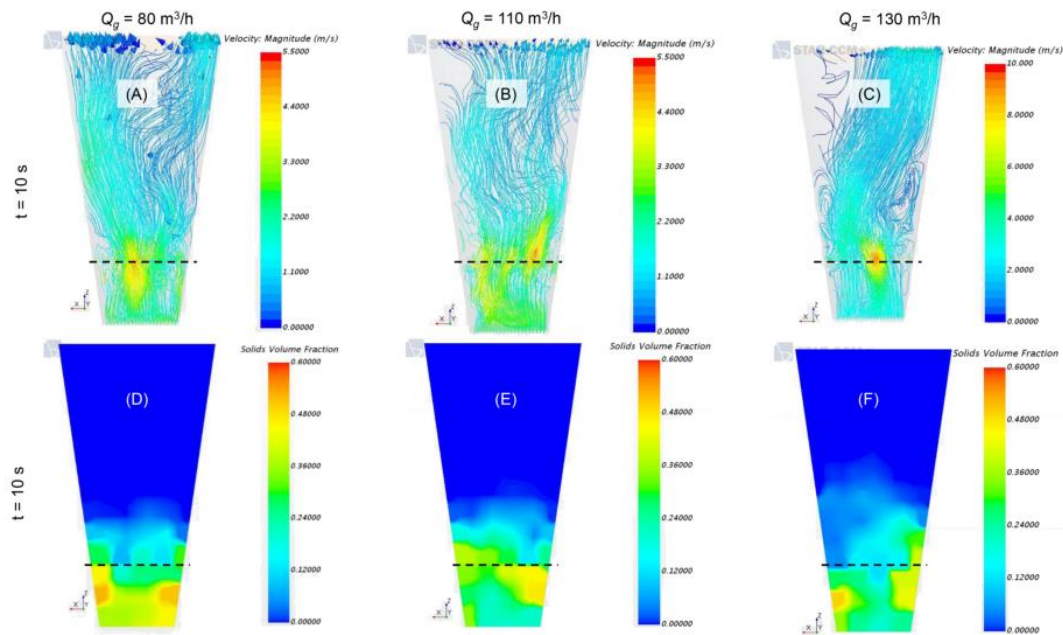


Figure 6.7: Instantaneous air flow velocities (Top) and solids volume fractions (Bottom) at different air flow rates (Q_g) at $T_g = 303$ K. **(A)** $Q_g = 80$ m³/h, $t = 10$ s, **(B)** $Q_g = 110$ m³/h, $t = 10$ s, and **(C)** $Q_g = 130$ m³/h, $t = 10$ s, **(D)** $Q_g = 80$ m³/h, $t = 10$ s, **(E)** $Q_g = 110$ m³/h, $t = 10$ s, and **(F)** $Q_g = 130$ m³/h, $t = 10$ s. The dashed lines represent demarcation of the Top and Bottom compartments.

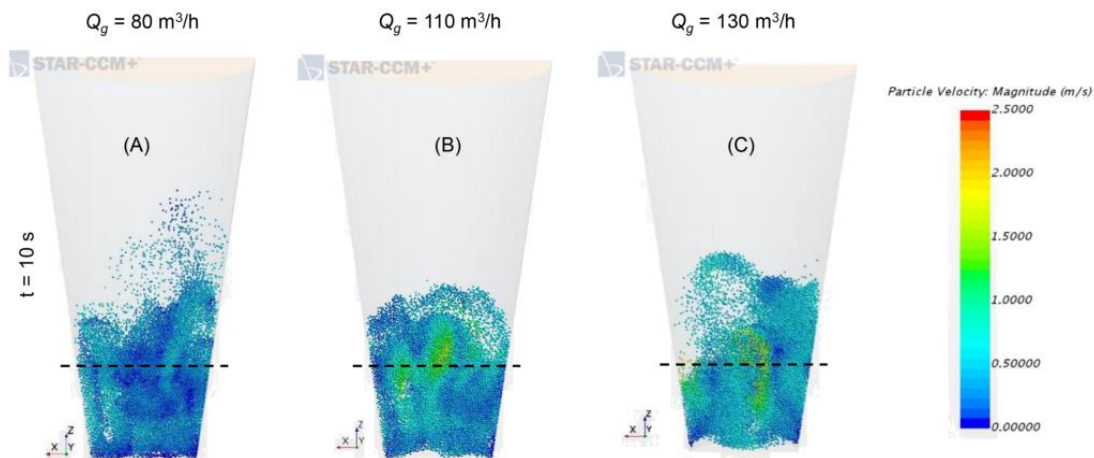


Figure 6.8: Instantaneous particle velocities and positions at different air flow rates (Q_g) at $t = 10$ s and $T_g = 303$ K. **(A)** $Q_g = 80$ m³/h, **(B)** $Q_g = 110$ m³/h and **(C)** $Q_g = 130$ m³/h.

particle velocity is provided in Figure 6.9. As seen in the simulation snapshots, the average particle velocities (v_p) increases proportionally with the increase in Q_g . Comparing the v_p for the overall particles in the granulator, the v_p for the 110 m^3/h and the 130 m^3/h trials are almost +30% and +50% higher respectively in relation to the 80 m^3/h inlet air flow rate simulations. On the other hand, the change in inlet air temperature does not seem to influence the particle velocities. Across the different air flow rates, the increase in T_g seem to negligibly alter the v_p values (< 4% change).

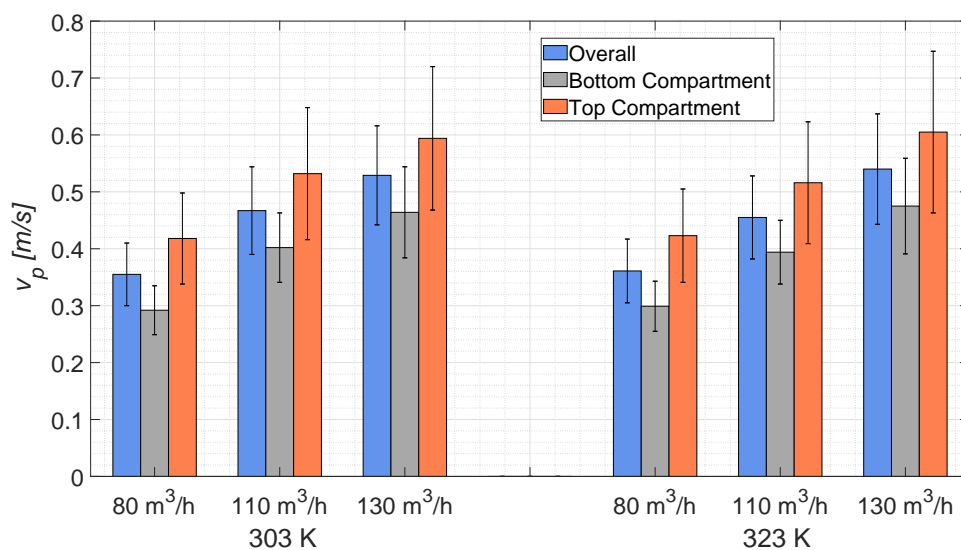


Figure 6.9: Time-averaged particle velocities (v_p) at different inlet air flow rates (Q_g) and at different inlet air temperatures (T_g)

A significant difference, however, can be observed between the particle velocities in the two compartments: particles in the Top compartment are moving at a much higher v_p compared to those in the Bottom compartment. This difference is likely due to the tapered shape of the vessel. Particles are generally packed more tightly at the bottom of the fluidized bed leading to more collisions and low velocities. The instantaneous solid volume fraction illustrations in Figure 6.7 corroborate this explanation. Even as fluidization proceeds to $t = 10s$, the solid concentration at the Bottom compartment is generally much larger compared to the Top.

Compartmental distribution of particles: The distribution of particles between

the compartments over the fluidization operation is highly dependent on the inlet air flow rate and the particle circulation. Figure 6.10 shows the time-averaged division of total particle number (N_p) over the top and bottom compartments. With the higher inlet air flow rate, the increased gas velocity is able to support a larger particle mass in the Top compartment. On average, the simulation results show that the number of particles in the Bottom compartment is generally $2.6\times$ greater than the number of particles in Top compartment for $Q_g = 80 \text{ m}^3/h$. With increase in the air flow rate, a more homogeneous distribution of particles between the compartments is observed: at $Q_g = 110 \text{ m}^3/h$ and $130 \text{ m}^3/h$, the same difference in particle number is reduced to $1.5\times$ and $1.2\times$ respectively.

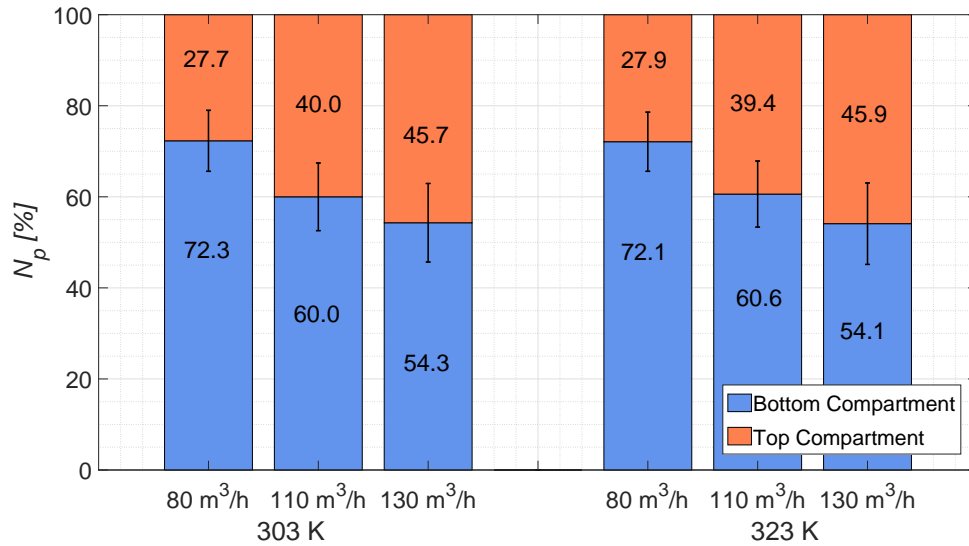


Figure 6.10: Time-averaged division of total particle number over top and bottom compartments at different initial conditions.

Inter-compartmental particle transfer: In order to investigate the circulation of granules within the fluidized bed, an internal flux interface was setup between the Top and Bottom compartments within the CFD-DEM geometry to track the number of particles passing from one region to the other. The interface created in this framework does not affect the particle and fluid flow simulations. In Figure 6.11, the time-averaged ratio of particles transferring through the virtual interface for inlet air flow rate of 80

m^3/h , $110m^3/h$ and $130 m^3/h$ are shown. The particle transfer parameter (ψ) values plotted represent the percentage of particles from the respective compartments moving into the adjacent compartment per unit time due to the bed circulation. Since the number of particles in the two compartments vary due to the initial conditions as shown in Figure 6.10, the percentage of particles moving from the Top compartment (ψ_2) with generally fewer number of total particles than the Bottom compartment are seen to be higher than the (ψ_1) values.

The simulation results show that for both inlet air temperature conditions, the particle transfer from Bottom to Top compartment increases with increasing air flow rate. Conversely, the particle transfer from the Top to Bottom compartment decreases with increasing air flow rate. At higher inlet air flow rates, not only does the increased fluid flow support a larger number of particles in the Top compartment but the particles themselves also reach higher velocities (Figure 6.9). As a result, more particles move between the two compartments with higher air velocities. In addition, a comparison between the two different inlet air temperatures are also shown in the figure. The dotted lines in Figure 6.11 represent the simulations with $T_g = 303K$ while the dashed line represent $T_g = 323K$ simulations. Between the two inlet air temperatures, minimal difference in particle transfer rate is observable at lower inlet flow rates. With higher Q_g , the percentage of particle transfer is seen to get homogeneous more quickly with a higher inlet air temperature.

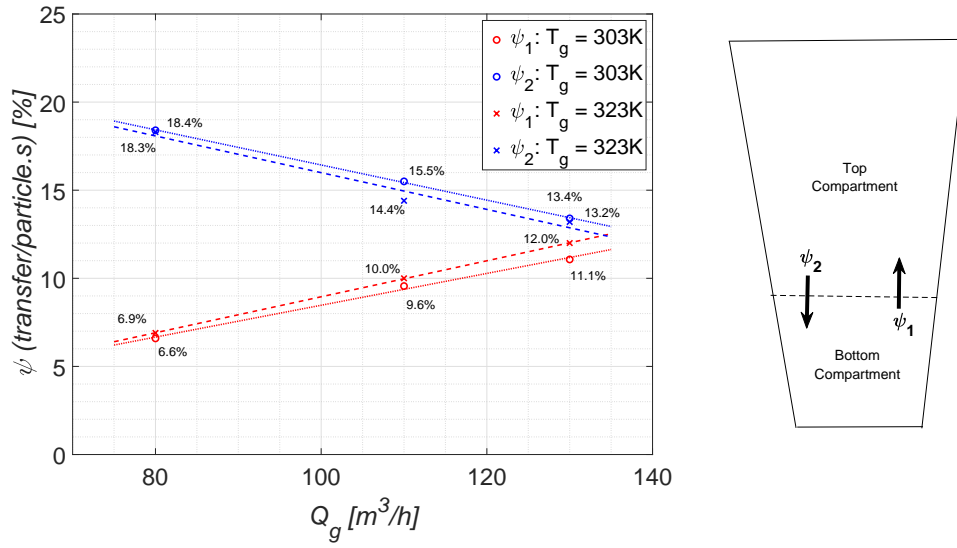


Figure 6.11: Time-averaged particle transfer ratio from one compartment to the other at different air flow rates and inlet air temperatures.

6.5.2 Impact on particle collision dynamics

Collision Frequencies: In order to investigate the impact of operating parameters on the particle collision dynamics within the fluidized bed, information on the number of collisions between particles in both compartments are extracted from the CFD-DEM simulations. Figure 6.12 shows the particle collision frequencies in the fluidized bed granulator for the different inlet air flow rates separated for the top and bottom compartments. The $C_{P,1}$ values plotted in the figure represent the number of collision events experienced by two particles in a unit time interval (Equation 6.28).

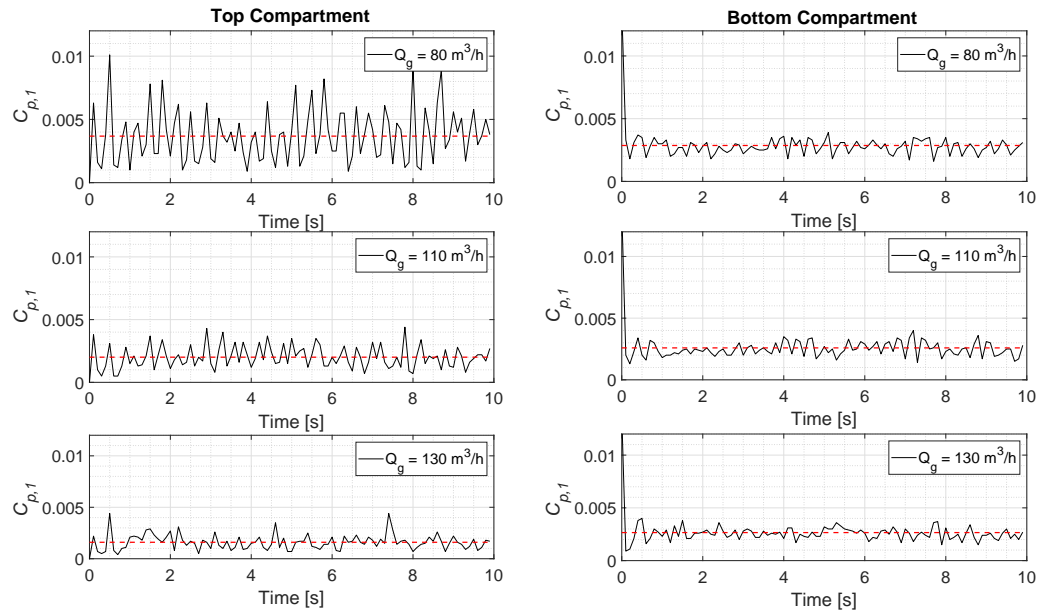


Figure 6.12: Comparison of particle collision frequencies (collisions per particle per particle sec) in Top and Bottom compartments over time at different inlet air flow rate (Q_g) conditions. $T_g = 303\text{K}$. The time-averaged mean values are plotted as dotted red lines.

In general, the collision frequency of particles is seen to be oscillating over time as the excess air passes through the powder bed via bubbles. From the simulation results, three distinct collision frequency trends are observable:

1. The amplitude of the $C_{P,1}$ oscillations are typically higher in the Top compartment compared to the Bottom compartment. This is likely due to the tapered geometry of the vessel (higher bed voidage in Top compartment) as well as the bursting of the air bubbles at the surface of the powder bed.
2. With the increase in inlet air velocity, the collision frequency oscillations in the Top compartment are more subdued with lower amplitudes and lower time-averaged mean values. This is likely due to the increased expansion of the bed at higher flow rates as well as the increased frequency of bubbling. Since the average solid volume fraction of the fluidized bed decreases with higher gas velocity, fewer particles are likely to meet and collide with each other. Moreover, at higher inlet air fluidization, bubbles are formed more frequently thus leaving little room for

the large fluctuations in the bed voidage seen for $Q_g = 80 \text{ m}^3/h$.

3. For the Bottom compartments, where the solid volume fractions are still very high, minimal decrease in collision frequency values are observed even with increasing gas velocity.

Figure 6.13 shows the time-averaged collision frequencies in Bottom and Top Compartments as well as the overall system for all six simulation conditions. For both inlet air temperatures, simulation results show that the above-mentioned trends hold true. It must be noted here that the large error bars seen in Figure 6.13 are due to the time-averaged values of the oscillating collision frequencies calculated.

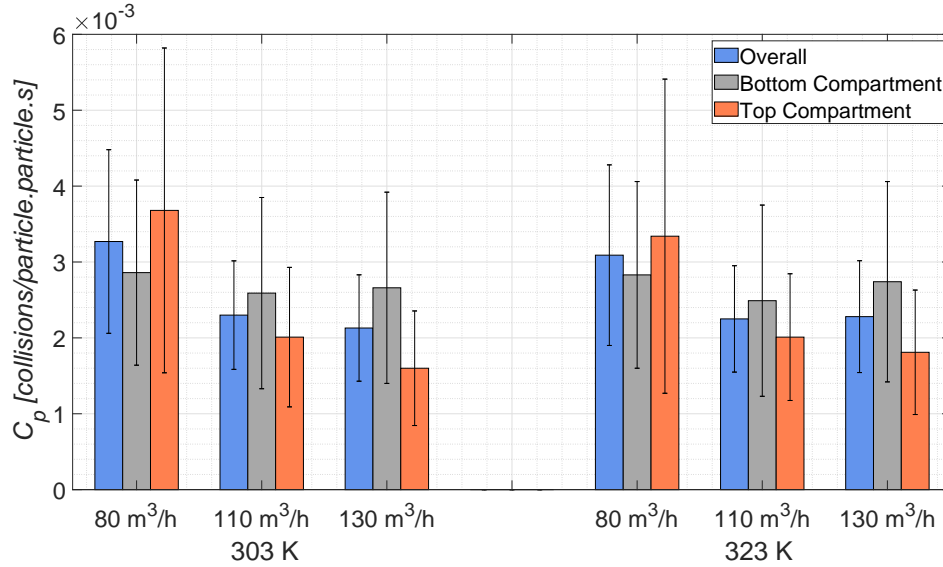


Figure 6.13: Comparison of time-averaged particle collision frequencies ($C_{P,1}$) over bottom and top compartments at different inlet conditions.

Collision Energies: Figure 6.14 shows the time-averaged particle collision energies calculated using Equation 6.31 in Bottom and Top Compartments for different initial conditions. The simulation results show that the average E_c of particles within the fluidized bed increase with an increase in air flow rate. Since the collision energy is dependent on the square of relative particle velocities, the trend is very similar to the time-averaged velocities of particles shown in Figure 6.9.

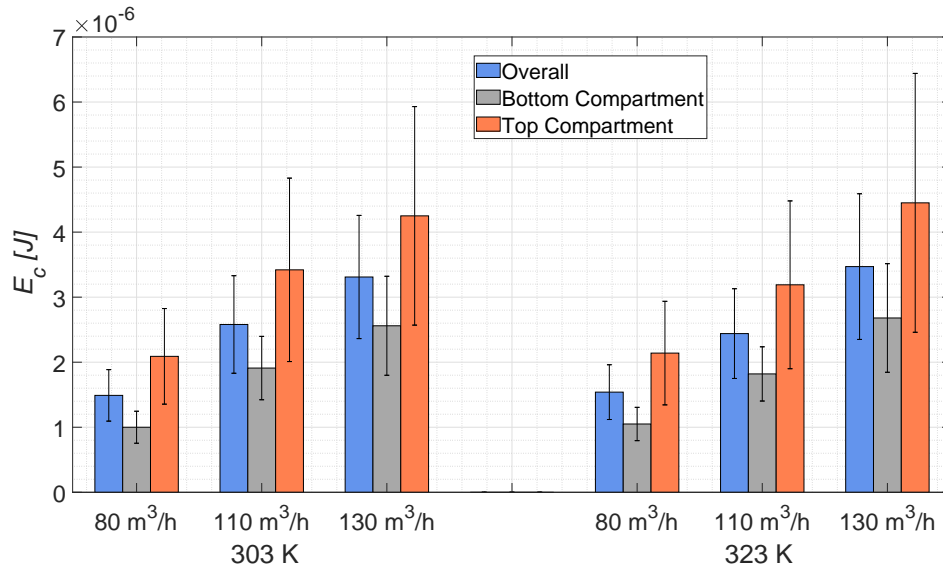


Figure 6.14: Comparison of time-averaged particle collision energies (E_c) over bottom and top compartments at different inlet conditions.

On the whole, the CFD-DEM simulations show that increasing the inlet air flow rate leads to fewer but stronger collisions between particles. Conversely, at lower gas velocities, the frequency of collisions between particles is much higher but each collision takes place with lower amount of energy. A similar difference is also noticeable for Top and Bottom compartments, with particles in bottom compartment having a higher collision frequency but lower collision energy.

6.5.3 Impact on particle wetting and drying dynamics

Particle residence time within spray zone: Figure 6.15 shows the instantaneous residence time of the particles inside the spray zone for different inlet air flow rates at 2 and 10 seconds. The particles in the snapshots are colored according to the time spent by the particle within the spray zone as calculated by the Passive scalar model. Higher particle residence time in Figure 6.15 are represented by lighter blue colors (denoting wetter particles) and lower residence time by darker blue colors respectively. At early time points, since the particles in the Top compartment spend more time inside the spray zone, more particles with higher residence time are observable in the top of the

fluidized bed. As liquid addition proceeds and the circulation of particles take place, particle wetting eventually becomes more homogeneous between the two compartments.

Figure 6.16 illustrates the residence time distributions of particles within the spray zone at $t = 2s$, $t = 5s$ and $t = 10s$ at an inlet air flow rate of $110 \text{ m}^3/h$. As seen in the inset in Figure 6.16, the residence time distribution $E(t)$ is very narrow at $t = 2s$ with 40% of particles having never passed through the spray zone. Over time, the distribution widens and moves towards the right as more particles pass through the spray zone. In addition, the cumulative residence time distribution $F(t)$ illustrates this increasing homogeneous wetting over time. On average, 50% of particles within the fluidized bed at $t = 2s$, $5s$ and $10s$ have spent respectively $0.030s$, $0.15s$ and $0.35s$ in the spray zone.

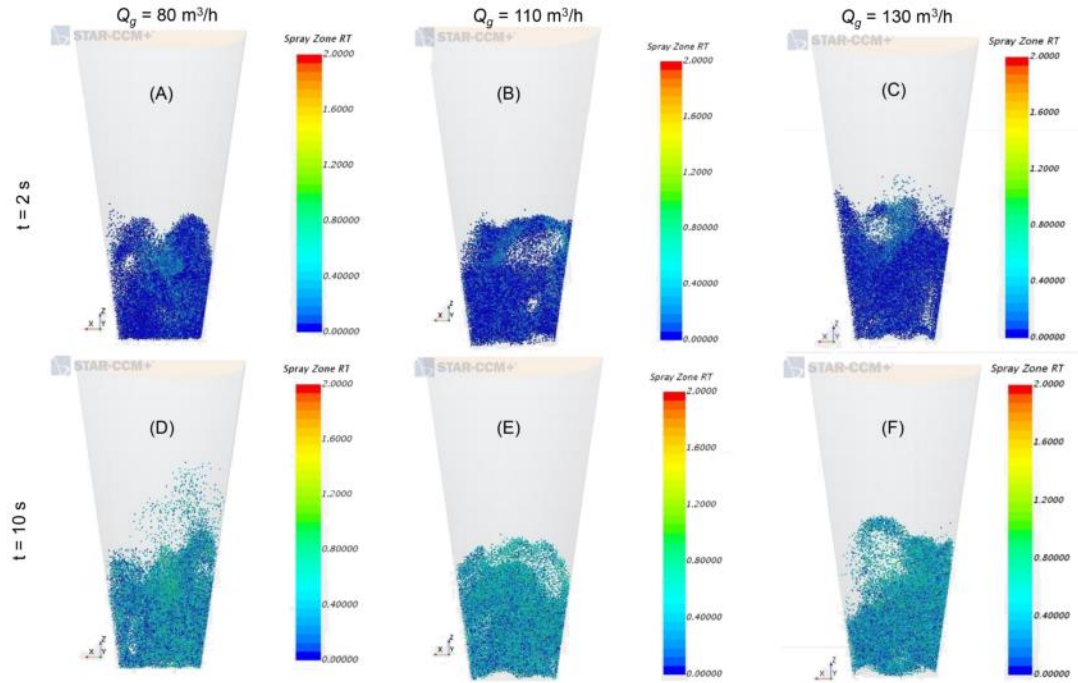


Figure 6.15: Instantaneous particle residence time (RT_p) inside the spray zone at different air flow rates (Q_g) at $T_g = 303 \text{ K}$. **(A)** $Q_g = 80 \text{ m}^3/h$, $t = 2 \text{ s}$, **(B)** $Q_g = 110 \text{ m}^3/h$, $t = 2 \text{ s}$, and **(C)** $Q_g = 130 \text{ m}^3/h$, $t = 2 \text{ s}$, **(D)** $Q_g = 80 \text{ m}^3/h$, $t = 10 \text{ s}$, **(E)** $Q_g = 110 \text{ m}^3/h$, $t = 10 \text{ s}$, and **(F)** $Q_g = 130 \text{ m}^3/h$, $t = 10 \text{ s}$

In terms of the impact of inlet air flow rate on particle wetting behavior, Figure 6.17 shows the residence time distributions $E(t)$ and the mean residence time (τ_{spray})

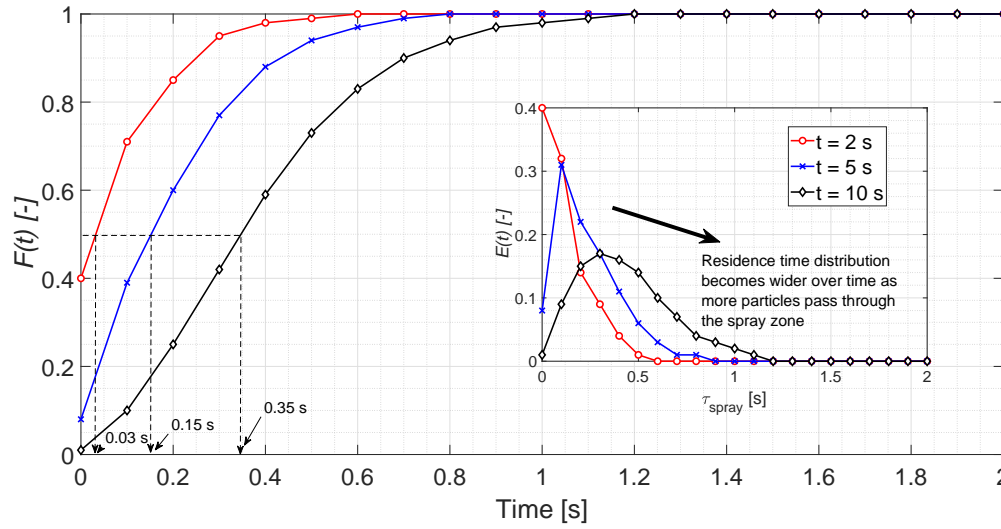


Figure 6.16: Progression of particle residence time distribution inside the spray zone over time. $Q_g = 110 \text{ m}^3/\text{h}$, $T_g = 303 \text{ K}$

of particles inside the spray zone at the end of the 10s simulation. The residence time distribution of particles in the Top and Bottom compartments are plotted individually and the (τ_{spray}) values calculated using Equation 6.20 is annotated in the figure. The CFD-DEM simulation results show that by the end of 10 s, particles in both compartments are sprayed homogeneously. In fact, minimal differences in the mean residence time of particles are observed for all inlet air flow rates. Quantitatively, the (τ_{spray}) values for the Top compartment are very minimally higher than those of Bottom compartment suggesting that higher inter-compartmental particle transfer (Figure 6.11) does not significantly affect the particle wetting behavior at the flow rates simulated.

Particle temperatures: In terms of heat transfer from gas to solid particles, simulations results show that increasing the temperature of the inlet air increases the rate at which particles are heated within the fluidized bed. Visually, the particle temperature profiles captured in Figure 6.18 clearly show the higher temperatures attained by particles with $T_g = 323 \text{ K}$ compared with $T_g = 303 \text{ K}$ within the first 10s. Another thing to note is the almost homogeneous spread of temperature profile among the top and bottom compartments even at $80 \text{ m}^3/\text{h}$ air flow rate. A detailed comparison of the effect of operating parameters on the particle temperatures are illustrated in Figure

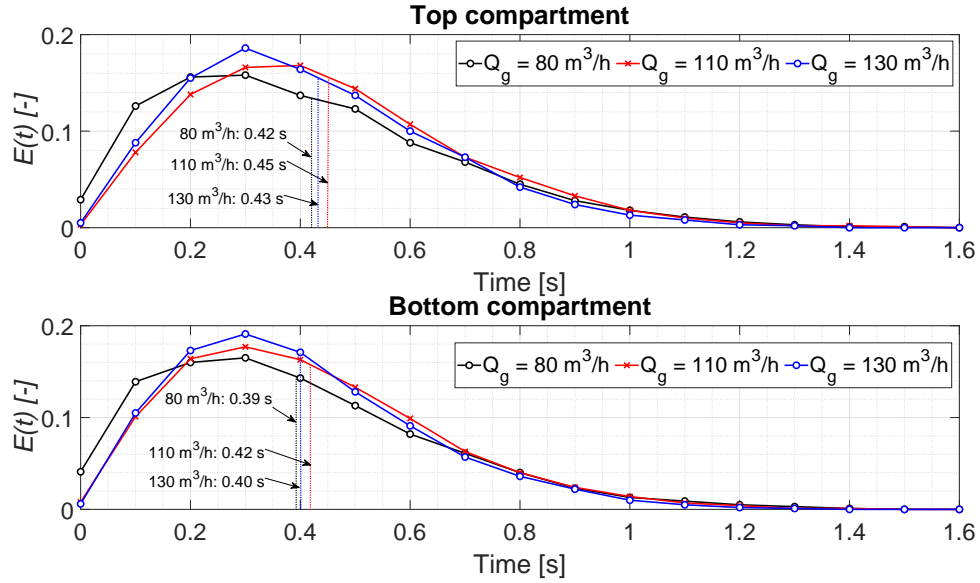


Figure 6.17: Particle residence time distributions inside the spray zone at different inlet air flow rates for the Top and Bottom compartments. The mean residence time is annotated.

6.19 which shows the rate of change in average particle temperatures, \mathfrak{R}_{Tp} [in K/s], in both bottom and top compartments for all initial conditions.

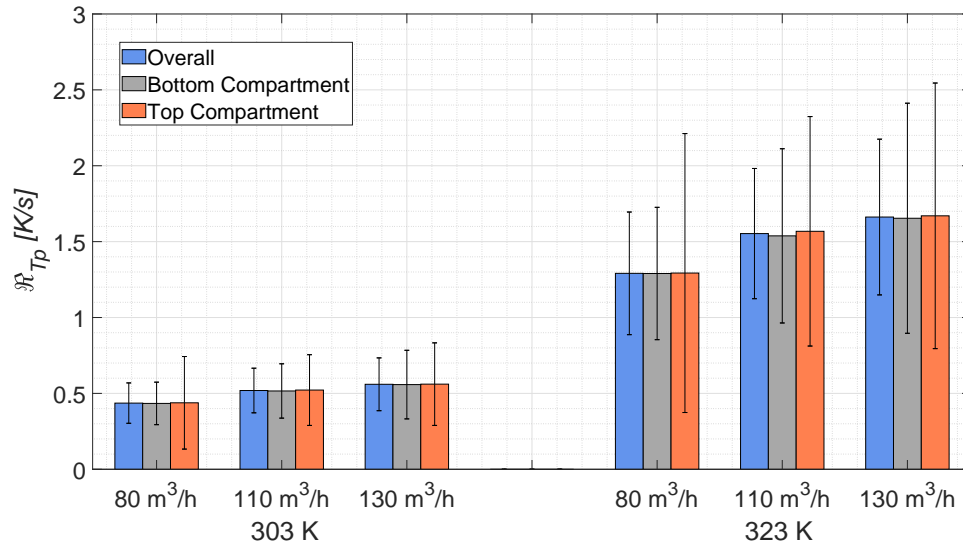


Figure 6.19: 'Average rate of change in particle temperatures, \mathfrak{R}_{Tp} '

As seen with the simulation snapshots, three distinct trends are visible in Figure 6.19:

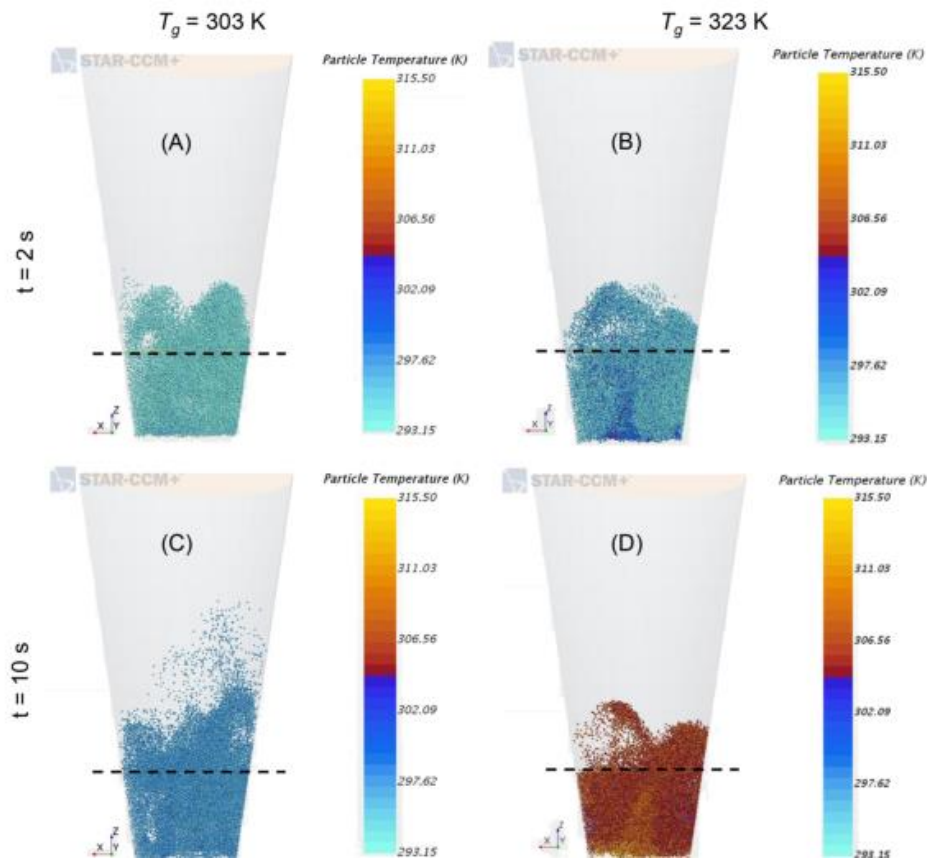


Figure 6.18: Instantaneous particle temperatures at different inlet air temperatures (T_g).
(A) $Q_g = 80 \text{ m}^3/\text{h}$, $T_g = 303 \text{ K}$, $t = 2 \text{ s}$, **(B)** $Q_g = 80 \text{ m}^3/\text{h}$, $T_g = 323 \text{ K}$, $t = 2 \text{ s}$, **(C)** $Q_g = 80 \text{ m}^3/\text{h}$, $T_g = 303 \text{ K}$, $t = 10 \text{ s}$, and **(D)** $Q_g = 80 \text{ m}^3/\text{h}$, $T_g = 323 \text{ K}$, $t = 10 \text{ s}$

1. *Higher inlet air temperature results in faster heat transfer:* The largest impact on the \Re_{Tp} values is seen due to the change in T_g . The \Re_{Tp} values for all air flow rates at $T_g = 323$ K are almost 3 times the values observed for $T_g = 303$ K. Expectedly, the higher temperature gradient between the fluid and solid phases result in proportionally faster heat transfer. Temperature gradient ($T_g - T_p$) for 323 K inlet air temperature is 3 times the value for 303 K.
2. *Higher flow rates of air leads to higher rates of heat transfer from fluid phase to solid phase:* A lesser impact of gas velocity is also observable on the rate of particle temperature change. Compared to $Q_g = 80 \text{ m}^3/\text{h}$, the \Re_{Tp} values for 110 m^3/h and 130 m^3/h air flow rates are almost 20% and 30% higher respectively for both inlet air temperature conditions. In the fluid flow field diagrams shown in Figure 6.20, within the 10s of simulation, the higher flow rate results in a wider spread of heated air within the granulator. This is likely to have caused the small differences in the \Re_{Tp} values.
3. *No difference is seen across the top and bottom compartments:* At a fixed air flow rate, the particles in both compartments seem to be uniformly heated - with differences in the \Re_{Tp} values $\leq 2\%$.

To put this result into context: during an FBG process, increasing the \Re_{Tp} value through either increases in the inlet air temperature (higher impact) or air flow rate (lower impact) can lead to enhanced evaporation rate of the binder solution. As the liquid content from the granules are removed at a faster rate, the probability of granules with smaller size distribution or higher porosity increases.

6.5.4 Comparison with experimental data

Figure 6.21 compares the granule growth dynamics between the modeled system and the experimental data for representative batches #5, #6 and #9 run at constant atomization air pressure of 4 bar. In the validation experiments, roughly 5 g of granule samples were taken after 200 g, 400 g and 667 g of binder solution were sprayed. The model predicted geometric mean diameter (GMD) values for these batch conditions

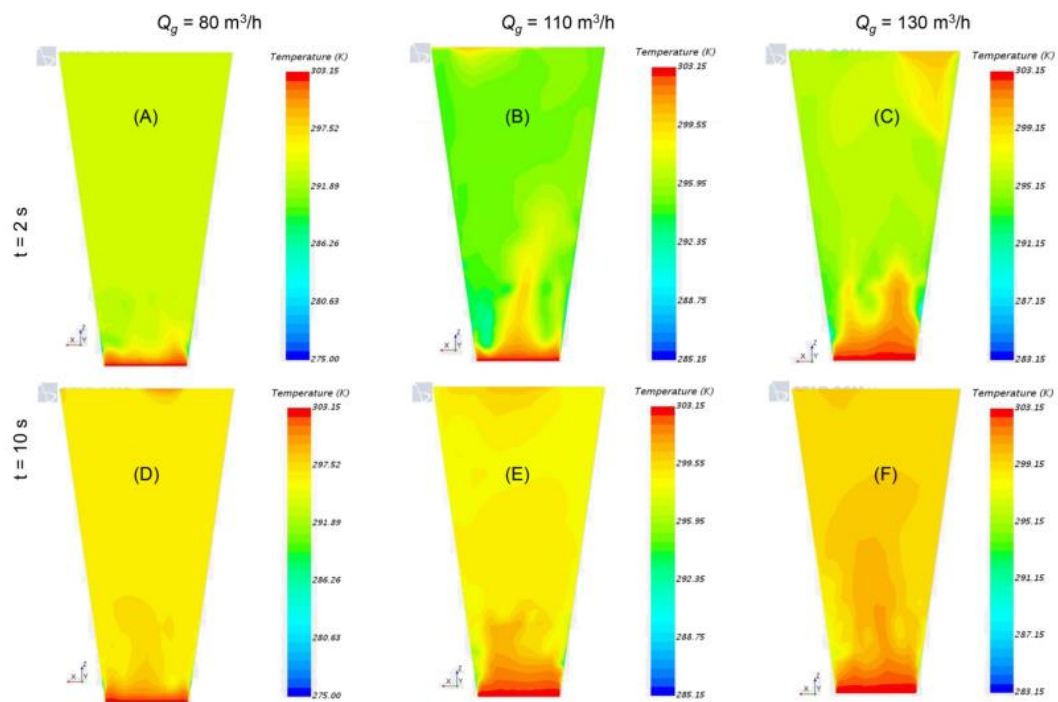


Figure 6.20: Average air temperatures within the fluidized bed at $T_g = 303$ K. **(A)** $Q_g = 80 \text{ m}^3/\text{h}$, $t = 2$ s, **(B)** $Q_g = 110 \text{ m}^3/\text{h}$, $t = 2$ s, **(C)** $Q_g = 130 \text{ m}^3/\text{h}$, $t = 2$ s, **(D)** $Q_g = 80 \text{ m}^3/\text{h}$, $t = 10$ s **(E)** $Q_g = 110 \text{ m}^3/\text{h}$, $t = 10$ s and **(F)** $Q_g = 130 \text{ m}^3/\text{h}$, $t = 10$ s.

were calculated and assessed for both validation of the framework design as well as quantification of the granule growth progression as a function of processing parameters. It must be noted that the experimental GMD values for the $t = 0s$ were taken from the pre-blend powder data instead of sampling after the pre-warming phase which lasted for 5 mins. The model predicted data assumes this pre-blend powder size distribution as the initial PSD and calculates the granule growth data accordingly. The deviation between the model prediction and experimental data - especially at the early time points - are likely due to this discrepancy.

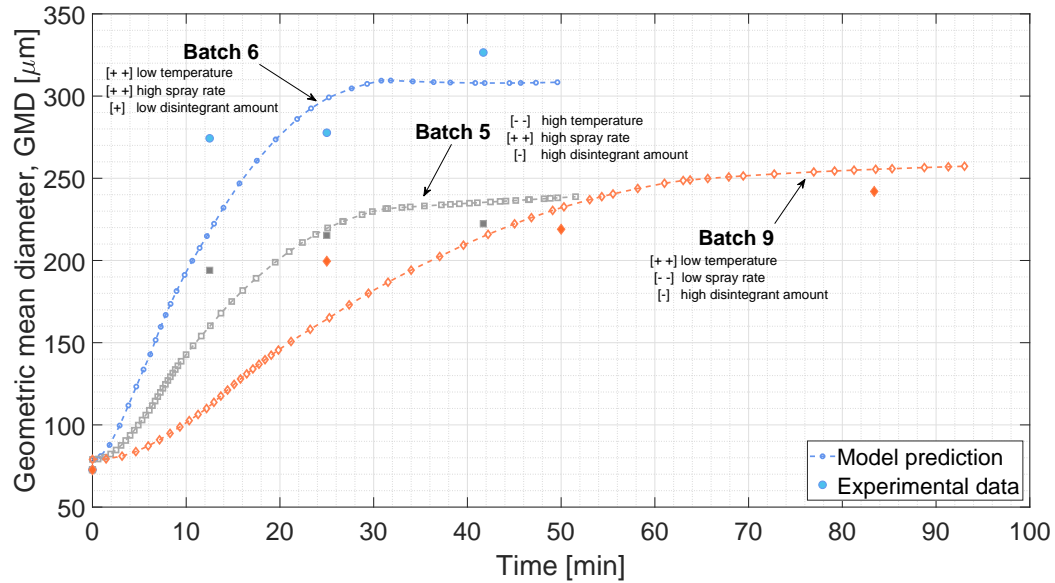


Figure 6.21: Validation of CFD-DEM-PBM framework through comparison with experimental data for Batch #5, #6 and #9: Geometric mean diameter versus time.

Granule growth trends : In both model results and experimental trends in Figure 6.21, the following impact of process parameters are observable on the *GMD* of granules over time:

1. Spray rate \uparrow , Granule growth rate \uparrow : Higher liquid spray rate for Batch #6 and #5 encourages faster growth rate of granules compared to Batch #9. As particles get wetted more quickly, more collision events successfully end in agglomeration early in the granulation process.
2. Air temperature \downarrow , Granule size \uparrow : Despite having lower spray rate, the lower inlet

temperature for Batch #9 enhances the growth rate of granules due to reduced evaporation rate. The granule size produced is comparable to Batch #5 with higher spray rate. Moreover, Batch #5 which has high inlet air temperature is seen to have lower GMD compared to Batch #6 despite both having a high spray rate.

3. Disintegrant \uparrow , Granule size \downarrow : Higher disintegrant amount is seen to contribute to smaller granule growth. When comparing Batch #5 and #6 with constant spray rate but with high (10%) and low (5%) disintegrant amount respectively, Batch #6 shows significantly larger granules.

A similar comparison was further carried out between batches #1, #2 and #7 run at a much lower atomization air pressure of 1 bar. Experimental and model predicted *GMD* of the granules over time are plotted in Figure 6.22. Compared to Figure 6.21 which has the final GMD in the range of 200 - 300 μm , the trials run at a lower atomization pressure in Figure 6.22 show much higher granule size range (350 - 450 μm). In addition, the prediction results show similar trends:

1. Spray rate \uparrow , Granule growth rate \uparrow : Batch #7 and #1 with higher spray rate has faster granule growth compared to Batch #2.
2. Air temperature \downarrow , Granule size \uparrow : Batch #2 with low inlet air temperatures, has comparable final granule size as Batch #7 despite having lower spray rate.
3. Disintegrant \uparrow , Final granule size \downarrow : Between Batch #7 and #1 with both high spray rates, Batch #1 with higher disintegrant produced smaller granules.

Prediction error: The dynamic *GMD* trend of the granules within the fluid bed granulator over time from the model predictions closely follows the experimental trend observed for the six representative batches. When compared with the experimental data points in Figure 6.21 and 6.22, the general trends of varying the inlet air temperature, disintegrant amount and the spray rate is captured fairly accurately. Table 6.8 below shows the absolute error in prediction of the granule *GMD* measured after specific

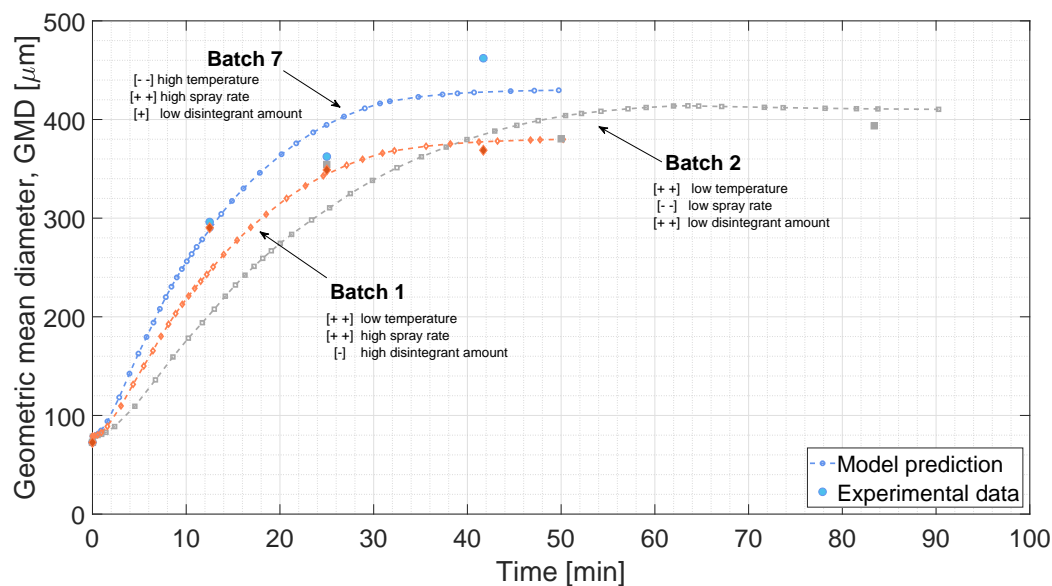


Figure 6.22: Geometric mean diameter versus time for Batch #5, #6 and #9.

amount of binder liquid is added. In general, the model predictions get better over time with GMD at early stages of granulation off by roughly 14% while at the end of the liquid addition stage by only 5.3%. Averaged out over the batch, the absolute error in predictions of the coupled framework are below 10%.

Table 6.8: Error in prediction of granule geometric mean diameter

	after 200g			after 400g			after 600g			Avg
Batch	exp	model	abs.	exp	model	abs.	exp	model	abs.	error
No.	GMD	GMD	error	GMD	GMD	error	GMD	GMD	error	over
	(μm)	(μm)	(%)	(μm)	(μm)	(%)	(μm)	(μm)	(%)	Batch
6	274.3	222.3	19.0	277.7	299.2	7.7	326.5	307.9	5.7	10.8
5	194.0	160.3	17.4	215.3	219.8	2.1	222.3	235.6	6.0	8.5
9	199.5	165.2	17.2	219	232.6	6.2	242	255.5	5.6	9.7
7	296.1	290.3	2.0	362.4	394.5	8.9	462.1	427.5	7.5	6.1
2	354.4	310.5	12.4	380.4	404	6.2	393.6	410.7	4.4	7.7
1	290.3	250.5	13.7	348.9	342.9	1.7	368.8	378.1	2.5	6.0
Avg. error over time			13.6	5.5			5.3			

It must be mentioned that the model predictions of the second set of batches (#7, #2 and #1) operated at lower spray atomization pressure shows better agreement with experimental data than for those operated at higher atomization pressure (#6, #5 and #9) likely due to the limitation of the current framework in incorporating the complexities of nozzle spray. It is generally understood that the nozzle pressure not only impacts the size of droplets but also the velocity of droplets sprayed in the fluidized bed which can affect the particle flow, wetting dynamics as well as nucleation growth rate. Additional development of the framework should consider analyzing the impact of the nozzle spray dynamics explicitly in the CFD-DEM simulations.

6.6 Conclusions

To understand the fluid-particle dynamics of a fluid bed granulation system, a framework of coupled multi-phase model is presented. First, a two-way coupled CFD – DEM model is developed for a top spray fluid bed granulator to study the effects of inlet gas flow rate and inlet gas temperature on the particle flow behavior as well as the residence time of particles in the spray zone. Then, a one-way transfer of data from CFD-DEM simulations to a two-compartmental PBM is applied to relate the effects of particle-fluid interactions to granulation behavior occurring within the fluidized bed system. In this work, critical product quality attribute in terms of the geometric mean diameter (GMD) of the granule size distribution was predicted over time using the coupled CFD-DEM-PBM framework and compared to dynamic experimental data. From comparison with the granule size measurements of samples taken during fluidization, the framework presented shows good accuracy at capturing the overall dynamics of the wet granulation system. A summary of the simulation framework findings is given in Table 6.9, Table 6.10 and Table 6.11.

Table 6.9: Summary of impact of operating air flow rate on FBG operation

Process variable	Effect of increasing variable	Overall impact
Airflow rate (Q_g)	On particle flow dynamics	Excess air flow rates
	Increase in bed expansion and average bed voidage	during an FBG operation leads to
	Increase in particle velocities; greater increase in Top compartment	collisions with high energy. This likely
	Increase in uniformity of particle distribution over the two compartments	results in increased breakage and attrition
	Increase in particle transfer rate from Bottom to Top compartment	of particles.
	On particle collision dynamics	
	Decrease in frequency of collisions between particles	
	Increase in average particle collision energy	
	On particle wetting and drying dynamics	
	Minimal increase in the mean residence time within spray zone	
	Increase in spread of heated air within granulator	
	Increase in rate of particle temperature change	

Table 6.10: Summary of impact of operating air temperature on FBG operation

Process variable	Effect of increasing variable	Overall impact
Inlet air temperature (T_g)	On particle flow dynamics	Evaporation rate is
	Negligible change in particle velocities	greatly enhanced with
	Minimal increase in particle transfer rate between compartments	increase in inlet air temperature. This can lead to increased
	On particle collision dynamics	breakage of particles
	Negligible change in particle collision frequency	and hence smaller
	Minimal increase in particle collision energy	granule size.
	On particle wetting and drying dynamics	
	Significant increase in heat transfer rate from gas to solid	

Table 6.11: Summary of impact of operating binder spray rate on FBG operation

Process variable	Effect of increasing variable	Overall impact
Binder spray rate (u_{spray})	Faster increase in liquid content of particles	Higher binder solution
	Increase in particle agglomeration rate	spray rate significantly increases the size and speed of granule growth.

Part IV

Conclusion

Granule growth is a complex particle process often occurring intentionally or unintentionally during various granular processes. The change of particulate size, whether through controlled granulation operations or undesired agglomerate formation, are common granule growth processes that occur at various stages of particulate production in powder manufacturing industries. Typically, the desirable size enlargement of microscopic powders is carried out through wet granulation operations to improve the handling of powder substances. During this unit operation, a mechanically stirred powder bed is introduced to dissolved binders through wet or dry addition to initiate granule growth. Granulating micron-scale, highly cohesive fine particles into larger agglomerates not only enhances the flowability of the powders but also improves several characteristics of the bulk powder including reduction of particle segregation which increases blend uniformity in the final product and improvement of powder compressibility which allows for adjustment and control of dissolution. Conversely, a common industrial occurrence of unwanted granule growth occurs during the mechanical agitation of wet filter cake during filter-dryer operations. The extensive use of agitation during different stages of filter-drying processes when combined with the effects of moisture content of the cake can induce attrition (breakage) or agglomeration of powder particles that were only meant to be isolated from the mother liquor. Enhanced process understanding of such granule growth phenomena are thus required to facilitate design, control, and optimization of such unit operations.

Understanding and predicting these granule growth processes, however, remains particularly challenging due to the simultaneous mass, momentum and heat transfers that could be occurring between particles in the system. Moreover, due to the wide variety of physicochemical properties of the wet granular systems and complex interacting influence of operating conditions, there are no universal models available to understand the particle-level behavior inside the vessels. The particle wetting rates during granulation, for instance, is highly dependent on the particle flow pattern which in turn is affected by the material properties of solids and fluids in the vessel as well as the operating conditions. The flow behavior of the powder within the granulator also depends on the geometry of the vessel. Several attempts are being made to understand the granular

flow pattern but many aspects of it (i.e., a more detailed study of the vessel geometry, particulate flow dynamics, collision frequencies etc.) using sophisticated modeling tools and techniques are yet to be developed. At a time when the Food and Drug Administration (FDA) guidelines strongly encourage the pharmaceutical industry to adopt the Quality by Design (QbD) approach and utilize Process Analytical Technology (PAT), the endeavor to investigate the complicated mechanistic phenomena of granule growth through experiment-only methods can be an arduous and expensive task. The traditional approach to rely heavily on experimentation programs for product and process design can thus be costly and time consuming and lengthen the time-to-market.

On the other hand, predictive models and simulations - such as those described in this work - that can link critical process and formulation parameters to quality attributes offer an alternate investigation platform that offers several advantages. One of the most important perks of adding a mechanistic model is the better physical understanding into the process mechanisms compared to the empirical relationship fitted using experimental data. The detailed mathematical models of the experimental process, for instance, can be used to develop model-based experimentation techniques which offers a means for analyzing experimental data and even for optimizing the design of the experiments themselves. While an empirical relationship maybe able to offer predictive capability within the design space tested, a model-based approach can maximize the information content of experiments, provide model parameters that increase the accuracy of process design, inform about risks, optimize process operation as well as increase the capability of describing process behavior accurately over a wide range of conditions.

This work provides an in-depth description of the development, implementation and assessment of various predictive tools and techniques of granular growth processes including use of dimensionless groups, advanced computational models as well as multi-scale frameworks to improve the performance of these models. This study presents a comprehensive look at the current state-of-the-art computational techniques used in granular and multi-phase flows and presents a practical framework for incorporating design-based principles and developing predictive model-based analysis to understand

granular processes through case studies. In the following thesis, three case studies involving manufacturing issues encountered in common unit operations are highlighted: (i) generation of undesired agglomeration during agitated filter-drying, (ii) formation of high/ low viscous regions during high-shear wet granulation with wet and dry binder addition, and (iii) prediction of granule size during top-spray fluidized bed wet granulation. The frameworks presented in this study demonstrate a pragmatic process model development methodology by efficiently coupling multi-scale/multi-phase simulations and numerical techniques which can be used for effective process design, development and scale-up purposes.

Part V

Acknowledgment of Previous Publications

The work presented in this dissertation represents original research by the author. The individual chapters presented here have previously appeared in prior publications of which the author of this dissertation is the first author. Parts of these publications have been modified to avoid redundancy and improve readability in this form.

The following publications were used as chapters in this thesis with the permission of the original publishers and co-authors:

- **A. Tamrakar**, A. Gunadi, P. M. Piccione, R. Ramachandran. Dynamic agglomeration profiling during the agitated drying phase in an agitated filter dryer: parametric investigation and regime map studies, *Powder Technology* 303 (2016) 109–123.
- **Tamrakar, A.**, Chen, S., Ramachandran, R. **2019**. A DEM model-based study to quantitatively compare the effect of wet and dry binder addition in high-shear wet granulation processes. *Chemical Engineering Research and Design*, 142, 307-326.
- **Tamrakar, A.**, Zheng, A., Piccione, P. M., Ramachandran, R. **2019** Investigating particle-level dynamics to understand bulk behavior in lab-scale agitated filter dryer (AFD) using Discrete Element Method (DEM) (*Manuscript in preparation*).
- **Tamrakar, A.**, Ramachandran, R. **2019**. CFD-DEM-PBM coupled model development and validation of a 3D top-spray fluidized bed wet granulation process, *Computers and Chemical Engineering*, 125, 249-270.
- **Tamrakar, A.**, Devarampally, D.R., Ramachandran, R. **2018**. Advanced multi-phase hybrid model development of fluidized bed wet granulation processes. *Book chapter in Process Systems Engineering for Pharmaceutical Manufacturing, Computer Aided Chemical Engineering*, 41, 159-187.
- **Tamrakar, A.**, Barrasso, D., Cruz, C.N., Ramachandran, R. **2015**. Multi-scale modelling of fluid bed granulation processes through a coupled PBM-DEM-CFD framework to facilitate QbD in pharmaceutical drug product manufacturing, *In conference proceedings: 7th International Granulation Workshop*.

Bibliography

- Adams, M., Edmondson, B., 1987. Forces between particles in continuous and discrete liquid media. *Tribology in particulate technology* 154, 172.
- Adamson, J., Faiber, N., Gottlieb, A., Hamsmith, L., Hicks, F., Mitchell, C., Mittal, B., Mukai, K., Papageorgiou, C. D., 2015. Development of suitable plant-scale drying conditions that prevent api agglomeration and dehydration. *Organic Process Research & Development* 20 (1), 51–58.
- Agrawal, R., Naveen, Y., 2011. Pharmaceutical processing—a review on wet granulation technology. *International journal of pharmaceutical frontier research* 1 (1), 65–83.
- Ålander, E. M., Å. C. Rasmuson, 2005. Mechanisms of crystal agglomeration of paracetamol in acetone-water mixtures. *Industrial and Engineering Chemistry Research* 44, 5788–5794.
- Ålander, E. M., Rasmuson, A. C., 2007. Agglomeration and adhesion free energy of paracetamol crystals in organic solvents. *AIChE Journal* 53 (10), 2590–2605.
- Ålander, E. M., Uusi-Penttilä, M. S., Å. C. Rasmuson, 2003. Characterization of paracetamol agglomerates by image analysis and strength measurement. *Powder Technology* 130, 298–306.
- Alobaid, F., Ströhle, J., Eppe, B., 2013. Extended cfd/dem model for the simulation of circulating fluidized bed. *Advanced Powder Technology* 24 (1), 403–415.
- Amritkar, A., Deb, S., Tafti, D., 2014. Efficient parallel cfd-dem simulations using openmp. *Journal of Computational Physics* 256, 501–519.
- Anand, A., Curtis, J. S., Wassgren, C. R., Hancock, B. C., Ketterhagen, W. R., 2009. Predicting discharge dynamics of wet cohesive particles from a rectangular hopper

- using the discrete element method (dem). *Chemical Engineering Science* 64 (24), 5268–5275.
- Arlabosse, P., Chitu, T., 2007. Identification of the limiting mechanism in contact drying of agitated sewage sludge. *Drying Technology* 25 (4), 557–567.
- Ashland, 2012. Klucel(tm) hydroxypropylcellulose physical and chemical properties.
- Barrasso, D., Ramachandran, R., 2012. A comparison of model order reduction techniques for a four-dimensional population balance model describing multi-component wet granulation processes. *Chemical Engineering Science* 80, 380–392.
- Barrasso, D., Ramachandran, R., 2015. Multi-scale modeling of granulation processes: Bi-directional coupling of pbm with dem via collision frequencies. *Chemical Engineering Research and Design* 93, 304–317.
- Barrasso, D., Tamrakar, A., Ramachandran, R., 2014. A reduced order PBM-ANN model of a multi-scale PBM-DEM description of a wet granulation process. *Chemical Engineering Science* 119, 319–329.
- Barrasso, D., Walia, S., Ramachandran., R., 2013. Multi-component population balance modeling of continuous granulation processes: A parametric study and comparison with experimental trends. *Powder Technology* 241, 85–97.
- Bharadwaj, R., Smith, C., Hancock, B. C., 2010. The coefficient of restitution of some pharmaceutical tablets/compacts. *International Journal of Pharmaceutics* 402 (1), 50–56.
- Birch, M., Marziano, I., 2013. Understanding and avoidance of agglomeration during drying processes: A case study. *Organic Process Research and Development* 17, 1359–1366.
- Blumberg, W., 1994. Atmospheric contact drying of granular beds wetted with a binary mixture. *Drying Technology* 12 (6), 1471–1484.

- Bokkers, G., van Sint Annaland, M., Kuipers, J., 2004. Mixing and segregation in a bidisperse gas–solid fluidised bed: a numerical and experimental study. *Powder Technology* 140 (3), 176–186.
- Börner, M., Peglow, M., Tsotsas, E., 2013. Derivation of parameters for a two compartment population balance model of wurster fluidised bed granulation. *Powder Technology* 238, 122–131.
- Bouwman, A. M., Henstra, M. J., Westerman, D., Chung, J. T., Zhang, Z., Ingram, A., Seville, J. P. K., Frijlink, H. W., 2005. The effect of the amount of binder liquid on the granulation mechanisms and structure of microcrystalline cellulose granules prepared by high shear granulation. *International Journal of Pharmaceutics* 290(1-2), 129–136.
- Bouwman, A. M., Visser, M. R., Meesters, G. M. H., Frijlink, H. W., 2006. The use of stokes deformation number as a predictive tool for material exchange behaviour of granules in the equilibrium phase in high shear granulation. *International Journal of Pharmaceutics* 318(1-2), 78–85.
- Börner, M., Bück, A., Tsotsas, E., 2017. DEM-CFD investigation of particle residence time distribution in top-spray fluidised bed granulation. *Chemical Engineering Science* 161, 187–197.
- Burggraef, A., Monteyne, T., Vervaet, C., Remon, J. P., Beer, T. D., 2005. Process analytical tools for monitoring, understanding, and control of pharmaceutical fluidized bed granulation: A review. *European Journal of Pharmaceutics and Biopharmaceutics* 83 (1), 2–15.
- Cameron, I., Wang, F., Immanuel, C., Stepanek, F., 2005. Process systems modelling and applications in granulation: A review. *Chemical Engineering Science* 60 (14), 3723–3750.
- Capece, M., Bilgili, E., Davé, R. N., 2014. Formulation of a physically motivated specific breakage rate parameter for ball milling via the discrete element method. *AIChE Journal* 60 (7), 2404–2415.

- Cavinato, M., Bresciani, M., Machin, M., Bellazzi, G., Canu, P., Santomaso, A. C., 2010a. Formulation design for optimal high-shear wet granulation using on-line torque measurements. *International Journal of Pharmaceutics* 387 (1), 48–55.
- Cavinato, M., Franceschinis, E., Cavallari, S., Realdon, N., Santomaso, A., 2010b. Relationship between particle shape and some process variables in high shear wet granulation using binders of different viscosity. *Chemical Engineering Journal and the Biochemical Engineering Journal* 164 (2-3), 292–298.
- CD-adapco, 2016. StarCCM+ Ver. 11.06.010 Documentation.
- Chang, S. A., Gray, D. G., 1978. The surface tension of aqueous hydroxypropyl cellulose solutions. *Journal of Colloid and Interface Science* 67 (2), 255–265.
- Chaturbedi, A., Bandi, C. K., Reddy, D., Pandey, P., Narang, A., Bindra, D., Tao, L., Zhao, J., Li, J., Hussain, M., et al., 2017. Compartment based population balance model development of a high shear wet granulation process via dry and wet binder addition. *Chemical Engineering Research and Design* 123, 187–200.
- Chaudhuri, B., Muzzio, F. J., Tomassone, M. S., 2006. Modeling of heat transfer in granular flow in rotating vessels. *Chemical Engineering Science* 61 (19), 6348–6360.
- Chaudhury, A., Armenante, M. E., Ramachandran, R., 2015a. Compartment based population balance modeling of a high shear wet granulation process using data analytics. *Chemical Engineering Research and Design* 95, 211–228.
- Chaudhury, A., Kapadia, A., Prakash, A. V., Barrasso, D., Ramachandran, R., 2013a. An extended cell-average technique for a multi-dimensional population balance of granulation describing aggregation and breakage. *Advanced Powder Technology* 24 (6), 962–971.
- Chaudhury, A., Niziolek, A., Ramachandran, R., 2013b. Multi-dimensional mechanistic modeling of fluid-bed granulation processes: An integrated approach. *Advanced Powder Technology* 24 (1), 113–131.

- Chaudhury, A., Tamrakar, A., Schöngut, M., Smrčka, D., Štěpánek, F., Ramachandran, R., 2015b. Multidimensional population balance model development and validation of a reactive detergent granulation process. *Industrial and Engineering Chemistry Research* 54, 842–857.
- Chaudhury, A., Wu, H., Khan, M., Ramachandran, R., 2014. A mechanistic population balance model for granulation processes: Effect of process and formulation parameters. *Chemical Engineering Science* 107, 76–92.
- Cliff, M., Parker, M., 1990. Scale-up of mixer granulators. In: *Proceedings of the 12th Interphex Conference*. Vol. 5. pp. 17–32.
- Cryer, S. A., 1999. Modeling agglomeration processes in fluid-bed granulation. *AIChE Journal* 45 (10), 2069–2078.
- Cundall, P. A., Strack, O. D., 1979. A discrete numerical model for granular assemblies. *geotechnique* 29 (1), 47–65.
- D'alonzo, G. D., O'connor, R. E., Schwartz, J. B., 1990. Effect of binder concentration and method of addition on granule growth in a high intensity mixer. *Drug Development and Industrial Pharmacy* 16 (12), 1931–1944.
- (DDB), T. D. D. B., 2016. Dortmund data bank software and separation technology (ddbst) thermophysical online database. <http://www.ddbst.com/>.
- DEMSolutions, 2014. EDEM 2.6 Theory Reference Guide. DEM Solutions.
- Di Renzo, A., Di Maio, F. P., 2004. Comparison of contact-force models for the simulation of collisions in DEM-based granular flow codes. *Chemical Engineering Science* 59 (3), 525–541.
- Ding, J., Gidaspow, D., 1990. A bubbling fluidization model using kinetic theory of granular flow. *AIChE Journal* 36 (4), 523–538.
- Dittler, A., Bamberger, T., Gehrman, D., Schlünder, E.-U., 1997. Measurement and simulation of the vacuum contact drying of pastes in a list-type kneader drier. *Chemical Engineering and Processing: Process Intensification* 36 (4), 301–308.

- Dosta, M., Antonyuk, S., Heinrich, S., 2012. Multiscale simulation of the fluidized bed granulation process. *Chemical Engineering & Technology* 35 (8), 1373–1380.
- Dosta, M., Antonyuk, S., Heinrich, S., 2013. Multiscale simulation of agglomerate breakage in fluidized beds. *Industrial & Engineering Chemistry Research* 52 (33), 11275–11281.
- Dosta, M., Heinrich, S., Werther, J., 2010. Fluidized bed spray granulation: analysis of the system behaviour by means of dynamic flowsheet simulation. *Powder Technology* 204 (1), 71–82.
- Drumm, C., Attarakih, M. M., Bart, H.-J., 2009. Coupling of cfd with dpbm for an rdc extractor. *Chemical Engineering Science* 64 (4), 721–732.
- Dürrig, T., 2016. Handbook of pharmaceutical granulation technology, 3rd Edition. CRC Press, Boca Raton, FL, Ch. Ch. 4: Binders in Pharmaceutical Granulation.
- Ende, D., Birch, M., Brenek, S., Maloney, M., 2013. Development and application of laboratory tools to predict properties upon scale-up in agitated filter-dryers. *Organic Process Research and Development* 17, 1345–1358.
- Ennis, B. J., Li, J., Robert, P., et al., 1990. The influence of viscosity on the strength of an axially strained pendular liquid bridge. *Chemical Engineering Science* 45 (10), 3071–3088.
- Freireich, B., Li, J., Litster, J. D., Wassgren, C., 2011. Incorporating particle flow information from discrete element simulations in population balance models of mixer-coaters. *Chemical Engineering Science* 66(15), 3592–3604.
- Freireich, B., Litster, J., Wassgren, C., 2009. Using the discrete element method to predict collision-scale behavior: a sensitivity analysis. *Chemical Engineering Science* 64 (15), 3407–3416.
- Fries, L., Antonyuk, S., Heinrich, S., Dopfer, D., Palzer, S., 2013. Collision dynamics in fluidised bed granulators: A dem-cfd study. *Chemical Engineering Science* 86, 108–123.

- Fries, L., Antonyuk, S., Heinrich, S., Palzer, S., 2011. DEM-CFD modeling of a fluidized bed spray granulator. *Chemical Engineering Science* 66 (11), 2340–2355.
- Ganderton, D., Jones, T., McGinity, J., 1995. *Advances in Pharmaceutical sciences*. Vol. 7. Elsevier.
- Gantt, J. A., Cameron, I. T., Litster, J. D., Gatzke, E. P., 2006. Determination of coalescence kernels for high-shear granulation using dem simulations. *Powder Technology* 170 (2), 53–63.
- Gantt, J. A., Gatzke, E. P., 2005. High-shear granulation modeling using a discrete element simulation approach. *Powder Technology* 156 (2), 195–212.
- Geldart, D., 1973. Types of gas fluidization. *Powder Technology* 7 (5), 285–292.
- Gernaey, K. V., Cervera-Padrell, A. E., Woodley, J. M., 2012. A perspective on pse in pharmaceutical process development and innovation. *Computers & Chemical Engineering* 42, 15–29.
- Gevaudan, A., Andrieu, J., 1991. Contact drying modelling of agitated porous alumina beads. *Chemical Engineering and Processing: Process Intensification* 30 (1), 31–37.
- Ghoroi, C., Gurumurthy, L., McDaniel, D. J., Jallo, L. J., Dave, R. N., 2013. Multifaceted characterization of pharmaceutical powders to discern the influence of surface modification. *Powder Technology* 236, 63–74.
- Gidaspow, D., 1994. *Multiphase flow and fluidization: continuum and kinetic theory descriptions*. Academic press.
- Goldman, A. J., Cox, R. G., Brenner, H., 1967. Slow viscous motion of a sphere parallel to a plane wall-i motion through a quiescent fluid. *Chemical Engineering Science* 22 (4), 637–651.
- Gopalakrishnan, P., Tafti, D., 2013. Development of parallel dem for the open source code mfix. *Powder Technology* 235, 33–41.

- Granberg, R. A., Rasmuson, A. C., 1999. Solubility of paracetamol in pure solvents. *Journal of Chemical and Engineering Data* 44(6), 1391–1395.
- Green, D. W., Perry, R. H., 1999. *Perry's chemical engineers' handbook*. McGraw-Hill Professional.
- Grünewald, G., Dinkova, A., Kind, M., 2007. Fluidized bed spray granulation - from process understanding to modeling of nucleation and dust integration. In: *European Congress of Chemical Engineering (ECCE-6)*.
- Hamilton, P., Littlejohn, D., Nordon, A., Sefcik, J., Slavin, P., Andrews, J., Dallin, P., 2013. Investigation of factors affecting isolation of needle-shaped particles in a vacuum-agitated filter drier through non-invasive measurements by raman spectrometry. *Chemical Engineering Science* 101, 878–885.
- Hancock, B., York, P., Rowe, R., 1994. An assessment of substrate-binder interactions in model wet masses. 1: Mixer torque rheometry. *International Journal of Pharmaceutics* 102 (1), 167–176.
- Hapgood, K. P., Litster, J. D., Biggs, S. R., Howes, T., 2002. Drop penetration into porous powder beds. *Journal of Colloid and Interface Science* 253 (2), 353–366.
- Hapgood, K. P., Litster, J. D., Smith, R., 2003. Nucleation regime map for liquid bound granules. *AIChE Journal* 49 (2), 350–361.
- Hare, C., Ghadiri, M., Dennehy, R., 2011. Prediction of attrition in agitated particle beds. *Chemical Engineering Science* 66, 4757–4770.
- Hattori, Y., Haruna, Y., Otsuka, M., 2013. Dissolution process analysis using model-free noyes–whitney integral equation. *Colloids and Surfaces, B: Biointerfaces* 102, 227–231.
- Heinrich, S., Peglow, M., Ihlow, M., Henneberg, M., Mörl, L., 2002. Analysis of the start-up process in continuous fluidized bed spray granulation by population balance modelling. *Chemical Engineering Science* 57(20) (20), 4369–4390.

- Hoomans, B., Kuipers, J., Briels, W., Van Swaaij, W., 1996. Discrete particle simulation of bubble and slug formation in a two-dimensional gas-fluidised bed: a hard-sphere approach. *Chemical Engineering Science* 51 (1), 99–118.
- Hotta, K., Takeda, K., Iinoya, K., 1974. The capillary binding force of a liquid bridge. *Powder Technology* 10 (4-5), 231–242.
- Hounslow, M., 1998. The population balance as a tool for understanding particle rate processes. *Kona Powder and Particle Journal* 16 (0), 179–193.
- Ierapetritou, M. G., Ramachandran, R., 2016. Process simulation and data modeling in solid oral drug development and manufacture. Humana Press.
- Iveson, S. M., Litster, J. D., 1998. Growth regime map for liquid-bound granules. *AIChE Journal* 44, 1510–1518.
- Iveson, S. M., Litster, J. D., Hapgood, K., Ennis, B. J., 2001. Nucleation, growth and breakage phenomena in agitated wet granulation processes: a review. *Powder Technology* 117 (1), 3–39.
- Iveson, S. M., Wauters, P. A. L., Forrest, S., Litster, J. D., Meesters, G. M. H., Scarlett, B., 2001. Growth regime map for liquid-bound granules: further development and experimental validation. *Powder Technology* 117, 83–97.
- Johnson, K. L., Johnson, K. L., 1987. Contact mechanics. Cambridge university press.
- Kafui, K., Thornton, C., 2000. Numerical simulations of impact breakage of a spherical crystalline agglomerate. *Powder Technology* 109 (1-3), 113–132.
- Kayrak-Talay, D., Dale, S., Wassgren, C., Litster, J., 2013. Quality by design for wet granulation in pharmaceutical processing: Assessing models for a priori design and scaling. *Powder Technology* 240, 7–18.
- Kayrak-Talay, D., Litster, J. D., 2011. A priori performance prediction in pharmaceutical wet granulation: Testing the applicability of the nucleation regime map to a formulation with a broad size distribution and dry binder addition. *International Journal of Pharmaceutics* 418 (2), 254–264.

- Ketterhagen, W. R., Bharadwaj, R., Hancock, B. C., 2010. The coefficient of rolling resistance (corr) of some pharmaceutical tablets. *International Journal of Pharmaceutics* 392 (1), 107–110.
- Kim, S., Lotz, B., Lindrud, M., Girard, K., Moore, T., Nagarajan, K., Alvarez, M., Lee, T., Nikfar, F., Davidovich, M., et al., 2005. Control of the particle properties of a drug substance by crystallization engineering and the effect on drug product formulation. *Organic process research & development* 9 (6), 894–901.
- Kohout, M., Collier, A. P., Stepanek, F., 2005. Vacuum contact drying kinetics: An experimental parametric study. *Drying Technology* 23, 1825–1839.
- Kom, P. K., Cook, W., Koungoulos, E., 2011. Impact of laboratory vacuum contact drying on material drying rates and physical properties. *Organic Process Research and Development* 15, 360–366.
- Koungoulos, E., Chadwick, C., Ticehurst, M., 2011. Impact of agitated drying on the powder properties of an active pharmaceutical ingredient. *Powder Technology* 210, 308–314.
- Kudra, T., Hashmi, K., 2010. Concentration of liquid feed in hydrocyclone to reduce drying energy use. *Drying Technology* 28, 1227–1232.
- Kudra, T., Mujumdar, A., 2009. *Advanced Drying Technologies*. CRC Press (Taylor and Francis Group).
- Kuipers, J., Van Duin, K., Van Beckum, F., Van Swaaij, W., 1993. Computer simulation of the hydrodynamics of a two-dimensional gas-fluidized bed. *Computers & Chemical Engineering* 17 (8), 839–858.
- Kuo, H., Knight, P., Parker, D., Adams, M., Seville, J., 2004. Discrete element simulations of a high-shear mixer. *Advanced Powder Technology* 15 (3), 297–309.
- Lambert, P., Chau, A., Delchambre, A., Régnier, S., 2008. Comparison between two capillary forces models. *Langmuir* 24 (7), 3157–3163.

- Lamberto, D. J., Cohen, B., Marencic, J., Miranda, C., Petrova, R., Sierra, L., 2011. Laboratory methods for assessing api sensitivity to mechanical stress during agitated drying. *Chemical Engineering Science* 66, 3868–3875.
- Landin, M., York, P., Cliff, M., Rowe, R., Wigmore, A., 1996. Scale-up of a pharmaceutical granulation in fixed bowl mixer-granulators. *International Journal of Pharmaceutics* 133 (1-2), 127–131.
- Larsson, A., Vogt, M. H., Herder, J., Luukkonen, P., 2008. Novel mechanistic description of the water granulation process for hydrophilic polymers. *Powder Technology* 188 (2), 139–146.
- Lee, H., Cho, H., Kwon, J., 2010. Using the discrete element method to analyze the breakage rate in a centrifugal/vibration mill. *Powder Technology* 198 (3), 364–372.
- Lekhal, A., Girard, K., Brown, M., Kiang, S., Glasser, B., Khinast, J., 2003. Impact of agitated drying on crystal morphology: K-cl-water system. *Powder Technology* 132, 119–130.
- Lekhal, A., Girard, K. P., Brown, M. A., Kiang, S., Khinast, J. G., Glasser, B. J., 2004. The effect of agitated drying on the morphology of l-threonine (needle-like) crystals. *International Journal of Pharmaceutics* 270, 263–277.
- Leuenberger, H., Bier, H., Sucker, H., 1981. Determination of the liquid requirement for a conventional granulation process. *Ger Chem Eng* 4, 13–18.
- Li, J., Freireich, B., Wassgren, C., Litster, J. D., 2012. A general compartment-based population balance model for particle coating and layered granulation. *AIChE Journal* 58(5), 1397–1408.
- Lian, G., Thornton, C., Adams, M. J., 1993. A theoretical study of the liquid bridge forces between two rigid spherical bodies. *Journal of Colloid and Interface Science* 161 (1), 138–147.
- Lian, G., Thornton, C., Adams, M. J., 1998. Discrete particle simulation of agglomerate impact coalescence. *Chemical Engineering Science* 53 (19), 3381–3391.

- Lim, H. L., Hapgood, K. P., Haig, B., 2016. Understanding and preventing agglomeration in a filter drying process. *Powder Technology* 300, 146–156.
- Link, J., Godlieb, W., Tripp, P., Deen, N., Heinrich, S., Kuipers, J., Schönherr, M., Peglow, M., 2009. Comparison of fibre optical measurements and discrete element simulations for the study of granulation in a spout fluidized bed. *Powder Technology* 189 (2), 202–217.
- Litster, J., Hapgood, K., Michaels, J., Sims, A., Roberts, M., Kameneni, S., 2002. Scale-up of mixer granulators for effective liquid distribution. *Powder Technology* 124 (3), 272–280.
- Litster, J., Hapgood, K., Michaels, J., Sims, A., Roberts, M., Kameneni, S., Hsu, T., 2001. Liquid distribution in wet granulation: dimensionless spray flux. *Powder Technology* 114 (1-3), 32–39.
- Liu, H., Li, M., 2014. Two-compartmental population balance modeling of a pulsed spray fluidized bed granulation based on computational fluid dynamics (CFD) analysis. *International Journal of Pharmaceutics* 475(1-2), 256–269.
- Liu, P., Yang, R., Yu, A., 2011. Dynamics of wet particles in rotating drums: effect of liquid surface tension. *Physics of Fluids* 23 (1), 013304.
- Lourenco, V., Lochmann, D., Reich, G., Menezes, J. C., Herdling, T., Schewitz, J., 2012. A quality by design study applied to an industrial pharmaceutical fluid bed granulation. *European Journal of Pharmaceutics and Biopharmaceutics* 81, 438–447.
- Luukkonen, P., Maloney, T., Rantanen, J., Paulapuro, H., Yliruusi, J., 2001. Microcrystalline cellulose-water interaction-a novel approach using thermoporosimetry. *Pharmaceutical Research* 18 (11), 1562–1569.
- Lyngberg, O., Bijns, L., Geens, J., Marchut, A., Mehrman, S., Schafer, E., 2016. Applications of modeling in oral solid dosage form development and manufacturing. *Process Simulation and Data Modeling in Solid Oral Drug Development and Manufacture*, 1–42.

- Martinez, J., Setterwall, F., 1991. Gas-phase controlled convective drying of solids wetted with multicomponent liquid mixtures. *Chemical Engineering Science* 46 (9), 2235–2252.
- Mazzone, D., Tardos, G., Pfeffer, R., 1987. The behavior of liquid bridges between two relatively moving particles. *Powder Technology* 51 (1), 71–83.
- McCabe, W. L., Smith, J. C., Harriott, P., 2005. Unit operations of Chemical Engineering, Seventh edition. Vol. 7. McGraw Hill.
- McCarthy, J. J., Khakhar, D. V., Ottino, J. M., 2000. Computational studies of granular mixing. *Powder Technology* 109 (1), 72–82.
- McLoughlin, C. M., McMinn, W. A. M., Magee, T. R. A., 2003. Physical and dielectric properties of pharmaceutical powders. *Powder Technology* 134(1-2), 40–51.
- Metta, N., Ierapetritou, M., Ramachandran, R., 2018. A multiscale dem-pbm approach for a continuous comilling process using a mechanistically developed breakage kernel. *Chemical Engineering Science* 178, 211–221.
- Mezdour, S., Cuvelier, G., Cash, M., Michon, C., 2007. Surface rheological properties of hydroxypropyl cellulose at air–water interface. *Food Hydrocolloids* 21 (5), 776–781.
- Michaud, A., Peczalski, R., Andrieu, J., 2008. Optimization of crystalline powders vacuum contact drying with intermittent stirring. *Chemical Engineering Research and Design* 86, 606–611.
- Mikami, T., Kamiya, H., Horio, M., 1998. Numerical simulation of cohesive powder behavior in a fluidized bed. *Chemical Engineering Science* 53 (10), 1927–1940.
- Millennium, E., Accessed: 2014. Equipment Range: Agitated Nutsche Filter Dryer (ANFD).
URL <http://www.millenniumequipments.com/images/mep1.pdf>
- Muddu, S., Tamrakar, A., Pandey, P., Ramachandran, R., 2018. Model development and validation of fluid bed wet granulation with dry binder addition using a population balance model methodology. *Processes* 6 (9), 154.

- Mujumdar, A. S., 2006. Handbook of industrial drying. CRC press.
- Murru, M., Giorgio, G., Montomoli, S., Ricard, F., Stepanek, F., 2011. Model-based scale-up of vacuum contact drying of pharmaceutical compounds. *Chemical Engineering Science* 66, 5045–5054.
- Nere, N. K., Allen, K. C., Marek, J. C., Bordawekar, S. V., 2012. Drying process optimization for an api solvate using heat transfer model of an agitated filter dryer. *Journal of Pharmaceutical Sciences* 101 (10), 3886–3895.
- Nordstrom, J., Welch, K., Frenning, G., Alderborn, G., 2008. On the role of granule yield strength for the compactibility of granular solids. *Journal of Pharmaceutical Sciences* 97 (11), 4807–4814.
- Norouzi, H. R., Mostoufi, N., Zarghami, R., Sotudeh-Gharebagh, R., 2016. Coupled CFD-DEM Modeling: Formulation, Implementation and Application to Multiphase Flows. John Wiley & Sons.
- Noyes, A. A., Whitney, W. R., 1897. The rate of solution of solid substances in their own solutions. *Journal of the American Chemical Society* 19 (12), 930–934.
- Osborne, J. D., Sochon, R. P., Cartwright, J. J., Doughty, D. G., Hounslow, M. J., Salman, A. D., 2011. Binder addition methods and binder distribution in high shear and fluidised bed granulation. *Chemical Engineering Research and Design* 89 (5), 553–559.
- Pandey, P., Levins, C., Pafiakis, S., Zacour, B., Bindra, D. S., Trinh, J., Buckley, D., Gour, S., Sharif, S., Stamato, H., 2018. Enhancing tablet disintegration characteristics of a highly water-soluble high-drug-loading formulation by granulation process. *Pharmaceutical Development and Technology* 23 (6), 587–595.
- Pandya, J., Spielman, L., 1983. Floc breakage in agitated suspensions: effect of agitation rate. *Chemical Engineering Science* 38 (12).
- Papageorgiou, C. D., Langston, M., Hicks, F., am Ende, D., Martin, E., Rothstein, S., Salan, J., Muir, R., 2016. Development of screening methodology for the assessment

- of the agglomeration potential of apis. *Organic Process Research & Development* 20 (8), 1500–1508.
- Parikh, D. M., 2010. *Handbook of Pharmaceutical Granulation Technology* (3rd. Ed.). CRC Press- Taylor and Francis Group.
- Parikh, D. M. (Ed.), 2016. *Handbook of Pharmaceutical Granulation Technology*, 3rd Edition. CRC Press, Taylor & Francis Group, Boca Raton, FL.
- Parker, M., York, P., Rowe, R., 1990. Binder-substrate interactions in wet granulation. 1: The effect of binder characteristics. *International Journal of Pharmaceutics* 64 (2-3), 207–216.
- Pelofsky, A. H., 1966. Surface tension-viscosity relation for liquids. *Journal of Chemical and Engineering Data* 11 (3), 394–397.
- Perlmutter, B. A., 2007. New techniques for solvent recovery and elimination of wastewater emissions during vacuum process operations. *Environmental Progress* 16(2), 132–136.
- Picker-Freyer, K. M., Dürig, T., 2007. Physical mechanical and tablet formation properties of hydroxypropylcellulose: in pure form and in mixtures. *AAPS PharmSciTech* 8 (4), 82.
- Pietsch, W. B., 1969. The strength of agglomerates bound by salt bridges. *Canadian Journal of Chemical Engineering* 47, 403–409.
- Pinto, M. A., Immanuel, C. D., Doyle III, F. J., 2007. A feasible solution technique for higher-dimensional population balance models. *Computers & chemical engineering* 31 (10), 1242–1256.
- Poon, J. M.-H., Immanuel, C. D., Doyle Iii, F. J., Litster, J. D., 2008. A three-dimensional population balance model of granulation with a mechanistic representation of the nucleation and aggregation phenomena. *Chemical Engineering Science* 63 (5), 1315–1329.

- Rabinovich, Y. I., Esayanur, M. S., Moudgil, B. M., 2005. Capillary forces between two spheres with a fixed volume liquid bridge: theory and experiment. *Langmuir* 21 (24), 10992–10997.
- Rajagopal, K., Renold, G. R. R., 2015. Effect of temperature on the volumetric, compressibility and viscometric properties of paracetamol in aqueous methanol solution. *Int. J. PharmTech Res.* 8(8), 180–195.
- Rajniak, P., Chern, R., Stepanek, F., 2006. Solution of population balance equations for wet granulation and combination with the FLUENT software.
- Rajniak, P., Mancinelli, C., Chern, R., Stepanek, F., Farber, L., Hill, B., 2007. Experimental study of wet granulation in fluidized bed: impact of the binder properties on the granule morphology. *International Journal of Pharmaceutics* 334 (1), 92–102.
- Rajniak, P., Stepanek, F., Dhanasekharan, K., Fan, R., Mancinelli, C., Chern, R., 2009. A combined experimental and computational study of wet granulation in a wurster fluid bed granulator. *Powder Technology* 189 (2), 190–201.
- Ramachandran, R., Immanuel, C. D., Štěpánek, F., Litster, J. D., Doyle III, F. J., 2009. A mechanistic model for breakage in population balances of granulation: Theoretical kernel development and experimental validation. *Chemical Engineering Research and Design* 87 (4), 598–614.
- Ramaker, J., Jelgersma, M. A., Vonk, P., Kossen, N., 1998. Scale-down of a high-shear pelletisation process: flow profile and growth kinetics. *International Journal of Pharmaceutics* 166 (1), 89–97.
- Reichardt, C., 2003. *Solvents and Solvent Effects in Organic Chemistry*. Wiley-VCH.
- Remy, B., Glasser, B. J., Khinast, J. G., 2010. The effect of mixer properties and fill level on granular flow in a bladed mixer. *AIChE Journal* 56 (2), 336–353.
- Remy, B., Kightlinger, W., E. M Saurer, N. D., Glasser, B., 2014. Scale-up of agitated drying: Effect of shear stress and hydrostatic pressure on active pharmaceutical ingredient powder properties. *AIChE Journal*, 1–12.

- Remy, B., Kightlinger, W., Saurer, E. M., Domagalski, N., Glasser, B. J., 2015. Scale-up of agitated drying: Effect of shear stress and hydrostatic pressure on active pharmaceutical ingredient powder properties. *AIChE Journal* 61 (2), 407–418.
- Reynolds, G., Fu, J., Cheong, Y., Hounslow, M., Salman, A., 2005. Breakage in granulation: a review. *Chemical Engineering Science* 60 (14), 3969–3992.
- Rhodes, M. J., 2008. *Introduction to particle technology*. John Wiley & Sons.
- Roberts, R., Rowe, R., York, P., 1994. The poisson's ratio of microcrystalline cellulose. *International Journal of Pharmaceutics* 105 (2), 177–180.
- Rojas, J., Lopez, A., Guisao, S., Ortiz, C., 2011. Evaluation of several microcrystalline celluloses obtained from agricultural by-products. *Journal of advanced pharmaceutical technology & research* 2 (3), 144.
- Rough, S. L., Wilson, D. I., York, D. W., 2005. A regime map for stages in high shear mixer agglomeration using ultra-high viscosity binders. *Advanced Powder Technology* 16(4), 373–386.
- Rowe, R., Sadeghnejad, G., 1987. The rheology of microcrystalline cellulose powder/water mixes-measurement using a mixer torque rheometer. *International Journal of Pharmaceutics* 38 (1-3), 227–229.
- Rumpf, H., Knepper, N., 1962. *Agglomeration interscience*.
- Sahni, E. K., Bogner, R. H., Chaudhuri, B., 2013. Systematic investigation of parameters affecting the performance of an agitated filter-dryer. *Journal of Pharmaceutical Sciences* 102, 2198–2213.
- Sahni, E. K., Chaudhuri, B., 2012. Contact drying: A review of experimental and mechanistic modeling approaches. *International Journal of Pharmaceutics* 434 (1), 334–348.
- Sastry, K. V., Fuerstenau, D., 1973. Mechanisms of agglomerate growth in green pelletization. *Powder Technology* 7 (2), 97–105.

- Sau, D., Biswal, K., 2011. Computational fluid dynamics and experimental study of the hydrodynamics of a gas–solid tapered fluidized bed. *Applied Mathematical Modelling* 35 (5), 2265–2278.
- Schlünder, E., 1980. Contact drying of particulate material under vacuum. In: *First Intl. Vol. 6*. pp. 3–5.
- Schlünder, E.-U., 1984. Heat transfer to packed and stirred beds from the surface of immersed bodies. *Chemical Engineering and Processing: Process Intensification* 18 (1), 31–53.
- Schlünder, E.-U., Mollekopf, N., 1984. Vacuum contact drying of free flowing mechanically agitated particulate material. *Chemical Engineering and Processing: Process Intensification* 18 (2), 93–111.
- Seader, J., Henley, E., 2001. *Separation Process Principles*, 2nd Edition. John Wiley and Sons, Inc.
- Sen, M., Barrasso, D., Singh, R., Ramachandran, R., 2014. A multi-scale hybrid cfd-dem-pbm description of a fluid-bed granulation process. *Processes* 2 (1), 89–111.
- Sen, M., Dubey, A., Singh, R., Ramachandran, R., 2012. Mathematical development and comparison of a hybrid pbm-dem description of a continuous powder mixing process. *Journal of Powder Technology*.
- Shaikh, M., Shafiq, M., Farooqui, M., 2011. Density and viscosity studies of paracetamol in ethanol + water system at 301.5k. *Journal ISSN: 0976-9595* 2(2), 21–26.
- Sharratt, P. N., 1997. *Handbook of Batch Process Design*. Blackie Academic and Professional.
- Shi, D., McCarthy, J. J., 2008. Numerical simulation of liquid transfer between particles. *Powder Technology* 184 (1), 64–75.
- Siebold, A., Walliser, A., Nardin, M., Oppliger, M., Schultz, J., 1997. Capillary rise for thermodynamic characterization of solid particle surface. *Journal of Colloid and Interface Science* 186 (1), 60–70.

- Sören, S., Jürgen, T., 2012. Simulation of a filtration process by DEM and CFD. *Journal* ISSN: 1929-2724 1(1), 28–35.
- Tamrakar, A., Barrasso, D., Cruz, C., Ramachandran, R., 2015. Multi-scale modelling of fluid bed granulation processes through a coupled pbm-dem-cfd framework to facilitate qbd in pharmaceutical drug product manufacturing. In: 7th International Granulation Workshop.
- Tamrakar, A., Devarampally, D. R., Ramachandran, R., 2018. Advanced multiphase hybrid model development of fluidized bed wet granulation processes. *Computer Aided Chemical Engineering* 41, 159–187.
- Tamrakar, A., Gunadi, A., Piccione, P. M., Ramachandran, R., 2016. Dynamic agglomeration profiling during the drying phase in an agitated filter dryer: Parametric investigation and regime map studies. *Powder Technology* 303 (Supplement C), 109 – 123.
- Tan, H., Salman, A., Hounslow, M., 2006. Kinetics of fluidized bed melt granulation–ii: modelling the net rate of growth. *Chemical Engineering Science* 61 (12), 3930–3941.
- Tan, H. S., Goldschmidt, M. J. V., Boerefijn, R., Hounslow, M. J., Salman, A. D., Kuipers, J. A. M., 2004. Building population balance model for fluidized bed melt granulation: lessons from kinetic theory of granular flow. *Powder Technology* 142 (2), 103–109.
- Tardos, G. I., Hapgood, K. P., Ipadeola, O. O., Michaels, J. N., 2004. Stress measurements in high-shear granulators using calibrated 'test' particles: application to scale-up. *Powder Technology* 140 (3), 217–227.
- Tardos, G. I., Khan, M. I., Mort, P. R., 1997. Critical parameters and limiting conditions in binder granulation of fine powders. *Powder Technology* 94 (3), 245–258.
- Thurner, F., Schlünder, E., 1986. Progress towards understanding the drying of porous materials wetted with binary mixtures. *Chemical Engineering and Processing: Process Intensification* 20 (1), 33–41.

- Tsotas, E., Mujumdar, A., 2012. Modern Technology: Volume 4-Energy Savings. Wiley-VCH Verlag GmbH and Co. KGaA.
- Tsotsas, E., Kwapinska, M., Saage, G., 2007. Modeling of contact dryers. *Drying Technology* 25 (7-8), 1377–1391.
- Tsotsas, E., Schlünder, E., 1986a. Contact drying of mechanically agitated particulate material in the presence of inert gas. *Chemical Engineering and Processing: Process Intensification* 20 (5), 277–285.
- Tsotsas, E., Schlünder, E., 1986b. Vacuum contact drying of free flowing mechanically agitated multigranular packings. *Chemical Engineering and Processing: Process Intensification* 20 (6), 339–349.
- Tsotsas, E., Schlünder, E., 1987. Vacuum contact drying of mechanically agitated beds: the influence of hygroscopic behaviour on the drying rate curve. *Chemical Engineering and Processing: Process Intensification* 21 (4), 199–208.
- Tsuji, Y., Kawaguchi, T., Tanaka, T., 1993. Discrete particle simulation of two-dimensional fluidized bed. *Powder Technology* 77 (1), 79–87.
- Tu, W., Ingram, A., Seville, J., Hsiau, S., 2009. Exploring the regime map for high-shear mixer granulation. *Chemical Engineering Journal and the Biochemical Engineering Journal* 145(3), 505–513.
- Verkoeijen, D., Pouw, G. A., Meesters, G. M. H., Scarlett, B., 2002. Population balances for particulate processes-a volume approach. *Chemical Engineering Science* 57 (12), 2287–2303.
- Vidaurre, M., Martínez, J., 1997. Continuous drying of a solid wetted with ternary mixtures. *AIChE Journal* 43 (3), 681–692.
- Vreman, A., Van Lare, C., Hounslow, M., 2009. A basic population balance model for fluid bed spray granulation. *Chemical Engineering Science* 64 (21), 4389–4398.

- Walker, G., Bell, S., Vann, M., Zhai, H., Jones, D., Andrews, G., 2007. Pharmaceutically engineering powders using flhmg: The effects of process parameters and formulation variables. *Chemical Engineering Research and Design* 85 (7), 981–986.
- Washino, K., Miyazaki, K., Tsuji, T., Tanaka, T., 2016. A new contact liquid dispersion model for discrete particle simulation. *Chemical Engineering Research and Design* 110, 123–130.
- Wen, C., Yu, Y., 1966. A generalized method for predicting the minimum fluidization velocity. *AIChE Journal* 12 (3), 610–612.
- Yadav, P., Chauhan, J., Kannoja, P., Jain, N., Tomar, V., 2010. A review: On scale-up factor determination of rapid mixer granulator. *Der. Pharmacia Lettre* 2 (5), 23–38.
- Yan, J.-H., Deng, W.-Y., Li, X.-D., Wang, F., Chi, Y., Lu, S.-Y., Cen, K.-F., 2009. Experimental and theoretical study of agitated contact drying of sewage sludge under partial vacuum conditions. *Drying Technology* 27 (6), 787–796.
- Yan, W.-C., Luo, Z.-H., Guo, A.-Y., 2011. Coupling of cfd with pbm for a pilot-plant tubular loop polymerization reactor. *Chemical Engineering Science* 66 (21), 5148–5163.
- York, P., Rowe, R., 1994. Monitoring granulation size enlargement process using mixer torque rheometry. In: *First International Particle Technology Forum*, Denver, USA.
- Yuu, S., Umekage, T., Johno, Y., 2000. Numerical simulation of air and particle motions in bubbling fluidized bed of small particles. *Powder Technology* 110 (1), 158–168.
- Zhang, S., Lamberto, D. J., 2014. Development of new laboratory tools for assessment of granulation behavior during bulk active pharmaceutical ingredient drying. *Journal of Pharmaceutical Sciences* 103, 152–160.
- Zhu, H., Zhou, Z., Yang, R., Yu, A., 2007. Discrete particle simulation of particulate systems: theoretical developments. *Chemical Engineering Science* 62 (13), 3378–3396.